Wind Shielding Analysis for Cold Regions Using Experimental and Numerical Techniques

A thesis Submitted to the University of Hertfordshire in Partial Fulfilment of the Requirements for the Degree of

Doctor of Philosophy

By

Yizhong Xu

Supervised by

Drs: George Haritos, Mohamad Y. Mustafa, Muhammad S. Virk and Jason Knight

February 2016

PUBLICATIONS

Journal Papers:

1. Mustafa, M. Y., Xu, Yizhong., Haritos, G. & Kenji, K., 2016. Measurement of wind flow behavior at the leeward side of porous fences using ultrasonic anemometer device. Journal of *Energy Procedia,* Volum 85, pp. 350-357.
2. Xu, Yizhong. & Mustafa, M. Y., 2015. Investigation of the structure of airflow behind a porous fence aided by CFD based virtual sensor data. Journal of *Sensors & Transducers*, 185(2), pp. 149-155.
3. Xu, Yizhong. et al., 2013. Factors influencing the performance of porous wind shields. Journal of *Applied Mechanics and Materials,* Volum 321, pp. 799-803.

Conference Papers:

1. Xu, Yizhong., Mustafa, M. Y. & Polanco, G., 2014. *3D CFD investigation of air flow behind a porous fence using different turbulence models.* Copenhagen, Denmark, ASME 2014 12TH Biennial Conference on Engineering Systems Design and Analysis.
2. Xu, Yizhong., Mustafa, M. Y. & Solvang, W. D., 2014. *CFD aided cognitive capabilities for analyzing snowdrift development around a porous fence.* Vietri sul Mare, Italy, 5th IEEE International Conference on Cognitive Infocommunications.
3. Xu, Yizhong. et al., 2013. *3D CFD modelling of air flow through a porous fence.* Budapest, Hungary, 4th IEEE International Conference on Cognitive Infocommunications.
4. Polanco, G., Xu, Yizhong. & Mustafa, M. Y., 2013. *Conceptual approach applied to experiments design for noise mitigation in porous panels used on oil and gas platforms.* Budapest, Hungary, 4th IEEE International Conference on Cognitive Infocommunications.

ABSTRACT

The thesis presents a systematic experimental and numerical study on the interactions among porous fence, airflow, and windblown snowdrifts, a knowledge that will contribute to optimize the performance of porous wind shielding system in Cold Regions. A comprehensive review of the concepts, theories, techniques, and key findings associated with the research work has been undertaken. The key technical parameters influencing fence performance have been systematically studied by means of wind tunnel experimental investigations and Computational Fluid Dynamics (CFD) simulations.

The study has found that porosity is the most influential structural parameter affecting the performance of porous fences in many aspects. Fence height stands a significant positive position in terms of its performance. It was found that fence performance is not sensitive to the changes of approaching atmospheric airflow velocity. Nevertheless, a bottom gap can improve snow fence trap efficiency. All of those findings agree with most of the findings of other researchers, which affirms that the research methodology adopted in this research is sound.

Physical experimental work was performed to assess the reliability and credibility of the numerical models. Those models have been intentionally simplified, which made them easier to construct and quicker to obtain numerical solutions at a lower computational cost. Furthermore, the numerical models demonstrate the level of competence acquired through this research that is implemented in the optimisation of fence design.

Special attention has been paid to the issues where elaborate research work has not been systematically reached in the open literature, this includes areas such as the effects of arrangement of porous holes, fence surface shear, and directions of wind load with respect to the fence, etc. Correlation between the reattachment length, the shelter distance, and the creation and distribution of fence surface shear is reported, to the author's knowledge, for the first time in the open literature. General guidelines for the design of shelters based on porous fences have been established through this study. For example, the desirable size of hole range should be identified beforehand, and porous holes with sharp angular corners should usually be avoided in the fence design. It is recommended to place the fence within an angle of 30° to the wind load, where the effective shelter distance can be

estimated in a linearized equation, and the normal drag coefficient can be described as a function of $cos^2\theta$. Optimal design of the arrangement of porous holes will maximize the fence performance, especially when the close fence environment is of concern.

Although the definition of fence effective zone is still vague in the research field, the key factors influencing the fence effective zone have been investigated by evaluating the reduction of wind velocity leeward of the fence in this thesis. It is found that the fence effective zone is not sensitive to the change of approaching airflow velocity, and that increasing fence height will increase the physical size of the fence effective zone, but not in a proportional manner. It is also concluded that fence effective zone will be significantly reduced when the non-normal wind load is inclined at an angle greater than *30°* to the fence. The effective zone increases effectively when the fence porosity is optimal.

In contrast to the majority of published research work, the transient snow transport model presented in this work considers the snow transport rate as a whole without distinguishing the rate in saltation and suspension layer. The numerical study indicated that the position of the snow crest is mainly determined by the fence height, while porosity and bottom gap mainly affect the downwind deposition length. The optimal porosity for snow fences is in the range of *0.4* to *0.5*, which is greater than the one for wind fences, which lies in the range from *0.25* to *0.35*. *Two* snow crests have been observed leeward the fence at the onset of snow deposition, when the fence was placed without a bottom gap to the snow ground. This finding has not been encountered in any of the reported research work.

Wind tunnel simulations of snowdrift around the fences have marginally under-predicted the sizes of snow deposition. The numerical predictions were quantitatively and qualitatively in good agreement with the field observations. This incompetence of wind tunnel experiments on porous fences implies that numerical modelling can play a more important role in snow fence research.

Keywords: porous fence; Cold Regions; wind tunnel experiment; CFD modelling; evaluation & design;

CONTENTS

NOMENCLATURE

CFD	Computational Fluid Dynamics
NOK	Norwegian Kroner
PIV	Particle Image Velocimetry
2D	2 Dimensional
3D	3 Dimensional
CCD	Charge-Coupled Device
ABL	Atmospheric Boundary Layer
PMT	Point-Measuring Technique
HWA	Hot-Wire Anemometer
PWA	Pulsed-Wire Anemometer
LDA	Laser-Doppler Anemometer
PDA	Phase-Doppler Anemometer
UA	Ultrasonic Anemometer
WFMT	Whole-Field-Measuring Technique
PTV	Particle Tracking Velocimetry
NSE	Navier-Stokes Equation
DNS	Direct Numerical Simulation
LES	Large Eddy Simulation
RANS	Reynolds-Averaged Navier-Stokes Equation
RNG	Renormalization Group
RSM	Reynolds Stress Model
VLES	Very Large Eddy Simulation
EVM	Eddy-Viscosity Model
VOF	Volume of Fluid

FAVOR	Fractional Area/Volume Obstacle Representation Technique
LDM	Laser Displacement Meter
TKE	Turbulent Kinetic Energy
DES	Detached Eddy Simulation
SST	Shear Stress Transport
FVM	Finite-Volume Method
PDE	Partial-Differential Equation
SIMPLE	Semi-Implicit Method for Pressure Linked Equations

LIST OF FIGURES

LIST OF APPENDIX FIGURES

LIST OF TABLES

Acknowledgement

I would like to express my deepest gratitude to Drs George Haritos from University of Hertfordshire and Mohamad Y. Mustafa from the Arctic University of Norway, for the dedicated and excellent supervisions of this work. It would be impossible for me to bring the research to a completion without their guidance, encouragement and support throughout the duration of this research. Many thanks to the supervision team, Professor Muhammad S. Virk from the Arctic University of Norway and Dr Jason Knight from University of Portsmouth, for their professional help and valuable advises.

I would like to thank the School of Engineering and Technology, University of Hertfordshire, for supporting the research.

I am grateful to my employer the Arctic University of Norway for providing research resources and financial support. I would also thank all of my colleagues, especially to Professors Bjørn R. Sørensen, Børre Bang, Wei Deng Solvang and Rajnish K. Calay, for giving instructive advises and unreserved support.

Many thanks to Dr Christian Petrich, the ColdTech Project Manager from Norut Northern Research Institute, for his kind support.

Thanks to the industrial partner IKM dsc AS, Norway for providing the experimental materials and technical guides. My thanks must go to the members of Shinjo Cryospheric Environment Laboratory, Japan. In particular to Drs Kosugi Kenji and Genzo Okawa. It would have been difficult for me to complete the wind tunnel experiment without their help and support.

Special thanks to my former supervisor Dr William Tiu.

Finally, I would like to thank my family and friends for all their support. My special thanks go to my beloved wife Tingting Xie and my parents for their endless love, understanding, and everything.

Chapter 1 INTRODUCTION

1.1. BACKGROUND OF THE RESEARCH

Cold regions are part of the earth system characterized by the presence of snow and ice at least part of the year. There are three accepted ways to define a "Cold Region": 1) Air temperature; 2) Ice cover in lakes, rivers and harbours (on land) and sea ice extent (over the ocean); and 3) Permafrost. A broadly accepted definition of Cold Region is to use the *0°C* isotherm in the coldest month of the year (Bates & Bilello, 1966). Geologically, Cold Regions may be loosely categorized as the Polar and sub-Polar regions. Chronologically, Cold Regions have experienced three periods of human activities: exploration, engineering development, and scientific research. Large engineering projects in Cold Regions include both on land and in marine environment, such as new human habitations, dams, bridges, airports and seaports, offshore platforms, highways and railroads, etc. With the development of technology, these Cold Regions, previously too cold for human activities, become more accessible and sustainable.

The lure of uncovered natural resources in Cold Regions further attracts humans to develop. In Cold Regions like Norway, exports of oil and gas have become the most important elements of the economy since the discovery of North Sea oil in Norwegian waters during the late 1960s. In its *2014* business trend report (Norwegian Oil and Gas Association, 2014), the offshore resource based on which the petroleum sector builds has contributed to about *250 000* jobs nationwide through the high-tech and internationally competitive activities and substantial spin-offs for Norwegian society. Since activities began on the Norwegian continental shelf, the industry has created value totalling more than NOK *11 000* billion in current money. Moreover, an extensive supplies industry has been built up into Norway's second largest export sector after petroleum itself. It employs almost *200 000* people in *4 000* companies and has an annual turnover of more than NOK *360* billion (Norwegian Oil and Gas Association, 2014).

The majority of oil and gas resources are deposited offshore around Norway. Using oil platforms to extract oil and gas is therefore a general practice in the Norwegian petroleum

industry. An oil platform, also referred to as an offshore platform, is a large structure with facilities to drill wells, to extract and process oil and natural gas, and to temporarily store the product until it can be brought to shore for refining and marketing. With the prospect of exploration for oil and gas in the Barents Sea, there is an increasingly strong need to design an optimal wind shielding system in the offshore platform. It should not only offer the effective protection for workforce and facilities from the harsh weather conditions, but also secure natural ventilation to remove any ejected fumes within the confined space.

A porous fence is an artificial structure with openings of certain shape, size and distribution to effectively reduce the damages caused by wind and sediments transported (i.e. drifting snow and accumulating ice), and improve work conditions for workers and machinery. It is one of the artificial wind shielding structures widely applied in Cold Region, in the form of windbreaks allowing the natural climate to be controlled.

Basically, the performance of a porous fence is evaluated by the reduction of the wind velocity and the effective shelter distance (Tabler, 2003) (Dong, et al., 2010). An optimum wind fence is required to create the greatest wind reduction over the longest shelter distance. Experimental results revealed that as a wind flow impinges on a porous fence, the momentum in the wake region is enhanced (Raine & Stevenson, 1977). It implies the complex variations in turbulence intensity, shear stress and pressure, caused by the presence of a wake flow behind the porous fence, will affect the shelter distance. A porous fence should therefore be able to provide the optimal shelter effects by balancing the reduction in wind velocity and the effects on shelter distance caused by the changes in turbulence and the other factors, which include the fence height, overall porosity, opening size and shape, porosity distribution and fence orientation (Cornelis & Gabriels, 2005).

Most experimental tests have been conducted in wind tunnels to investigate the physical behaviors of downstream wind flow (Fang & Wang, 1997) (Shiau & Kim, 1999) (Yeh, et al., 2010) (Otakeguchi, et al., 2012) (Ping , et al., 2013) (Telenta, et al., 2014) (Li & Sherman, 2015). Computational Fluid Dynamics (CFD) simulation, as a flexible, efficient and relatively cheap alternative with the continued development of numerical models and the availability of powerful computational capacities, is now widely employed in commercial wind engineering in recent decades (Alhajraf, 2004) (Hargreaves & Wright,

2007) (Andres , et al., 2011) (Blocken, 2014) (Telenta, et al., 2014) (Li & Sherman, 2015) (Hong, et al., 2015). Many researchers discovered that porosity of a wind fence is the most influential design structural parameter in determining the wake characteristics behind the fence. Interesting findings include that, at different porosity, the downstream flow exhibits a range of phenomena: full separation at a fence at low porosity, a downstream separation and reattachment at moderate porosity, and no separation at high porosity (Packwood, 2000). However, due to the complex characteristics of airflow around the porous fence, systematic numerical and experimental research is required to achieve a further scientific understanding of the interactions among the porous fence, the wind flow and the drifting snow, a knowledge that will lead to the optimization of the porous fence design.

1.2. APPLICATIONS OF POROUS FENCES IN COLD REGIONS

Fence is one of the earliest measures used to improve windy and snowy climatic conditions to serve human needs. It has been widely used in coastal, arid, and cold areas to control wind and to retard wind driven sediments (i.e. snow or sand particles).

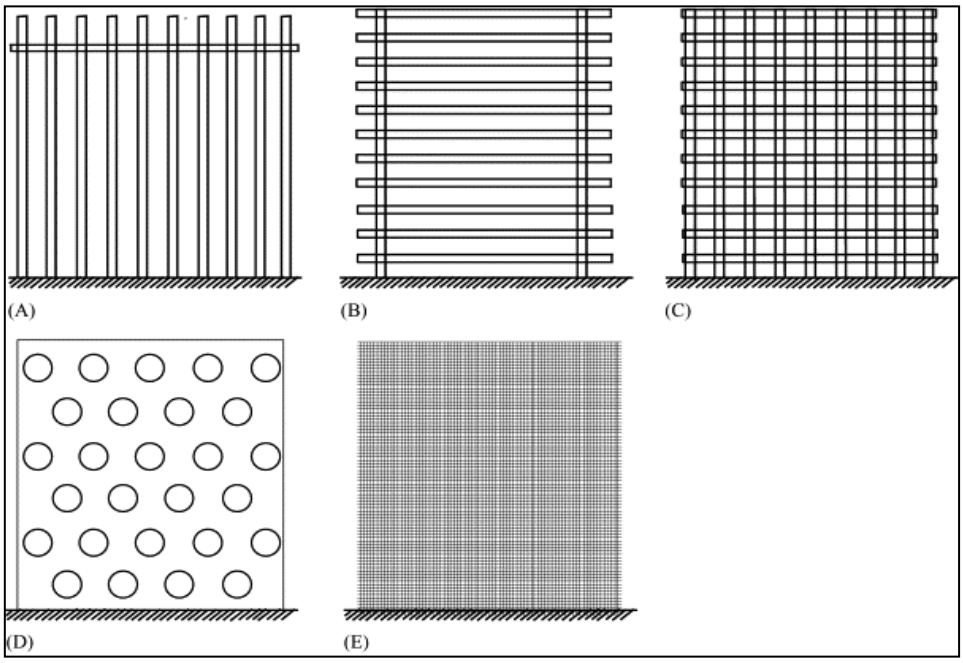

Figure 1-1:Types of artificial fence: (A) upright fence, (B) horizontal fence, (C) gridded fence, (D) holed-plank fence, and (E) wind-screened fence (Dong, et al., 2007).

Wind shielding systems can be in the form of natural windbreaks or artificial fences. Natural windbreaks such as natural foliage, tall hedgerows, and tree-lines can create low velocity regions by blocking or retarding ground level winds and diverting higher winds over the area to be shielded (Wang & Takle, 1995) (Torita & Satou, 2007).

A properly designed porous wind shielding system can not only serve as the windbreaks to effectively reduce the damages caused by wind and sediments transported (i.e. drifting snow and accumulating ice) but also provide the natural ventilation to remove any ejected fumes within the confined space. Figure 1-1 shows the various types of artificial wind fences commonly used to produce artificial windbreaks and block small particle intrusions. Materials of an artificial fence can be metal, plastics, or wood, etc.

In Cold Regions, heavy snow is a common phenomenon in the wintry seasons that induces hazards to human activities. Artificial snow fences are often applied to mitigate such damages. Figure 1-2 shows the picture of the snow fences placed to protect the driveway in Norway.

Figure 1-2: Snow fences to protect the driveway in Norway

Figure 1-3 (a) shows the picture of the Ekofisk Conoco-Philips Platform taken during the visit of the construction site at Aker Solution AS, Norway in July 2013. The red coloured arrows point at the wind shielding panels installed on the platform. Figure 1-3 (b) shows the details of the porous wind fence installed on the Ekofisk Conoco-Philips Platform.

(a) **(b)**

Figure 1-3: (a) The Ekofisk Conoco-Phillips platform under construction, (b) detailed view of the porous fence on the platform.

Countries such as Norway have comprehensively regulations regarding the issues related to environment, emergency preparedness, health, and safety in the petroleum industry. Details of the standard requirements with regard to wind shielding panels set up by Standards Norway are as follows (Standards Norway, 2006):

- The minimum metal thicknesses of wind shielding panels shall be in accordance with project requirements, but never less than *0.8mm* for stainless steel and coated galvanized steel, and *1.0mm* for aluminum;
- The wind shielding panel system shall be bolted to pre-installed back-up steel on the module to receive the system. The windshield panel joints shall be either overlapping with bolting through separation gaskets, or of a 'lock form' type;
- Fire resistant flute fillers shall be provided, if required.

1.3. AIMS AND OBJECTIVES OF THE THESIS

While porous fences as common wind shielding devices have been used for a long time, study on the optimization of the performance still attracts the scientific and industrial interest. Especially for the applications in Cold Regions, knowledge of adverse environmental implications is still limited.

The research aims to:

- Apply a joint approach using experimental and numerical techniques that

systematically investigates the mechanism and interactions among various porous fences, airflows, and windblown sediment transport, which contributes knowledge to the optimal designs and applications of porous fences, particularly for Cold Regions.

The objectives of the research are as follows:

- To carry out a comprehensive literature review of the fundamental knowledge and techniques related to the optimum design of porous fence and the up to date research outcomes of the interactions among the porous fence, wind flow and snowdrifts;
- To identify the key technical parameters on the performance of porous fence;
- To evaluate the performance of the different porous fences by the means of experimental and numerical techniques;
- To provide useful and new knowledge to the optimal porous fence design especially applicable in Cold Regions.

1.4. LAYOUT OF THE THESIS

This thesis presents the research work carried out for the PhD study titled "Wind shielding study for Cold Regions using experimental and numerical techniques". It consists of seven Chapters as follows.

Chapter 1 gives a brief introduction of the background and the applications of porous fences and defines the research aim and objectives.

Chapter 2 is a comprehensive literature review of the concept, theories, techniques, and key findings in the field related. The literature survey obtains the fundamental and updated knowledge in the research field, through which, the issues to be addressed in this thesis are identified.

Chapter 3 explains the research methodology employed in the thesis. The design and justification of the experiments and numerical simulations are discussed, and a flowchart of the research methodology is presented too.

Chapter 4 presents the experimental study of single-phase airflow and two-phase snowdrift flow around different porous fences. It provides the details of the wind tunnel test set-up & testing procedures and the experimental results. The effects of key technical parameters on the fence performance have been investigated and discussed. The justification of the experimental study is included.

Numerical studies are presented in Chapter 5 and Chapter 6. The numerical study on the single-phase airflow around the different porous fences is concluded in Chapter 5. Chapter 6 is the numerical study on the two-phase snowdrift flow around the different porous fences. The numerical models are assessed against corresponding experimental results before carrying out further study. The detailed model set-up and justifications of the simulations are included. The studies focus the investigations on the issues that systematic research work has not yet achieved up to now, or which is in difficulty to be investigated by the present experiments.

Conclusions and recommended future work are given in Chapter 7.

Chapter 2 LITERATURE REVIEW

2.1. CHARACTERISTICS OF AIRFLOW BEHIND POROUS FENCES

2.1.1. Airflow profiles behind a porous fence

Airflow around a porous fence is a dynamic process that involves interactions among the fence, airflow, and windblown particles. It changes the airflow velocity and pressure distribution, and hence can be applied to reduce the damage and control the windblown particles (e.g. snow particles). Airflow behind a porous fence is complex in the presence of both the bleed flow passing through the openings, as a series of miniature jets depending on the geometry of the fence and the displaced flow diverted over the fence. The most important design parameter affecting the characteristics of airflow behind a porous fence is the overall fence porosity (Seginer, 1972) (Heisler & Dewalle, 1988) (Ki-Pyo & Young-Moon, 2009) (Dong, et al., 2006) (Dong, et al., 2007) (Dong, et al., 2011), which is defined as:

$$\beta = A_{open}/A_{total} \qquad \textbf{Eqn.2-1}$$

where: $A_{open}$is the area of the opening in the fence and A_{total} is the total area of the fence.

Figure 2-1 illustrates the difference of airflow profiles behind porous fences with different porosities. When the porosity is above a critical level (β_{cr}), the bleed flow dominates and the airflow in the leeward side of the fence is generally in the same direction as the windward flow as shown in Figure 2-1 (top). When the porosity is below this critical level, the leeward airflow directly behind the fence reverses, resulting in a region of recirculating air as shown in Figure 2-1 (bottom).

The size of the separated zone depends on the porosity, and at some point downstream, the diverted air re-attaches. Further downstream in the mixing zone, the flow may still suffer from a velocity deficit due to the interaction with the fence, but gradually returns to normal boundary-layer flow through momentum transfer.

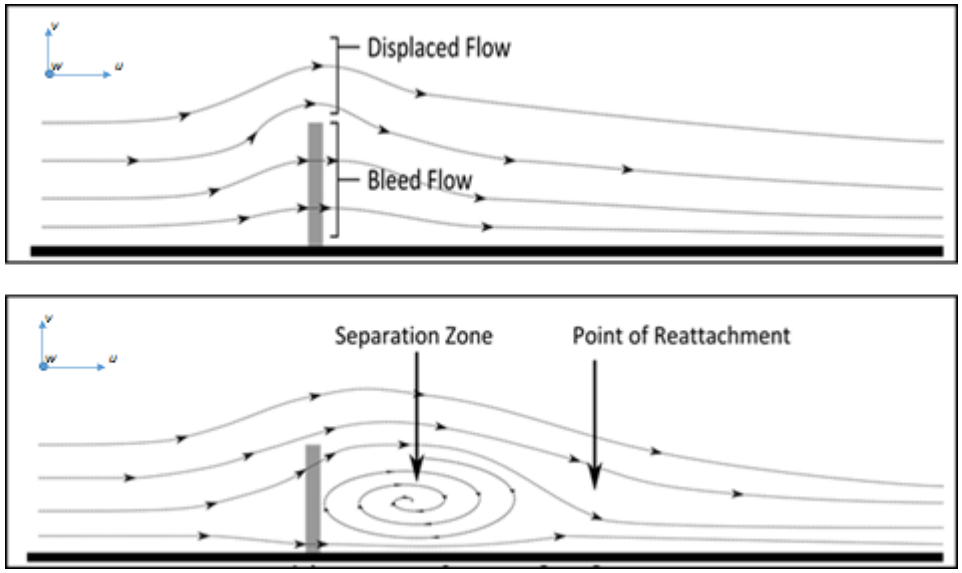

Figure 2-1: Difference in airflow profiles behind porous fences with different porosities: (Top) $\beta>\beta_{cr.}$ (Bottom) $\beta<\beta_{cr.}$ (Tabler, 2003)

The characteristics of airflows behind porous fences are closely associated with the porosity of the fence. Accurate division of these regions is difficult due to the gradually transitional nature of the regions behind the porous fence. Seven flow regions shown in Figure 2-2 were identified by using particle image velocimetry (PIV) for the fence with low porosity ($\beta=0.1$) under the free-stream wind velocity of *10m/s* (Dong, et al., 2007).

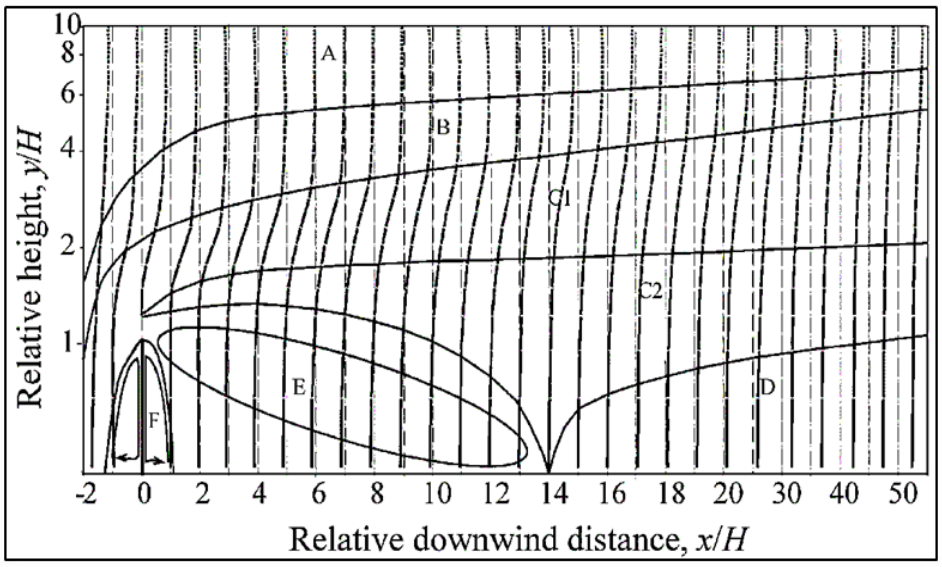

Figure 2-2: Seven flow regions observed by (Dong, et al., 2007) for a fence of low porosity.

Region A is the outer flow region determined by the conditions in the undisturbed boundary layer far-upstream from the shield. Region B is the overflow region representing a transitional region between the outer flow and the wake regions. The velocity gradient in the region A tends to increase with the distance downwind. Regions C1 and C2 constitute a wake region between the overflow region (Region B) and the internal boundary layer (Region D) & the reversed cell (Region E). The wake region is a region of flow recovery where the flow is accelerated downwind by downward transfer of momentum from the overlying layers with higher wind velocities. Region C1 has faster wind velocity and a higher velocity gradient while Region C2 has lower wind velocity and velocity gradient.

The higher velocity gradient in Region C1 is due to the rapid downward turbulent momentum transfer from the accelerated overflow in Region B. The lower velocity gradient in Region C2 is due to the momentum transfer with the slower and sheltered flow of the reverse cell in Region E. Region D represents an internal boundary layer characterized by increasing shear and thickness with the increase of the downwind distance. The velocity profile becomes more uniformed in shape with increasing distance downwind from the reattachment point. Region E represents a reverse cell where the velocity gradient increases with the downwind distance to a certain distance, but then decreases. Region F is a small vortex where the wind is almost stagnant in the proximity of the fence. It results from the high pressure and the action of viscosity immediately behind the fence when its porosity is small. It causes a loss in wind energy and may generate a lifting force capable of suspending sediment particles behind the fence. Region E will disappear when the porosity is greater than *0.20* and Region F will disappear when the porosity is greater than *0.10* (Dong, et al., 2007).

2.1.2. Turbulence due to porous fences

A porous fence exerts a drag force on the wind flow and creates a region of intensive turbulence at the top of the fence through the creation of a shear layer. It may also generate turbulence behind the fence due to the porous holes in the fence under certain conditions. The turbulence intensity of the stream wise and the vertical velocity components can be calculated as follows:

$$T_u = \sqrt{\overline{u'^2}}/U \quad \textbf{Eqn.2-2}$$

$$T_v = \sqrt{\overline{v'^2}}/U \quad \textbf{Eqn.2-3}$$

$$T_w = \sqrt{\overline{w'^2}}/U \quad \textbf{Eqn.2-4}$$

where T_u, T_v and T_w are the turbulence intensities of the stream wise and vertical velocity components, U is the mean free-stream wind velocity. u', v' and $w'$are the fluctuation velocities of the stream wise, vertical velocity and lateral velocity components, which are derived using $u' = u - \bar{u}$, $v' = v - \bar{v}$ and $w' = w - \overline{w}$, where (u, v, w) is the instantaneous velocity field, and $(\bar{u}, \bar{v}, \overline{w})$ is the mean turbulent velocity field.

The mean Turbulent Kinetic Energy *k* can be calculated as:

$$k = \frac{1}{2}\rho\left(\overline{u'^2} + \overline{v'^2} + \overline{w'^2}\right) \quad \textbf{Eqn.2-5}$$

The turbulent shear layer at the top of the fence exists irrespective of the porosity (Patton & Shaw, 1998) (Lee & Kim, 1999) (Boldes, et al., 2003). As the porosity increases, the level of shear decreases with a proportional decrease in turbulence, resulting to a thinner shear layer (Lee & Kim, 1999). For the extreme case of a solid fence with zero porosity, the peak *k* occurs just above the fence at around *y/H = 1.2* (Patton & Shaw, 1998) (Lee & Kim, 1999) (Kim & Lee, 2002). The increase of porosity results in a much less energetic wake with *k* increasingly concentrated behind the fence (Perera, 1981) (Lee & Kim, 1999). This is the result of the reduced diverted flow and the increased bleed flow. The downstream high *k* vortex introduced by the shear layer of the solid fence is reduced to a much-weakened state at the porosity of *0.2*. The vortex has almost disappeared when the porosity has reached a value of *0.4*.

Raine & Stephenson (1977) showed that the downstream flows in low porosity fences were dominant by this turbulence. Zhuang & Wilson (1994) identified coherent motions emanating from the fence top. Coherent motion is defined as a three-dimensional region of flow where at least one fundamental variable exhibits significant correlation with itself or with another variable over a space or time range significantly larger than the smallest local scales of the flow (Robinson, 1991). These motions grew as they travelled

downstream and were responsible for a degree of inter-layer mixing between the bleed flow and diverted flow, transferring momentum back to the retarded velocity region in the lee of the fence. The effectiveness of simple turbulence models to simulate such flows was related to the similarity of porous fence flows to turbulent mixing layers, whereby the turbulence was self-similar and reacted quickly to mean flow changes.

In the far downstream area ($x/H > 10$) of a porous fence, the normalized turbulence intensity becomes approximately self-similar irrespective of the porosity, reminiscent of the downstream behaviour of turbulent mixing layers (Abramovich, 1963) (Zhuang & Wilson, 1994). This observation is consistent to the results of (Perera, 1981) (Bradley & Mulhearn, 1983) (Shiau, 1998) and the analytically derived results from (Counihan, et al., 1974). (Counihan, et al., 1974) & (Perera, 1981) concluded that turbulence stress profiles in the far-wake region decay downstream as a function of $x^{-3/2}$. The data observed by (Bradley & Mulhearn, 1983) however exhibited a more rapid decay of Reynolds stress than the $x^{-3/2}$ correlation.

2.1.3. Flow behavior further downstream

It is reasonable to assume that the vertical velocity profile and turbulence statistics will return similar values to the upstream profile at some distance downstream behind a single porous fence. However, based on the knowledge of both the jet and the bluff-body flows, wakes behind obstacles tend to return asymptotically (Abramovich, 1963) (Counihan, et al., 1974) rather than at some definite distance downstream. Combined with the experimental results of (Bradley & Mulhearn, 1983), the variation of velocity deficit with downstream distance from the fence was shown to approximately follow a $(x/H)^{-1}$ correlation.

For practical purposes, the main shelter region lies within $x/H < 10$, beyond which the shear layer from the top of the fence has descended and the remaining flow downstream has returned to the upstream profile. The downstream distance over which any shelter effect or velocity deficit exists is also dependent on the width of the fence, as low aspect ratio fences may exhibit significant end-effects, which will be explained further in Section 2.4.

2.1.4. Separation and reattachment of airflows leeward a porous fence

As illustrated in Figure 2-1, a separation region forms leeward of the porous fence when the porosity goes below the critical porosity. The separation and reattachment zone immediately downwind of a porous fence has many similar characteristics to other flows, such as backwards facing steps, turbulent mixing layers and bluff body flows. It is widely accepted that the overall fence porosity is the main structural parameter affecting the separation and reattachment of airflows leeward a porous fence. In the extreme case of zero porosity representing a solid fence, the separation region is similar to that of a bluff body wake. With the increase of the fence porosity, the bleed flow will have significant influence on the flow in the downstream region.

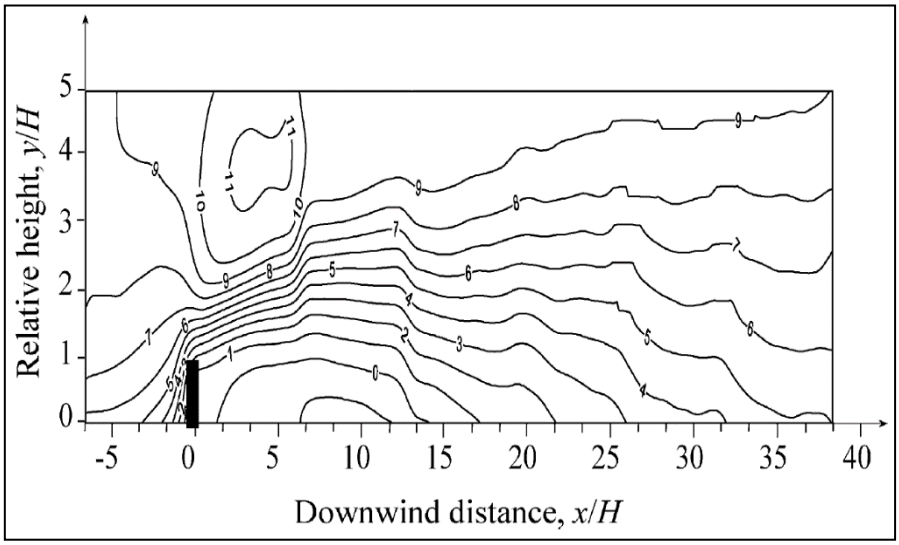

Figure 2-3: A typical Iso-wind velocity chart behind a porous shield (Dong, et al., 2007).

A typical Iso-wind-velocity chart shown in Figure 2-3 was obtained from the wind tunnel experiment for a fence with the porosity of *0.10* (Dong, et al., 2007). The streamlines were lifted to the different extents, resulting in higher velocities above the fence as the airflow approaches. It can be observed that flow separation was initiated from the top of the fence and the separation line extended downstream at *8* to*16* times of the fence.

Figure 2-4 is the amplified illustration of the reattachment point *R* for a fence with a porosity of *0.05* under the free flow velocity of *10m/s*. *R* is determined by examining the

horizontal velocity component at ground level to identify the point where the horizontal velocity changes sign from upwind (negative) to downwind (positive). Theoretically, the downwind apex of the reverse cell and the reattachment point are located at different positions. The former can be above the surface but the latter must be at the surface. In practice, the difference in their positions is so small that it can be negligible. Hence, the locations of both the downwind apex of the reverse cell and the reattachment point can be characterized by a single parameter: the reattachment length (Dong, et al., 2007).

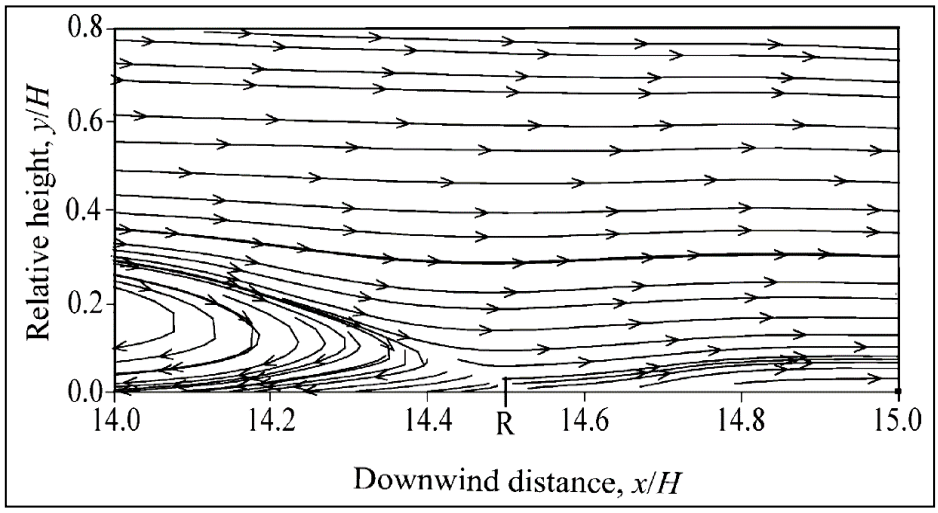

Figure 2-4: Amplified streamlines showing the reattachment point R (Dong, et al., 2007).

The reattachment point is dependent on multiple variables including the porosity, wind velocity and fence geometry. Santiago et al. (2007) qualitatively found that a zone of recirculation disappeared somewhere between porosities of *0.35* and *0.24*. The reattachment length moved downstream as the porosity increased up to the critical porosity. Using scaled wind tunnel experiments, Dong et al. (2007) identified a lower critical porosity between *0.2* and *0.3*, and the maximum reattachment length was about *8* to*16* times of the fence height downstream under different upstream wind velocities when the porosity was *0.2* or less. The porosity had greater influence on the reattachment point position than the upstream wind velocity did. Their results also suggested that the greatest reattachment distance (*x/H=13-16*) occurred at a porosity of *0.1* under different upstream wind velocities. For a solid fence, the reattachment distance was about *x/H=13-14*, which was slightly less than the peak value for a fence with a porosity of *0.1*. Also worth noting

is the fact that different measurement techniques may affect the measurement results. For example, a previous study by Dong et al. (2006) using particle tracer analysis found that the reattachment distance peaked at *x/H = 17* at the porosity of *0.05*, which is different to the observation that the greatest reattachment distance *x/H=13-16* occurred at a porosity of *0.1* (Dong, et al., 2007). The difference is however caused by the use of different measurement techniques with the particle image velocimetry method (Dong, et al., 2007) representing the result at some distance above the surface while the visual particle movement detection method (Dong, et al., 2006) representing the reattachment distance measured on the ground.

2.2. CONTROL OF WINDBLOWN SNOW PARTICLES

2.2.1. Transport modes of windblown snow particles

Apart from the strong wind, heavy snow is another hazard to be addressed in Cold Regions. Snow will be eroded in areas where the wind is strong enough and will be transported downstream until the energy of the airflow can no longer maintain the upstream vertical drift profile. Porous fences can be used to control the transport and deposition of windblown snow particles effectively.

The effects of porous fences on controlling the movement of snowdrifts have received fair amount of attentions from the scientific and industrial communities (Tabler, 1980) (Naaim-Bouvet & Mullenbach, 1998) (Tabler, 2003) (Otakeguchi, et al., 2012) (Ping , et al., 2013) (Blocken, 2014) (Li & Sherman, 2015). The mechanism of snow transported through a turbulent airflow can be traced back to the pioneering work of Bagnold (1941) on the transport of sand by wind. Three particle transport modes are categorized, which are creeping, saltation and suspension.

- Creeping happens along the ground when particles are agitated by impinging particles. During creeping, the moving particles keep their contact with the immobilized particles forming the surface. This process does not directly depend on the wind velocity. It is linked to the impact among particles and can therefore be seen as part of the saltation process.
- When the shear stress at the ground is high enough, particles can be entrained from

the surface. Particles take off and follow ballistic trajectories before they bounce back onto the ground. This hopping transport mode of particles by wind is called saltation. When impinging on the ground they can entrain other particles into creeping or saltation, or bounce themselves back up again.

- Suspension refers to the transport mode that small and light particles can reach higher elevations, where the wind field has significantly more influence on the trajectories. Instead of being dominated by the gravity, the trajectories are controlled by the arbitrariness of the wind speed. The drag forces exerted by the turbulent airflow make the particles follow paths through the air that are close to random walks. The intermediate state between saltation and suspension is referred to as a modified saltation, where the particles show characteristics of both.

Figure 2-5 shows the typical trajectories of particles associated with the three transport modes by wind (Kind, 1990). It should be noted that a natural mixture of snow consists of particles with a wide range of sizes. In most cases, snow transport involves all of the three mentioned modes. Large snow particles will either become immobile or creep on the surface. Intermediate snow particles will largely remain in the saltation layer, while small light snow particles will go into suspension. The proportion of transported snow particles in each transport mode is dependent on many factors such as wind velocity, snow properties, boundary conditions, and distribution of particle size and shape.

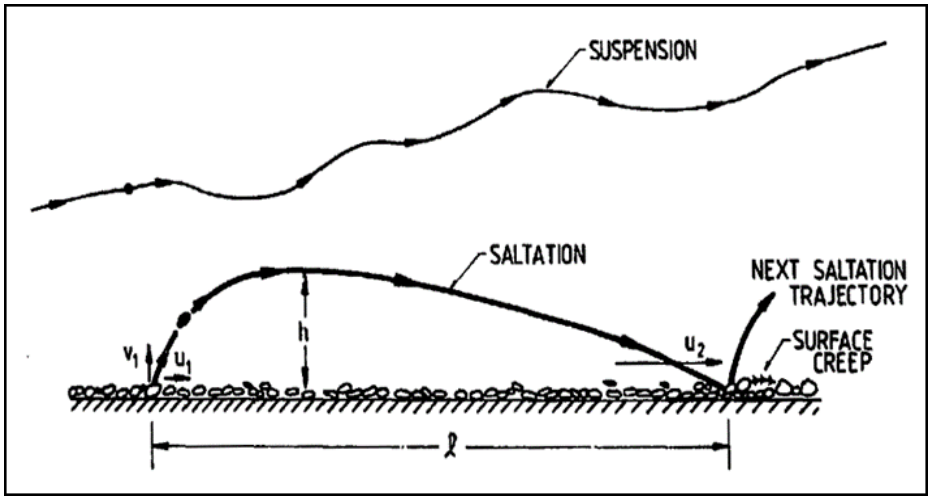

Figure 2-5: Typical trajectories of particles blown by wind (Kind, 1990).

The presence of particles in air will modify the wind profile due to the momentum exchange between the airflow and the particles. Wind velocity is reduced when snow particles are present in the air. The amount of snow in air decreases with the increase of the altitude. Nemoto et al. (2004) hence assumed that above a certain height, the influence of particles on the wind profile becomes small, and can be negligible. Based on this assumption, the transport domain of windblown particles can be divided into two layers with different physical properties as shown in Figure 2-6 (Clifton & Lehning, 2008). In the saltation layer below a certain altitude, momentum exchange should be considered. In the suspension layer above certain altitude, momentum exchange can be neglected.

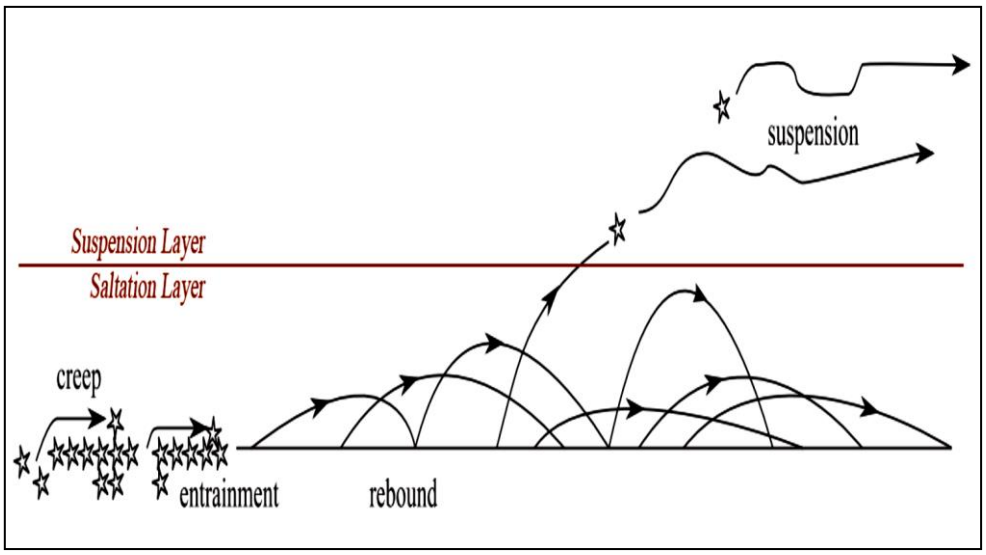

Figure 2-6: The two layer transport model for windblown particles (Clifton & Lehning, 2008).

2.2.2. Size of snow particles

The size of snow particles varies from less than 100 microns for strongly fractional particles to more than a centimetre in diameter for fresh snow flakes. During the transport in the cold and rather dry environment representing the winter condition in northern Norway, big snow particles are rapidly fractionated into small particles. It is therefore reasonable to assume that bigger snow particles are only present at the very beginning of a transport event. They are quickly broken up into smaller particles with a range of diameters below 1000 microns. Figure 2-7 is the typical grain sizes of snow particles corresponding to each individual transport mode (Gauer, 1999). The snow particles may

be simplified further to spherical particles of constant diameter to ignore the orientation and eventual rotation of snow particles in the process of transport by wind (Sato, et al., 2008).

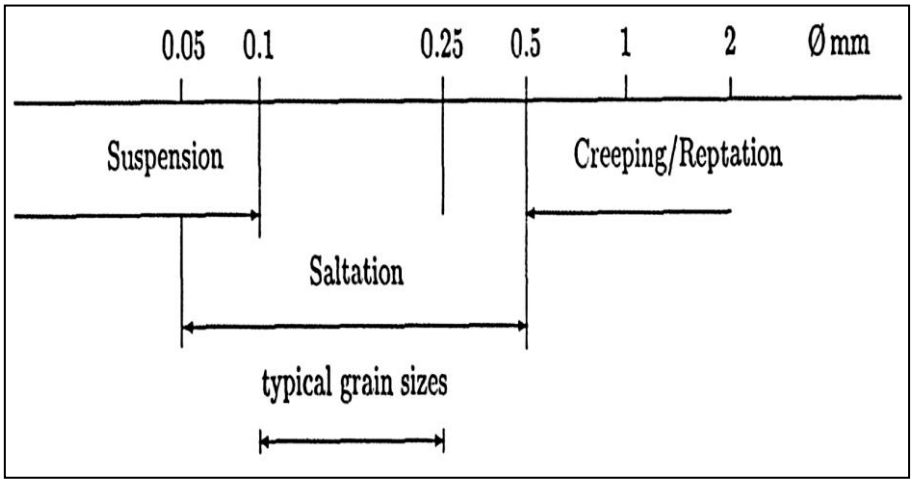

Figure 2-7: Size range of snow particles to each transport mode (Gauer, 1999).

2.2.3. Control of windblown snow particles using porous fences

Porous fences have been widely employed to control windblown snowdrifts. They will change airflow velocity and pressure distribution to weaken wind velocity and decrease quantities of windblown particles leeward. Windblown snow movement around a porous fence is complex since the oncoming wind velocity does not simply decrease after passing through the fence. The bleed flow passing through the porous holes of the fence interacts actively with the displaced flow passing above the fence. This interaction induces a recirculation region in the fence wake zone, modifying the trajectories of windblown snow particles. In addition, the direct collisions of snow particles with the fence surface and the enhanced flow turbulence increase the complexity of the motion of the windblown snow particles.

Windblown snow transport can be treated as a special case of air-solid two-phase flow similar to windblown sand transport. Dong et al. (2002) measured velocity profiles of a sand cloud blowing over a gravel surface and concluded that the windblown sand erosion was mainly dependent on the kinetic energy of the oncoming wind, which was closely

related to the stream wise mean velocity and mass flux of saltation sand particles. The total of mass flux of saltation sand was proportional to the cube of the friction wind speed (Greeley, A.D.; Iversen, J.D.;, 1986), and it decayed exponentially with the increase of the altitude (Nalpanis, 1985). The friction wind speed is also named as the friction velocity that is often used as a scaling parameter for the fluctuating component of velocity in turbulent flow, which can be obtained through non-dimensionalization of the turbulent equations of motion (White, 1998). Abrasion is the process of scrapping of a snow bed by friction between the bed and the moving particles. The extent of abrasion is often expressed in the abrasion intensity, and depends on the mass flux, the velocity of saltation snow.(Zaghloul , 1997) (Taniere, et al., 1997) (Yang, et al., 2007). Zhang et al. (2010) investigated the shelter effect of a porous wind fence on saltating sand in a simulated atmospheric boundary layer (ABL). Wind tunnel tests were conducted to evaluate the effect of porous fence on mean velocity, volume concentration of saltating sand, mass flux, and kinetic energy. It was found that the mean velocity decreased dramatically at the leeward side of the fence, and a high-velocity region existed in the shear layer above the fence. The mass flux distributions with height around the fence were expressed as an exponential function. Both the particle concentration and mass flux decayed largely in the leeward region.

Wind erosion with regard of windblown snow particles is a process to detach snow particles from the land surface and transport them by wind. To abate windblown snow, some researchers (Bagnold, 1941) (Shao, 2000) (Dong, et al., 2006) proposed the threshold velocity as a key variable in wind erosion control. The threshold velocity is the minimum wind velocity required to initiate wind erosion. The reduction of wind erosion can be achieved through certain control measures by increasing the threshold wind velocity. Therefore, the performance of porous fences on reducing wind erosion can be directly defined by measuring the effect of the fence on the threshold velocity as a function of the characteristics (porosity and geometries) of the fence. A normalized dimensionless threshold wind velocity is commonly used to assess the performance of difference fences using the following equation (Dong, et al., 2006):

$$U_{tr} = U_{tf}/U_{t0} \qquad \textbf{Eqn.2-6}$$

where U_{tr} is the dimensionless relative threshold wind velocity, $U_{tf}$is the threshold wind velocity as influenced by the shield, andU_{t0} is the threshold open-field wind velocity without the porous fence. Dong et al.'s (2006) wind tunnel simulation indicated that fences with porosities of *0.3-0.4* had the maximum relative threshold wind velocity and maximum effective shelter distance, and most suitable for controlling wind erosion.

Based on the extensive research on snow drift control, Tabler (1980) (2003) concluded that a fence of porosity of *0.5* had the best performance in terms of snow capture as shown in Figure 2-8, where Q_c is the snow storage capacity of the fence and H is the height of the fence. Q_c is the maximum quantity of snow that a fence system is designed to retain. The observation is consistent with Wang et al.'s result that fences of porosities around *0.5* have the larger downstream velocity reduction whilst not causing the highest reduction in leeside wind velocity (Wang, et al., 2001). Solid fences had a significantly reduced snow capturing capacity due to the larger upstream drift caused by the lower wind speeds on the immediate windward side of the fence.

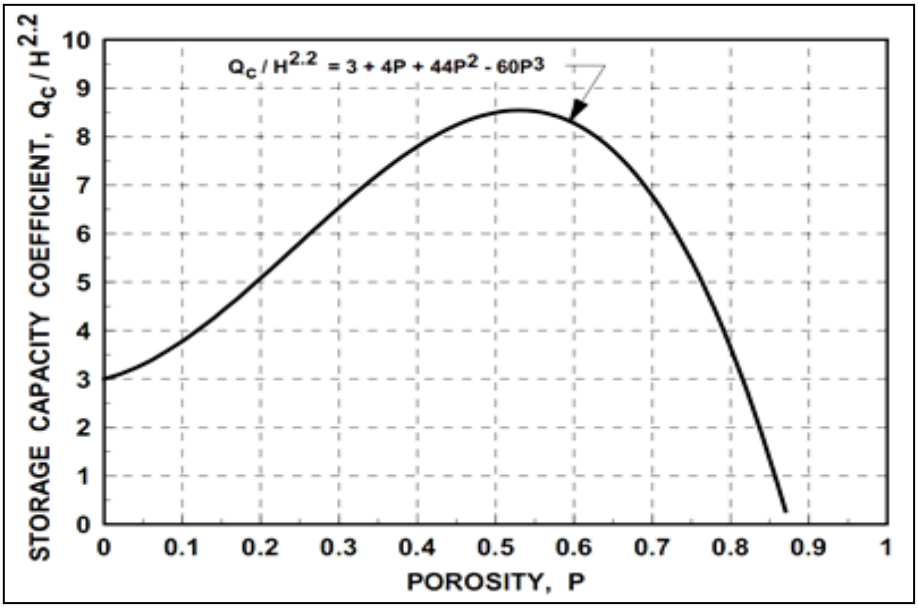

Figure 2-8: Variation of snow storage capacity with porosity (Tabler, 2003)

2.3. FACTORS AFFECTING THE PERFORMANCE OF FENCES

Windshields have been studied in a systematic way since the 1940s, with the aim to

achieve optimal protection at the minimum cost (Bagnold, 1941) (Jensen, 1954) (Tani, 1958) (Ping , et al., 2013) (Blocken, 2014) (Telenta, et al., 2014) (Hong, et al., 2015) (Li & Sherman, 2015). It is widely accepted that a porous fence exerts a drag force on the wind flow, causing a net loss of momentum in the incompressible airflow and hence a shielding effect. By changing the airflow velocity and the resulting pressure distribution, a porous fence can reduce the damage by wind and prevent entrainment of particles or increase their deposition (Liu & Liu, 1991). The performance of a porous fence is generally evaluated by the reduction of the wind velocity and the effective shelter distance. An ideal wind shelter is required to create the greatest wind reduction over the longest shelter distance (Plate, 1971) (Hagen, 1976) (Cornelis & Gabriels, 2005) (Dong, et al., 2010) (Dong, et al., 2011). A porous fence causes the downstream wind velocity deficit and creates complex downstream flow characteristics, particularly in the wake flow region where high shear rate, large pressure gradient, and high turbulence intensity exist (Wilson, 1997) (Park & Lee, 2001). A maximum wind reduction for a fence with low porosity may result in a shortened shelter distance due to the high turbulence downwind. The complexity of the characteristics of downstream wind flow makes it difficult to achieve an optimal fence design (Plate, 1971) (Hagen, 1976) (Cornelis & Gabriels, 2005) (Dong, et al., 2011). Many factors (e.g., overall fence porosity, porosity distribution, opening size and shape, fence height and width, and fence orientation, etc.) need to be considered in the design of porous fences.

2.3.1. Overall fence porosity

2.3.1.1. Overall observations

The overall fence porosity is the ratio of the area of the opening in the fence to the total area of the fence as defined by Eqn. 2-1 in Section 2.2.1. Extensive research evidences have indicated that the fence porosity is the most influential design parameter affecting the wake characteristics behind the shield (Seginer, 1972) (Heisler & Dewalle, 1988) (Ki-Pyo & Young-Moon, 2009) (Dong, et al., 2006) (Dong, et al., 2007) (Dong, et al., 2011). Optimal design of a porous fence often depends on choosing the optimal porosity.

A reduction in porosity means less an amount of fluid passing through the fence and greater an amount of fluid flowing over the fence, causing a higher drag force on the wind flow. Fence with very low porosity produces stronger turbulence downwind than medium- and high-porosity fences, resulting in a quick recovery of mean horizontal wind velocities of the upstream conditions. It is widely accepted that the decrease of porosity will reduce the wake velocity but increase the turbulence intensity, which can compromise the effective shelter distance (Skidmore & Hagen, 1970) (Hagen, 1976) (Heisler & Dewalle, 1988) (Wang, et al., 2001) (Cornelis & Gabriels, 2005) (Dong, et al., 2010) (Dong, et al., 2011). Figure 2-9 illustrates this effect by showing that higher porosities can lead to longer shelter distance (Wang, et al., 2001). It implies that the optimal fence performance should balance the reduction of wind velocity (or pressure) with the maximization of effective shelter distance.

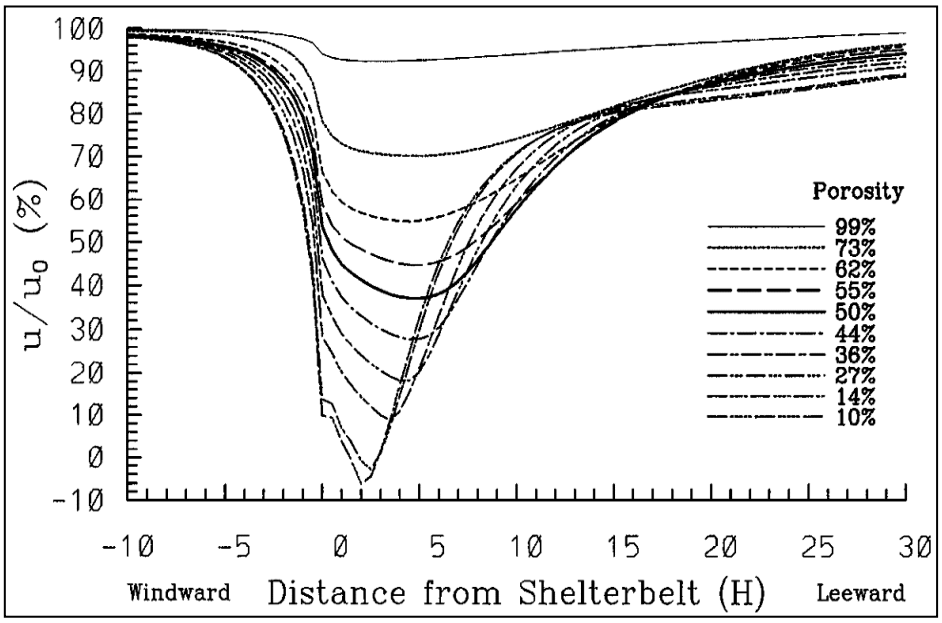

Figure 2-9: Variation of normalized downstream velocity with porosity (Wang, et al., 2001).

2.3.1.2. Critical porosity

As illustrated in Figure 2-1, it exists a porosity level below which flow separation and recirculation occur. The porosity, which triggers the formation of a recirculation region behind the fence, is termed as the critical porosity.

When porosities approach the critical porosity from a higher value, flow directly

downstream of the fence is still axial (as opposed to recirculating), but further downstream may exhibit separation and reattachment, i.e. a pocket of recirculation some distance downstream from the fence (Perera, 1981) (Packwood, 2000). Perera (1981) noted that starting from a fully blocked fence, incrementally increasing porosity caused the recirculation region to decrease in size and move downstream, disappearing at a porosity of around 0.3. Given the uncertainty concerning the critical porosity, the effect of a detached recirculation region is likely to be subject to a degree of error with regard of correlating the porosities at which they occur. Another factor is that porosity is not the only variable that governs the flow through and around a porous fence. As such, while the definition of the critical porosity is relatively simple, the accurate identification of the critical porosity is not easy. Table 2-1 shows a range between 0.2 and 0.4 for the critical porosities reported by various researchers in the field.

Table 2-1: Typical critical porosity values reported in literature.

Critical Porosity β_{cr}	Method	Reference
0.3	Wind Tunnel, 1:200	(Perera, 1981)
< 0.2	Wind Tunnel	(Lee & Kim, 1999)
0.3 - 0.4	Wind Tunnel, 1:50	(Dong, et al., 2006)
0.2 - 0.3	Wind Tunnel, 1:50	(Dong, et al., 2007)
0.4	CFD, Large Eddy	(Fang & Wang, 1997)
0.24-0.35	CFD, K-Epsilon	(Santiago, et al., 2007)

2.3.1.3. Range of optimal porosities

In general, fence porosity below *0.4* is found to give noticeable changes to the flow characteristics (Jensen, 1954) (Tani, 1958) (Hagen & Skidmore, 1971) (Skidmore & Hagen, 1970) (Raine & Stevenson, 1977) (Perera, 1981) (Lee & Kim, 1998) (Lee, et al., 2002) (Tabler, 2003) (Cornelis & Gabriels, 2005) (Dong, et al., 2007). The field measurements (Hagen & Skidmore, 1971) indicated that a windbreak with a porosity of *0.4* produced the lowest wind velocity over the largest downwind area. Raine and Stevenson (1977) found that a porosity of *0.2* gave the best overall reduction in leeward mean velocity. Perera (1981) observed that Reynolds shear stress and turbulent kinetic energy were strong behind the fence when the porosity was less than *0.3*, whereas the

bleed flow was strong when the porosity was greater than *0.4*. Lee and Kim (1998) (1999) measured the velocity fields and surface pressure distributions under a series of porous wind fences, and discovered that a porous fence with a porosity of *0.3-0.4* to be the most effective for reducing the mean velocity and surface pressure fluctuations. Lee et al.'s (2002) wind tunnel testing results found that a porous wind fence with the porosity of *0.3* was the most effective for abating windblown sand particles because this fence had the maximum threshold velocity among the porous fences. Dong et al.'s (2006) wind tunnel testing results indicated that fences with porosities of *0.3-0.4* were most suitable for wind erosion control.

It should be noted that the identification of the optimal porosity is complicated since the performance of a porous fence has been affected by many other factors such as porosity distribution, size and shape of porous holes, fence height and width, and fence orientation. Also worth noting is that the optimal design of porous fences is dependent on the specific purpose of the fence. For example, the wind fences along the railway from Hami to Urumqi in China were designed to protect trains against strong winds, where the maximum reduction of wind drag on a train behind the fences is the target of the optimal design of the fence. However, for the wind fence constructed at the frontal edge of the shelter system along the highway crossing the Taklimakan Desert of China, the maximum reduction of the wind shear on the ground surface behind the fence is the target of the optimal design of the fence to minimize the wind erosion (Dong, et al., 2007). For the control of snow drifting in Cold Regions, the fence is designed not to have a maximum reduction in leeside wind velocity retardation, but to maximize the amount of snow captured downstream of the fence by introducing larger downstream velocity reduction. It is therefore clear that the optimal porosity of the porous fence is purpose-dependent and can only be presented as a range rather than a single value.

2.3.1.4. Porosity distribution

While a majority of the research is focused on the performance of fences of uniform porosity, some investigations have been carried out on fences of variable porosities to understand the effect of porosity distribution (Hagen & Skidmore, 1971) (Rosenberg, 1974) (Raine & Stevenson, 1977) (Saif, et al., 2010). It is anticipated that an optimal

design of porosity distribution may be able to control the velocity and turbulence distributions downstream of the fence more effectively. However, the literature results are not consistent in terms of the effect of porosity distribution on the performance of the fence. Hagen & Skidmore (1971) reported that a porosity of less than *0.4* near the fence top caused excessive shear and turbulence, while low porosity near the bottom created low pressure leading to a recirculation zone in the leeward area. Rosenberg (1974) suggested that the porosity should decrease with height in proportion to the logarithmic nature of the wind-velocity profile. Raine & Stevenson (1977) however proposed a fence with a porosity increasing from *0.0* at the base to *1.0* at the top, with an overall porosity of *0.2-0.3*.

Considering the fact that the strong shear flow at the top of the fence will quickly diffuse high wind velocities back to the surface, an optimum fence should avoid the concentration of a region of strong shear in the flow at the fence top in order to achieve lower turbulence intensity for a given mean velocity reduction. It is therefore questionable that either the top or bottom of an optimum porous fence should be of very low porosity (Hagen, 1976) as suggested in (Rosenberg, 1974) (Raine & Stevenson, 1977). Further research is required to understand the effect of porosity distribution on the performance of wind fences properly.

2.3.2. Size and shape of porous holes and fence thickness

Little research data were available in the literature with regard of the effects of shape and size of porous holes, and fence thickness on the effectiveness of porous shields. Nevertheless, it has been mentioned by some researchers that these structural parameters may affect the performance of a porous fence and require further detailed investigations.

Allori et al. (2013) conducted such an investigation on the fence performance evaluated by the drag coefficient. The fences had porosities in the range of 0.23 – 0.70. Fences with round, square, oblong, hexagonal, and cross-shaped holes were tested in the wind tunnel study. Figure 2-10 shows the variations of the drag coefficient CD and the dimensionless parameter b/H against the global Reynolds number ReH.

The following equations provide the definitions of these parameters.

$$C_D = F_D/(1/2\ \rho \cdot u_\infty^2 \cdot L \cdot H) \quad \textbf{Eqn.2-7}$$

$$R_{eH} = (\rho \cdot u_\infty \cdot H)/\vartheta \quad \textbf{Eqn.2-8}$$

$$b/H = M/(F_D \cdot H\ ) \quad \textbf{Eqn.2-9}$$

$$k_r = \Delta p/(1/2\ \rho \cdot \bar{u}^{-2}\ ) \quad \textbf{Eqn.2-10}$$

where u_∞ is the undisturbed flow velocity and $\bar{u}$ is the mean wind velocity inside a PVC pipe in front of the fence. ρ is the air density and ν is the air kinematic viscosity. F_D and M are the drag force and the moment acting on the fence. Δp is the drop of pressure in correspondence of the porous element. L is the length of the fence and H is its height. k_r is the loss coefficient. b represents the point of application of the drag from the base of the fence as the moment is considered as the result of the drag force acting at a certain distance b from the base of the fence. As such, the dimensionless parameter b/H is another useful parameter to measure the performance of the fence.

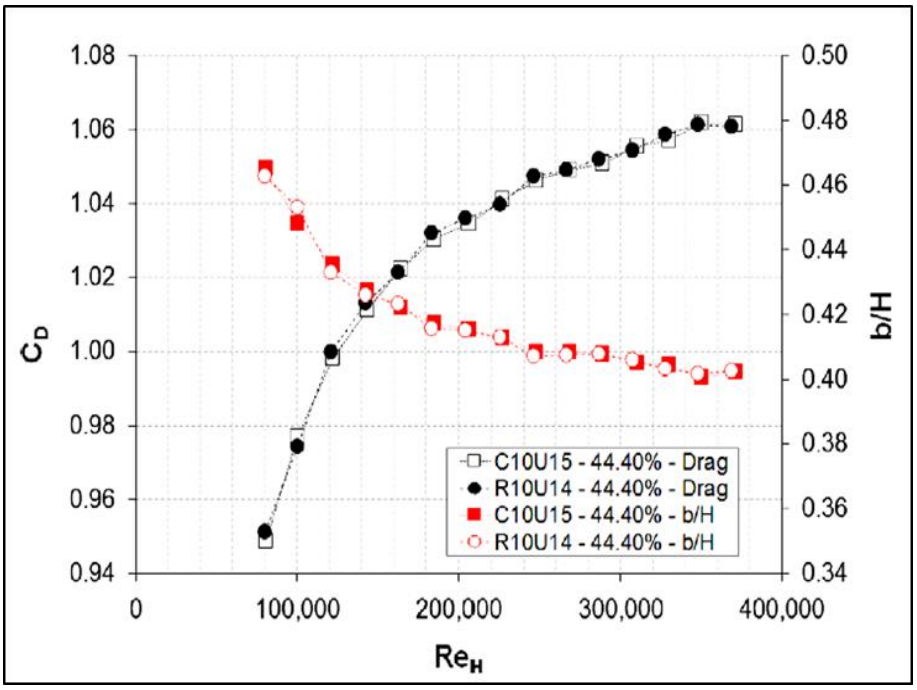

Figure 2-10: Effect of holed shapes on the performance of porous fences (Allori, et al., 2013).

The test results in Figure 2-10 show very little difference between the data for round and square shaped holes considering the potential errors made by measurement instruments.

To investigate the impact of size of holes and fence thickness, Allori et al (2013) tested 11 different typologies of porous fences with panel thicknesses varying from *1mm* to *6mm* and the diameter of holes varying from *1.5mm* to *10mm*. The shape of holes for these fences was round and the fence porosity was maintained to a constant of *0.4*. A loss coefficientk_r defined in Eqn. 2-10 was measured to evaluate the impact of the sizes of holes and the panel thicknesses on the fence performance. It was observed that the loss coefficient was higher when the samples had smaller values of the thickness. On the other hand, the increase of the diameter of holes increased the value of the loss coefficient.

Up to date, the effects of shape & size of holes, and the panel thickness on the effectiveness of porous fences are few found in the literature. Further detailed investigation is required in this area to optimize the design of porous fences

2.3.3. Fence height and width

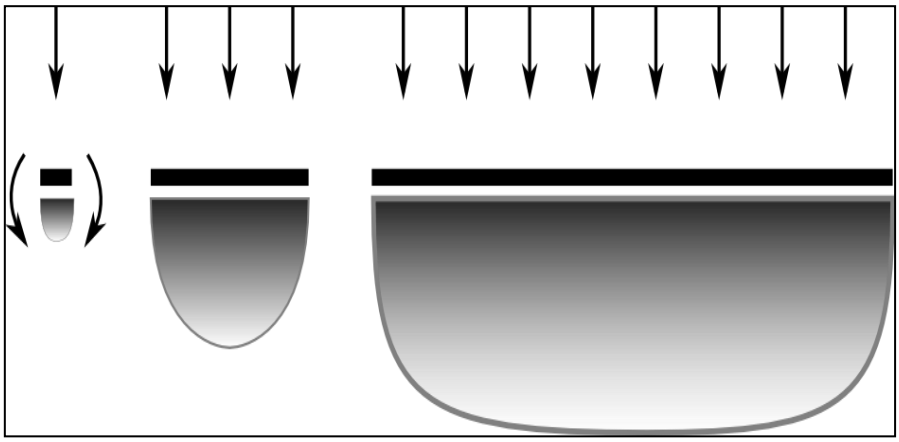

Figure 2-11: Impact of end-effects on snow capacity (Tabler, 1980).

Similar to aerospace applications, the effect of three-dimensionality in porous fences occurs due to a finite aspect ratio of the fence, as it is not infinitely wide. Based on the study on snowdrift shown in Figure 2-11, Tabler (1980) reported that end effect extended inwards for about twelve times of the fence height from the fence ends when examining the storage capacity of snow fences, indicating that end effects can have a large degree of influence. Wang et al (2001) reported a number of other aspects to three-dimensionality. As fence aspect ratio increases, the minimum velocity through the fence moves from being slightly in the lee to slightly upwind of the fence. Additionally, the minimum

velocity decreases slightly with the increase in width.

It should be noted that most of the 2D CFD simulations published in the literature does not consider the influence of end-effects on the models. The strict 2-dimensional model assuming an infinite aspect ratio for the fence will produce uniform up and downstream results in the span wise direction, which represents an extreme case and is not possible for real life scenario. It is widely accepted that the Reynolds numbers have influences on the characteristics of wind flow behind fences. The effect of fence height and width on fence performance can be expressed through the definitions of following geometry related Reynolds number in Eqns.2-11 and 2-12 (Subhas, et al., 1997):

Reynolds number based on step height:

$$R_{eh}=\rho \cdot U_{\infty} \cdot h/v \qquad \textbf{Eqn.2-11}$$

Reynolds number based on body width:

$$R_{ed}=\rho \cdot U_{\infty} \cdot D/v \qquad \textbf{Eqn.2-12}$$

where U_{∞} is the free-stream velocity, h is the step height, $D$is the body width, and v is kinematic viscosity of the wind flow.

Lee & Park (1998) tested various fences with different porosities and heights to investigate their effects on the surface pressure acted on a two-dimensional triangular prism, as a coal-pile model behind different porous fences at different locations. The results showed that the mean pressure coefficient decreased when the fence height was greater than the model height. In the near-wake region, the effect of the triangular prism location behind the fence was not significant compared to that of fence porosity and height. Ping et al. (2013) observed a high-pressure region upwind of the fence and a low-pressure region above the fence in their wind tunnel test. The pressure value at the center of the low-pressure area downwind of the fence decreased with the increase of the fence height and the free-stream wind velocity. Chen et al. (2012) conducted a 3D numerical simulation of the flow field around a triangular-shaped prism model behind a porous deflector. The results showed that the displaced low speed region enlarged as the fence height increased, and the protected region was increased with the increase of the fence height. These numerical simulation results (Chen, et al., 2012) are in good agreement with

the wind tunnel results (Ping , et al., 2013).

Mulati & Norio (2009) propose an empirical relation between the bulk drag coefficient Cd and the fence width W and height H, which is:

$$C_d = k_d \left(\frac{W}{H}\right)^{-b} \quad \textbf{Eqn.2-13}$$

where $k_d$and b are constants and are dependent on the *ad* value. *ad* represents the fractional volume of the flow domain and is calculated using Eqn. 2-14.

$$ad = d^2/\Delta S^2 \quad \textbf{Eqn.2-14}$$

where *d* is the diameter of the cylinder and ΔS is the mean space between the cylinders. It is concluded that the drag force increases with the increase of the fence width, but the increase is not linear due to the sheltering effect. The fence width has significant effect on the minimum wind velocity and location behind and downstream of the fence.

2.3.4. Fence orientation

While the work on the effect of upwind flow angle on the performance of porous fences is limited, it is fairly well understood from a general perspective. The effective opening size in terms of flow passage will be reduced due to the oblique angle between the wind flow and the opening surface, which increases the total drag force. With the increase of the oblique angle, bleed flow may follow a longer, sinuous path through the fence (Tabler, 2003), resulting in the flow being deflected laterally as it passes through.

From the point of view for drag force, the force acting on the fence will be split into a normal drag force perpendicular to the fence and a frictional drag force parallel to the plane of the fence when the fence is not perpendicular to the wind flow. The frictional drag force can be determined using a frictional drag force coefficient in the range of *0.01-0.04* depending on the surface roughness of the fence (Australia, 1989). However, the frictional drag force coefficient provided by the wind is valid for the case when the wind is parallel to the plane of the fence. It should be reduced by a factor of $sin(\theta)$ when the normal of the fence is at an angle θ to the onset wind flow (Holmes, 1988). The normal force coefficient C_n for a fence at an oblique angle θ can be expressed as the following

(Richards & Robinson, 1999):

$$C_n(\theta) = \frac{k_r \cos^2(\theta)}{(1+k_r \cos^2(\theta)/4)^2} \quad \textbf{Eqn.2-15}$$

where k_r is the loss coefficient defined by Eqn. 2-10.

Hence, the effect of oblique fence is a function of $\cos^2(\theta)$. For high aspect-ratio fences, Eqn. 2-15 can be used to obtain the ratio of normal force coefficient to oblique wind force coefficient to reflect the effect of fence orientation on the fence performance, which is:

$$\frac{C_n(\theta)}{C_n(Normal)} = cos^2(\theta)\left(\frac{4+k_r}{4+k_r\, cos^2(\theta)}\right)^2 \quad \textbf{Eqn.2-16}$$

The proportionality of $cos^2(\theta)$ compares well to experimental results on shelter distances reported by Wang & Takle (1996), who found a very similar cosine relationship relating the shelter distance of a fence under oblique winds to the distance under normal wind conditions. With decreasing porosity and thus increasing resistive loss, this cosine proportionality begins to fail.

2.4. ASPECTS ASSOCIATED WITH EXPERIMENTAL TEST

Experimental study on the performance of porous fences usually involves direct experimental measurements of the flow field around a scaled fence model in a wind tunnel or an on-site full-scale fence in a field, representing typical environmental conditions. The types of measurements taken during the test depend on the location and the test conditions. Under a particularly hostile environment, on-site measurements may have to be limited to visual or manometry recordings as the use of complex imaging or measurement systems can be difficult. Another difficulty for on-site measurement is to find suitable locations with upstream conditions that are not only controllable but also with appropriate “boundary conditions” to represent a generic case. Hence, while on-site test of full-scale fence may yield the most “realistic” experimental data, such a test is normally expensive, and limited by environmental conditions which restrict or interfere with installation, experiment, and removal operations.

Wind tunnel tests are more accessible than full-scale on-site tests as they are more controllable, and support more complex measuring systems. Measurement data can be

recorded using a data-logging system and analyzed after. It should however be aware that, while wind tunnel testing method is more convenient and potentially less expensive than the on-site full-scaled experiment, certain degree of similitude criteria needs to be satisfied for the scaled model to yield similar results to represent the real case. Besides, the use of a closed working section may also introduce some artificial effect on the flow behavior.

2.4.1. Basics of wind tunnel experiment

Open circuit and closed circuit are the two basic types of wind tunnels. The air flowing through an open circuit tunnel follows an essentially straight path from the entrance through a contraction to the test section, followed by a diffuser, a fan section, and an exhaust of air. The tunnel may have a test section with no solid boundaries (open jet or Eiffel type) or solid boundaries (closed jet or National Physical Laboratory (NPL) type). Air flowing in a closed return wind tunnel, Prandtl, or Göttingen type, recirculates continuously with little or no exchange of air with the exterior. The decision on the type of tunnel to be applicable is normally made on the measurement purpose and the funding available for the research.

Depending on the applications, the types of wind tunnel can be categorized as Aeronautical, smoke, automobile, Aero-acoustic, water, general-purpose and environmental wind tunnels (Barlow, et al., 1999). A majority of wind tunnel experimental investigations on the performance of porous fences were conducted in the environmental wind tunnels (Bradley & Mulhearn, 1983) (Dong, et al., 2007) (Dong, et al., 2006) (Giannoulis, et al., 2010) (Gurer, et al., 2002) (Lee, et al., 2002). One important feature of the environmental wind tunnel is that it is manipulated to obtain a flow distribution, which is non-uniform in time and space to represent the atmospheric boundary layer. It is accomplished by having adjustable roughness elements along the floor of the tunnel with a long span of the test section to ensure the wall-boundary atmospheric airflow to be simulated.

A typical experimental set-up for a wind fence model tested in the wind tunnel is demonstrated in Figure 2-12, which is applied non-intrusive techniques to measure the

airflow field. During test, the fence model must be positioned at a certain distance downwind from the entrance of the test section to ensure the development of wall-bounded atmospheric airflow. Airflow profile before the model is monitored by Pitot static tube manometer and the wind velocity field leeward the model is captured by a particle image velocimetry (PIV) (Otakeguchi, et al., 2012). Fine talcum powder with a mean diameter less than $10\mu m$ is used as a seeding material. An electric duster is used to spray the powder at the entrance of the test section so that the tracer powder can follow airflow. The charge-coupled device (CCD) camera of the PIV system is set to capture the lee airflow pattern and yields a wind-velocity database for analysis.

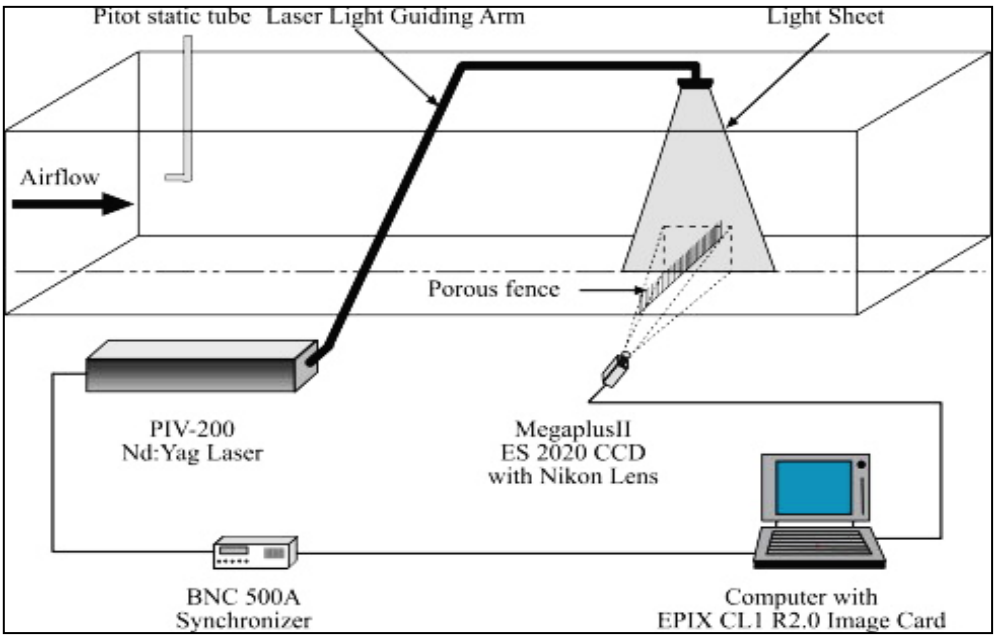

Figure 2-12: A schematic diagram of the experimental set-up (Dong, et al., 2010).

The wind tunnel flow should ideally have a mean longitudinal pressure gradient of zero. Any model should not exceed *10%* cross-sectional area blockage at any downwind location. This insures that local flow accelerations affecting the longitudinal pressure gradient will not distort the simulation flow. Ideally, a tunnel should be large enough to handle a full-scale structure. This can however be very costly and in most cases impossible. It is therefore very important to understand the scaling effect so that the model experiments can be representative of the performance of a real structure.

2.4.2. Similarity between scaled models and real structures

Similarity is a concept used during the test of scaled models to ensure that the model testing results can be representative of the behavior of the real engineering structures. A scaled model is defined to have similarity with the real application if the two share geometric similarity, kinematic similarity and dynamic similarity. Construction of a scaled model must therefore be accompanied by an analysis to determine what conditions are tested under.

Geometric similarity is to ensure the scaled model to have the same shape as the real structure. Kinematic similarity is to ensure the fluid flow of both the scaled model and real structure to undergo similar time rates of change motions, i.e., showing similar fluid streamlines. Dynamic similarity is to ensure ratios of all forces acting on corresponding fluid particles and boundary surfaces in the scaled model and the real structure to be constant. To achieve these three similarities, all parameters required to describe the system should be identified using the principles from continuum mechanics. Dimensional analysis should be carried out to express the system with as few independent variables and as many dimensionless parameters as possible. The values of the dimensionless parameters should be the same for both the scaled model and the real structure. This may be done because they are dimensionless and will ensure dynamic similitude between the model and the application. The resulting equations should be used to derive scaling laws, which dictate model-testing conditions (Kline, 1986) (Chanson, 2009) (Heller, 2011). Strict similarity is very difficult to achieve during a model test. The greater the departure from the application's operating conditions, the more difficult it is to achieve the required similitude.

2.4.3. Key aspects associated with the model similarity for airflow

2.4.3.1. Geometric scaling

The similarity criteria can be obtained from the equations of motion for a particular flow problem through dimensional analysis. The non-dimensional equations yield the governing similitude parameters as the coefficients of individual terms of the equations

of the motion. By matching the governing similitude parameters of the equations of motion between the scaled model and the real engineering structure, the same physical process of the full-scale flow can be simulated in the laboratories.

The non-dimensional momentum equation is given as (White, 1996):

$$\frac{\partial \hat{\bar{u}}_i}{\partial \hat{t}} + \hat{\bar{u}}_j \frac{\partial \hat{\bar{u}}_i}{\partial \hat{x}_j} + \left[\frac{L_0 \Omega_0}{u_0}\right] 2\varepsilon_{ijk} \hat{\Omega}_j \hat{\bar{u}}_k = -\frac{\partial \hat{\bar{p}}}{\partial \hat{x}_i} - \left[\frac{\Delta \bar{T}}{\bar{T}_0} \frac{L_0 g_0}{u_0^2}\right] \Delta \hat{\bar{T}} \hat{\bar{g}} \delta_{i3} + \left[\frac{v_0}{u_0 L_0}\right] \frac{\partial^2 \hat{\bar{u}}_j}{\partial^2 \hat{x}_k} + \frac{\partial \left(\overline{-\hat{u}_i' \hat{u}_j'}\right)}{\partial \hat{x}_j}$$

Eqn.2-17

where the dependent variables are represented by mean quantities (represented by a bar over the variable) and fluctuating values (no bar over the variable). The dimensionless variables are:

$$\hat{\bar{u}}_i = \bar{u}_0/u_0, \hat{u}_i' = u_i'/u_0, \hat{x}_i = x_i/L_0, \hat{t} = tu_0/L_0, \hat{\Omega}_j = \Omega_j/\Omega_0, \hat{\bar{p}} = \bar{p}/(p_0\, u_0^2), \Delta\hat{\bar{T}} = \Delta\bar{T}/\Delta\bar{T}_0, \ \hat{\bar{g}} = g/g_0.$$

where u is the velocity; $x = (x, y, z)$ is the position vector; L_0 is the reference length; ε is the rate of energy dissipation; g is the acceleration of gravity; $\bar{p}$ is the deviation of pressure from the atmospheric pressure associated with p_0; and Ω is the Coriolis effect caused by the rotation of the Earth.

To maintain the similarity between the scaled model and the real engineering structure, geometric scaling must be applied properly in the model testing. It is desirable to obtain equality of the ratios of the full-scaled object to roughness size of terrain, boundary layer thickness, and integral scale of the longitudinal component of turbulence.

2.4.3.2. Atmospheric boundary layer consideration

A majority of wind tunnel tests has been conducted in the environmental wind tunnels as they can simulate the surface-layer flow of the atmospheric boundary layer (ABL) for neutral stability conditions. Neutral stability is the condition where the natural motion of air neither grows nor decays, and remains at its initial amplitude. The surface layer of the

ABL varies in height as a function of surface roughness and the wind speed above the ABL called the geostrophic wind. Typical height of the surface layer ranges from tens of meters to an upper limit height of about hundred meters. The low portion of the turbulent boundary layer is relevant to the research of the current study. Exact modeling of the entire ABL in detail is not possible up to now. However, by relaxing the certain requirements and deleting certain non-essential similitude parameters, it is possible to obtain a reasonable laboratory simulation of atmospheric flows.

One of the basic features of the ABL is its turbulence. Turbulent flow has long been considered as three-dimensional with a random distribution of vertical eddies superimposed on the main flow. Studies of the turbulence boundary layer are extensive. For the case of a neutrally stratified ABL, Bagnold (1941) discovered that the velocity profile in the turbulent boundary is fitted using a logarithmic expression as the following:

$$\overline{u_{(z)}}/U_{free} = (u_*/K) \cdot \log(z/z_0) \qquad \textbf{Eqn. 2-18}$$

where $\overline{u_{(z)}}$ is the time averaged velocity that is a function of height z, U_{free} is the mean freestream wind velocity, u_* is the friction speed, K is the von Kármán's universal constant, and z_0 denotes the equivalent-surface-roughness height.

2.4.3.3. Boundary condition consideration

Critical non-dimensional boundary conditions should be identical between the scaled model and the real engineering structure to maintain the model similarity. Snyder (1972) listed following four most important non-dimensional boundary conditions, which should ideally be identical for wind tunnel experiments.

1) Normalized mean velocity, turbulence intensity, and turbulent energy spectra profiles

   Matching the normalized mean velocity profile involves selecting an appropriate wind-tunnel floor roughness that will produce the correct or desired value of the power-law exponent α. The power-law profile is known to describe the entire ABL and is given (White, 1996):

$$\frac{\bar{u}}{U_{ref}} = \left[{}^{z}/_{z_{ref}}\right]^{\bar{\alpha}} \qquad \textbf{Eqn.2-19}$$

where U_{ref} and z_{ref} are the mean speed and height of a reference location.

By changing the wind tunnel floor roughness, the simulation value of $\bar{\alpha}$ can be adjusted. With some cares, the wind tunnel $\bar{\alpha}$ value can be made to match the $\bar{\alpha}$ value of the real engineering structure. It is however not possible to match the entire normalized turbulence intensity profile due to the scaling effect in wind tunnel testing. A compromise to deal with this problem is to match the normalized turbulence intensity profile in the lower portion of the wind tunnel boundary to that of the ABL.

In wind tunnel simulation of ABL flow, the mean non-dimensional velocity profile is the easiest to match while the energy spectra profile is the most difficult to match. A fetch length refers to the actual longitudinal length of the test section of the wind tunnel. In general, a fetch length of *10-25* boundary layer height is required to match the mean non-dimensional velocity profile. To match the turbulence intensity profile, about *50* boundary layer height is required for the fetch length. To match the normalized turbulent energy spectra, about *100-500* boundary layer height is required for the fetch length.

2) The roughness Reynolds number $\boldsymbol{R_{e_r}}$

The roughness Reynolds number is defined as:

$$R_{e_r} = {}^{\rho \cdot z_0 \cdot u_*}/_{v} \qquad \textbf{Eqn.2-20}$$

where: z_0 is the roughness length, u_* is the friction speed, v is the kinematic viscosity of the fluid, and U_0 is the velocity at the reference height h_{ref} above the ground.

To simulate a naturally occurring ABL, the roughness Reynolds number needs to be greater than *2.5* as ABL flows are usually aerodynamically rough. For R_{e_r}>*2.5*, the Reynolds number independence can be achieved and the wind tunnel flow can therefore simulate the rough flow of full-scale test (White, 1996).

3) Jensen's length-scale criterion of $\boldsymbol{z_0/H}$

To obtain correct simulation of the pressure distribution on objects in the atmospheric layer of the wind tunnel testing, the surface roughness to object characteristic scaled height ratio z_0/H in the wind tunnel must be equal to that of the full-scale value (White, 1996).

4) The ratio of $\boldsymbol{H/\delta}$

The ratio of H/δ is the characteristic scaled height to boundary layer height ratio. If the H/δ ratio is greater than *0.2* for a full-scaled model, this ratio should be matched in the wind tunnel test. If the H/δ ratio is less than *0.2* for a full-scaled model, this ratio should be below *0.2* in the wind tunnel test.

To satisfy the critical non-dimensional boundary conditions, the testing wind tunnel should have a large span of the test section with adjustable floor, which has capability to simulate various Atmospheric Boundary Layers (ABLs) in needs. Usually it requires the wind tunnel to be able to produce a naturally developed simulated ABL with a nominal thickness in the range of *0.5-1m* at an ambient wind speed of about *10m/s*.

2.4.3.4. Reynolds number scaling

To maintain proper aerodynamic similarity, three similitude parameters should be matched to their full-scaled values in laboratory simulation, which are the Rossby number R_0 defined by Eqn. 2-21, the bulk Richardson number R_i defined by Eqn. 2-22, and the Reynolds number R_e defined by Eqn. 2-23.

$$R_0 = u_0/L_0\,\Omega_0 \qquad \textbf{Eqn.2-21}$$

$$R_i = [(\Delta\bar{T})_0/\bar{T}_0][L_0 g_0/u_0^2] \qquad \textbf{Eqn.2-22}$$

$$R_e = \rho \cdot u_0 L_0/v_0 \qquad \textbf{Eqn.2-23}$$

R_0 is associated with the ratio of advective (or local acceleration) to the Coriolis Effect caused by the rotation of the Earth. Tennekes (1973) proposed that the mean velocity profile is logarithmic over the lower *10%* to *15%* of the boundary layer for most non-rotating wind tunnels. A wind tunnel with sufficient fetch will produce a boundary-layer height of about one meter, which suggests that the lower *10* to *15cm* may be applicable

to simulate the surface layer of the ABL. Therefore, effects of R_0 can be negligible if laboratory testing is contained in the lower *10%* to *15%* of the height of the boundary layer. It also imposes a practical upper limit of a few kilometers on longitudinal length that may be modeled in the laboratory (White, 1996).

R_i represents buoyance to inertial forces. Small values of R_i suggest that inertial forces are dominant. If the atmospheric flow is of neutral stability, R_i can be considered as zero.

R_e is the ratio of inertial to viscous forces, and is perhaps the most important parameter in fluid dynamic analysis. Almost no field cases could be modeled in the laboratory if strict adherence to the Reynolds number criterion were required. Townsend (1956) discovered that in the absence of Rossby and Bulk Richardson number effects, scaled model flows were dynamically similar to the full-scale case if the Reynolds number was equal or greater than the minimum independence value. Such a phenomenon is called Reynolds Number Independence. As such, the roughness Reynold number $R_{e_r}>2$ is generally required in the practice (White, 1996).

It is also worth noting that there are two additional similarity parameters in model testing, which are Prandtl number and Eckert number. For wind tunnel simulation in air the Prandtl number criterion is automatically satisfied. The Eckert number criterion is only important in compressible flow, which is not so relevant to the current study.

2.4.4. Wind tunnel simulation of snowdrift transport

Scientists have performed snowdrift modelling in wind tunnels since 1930s. The similarity requirements are difficult to satisfy simultaneously due to the number of parameters involved. White (1996) provided a list of dimensionless parameters to be met for wind tunnel simulations of windblown particle transport. These dimensionless parameters include:

$u(h)/u_F$, $[u(h)]^2/(g\cdot L)$, e, l/H, z_0/H, z_0'/D_p, h/L, z_0/L^*, λ/L, u_F/u_{*t}, $u_{*t}\cdot D_p/\nu$, u_*/u_{*t}, $u(h)t/L$, $\rho\cdot u(h)L/\nu$.

where ρ is the mass density of atmosphere, ρ_p is the particle density, $u(h)$ is the reference velocity, u_F is the terminal velocity, g is the acceleration of gravity, h is the reference

height and L is the reference length. e is the coefficient of restitution, z_0 is the roughness length, z_0' is the equivalent roughness height in saltation, $L*$ is the Monin-Obhukov stability length, λ is the ripple wave length, u_* is the friction speed, and v is the kinematic viscosity of the fluid, u_{*t} is the threshold friction velocity.

The number of these dimensionless parameters to be satisfied for the two-phase flow (air-snow particles) model testing illustrates the challenging nature of the problem. Further investigations reveal that some of them are virtually impossible to match between the scaled model in wind tunnel and the full-scaled model in the reality. One foreseeable difficulty is the significant difference in the distribution of snow particles between the natural and the wind tunnel environments. The snow particle size is variable and can be very different to the characteristic length scale of the model.

The Froude number $[u(h)]^2/(g \cdot L)$ cannot be satisfied easily in the wind tunnel without having a tunnel speed far below the threshold speed. Hence, it is desirable to make the wind tunnel speed as small as possible yet still satisfy other parameters, e.g. $R_{e_r} > 2.5$. The coefficient of restitution e can be satisfied if the model and atmospheric materials have equivalent elastic properties. The aerodynamic roughness should be scaled. If the corresponding modelling surface in the wind tunnel is too smooth, it may be necessary to distort z_0/H in order to meet the turbulent boundary layer requirement of $R_{e_r} > 2.5$.

The equivalent roughness height in saltation z_0' is proportional to particle diameter D_p. Obviously z_0'/D_p cannot be satisfied in laboratory simulations since fine particles would have high threshold speeds. If introduced into the air stream, the fine particles would go into suspension and the saltation process would not occur.

Constrained by the dimensionless parameter of $u(h)t/L$, the characteristic time is the ratio of characteristic length L to reference velocity $u(h)$, which means that the time scale in the wind tunnel is much shorter than that of the full scale test in the field. The time necessary for pattern development in the field can thus be predicted from wind tunnel tests.

It is clear that not all of the similitude parameters can be satisfied simultaneously in a scaled model testing. Further analysis is required to identify the most important

parameters or combination of parameters for the model testing. Based on the analysis of the dimensionless analysis of the governing particle flow equation of motion, it has been suggested that following dimensionless parameters need to be justified for simulate windblown particle transport in the wind tunnel experiments (White, et al., 1975):

$$\left.\frac{H}{z_0'}\right]_{\substack{wind\\tunnel}} = \left.\frac{H}{z_0'}\right]_{field} \quad \textbf{Eqn.2-24}$$

$$\left.\frac{x}{D_d}\right]_{\substack{wind\\tunnel}} = \left.\frac{x}{D_d}\right]_{field} \quad \textbf{Eqn.2-25}$$

$$\left.\frac{C_D p D_d}{p_p D_p}\right]_{\substack{wind\\tunnel}} = \left.\frac{C_D p D_d}{p_p D_p}\right]_{field} \quad \textbf{Eqn.2-26}$$

$$\left.\frac{g D_d^2}{u_*^2}\right]_{\substack{wind\\field}} = \left.\frac{g D_d^2}{u_*^2}\right]_{field} \quad \textbf{Eqn.2-27}$$

2.4.5. Measurement techniques applied in the research field

The measurement techniques applied in the research field can be categorized as the point-measuring technique and the whole-field measuring technique.

- Point-measuring technique (PMT)

  PMT employs a probe to record the history of flow over time at one point in space. The measured parameters are expressed as a function of time and space, and the whole-field parameters are possible to be obtained by positioning multi-sensors at several measuring points simultaneously. The experimental results are in an Eulerian fame usually.

  Conventional cup type anemometer, hot-wire anemometer (HWA), pulsed-wire anemometer (PWA), laser-Doppler anemometer (LDA), phase-Doppler anemometer (PDA), and ultrasonic anemometer (UA) are PMT measuring sensors. All of these sensors provide time averaged velocity and turbulence intensity values at discrete measuring points. Apart from LDA and PDA, these anemometers are intrusive to the airflow field, and therefore reduce the accuracy of measurement.

The earliest attempt at measuring turbulent velocity fluctuations behind fences was made by Hagen & Skidmore (1971) in the field using conventional cup-type anemometers to have a rough estimate of the turbulence intensity. Bradley and Mulhearn (1983) used sonic anemometers to analyze the downstream variation of shear stress and turbulent kinetic energy in the field. Raine and Stevenson (1977) studied the velocity and turbulence fields using a HWA while Perera (1981) used a PWA.

- Whole-field measuring technique (WFMT)

WFMT measures parameters at different positions simultaneously by employed flow visualization techniques. The strategy of the technique is to make fluid movement visible by seeding suitable "fluid tracers", and high-speed and high-resolution cameras record the motion of the tracers. The whole velocity field can be recovered by analysing physical positions of the tracers at different image frames. If individual tracers are tracked, the result will be in a Lagrangian frame, which usually is named as Particle Tracking Velocimetry (PTV); if groups of tracers are tracked, the result will be in an Eulerian frame, which is named as Particle Image Velocimetry (PIV).

WFMT is non-intrusive to the airflow field with a high spatial resolution and quick response time for data acquisition. Dong.et al (2010) used PIV to measure the turbulence fields behind upright porous fences in the wind tunnel experiment. Lee and Kim (1999) measured the velocity and turbulence fields of the near-wake region behind porous fences using a two-frame PTV method. The improved measurement accuracy makes WFMT popular in the present research activities.

However, WFMT is expensive in purchase and extremely expensive in measuring three dimensional velocity field, and usually is not applicable to on-site field experiments. Besides, interpretation of the motion of the tracers at some positions may be difficult that could introduce errors in data acquisitions. As such, PMT is still not replaceable. Table 2-2 lists a comparison of measuring instruments applied in this research field.

Table 2-2: Comparison of measuring instruments

Category	Instrument	Advantages	Disadvantages
PMT	Cup-type	Cheap and easy to operate	• Low accuracy to low velocity¨ • Low spatial resolution • unlike to detect velocity direction and turbulence intensity • Intrusive
	Pitot Tube	Cheap and easy to install	• Slow response • Low accuracy to low velocity • Hard to align with airflow • Low spatial resolution • Intrusive
	HWA &PWA	• Cheap and easy to operate • Quick response time	• Low accuracy to low velocity • Expensive in detect velocity direction • Low spatial resolution • restraint to testing environment • Intrusive
	LDA&PDA	• Quick response time • High accuracy • Non-intrusive	• Expensive in purchase and operating • Low spatial resolution
	UA	• Moderate cost and easy to operate • Quick response time • High accuracy	• Low spatial resolution • Intrusive
WFMT	PIV&PTV	• High spatial resolution • Quick response time • Non-intrusive	• Expensive in purchase and operation • Usually reconstruct two dimensional velocity field

2.4.6. Other issues to be addressed for wind tunnel testing

Apart from the challenges of satisfying the similarity between the scaled model test and the full-scaled field test mentioned above, there are other issues to be addressed to improve accuracy and reliability of wind tunnel testing results. It is well recognized by the research community that the testing facilities employed in wind tunnels need to be to address following issues:

1) Limitation of wind tunnel space

   In theory, there is a simple solution to solve the challenge of model similarity requirement by establishing a big enough wind tunnel to meet the testing requirement. In practice, it is very difficult if not unrealistic to build bigger wind tunnels due to very high construction and operation costs. Further research is required to find an innovative way to improve wind tunnel design, which might solve the space issue of wind tunnel testing economically. This is achievable through a better understanding of the mechanism of wind flow and snow transport using combined research of wind tunnel testing and numerical simulation.

2) Resolution and reliability of measurement facilities

   Measuring the structure of airflow regime behind a porous fence is not an easy task. Both of PMT and WFMT have their limitations as discussed in Section 2.5.4, especially in inadequacy to measure the complex nature of turbulence developed by the fence with low or medium porosities.

It is not rare that inconsistent sometimes even contradictory results were reported in the literature. Some can be explained by the limitation of the resolution and reliability of the measurement facilities employed in the research. Carefully configuring spatial resolutions and appropriately selecting the type of measurement instruments can improve accuracy of the measurement. However, error analysis must be addressed and stated in the experimental reports.

2.5. ASPECTS ASSOCIATED WITH NUMERICAL STUDIES

2.5.1. Basics of computational fluid dynamics

Computational fluid dynamics (CFD) technique, as a supplementary tool in the fence study, has attracted increasing research interest over last three decades. It is often motivated by the limitations of measurement techniques and the challenges in meeting the model similarity requirement in wind tunnel test as mentioned in Section 2.5. Besides, testing in wind tunnels usually requires elaborate equipment, intensive labor and time, which could lead high costs. In contrast, numerical simulations are flexible as they are able to simulate whatever geometry or geography is required without the restraint of similitude requirement. Depending on the equations solved, the entire flow field can be solved to obtain the required information at any point in time for further derivation or analysis. Different commercial software packages such as ANSYS CFD, STAR CCM+ and open-source CFD codes are available to tackle engineering problems in a wide range. The continuing trend for greater computing power at lower costs allows investigating the performance of porous fences by using CFD techniques. Especially where fast solution and optimization are required, or when experimental study encounters difficulties in the similarity requirement, and the initial cost of model fabrication and experimental set-up (Alhajraf, 2004) (Wakes, et al., 2010) (Andres , et al., 2011).

Numerical study of the performance of porous fences involves a multi-stage approach that can generally be divided into the following steps:

1) Geometric modelling of the geometry
2) Division of geometry into computational “cells”
3) Boundary condition definition
4) Model solving
5) Post processing and data analysis

The limitation of CFD simulations is that they are restricted in terms of accuracy as the numerical models are solved approximately. Numerical approximations, parameterization schemes (e.g. turbulence models, discretization techniques) and the choice of boundary

conditions can introduce errors in solutions. This is especially true for those time-averaged turbulence models insufficient to simulate strong turbulence presented around porous fences, particularly for the fence with low or medium porosity. The accuracy of the numerical solution is also limited by the difficulty in modelling identical/correct boundary conditions. As a result, every CFD model faces a question of accuracy in its predictions and requires validation of its modelling.

2.5.2. Governing equations

CFD simulations involve discretization and solution of the Navier-Stokes-equations (NSE). The NSE describes the physics of liquids and gases in motion and can be written for incompressible fluids as:

$$\frac{\partial u_i}{\partial t} + u_j \frac{\partial u_i}{\partial x_j} = f_i - \frac{1}{\rho}\frac{\partial p}{\partial x_i} + v\frac{\partial^2 u_i}{\partial x_j \partial x_j} \qquad \textbf{Eqn.2-28}$$

where u_i is the velocity component in three dimensions, f_i is the body force per unit volume, ρ is the density and v the dynamic viscosity of the fluid.

The continuity equation for incompressible flows is:

$$\partial u_i / \partial x_i = 0 \qquad \textbf{Eqn.2-29}$$

Fluid turbulence occurs commonly in industrial or atmospheric flows. It is characterized by increased unsteadiness of the flow, resulting in higher rates of transfer to momentum through the fluid. Reynolds number is the key parameter in the study of fluid turbulence. Reynolds (1895) found that the laminar-turbulence transition in the pipes occurred between R_e equal to *2 000* and *13 000*, depending on the smoothness of the entry conditions. When extreme care taken, the transition can even happen with R_e as high as *40 000*. Due to the large length scales involved in atmospheric or industrial flows, turbulence is an aspect that is tightly intertwined with any industrial fluid flow, although there may be small areas that may be subject to local re-laminarization. Theoretically, direct numerical simulation (DNS) and Large Eddy Simulation (LES) can directly solve turbulent flow based on the NSE. However, it requires a very fine computational grid down to the millimeter scale (or even smaller at higher Reynolds numbers), which has an

extremely high demand on both computational power and accuracy of the numerical method to ensure that rounding errors do not profoundly affect the result. Hence, to make simulations of general flow problems more feasible, a set of turbulence models are introduced where the fluid motions are computed based on mean quantities, which allows a much coarser mesh to be used.

The most applied turbulent model approach is obtained by applying the Reynolds decomposition (Eqn.2-30) into the NSE (Eqn.2-28):

$$u_i = \overline{u_i} + u_i' \qquad \textbf{Eqn.2-30}$$

That comes to the Reynolds-averaged Navier-Stokes (RANS) equations expressed as the following:

$$\frac{d\overline{u_i}}{dt} + \overline{u_j}\frac{\partial \overline{u_i}}{\partial x_j} = -\frac{1}{\rho}\frac{\partial \bar{p}}{\partial x_i} + \overline{f_i} + \nu\frac{\partial^2 \overline{u_i}}{\partial x_j \partial x_j} - \frac{\partial \overline{u_i' u_j'}}{\partial x_j} \qquad \textbf{Eqn.2-31}$$

Where the variables marked by the bar are the time-averaged values. The additional terms of $\frac{\partial \overline{u_i' u_j'}}{\partial x_j}$ are the Reynolds stresses that cannot be solved by the RANS itself. This "closure problem" will be solved by a set of turbulence models discussed in Section 2.5.3.

2.5.3. Turbulence models

The "closure problem" can be addressed using the turbulent viscosity hypothesis by introducing a proportional relation between the Reynolds stresses and the mean rate of strain using a scalar coefficient. Two-equation models include two extra transport equations to represent the turbulent properties of the flow, which allows accounting for history effects like convection and diffusion of turbulent energy. Therefore, the "closure problem" can be solved.

2.5.3.1. Two-equation turbulence models

For two-equation models, most often the first transport variable is the turbulent kinetic energy k determining the energy in the turbulence. The second transport variable varies depending on what type of two-equation model is applied, and determines the scale of the turbulence (length-scaled or time-scaled). When the second transport variable is selected

as the turbulent dissipation ε, it is named the k-ε model; when the second transport variable is chosen as the specific dissipation ω, it is called the k-ω model. Two-equation models like k-ε and k-ω models have become industrial standard models and applied for most types of engineering problems.

The k- ε model is the most widely used and validated model with applications ranging from industrial to environmental flows. It focuses on the mechanisms that affect the turbulent kinetic energy and assumes that the turbulent viscosity is isotropic. In other words, the ratio between Reynolds stress and mean rate of deformations is the same in all directions. The two equations associated with the Standard k-ε model for incompressible fluid include Eqn.2-32 for turbulent kinetic energy k and Eqn.2-33 for dissipation ε (ANSYS, 2011), which are:

$$\frac{\partial(\rho k)}{\partial t}+\frac{\partial(\rho k u_i)}{\partial x_i}=\frac{\partial}{\partial x_j}\left[\left(\mu+\frac{\mu_t}{\sigma_k}\right)\frac{\partial k}{\partial x_j}\right]+G_k+G_b-\rho\epsilon \qquad \textbf{Eqn.2-32}$$

$$\frac{\partial(\rho \varepsilon)}{\partial t}+\frac{\partial(\rho \epsilon u_i)}{\partial x_i}=\frac{\partial}{\partial x_j}\left[\left(\mu+\frac{\mu_t}{\sigma_\epsilon}\right)\frac{\partial \epsilon}{\partial x_j}\right]+C_{1\epsilon}\frac{\varepsilon}{k}(G_k+C_{3\varepsilon}G_b)-C_{2\varepsilon}\rho\frac{\epsilon^2}{k} \qquad \textbf{Eqn.2-33}$$

where u_i represents velocity component in corresponding direction, G_k and $G_b$represents component of rate of deformation, $\mu_t\ (=\rho C_\mu k^2/\epsilon)$ represents eddy viscosity. σ_k, σ_ε, $C_{1\varepsilon}$, $C_{2\varepsilon}$ and C_μ are adjustable constants in the model and can be determined by numerous iterations of data fitting for a wide range of turbulent flows as (ANSYS, 2011): σ_k=1.00, σ_ε=1.30,$C_{1\varepsilon}$=1.44,$C_{2\varepsilon}$=1.92,C_μ=0.09.

It should be noted that the simplicity of using two equations to calculate turbulence effects in the k-ε model would affect the model performance. For example, second-moment flow features such as lateral flow motions in channels are not modelled. They are also subject to inaccuracies in other flow regimes, such as impingement flows (Laurence, 2002), or where there are strong pressure gradients or streamline curvature (Pope, 2000). These shortcomings motivates the modifications of the Standard k-ε model. The Realizable k-ε

and the Renormalization Group RNG *k-ε* models are modified *k-ε* models improving numerical predictions under different applications.

The *k-ω* model is another widely used to treat ω as the ratio of ε to *k*. The transport equations for the Standard *k-ω* model for incompressible fluid are presented as follows (ANSYS, 2011):

$$\frac{\partial}{\partial t}(\rho k) + \frac{\partial}{\partial x_i}(\rho k u_i) = \frac{\partial}{\partial x_j}\left(\Gamma_k \frac{\partial k}{\partial x_j}\right) + G_k - Y_k \qquad \textbf{Eqn.2-34}$$

$$\frac{\partial}{\partial t}(\rho \omega) + \frac{\partial}{\partial x_i}(\rho \omega u_i) = \frac{\partial}{\partial x_j}\left(\Gamma_\omega \frac{\partial \omega}{\partial x_j}\right) + G_\omega - Y_\omega \qquad \textbf{Eqn.2-35}$$

where G_k and G_ω are the generation of k and ω due to mean velocity gradients. Γ_k and Γ_ω represent the effective diffusivity of *k* and ω, respectively. Y_k and Y_ω are the dissipation of *k* and ω due to turbulence. Detailed set-up of each variable refers to ANSYS Theory(2011).The shear-stress transport SST *k-ω* model is modified by multiplying a blending function to the Standard *k-ω* model in the near-wall region and the transformed Standard *k-ε* model in the far field, so that achieves the *k-ε* is converted into a *k-ω* formulation.

Compared to the *k-ε* models, the *k-ω* models do not contain terms that are undefined at the wall in the equations, which can be integrated to the wall without using wall functions. For a wide range of boundary layer flows with pressure gradient, it is generally accepted that *k-ω* models are better than *k-ε* models in practice. Theoretically applying *k-ω* models may therefore result in better solutions for porous fence involved airflow study, as it is evident that such flows are often in the presence of flow rotation, separation, recirculation and strong adverse pressure gradients on the fence surface.

2.5.3.2. Brief overview of other turbulence models

With the developments of computational techniques and the capacity of computers, it provides possibilities to solve the "closure problem" with reducing the degree of hypotheses in the governing equations. These newly emerged turbulence models solve the "closure problem" based on more than two equations or partially based on DNS, and therefore increase the accuracy of numerical predictions especially for turbulence. The

general features of these models require high quality mesh, often encounter rounding errors in solution convergence, and significantly increase computational cost. The requirement of high quality mesh also limits these models to simple geometric models. Often, these models are limited to research applications rather than industrial applications.

Reynolds stress models (RSM) (Launder, et al., 1975) use six equations to model the different turbulence stresses, and the greater scope of modelling allows for a potentially more accurate solution as they are able to capture second moment flow features, and are able to cope with pressure gradients and significant streamline curvature. RSM however has much higher computing costs compared with the k-ε model. The coupling among the six equations may lead to reduced stability of the solution and the model is sensitive to wall effects.

Large eddy simulation (LES) (Smagorinsky, 1963) and very large eddy simulation (VLES) lying a method in between DNS and eddy-viscosity models (EVMs). LES solves the equations for a filtered velocity field for the larger-scale turbulence motions and applies turbulence models for non-resolved turbulent motions. It is proposed that the smaller scales of turbulence are more homogeneous, and thus can be represented by a simple turbulence model, but the larger scales of turbulent motion are expected to be captured by a finer mesh. The required mesh is denser than that used for the EVMs, but still orders of magnitude coarser than that required for DNS. This allows more detailed flow simulations, but requires more computational power compared with DNS. The turbulent-viscosity hypothesis introduces a proportional relation between the Reynolds stresses and the mean rate of strain using a scalar coefficient. This leads to the effective viscosity hypothesis (EVH) turbulence models that are ensemble-averaged.

RSM and LES models have demonstrated the improved accuracy of numerical predictions by many researchers (Launder, et al., 1975) (Alpman & Long, 2005) (Patton & Shaw, 1998), and have been started to be introduced for the industrial applications.

2.5.4. Numerical simulations of porosity and porous fence

2.5.4.1. Porous fence model creation

The availability of affordable computational resources allows porous problems to be solved computationally. Porous fences can be modelled in two ways: numerically and mathematically. The former assumes that any hole will be properly discretized, in that the computational "mesh" created to have enough cells in each hole to accurately simulate the flow through every hole. This method can be computationally heavy (especially in the case of panels involving multiple circular cutouts) but straightforward with less justification based on empirical knowledge. The complexity of this method is heavily dependent on the original geometry of the fence model. The latter mathematical method involves modelling the porous fence as a wall, and the porous effects are modelled by associating the porosity with a pressure drop. A fundamental law linking pressure drop and velocity in fluid flow through porous media is Darcy's law. In flows of less-than-unity Reynolds numbers, Darcy's Law states:

$$\Delta P = -\frac{\mu \cdot u}{\kappa} \qquad \textbf{Eqn.2-36}$$

where μ is the viscosity, u the upstream velocity and $\kappa$is the permeability of the porous media. This "linear" relationship between the pressure drop and the upstream velocity u is only valid when $Re < 1$. As Reynolds number increases, a smooth transition occurs from a linear to a quadratic relationship. Unlike the transition to turbulence in free fluid flow, the transition from linear to quadratic drag through porous media exhibits no sudden discontinuity, as the increase in form drag due to the solid blockage grows past that of friction (Vafai, 2005).

Darcy's Law correctly describes laminar flow through porous media but results a significant discrepancy in describing turbulent flow. Forchheimer linked this discrepancy to inertial effects and suggested an additional term representing kinetic energy to Eqn. 2-36. The Forchheimer equation describes fluid flow in porous media as:

$$\Delta P = -\frac{\mu}{K}u - c_F K^{-1/2}\rho_f u^2 \qquad \textbf{Eqn.2-37}$$

This equation includes a linear and a quadratic loss term, the latter of which is commonly referred to as the Forchheimer term (Nield & Bejan, 2006). In numerical simulations, Eqn. 2-37 is usually added to the momentum equations as two source terms: a linear loss term ($R_{lin} = -\frac{1}{K}$) and a quadratic loss term ($R_{Quad} = -\frac{c_v}{K^2}$).

It can be found that this model of porosity relies on two different losses. Assuming that the porous media is homogeneous these two loss terms can be consolidate either wholly or just the quadratic (Forchheimer) term into a single resistive loss term k_r (Fang & Wang, 1997) (Packwood, 2000) (Wang, et al., 2001).

$$k_r = \int_{-\infty}^{\infty} C_d A \cdot dx \qquad \textbf{Eqn.2-38}$$

Alternatively, it is possible to bypass this loss term altogether by equating the pressure loss with some form of the drag equation.

The dependence on porosity is through the derivation of the k_r term, of which some approximations can be found in literature (Hoerner, 1965). It is common in the industrial applications to characterize a fence using the value of k_r. Examples like modelling a porous fence as a porous zone or a porous jump (ANSYS, 2011).

The mathematic model greatly simplifies the porous fence model where the presence of porous holes are not physically modelled. Consequently, it reduces the efforts on meshing and computational cost. However, modelling a porous fence by associating its porosity with a pressure drop requires empirical knowledge derived from the physical experiments. The pressure drop is also linked to the surrounding environmental factors like terrain topology and approaching wind profiles. The complex structure of airflow regime around a porous fence makes it questionable if the pressure drop can be mathematically expressed or can be reasonably associated to the porosity, especially for the fences with low or medium porosities. This may explain the reason why numerically modelling porous fence attracts more and more research interest nowadays.

The method of numerically modelling a porous fence is usually performed with 3D modelling. It is straightforward with less empirical knowledge requirement, which benefits to the optimal fence design. These 3D models are able to provide detailed

information within the simulation domains. Information like flow behavior inside porous holes and the distribution of shear stresses and pressures on the fence surface can be difficult to be provided by those mathematically modelling porous fence. The treatment of porous jump for fences only can be performed in 2D modellings.

2.5.4.2. Simulation of airflow around porous fence

The literature is rich for numerical simulations of airflow around porous fences. An early work was made by Tani (1958) where a windbreak was treated as a source of momentum deficit controlled by turbulent diffusion. Wilson (1985) used the RANS equations to introduce a momentum sink involving the fence resistance coefficient to simulate a porous barrier. Other more complex models such as large-eddy simulations (LES) also have been applied. For example, Fang & Wang (1997) employed LSE technique together with a sub grid-scale turbulence model to account for the turbulence effects in the flow. Most early numerical simulations on porous fence were performed with 2D models. 3D models have been used until recent decades. Alhajraf (2004) performed 2D and 3D numerical models to study drifting particles at porous fences. Chen, et al. (2012) and Wang & Hu (2012) used 3D numerical simulation to study wind flow behind a porous fence.

Two-equation based turbulence models are widely applied (Wilson, 1985) (Wang & Takle, 1995) (Packwood, 2000) (Santiago, et al., 2007) in the numerical simulation of airflow around porous fences. The comparison between the numerical simulations and the wind tunnel experiments were favorable in general. It is however found that these two-equation based turbulence models experienced difficulties to accurately reflect the velocity in the immediate lee of the porous fence (Wilson, 1985) (Wilson & Flesch, 1999) (Santiago, et al., 2007). Additionally, the velocity recovery downstream is sometimes under-estimated (Wilson, 1985).

The presence of a porous fence results in an impingement region, which is a source of known inaccuracy in k-ε models (Packwood, 2000) (Laurence, 2002) (Wilson & Yee, 2003). Excessive turbulence is generated in impingement regions, which is then transported downstream. Besides, for the fences with lower porosities, the creation of

downstream separated regions is another known weakness in two equation based turbulence model and can cause additional inaccuracy.

Packwood (2000) attempted to mitigate these issues by modifying the Standard k-ε model using a different definition for turbulence dissipation. Instead of a mean rate-of-strain tensor used in the production term, it was split up into normal and shear rate tensors. In comparison to the implementation of a Reynolds stress model without wall reflection, his modified 'KE-PDM' model performed well. However, it must be noted that this modification did not modify the root cause of the problem associated with the equation for turbulence kinetic energy but merely reduced its impact.

Wilson (1985), using the data of Bradley & Mulhearn (1983) as a benchmark in comparison, applied constant viscosity, mixing length, k-ε and Reynolds stress models to numerically simulate a full-sized porous fence/shelter in 2D. The study looked at a wide range of aspects in the flow field, from more conventional velocity profiles to turbulent stresses up, down and across the fence. Of interest was that none of the models examined could re-produce an accurate velocity profile downstream of the fence (which grows non-uniformly to the free-stream velocity). Behind the fence, the predictions of (asymptotic) axial velocities under-predicted the recovery to free-stream airspeeds. This effect was more pronounced at the fence level height, as opposed to a height above the fence. Whilst Wilson found that the Launder-Reece-Rodi model (Launder, et al., 1975) performed better than the constant viscosity, mixing length and k-ε model, all four methods predicted similar results.

A more modern approach involves using LES, which numerically accounts for the larger scales of turbulence that are more likely to be inhomogeneous. A turbulence model (usually a one-equation Smagorinsky model (Smagorinsky, 1963)) is only used for the much smaller dissipative scales of turbulence, which are more likely to be homogeneous in nature. This method of turbulence simulation is more predominant in other simulation fields, while only a few examples exist in the examination of porous fences. Fang & Wang (1997) and Patton & Shaw (1998) took such an approach. Patton & Shaw (1998)'s work was able to predict the immediate lee flow well, but averaged turbulence statistics compared to Judd, et al.(1996) were less accurate past $x/H = 5$. They suggested that part

of the inaccuracy might lie with the SGS model, grid resolution (both of which are tightly coupled) and that the drag coefficient may have been overestimated.

2.6. ASPECTS ASSOCIATED WITH NUMERICAL SIMULATIONS OF WINDBLOWN SNOWDRIFTS

Numerical modelling of windblown snow transport has been an active research topic for many years. Pomeroy & Gray (1990) developed a useful semi-empirical saltation model applicable to flat areas. Subsequently, Liston & Sturm (1998) used the model without any explicit treatment of the snow crystal characteristics. Naaim et al. (1998) developed a 2D model based on continuum theory of erosion and deposition fluxes in order to simulate wind tunnel experiments. Gauer (2001) combined wind field and snow modelling with sophisticated phenomena descriptions at the expense of computer costs. Yves, et al.(2005) improved a numerical snowdrift model and field validation by coupling with the Safran-Crocus-Mepra (SCM) chain. The SCM chain has been developed by Meteo-France and operated a real-time operational suite aimed at snowpack simulation and avalanche risk forecasting about 10years (Durand, et al., 1999). Sundsbø (1997) investigated snow-accumulations around porous fences by a transient two-phase volume of fluid (VOF) 2D model. Similarly, Alhajraf (2004) analyzed snow transport around the fences by a transient homogenous two-phase mixture model under 2D and 3D domains, where the velocity profiles were modified by the evolution of snow deposition at the snow bed. Both of them have shown numerical results in good agreement with experimental results (Tabler, 2003). Bang et al. (1994) developed a two-phase snowdrift model named “a generalized drift-flux model” where 3D snow deposition was calculated around a group of houses with snow deposition expressed as surfaces, and the influence of saltation was not considered. Beyers & Waechter (2008) and Tominaga (2011) used a similar “conservative snowdrift model” to predict the rate of snow deposition or erosion at surface cells, where the snowdrift model was assigned to the first control volumes adjacent to the snow bed and solved by the means of coupled user subroutines. The significance of their model is quantitatively well-predicted snowdrift formation around a building model with time evolution.

Numerical modelling of windblown snowdrift transport may be solved based on Eulerian-Eulerian or Eulerian-Lagrangian phase frames, or may be simulated by steady or transient state. The majority of snowdrift transport models are heavily reliant on the empirical knowledge laid by Bagnold (1941), where the threshold friction velocity is the decisive parameter to define snow transport modes.

2.6.1. Empirical knowledge applied to CFD snowdrift models

The CFD snowdrift transport model was formed based on the empirical knowledge of Bagnold's threshold friction velocity theory (Bagnold, 1941). In his theory, if wind shear velocity (or named as wind friction velocity) exceeds its threshold friction velocity, wind driven particles will be entrained and set in motions, which results in an amount of particles to be transported. Due to the interactions between particles and wind, the wind field is modified and the friction velocity is updated, that leads to a probability to deposit or rebound particles. The threshold friction velocity is the minimum friction velocity required to maintain the movement of the particles, which is the core parameter to form wind driven snowdrift transport in CFD modellings (Alhajraf, 2004) (Beyers & Waechter, 2008) (Naaim-Bouvet & Martinez, 1998).

2.6.1.1. On saltation

Considerable experimental results indicates that the threshold velocity is a function of the particle size, shape and density (Bagnold, 1941) (Schmidt, 1980), which is expressed as the following:

$$u_{*t} = A_{i.e}\sqrt{\frac{\rho_p - \rho}{\rho} g D_p} \qquad \textbf{Eqn.2-39}$$

where $A_{i.e}$is the dimensionless threshold velocity that is neglected cohesive and adhesive forces among particles. The value of $A_{i.e}$for frozen snow particles is much higher than the one for newly fallen snow particles. Experimental results also reveals that $A_{i.e}$is not a function of the physical properties of the particles for high particle Reynolds number, at which U_{*t} has almost constant value for all particles (Greeley & Iversen, 1986). The particle friction Reynolds number is calculated as:

$$Re_{*t} = u_{*t} D_p / v$$ **Eqn.2-40**

Typical threshold friction velocities are $u_{*t} < 0.25 m/s$ for fresh snow and $0.25 m/s \leq u_{*t} \leq 1.0 m/s$ for old and wind hardened snow surface (Tabler, 2003) (Pomeroy & Gray, 1990).

The roughness length z_0 is coupled with the friction velocity $u_{*t}$when wind driven snow particles start to saltate (Owen, 1964) (Tabler, 2003), which can be expressed as:

$$z_0 = 0.12\, u_*^2 / 2g$$ **Eqn.2-41**

The saltation height is proportional to the particle lift velocity, which was suggested by Schmidt (1980) and Owen (1964). The saltation-layer height is estimated following Owen's expression:

$$h_{sal} = 1.6\, u_*^2 / 2g$$ **Eqn.2-42**

The mean saltation snow velocity u_p is proportional to the threshold shear velocity (Pomeroy & Gray, 1990), where *c=2.3*:

$$u_p = c u_{*t}$$ **Eqn.2-43**

The mean saltation density η_r is (Pomeroy & Gray, 1990):

$$\eta_r = Q_{sal} / h_{sal}\, u_p$$ **Eqn.2-44**

2.6.1.2. On suspension

The relationship between the snow-terminal-fall-velocity w_f and the wind friction velocity u_* is commonly used as a measure to distinguish different snow particle transport modes. w_f plays significant part in the suspension. If ignoring viscous and turbulent stresses, it can be assumed that w_f is directly related to its physical properties calculated by the Stokes' law (Lamb, 1932):

$$w_f = (\rho_p - \rho) g D_P^2 / 18\mu$$ **Eqn.2-45**

However, snow particle fall velocity is influenced by a shear field in reality where a snow particle moving through a shear field may subjected to a lift force proportional to the magnitude of a velocity gradient as well as the sign of the relative velocity between the

snow particle and the air. Eqn. 2-45 is underestimated the value of w_f. Baumeister & Marks (1958) gave an empirical formula where w_f is linearly proportional to the particle diameter:

$$w_f = CD_p \quad \textbf{Eqn.2-46}$$

where *C* is the proportionality coefficient depending on the shape of the particle where $C = 3880s^{-1}$ for spherical particles and $C = 2440s^{-1}$ for irregular shaped particles. In the present modelling, w_f is calculated by Eqn. 2-45 and is considered as a constant of *0.43m/s* for simplifying the model.

2.6.1.3. On snowdrift transport rate

1) Transport rate in saltation and creeping

There are more than ten different expressions found in the literature to predict the particle mass transport rate, which are all based on Bagnold's pioneering work (Bagnold, 1941). The semi-empirical formulae developed by Bagnold is based on the fact where the mass flow rate is strongly related to the wind shear forces applied on the particle surface. Due to the pressure difference between the upper and lower surfaces of a single particle, the particle is injected vertically into the flow with an initial horizontal velocity, and will settle to the ground after a certain distance with impact velocity. For a steady or equilibrium state, the total shear stress exerted by the flow is the sum of the shear stress to the saltation. The initial horizontal velocity to lift off particles is assumed proportional to the wind friction velocity with a factor of *0.8*. Therefore, he gave the mass transport rate in saltation is as the following:

$$Q_{sal} = 0.8\,\rho_p u_*^3/g \quad \textbf{Eqn.2-47}$$

Estimating the creeping is about *25%* of the total mass flow in saltation and creeping, he final gave the mass rate as:

$$Q_{sal+cre} = 1.1\,\rho_p u_*^3/g \quad \textbf{Eqn.2-48}$$

In this thesis, the Pomeroy and Gray's equation is adapted (Pomeroy & Gray, 1990):

$$Q_{s\_max} = \frac{0.68}{u_*}\left(\frac{\rho_p}{g}\right)u_{*t}(u_*^2 - u_{*t}^2) \quad \textbf{Eqn.2-49}$$

This equation is based on Bagnold's work but is better in prediction for snow particle transport rate in creeping and saltation.

2) Transport rate in suspension

The saltation layer acts as a snow source for turbulent entrainment. Snow particles will be entrained vertically into suspension if the turbulent kinetic energy in the surface is sufficient. The total suspended snow transport can be written by the general mass flux description as the following:

$$Q_{sus} = \int_{h_{sal}}^{\infty} \eta(y)\, u(y) dy \quad \textbf{Eqn.2-50}$$

For a steady or an equilibrium state with a fully developed turbulent atmospheric boundary layer condition, an empirical formula for a vertical suspended snow concentration profile is presented as (Pomeroy, J.W.; Male, D.H.;, 1992):

$$\eta_{sus}(y) = 0.8exp\left(-1.55(4.78u_*^{-0.544} - y^{-0.544})\right) \quad \textbf{Eqn.2-51}$$

Table 2-3 gives the distribution of total mass transport described in percentage for each modes, where wind speed measured at *10m* height is about *5-8m/s*. It shows that saltation weights the most to snow transport.

Table 2-3: Distribution of total mass transport, the values vary with wind speed (Gauer, 1999)

Transport mode	Distribution of total (%)
Creeping	5-25
Saltation	50-75
Suspension	3-40

These empirical knowledge based parameters are used to form snowdrift transport in a majority of the CFD simulations.

2.6.2. Simplification and assumption

Windblown snowdrift transport through porous fences is multi-physics. The structure of flow regime, the property of air and snow particles, the distribution of snow particles in air, the interaction of air and snow particles, temperature, and the topology of the surrounding environment will have significant impact on the mechanism of snowdrift transport. It leads to a difficulty to form a numerical model that comprehensively takes all of the mentioned factors into account, and could stretch or beyond the computational capacity. Reasonable simplification and assumption to CFD modelling are needed in the industrial and scientific research. The discussion about the issues is presented in Section 6.2.

2.6.3. Mesh and dynamic mesh

The total erosive or accumulative snow flux may be evaluated by snow transport equations at the first control volume adjacent to the snow surface. The control volume is separated into two regions: saltation and turbulent suspension. The change of the total saltation flux is determined by the friction wind velocity, while the change of the suspended snow is determined by the effects of turbulence diffusion and the terminal snowfall velocity. This is named as the conservative snowdrift approach, and has demonstrated in better predictions to the threshold-friction-velocity approach, which is based on saltation threshold shear velocity or shear stress conditions to determine either the onset of erosion or deposition.

The majority of numerical snowdrift models are based on these two approaches. All of which require correct distribution of friction velocities within the domain. Correct turbulence development from the snow surface with a good resolution must be ensured for the conservative snowdrift approach. As such, attention must be paid to ensure proper mesh arrangement, especially in the regions near the snow surface.

Snow deposition and erosion dynamically change the topology of snow surface before reaching an equilibrium snowdrift state; essentially the structure of the airflow regime around the fence dynamically changes too. This can be achieved by employing a transient model to dynamically simulate such changes with time evolution (Alhajraf, 2004) (Beyers

& Waechter, 2008) (Tominaga, et al., 2011).

For a control volume at a given time step, the mass balance of snow particles in the first control volume adjacent to the snow surface is calculated. If the amount of snow entering the control volume exceeds that exited, deposition occurs. Conversely, the snow surface is eroded. Figure 2-13 illustrates the calculation of mass balance in the control volume in a 2D configuration.

By this mean, variation of snow depth per unit time can be calculated. The variation of snow depth is a user subroutine coupled to the model to dynamically update the control volume with time evolution, where the deposited particles blocks the cell, while the eroded particles opens the cell. The blocked cell represents a new surface filled with snow. This approach is called as a dynamic mesh.

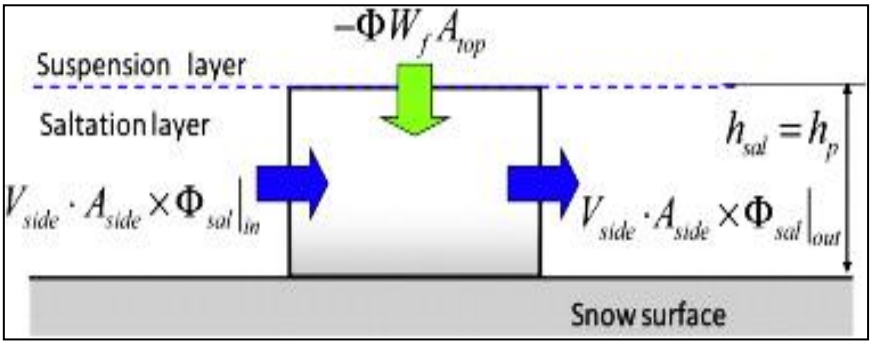

Figure 2-13: Mass balance in the control volume in 2D modelling (Tominaga, et al., 2011)

An alternative method is to consider computational surface cells as fractionally filled depending on snow contents. The Fractional Area/Volume Obstacle Representation technique (FAVOR) (Hirt, 1993) may be applicable for the purpose. Fractional filling of mesh cells will produce a more streamlined or curved snow surface, which can minimize possible numerical instabilities in air velocity calculations arising from the sudden block of mesh cells.

Another important issue with the mesh arrangement is properly to configure the relation between the particle response time τ_p and the system response time t_s, which can be expressed by the Stokes number S_t. The detailed calculations are as follows (ANSYS, 2009):

$$\tau_p = \rho_p D_p^2 / 18\mu \quad \textbf{Eqn.2-52}$$

$$t_s = L_s / U_s \quad \textbf{Eqn.2-53}$$

$$S_t = \tau_p / t_s \quad \textbf{Eqn.2-54}$$

where: ρ_p is the density of effective bulk snowpack, D_p the mean diameter of snow particles, and μ the dynamic viscosity of the surrounding air. L_s and U_s are the characteristic length and the characteristic velocity of the system under investigation respectively, which can be controlled by the arrangement of the meshed elements.

The Stokes number S_t is the most important dimensionless parameter in the two-phase snowdrift flow, which evaluates the ability of snow particles following the airflow movement. Snow particles will closely follow the air when $S_t < 1.0$, and will independently move relatively with the air when $S_t > 1.0$ (Brennen, 2005) (Beyers & Waechter, 2008) (Tominaga, et al., 2011).

Natural snow volume fractions are typically around 0.1% (Pomeroy & Gray, 1990). In Cold Regions, big snow particles are rapidly fractionated into small particles during the transport in the cold and rather dry climate, and the small particles may be simplified further to spherical particles of a constant diameter. It is therefore reasonable for numerical simulations to consider the air-snowdrift mixture as a highly diluted continuum, which the snow phase follows the air phase without influence. Hence, the Stokes number S_t is required less than the value of *1.0* and can be achieved by the proper mesh in the numerical models

Constructed elements are generally required. Quadrilateral element for 2D modelling and Hexahedron element for 3D modelling are preferable.

2.6.4. Two-phase snowdrift modelling

Over the years, the research community in the field of snow engineering has developed many windblown snow transport models. They can be grouped into three main groups: Eulerian continuum two-phase modelling, Lagrangian-Eulerian particle tracking modelling, and kinetic theory modelling (Decker, 1991).

2.6.4.1. Eulerian continuum two-phase modelling

Eulerian continuum two-phase modelling deals with fluid flows with continuum theory based on Eulerian description. The two phases, air and snow, are considered as two equivalent sets of equations for the conservation of mass and momentum. Additional modelling of phase interaction is required. The two-phase modelling is expensive in terms of computational costs. It is however possible to simplify the two-phase modelling by assuming the snow phase to be coupled with the airflow and therefore reducing the total number of governing equations.

One simplification of the two-phase modelling is to consider the mixture of air and snow by total conservation mass and momentum, and allows the snow phase to drift with the mixture of the air and the snow. For snowdrift, it may be assumed that the drift-velocity between the two phases is too small to contribute any significant transport of momentum for the snow phase. The relative velocity between the two phases must be calculated for all three directions. Another simplification of the two-phase modelling is to assume that only the air phase is governed by the conservation laws. The snow transport is mainly governed by the airflow. Since the snow phase is allowed to drift with respect to the airflow, this modelling may be referred to as a homogeneous model with slip velocity between the air and the snow.

The two-phase saltation modelling is based on two main drift principles. The development towards the saturated drift profile will occur gradually due to some inertness in the lift process, which is similar to the real conditions. The model obeys the necessary principles of the mass conservation and may be applied to two-way as well as one-way coupled models. The snow phase is generally treated as suspended in the airflow. The vertical fall velocity w_f is considered to be settled in the low velocity regions. The saltation equation is given as:

$$\frac{\partial f}{\partial t}+\frac{\partial (fu)}{\partial x}+\frac{\partial (fv)}{\partial y}+\frac{\partial \left(L(U(z))\right)}{\partial z}=-\frac{\partial (fw_f)}{\partial z} \qquad \textbf{Eqn.2-55}$$

where f is snow volume fraction, t is time and (u, v, w) are the air phase velocities in the directions of(x, y, z). The lift function $L\left(U(z)\right)$ depends on the horizontal velocity $U(z)$ and serves to maintain the snow density distribution above the surface.

Suspension of snow particles in an Eulerian continuum modelling can be reconsidered as the general transport-diffusion equation:

$$\frac{\partial f}{\partial t}+\frac{\partial(fu)}{\partial x}+\frac{\partial(fv)}{\partial y}+\frac{\partial(fw)}{\partial z}=\frac{\partial}{\partial x}\left(v_f\frac{\partial f}{\partial x}\right)+\frac{\partial}{\partial y}\left(v_f\frac{\partial f}{\partial y}\right)+\frac{\partial}{\partial z}\left(v_f\frac{\partial f}{\partial z}\right)-\frac{\partial}{\partial z}\left(fw_f\right) \quad \textbf{Eqn.2-56}$$

where v_f is the diffusion coefficient.

Suspension of snow particles is commonly described as a phenomenon related to turbulence. Turbulence effects are modelled through a variable dynamic viscosity.

2.6.4.2. Lagrangian-Eulerian particle tracking modelling

Motions of single snow particle in airflow can be modelled by Lagrangian-Eulerian particle tracking techniques. The air phase is considered as a continuum fluid, while the snow phase is presented by a certain number of drifting particles. The approach is named as Lagrangian-Eulerian since it represents a combination of Eulerian velocity evaluation and Lagrange particle modelling.

Lagrangian motions of suspended spherical particles in a frame of Eulerian velocities are governed by the general Basset- Buossinesq-Oseen equation. For the case of suspended snow particles with diameter *D*, this general equation of particle acceleration can be simplified as:

$$\frac{dV_p}{dt}=\frac{3}{4}\frac{C_d}{D}\frac{\rho}{\rho_P}\left|V-V_p'\right|\left(V-V_p'\right)-g,\ \ if\ \rho\ll\rho_p \quad \textbf{Eqn.2-57}$$

where V is the air velocity and V_p' is the particle velocity. Diffusion of snow can be described in terms of a mean particle velocity V_p and a particle diffusion velocity V_{dif}:

$$V_p'=V_p+V_{dif} \quad \textbf{Eqn.2-58}$$

$$V_{dif}=-\lambda\frac{\nabla(mc)}{mc} \quad \textbf{Eqn.2-59}$$

where m is the mass and c is particle concentration. The particle diffusion coefficient λ can be given as a function of the dynamic viscosity μ:

$$\lambda = c_{dif} + \frac{\mu}{\rho}\frac{1}{S_c} \qquad \textbf{Eqn.2-60}$$

where c_{dif} is a constant diffusion coefficient, ρ is the air density and S_c is the Schmidt number. The effect of turbulence on the particle dispersion is included by assuming that the dynamic viscosity varies with the level of turbulence.

Eqn.2-57 is proposed for modelling of both saltation and suspension in the particle tracking approach. Heavy particle transport is to be considered in the saltation region while the suspension region is characterized by smaller particles that are more strongly influenced by the drag. The statistical diffusion velocity serves both to lift the particles from the surface, and to produce the characteristics random distribution when applies to heavy particles in surface transport.

Deposition is modelled by omitting the diffusion effects and allows the particles to fall due to gravity. In a given time step, particles are situated in a thin layer innermost to the snow surface which are considered as trapped and accumulated. Each particle represents a small volume of snow and a computational surface cell is blocked to represent a new surface, when it is filled with snow.

2.6.4.3. Kinetic theory modelling

In kinetic theory modelling, snow and wind is considered to be composed of small units or molecules, which are moving in a fine lattice, and governed by a set of constitutive rules. The units will propagate and collide according to certain statistical rules (Masselot & Chopard, 1996).

Kinetic theory modelling needs a large number of numerical operations to be solved and parallel computing is used to reduce time during simulations. It represents an interesting alternative to the traditional numerical solution techniques that have been applied in snow transport modelling.

In the industrial applications, Eulerian continuum two-phase modelling is often simplified to a mixture two-phase snowdrift modelling. Snow particles are treated as a pseudo fluid solving both air and snow particles on the Eulerian reference frames. It has advantages of being computationally efficient when a large number of snow particles are assumed

having the same physical properties and snow particles are assumed one-way coupled to the airflow. Its foreseeable disadvantage is not possible to model the movements of individual snow particles. Therefore, Lagrangian-Eulerian particle tracking modelling is not dispensable even if it bears comparatively expensive computational cost.

To evaluate the performance of porous fences on wind induced snow problems, the macro scaled snow movement is of main concern rather than the individual particle movement.

As such, Eulerian continuum two-phase modelling is the popular approach for many researchers.

2.7. SUMMARY

Key aspects associated with the porous fence analysis of porous fences have been reviewed in this chapter. The developed knowledge and understanding on the characteristics of the flow around the porous fence in terms of the distinctive flow regions, turbulence, airflow separation and reattachment, and windblown snowdrift transport modes, have attributed greatly to the research.

While the research and industrial communities have made significant progress on the study of the performance of porous fences, robust and clear guidance for the optimal windshield design and application have not yet been achieved. The literature survey has found the limitations of the present experimental and numerical techniques in the field. Some findings from the scaled model tests, the real structure tests and the numerical predictions in the literature are not representative with some even contradictory to each other. Up to date, the existing knowledge gaps are summarized as follows:

- Physical experiments can be mainly classified on-site field and wind tunnel experiments. Compared with on-site field experiments, wind tunnel experiments can control the testing environments, less expensive in preparation and operation, but must satisfy the similarity criteria to the prototypes. To satisfy the similarity criteria between wind tunnel experiment and prototype, especially for two-phase flow such as sediments transport flow, remains a big challenge in the research field. Due to the complex characteristics of flow around porous fences and the

nature of turbulence induced, physical experiments can only provide results with limited accuracy at the present. Knowledge on the mechanism and interactions among porous fence, airflow, and windblown sediments remains to be further understood, which requires to develop and apply innovative methodologies and techniques that contributes to optimal fence designs for different applications;

- Application of Computational Fluid Dynamics (CFD) technique is prevail in the porous fence research nowadays. Rich published resources have proved the success of being a supplementary tool. However, there remain various issues to be tackled in the future, particularly the difficulties in numerical modelling to reflect the true cases, and weak sensitivity in predicting turbulence around porous fences;
- The arrangement of porous holes (i.e. shape, size and distribution, etc.), distribution of shear stress on the fence surface, and non-normal wind loads, etc. affecting the performance of porous fences have been observed by many researchers. However, a systematic study on these issues has not been reported by far;
- A majority of research work assessed the performance of porous fence based on the maximum wind reduction over the longest effective shelter distance, which the size of fence effective zone and the level of turbulence leeward porous fences should have but have not been considered;
- Study on the performance of porous fences targeting specific environments such as Cold Regions has not been systematically carried out.

The present research will focus on addressing the above issues by carrying out a systematical investigation. The research outcomes will contribute to fill the knowledge gaps in the field.

Chapter 3 RESEARCH METHODOLOGY

The focus of the research in the thesis is the development of further knowledge with regard of the key technical parameters of porous fences to their performance, which is valuable to the industry for the optimum windshield design and application. The technical challenge lies on the complex nature of the flow behind porous fence due to the interactions among fence, wind flow, and drifting snow. Current approaches to reveal the complicated characteristics of flows around porous fences include wind tunnel experimental and numerical simulation study. Direct on-site experiment involves the installation and the instrumentation of a segment of porous fences on the site representing the environment conditions to be investigated. The type of measurement is however, dependent on the site conditions as the systematic visual or measurement systems may not be applicable to a particularly hostile environment. A further complication is the difficulty in finding suitable locations with upstream conditions that are controllable, and with appropriate boundary conditions to represent a generic case. As such, while the direct on-site experimental study may generate the most 'realistic' test data, this approach has not been adopted in the research with respect of expensive cost and uncontrollable on-site environmental conditions. This research work has applied a joint approach using wind tunnel experimental and numerical techniques to address the challenge.

3.1. EXPERIMENTAL STUDY

3.1.1. Experiment design

The experimental study will be conducted in a wind tunnel to obtain the direct observation and measurement of the characteristics of flows around porous fences in the controlled physical environments. Various porous fences manufactured by IKM dsc AS will be used as the testing samples, of which are commercial products currently used in Norway. Important technical parameters to be investigated include different arrangements of fences themselves, different approaching wind velocities, and different directions of wind load, etc. The applied measurement sensors will include Pitot static tube manometer, HWA and UA. All of which are intrusive to the airflow field, calibration and justification

among them are therefore needed. Visualization will be conducted by the means of smoke generator, moisture molecule generator or directly seeded by fine snow particles. The motion of fluid will be captured by a high-speed camera aided by a laser sheet inside the wind tunnel. Due to the limitation of the resolution of the applied facilities, the available visualization facilities are not able to provide analytic data as PIV and PIT do.

In order to compare the experimental data with the corresponding numerical results, airflow in the testing wind tunnel is designed to obey logarithmic or power-law profiles. This must be investigated before the testing fence in position. The fence is designed to be positioned at a certain distance downwind from the entrance of the test section, where fully developed turbulent airflow will occur. Airflow before the porous fence model will be monitored by a Pitot static tube manometer, while the wind velocity field leeward of the model will be measured by an UA and a HWA. The DA-650 UA model with TR-92T probe is able to measure three-dimensional velocity vectors yielding *1 000* instantaneous data sets with the frequency of *10* seconds, which effectively capture the fluctuations of velocity vectors. Hence, turbulence intensity and turbulent kinetic energy can be derived from the experiment. The UA is attached to a 3D movable traverse, which enables to investigate the structure of flow regime at a great degree.

The two-phase snowdrift flow experiment is designed to be performed at the temperature of *-7°C*, which is approximate to the averaged out-door temperature in the northern Norway in winter season. A snow-feeding machine is placed just before the entrance of the test section, which enables the development of a saturated saltation layer above the snow ground. The testing snow is natural snow stored in a cold chamber at the temperature of *-7°C*. The snow particles will be selected by a filter ensuring small particles to be chosen. A laser displacement meter (LDM) will be used to measure the roughness of the snow surfaces before positioning the fence, and the depth of snow deposition after installing the fence. The threshold wind velocity at which particles start to move from the snow ground will be investigated before the fence in position. The evolutions of snow deposition height will be measured by the LDM at the pre-designed time interval. Testing cases will include the behaviours of snowdrift under different types of the fences, different fence heights and different inlet velocities. Each case will be ended

when the quasi-equilibrium snowdrift state has been identified.

3.1.2. Justification

The research team has the access to the required test facilities and specimens. IKM dsc AS is the industrial partner who will provide the testing porous fences. Measurement equipment such as pitot static manometer, HWA, UA, LDM, smoke generator, moisture molecule generator, etc. are available in this research. Earlier experiments were performed the single-phase airflow in the aeronautic wind tunnel at the Arctic University of Norway. It has the test section of *1.15m*0.89m*1.5m* with the maximum operation wind speed of *55m/s*. These earlier experiments helped to acquire improved knowledge and skill in wind tunnel test, and preliminary investigations on the performance of different fences. However, that wind tunnel cannot produce sufficient fully developed turbulent flow as the experiments required, due to the very limited span of the test section. The environmental wind tunnel at Shinjo Cryospheric Environment Laboratory, Japan, has a large span of the test section of *1.0m*1.0m*14m* situated in the cold room. Its maximum operation wind speed is *20*m/*s* with adjustable floors. It is sufficient to produce fully developed turbulent flow at the testing fences, and is capable of simulating windblown snowdrifts in the tunnel. A systematic wind tunnel experiment with regard of single airflow and two-phase snowdrift flow will be finalized.

3.2. NUMERICAL STUDY

3.2.1. Numerical simulation design

Parallel to the experimental study, a numerical study will be conducted through systematic CFD simulations to investigate the characteristics of flow around porous fences. The 2D and 3D CFD model will be firstly assessed by the corresponding experimental results under as identical conditions as possible. Issues like mesh arrangement, boundary conditions, selection of turbulence models, solution convergence criteria, snowdrift transport model, etc. will be discussed and justified. The ultimate goal is to provide a numerical fence modelling supplementary to the windshield design and application.

Similar to the experimental study, the numerical study will be conducted in two steps.

The first step is the CFD simulation of single airflow around porous fence. The model assessment, the effects of arrangement of porous holes, wind load at different angles, distribution of shear stress on the fence surface, assessment of fence effective zone, etc. will be of main concern. Most of which are few to be found in the previous research work. The second step is the CFD simulation of two-phase snowdrift flow around porous fences. The evolution of snow deposition will be simulated in 2D modelling. The identification of possible snow deposition area and snow transport rate will be investigated in 3D modelling. Numerical two-phase snowdrift model will be assessed based on the previous other researcher's work (Tabler, 2003). Cases like snowdrift around different fences and different fence installations will be included.

3.2.2. Justification

CFD simulation, as a flexible, efficient and relatively cheap alternative, is now widely employed in the windshield research community (Alhajraf, 2004) (Hargreaves & Wright, 2007) (Andres , et al., 2011) (Telenta, et al., 2014) (Blocken, 2014) (Hong, et al., 2015). Compared with on-site measurements and scaled wind tunnel testing, CFD simulations particular for those 3D modellings can provide detailed information on the characteristics of flow in the whole calculation domain, under well-controlled conditions and without the constraints of similarity criteria (Blocken, 2014). The development of computational technology and the computing capacity provides the probability of 3D modellings being more popular today. 2D simulation cannot model a physical porous fence that usually manipulates the fence as a porous medium or a porous jump, which requires assigning empirical knowledge based parameters into the model. It results in the numerical predictions having greater uncertainty since the complex nature of airflow around the fence is unlikely to be described by simply mathematic means. Additionally, 2D modelling only can provide limited information in an Iso-plane. Contrarily, 3D simulation can model the physical porous fence and provides information over an entire domain. As such, this study will pay great attention on 3D modelling, even if it may bear comparatively higher cost.

The present numerical study will not pay so much attention to those technical parameters, which have significant impact on the performance of fences and have however been

widely acknowledged in the field, i.e. the effective porosity range. The numerical study will focus on the issues to be further clarified, such as the effects of arrangement of porous holes, fence surface shear, directions of wind load, and different installation of snow fences, etc. Furthermore, assessment of fence effective zone will be added to the study.

The research team has the access to the required commercial software including ANSYS, ANSYS FLUENT, Rhinoceros, CATIA v5. The numerical study will be conducted mainly under ANSYS FLUENT 14.0 Academic Research version.

3.3. LIMITATIONS

The present research methodology is subject to the limitations as follows:

1) Limitation on the measurement instruments: The applied measurement instruments are intrusive to the flow field, which will reduce the accuracy of the experimental data.
2) Limitation on the similarity criteria: The similarity criteria have been carefully considered in the present research. However, a complete satisfaction of similarity between the wind tunnel experiments and the prototypes is still challengeable. Particularly, the property of natural snow and its distribution in air are unlikely to be simulated in the wind tunnel experiments. Such difficulties will introduce errors into the experiments.
3) Limitation on the CFD modelling: Numerical approximations, parameterization schemes, and the choice of boundary conditions can introduce errors in solutions. Especially the two-equation based turbulence models are weak in prediction of turbulence around porous fences, which compromise the numerical predictions of the structure of the flow regime and snowdrift transport around porous fences. The two-phase snowdrift models are subject to a certain degree of assumption and simplification, which also may compromise the predictions.

The above stated limitations will compromise the accuracy and reliability to the present research work. Discussions and analysis of these issues are presented in Chapter 4, 5 &6.

3.4. FLOWCHART

Figure 3-1 illustrates the flow of the research methodology. Industrial needs for the optimum design of porous fence will be studied first to set the scope of the research.

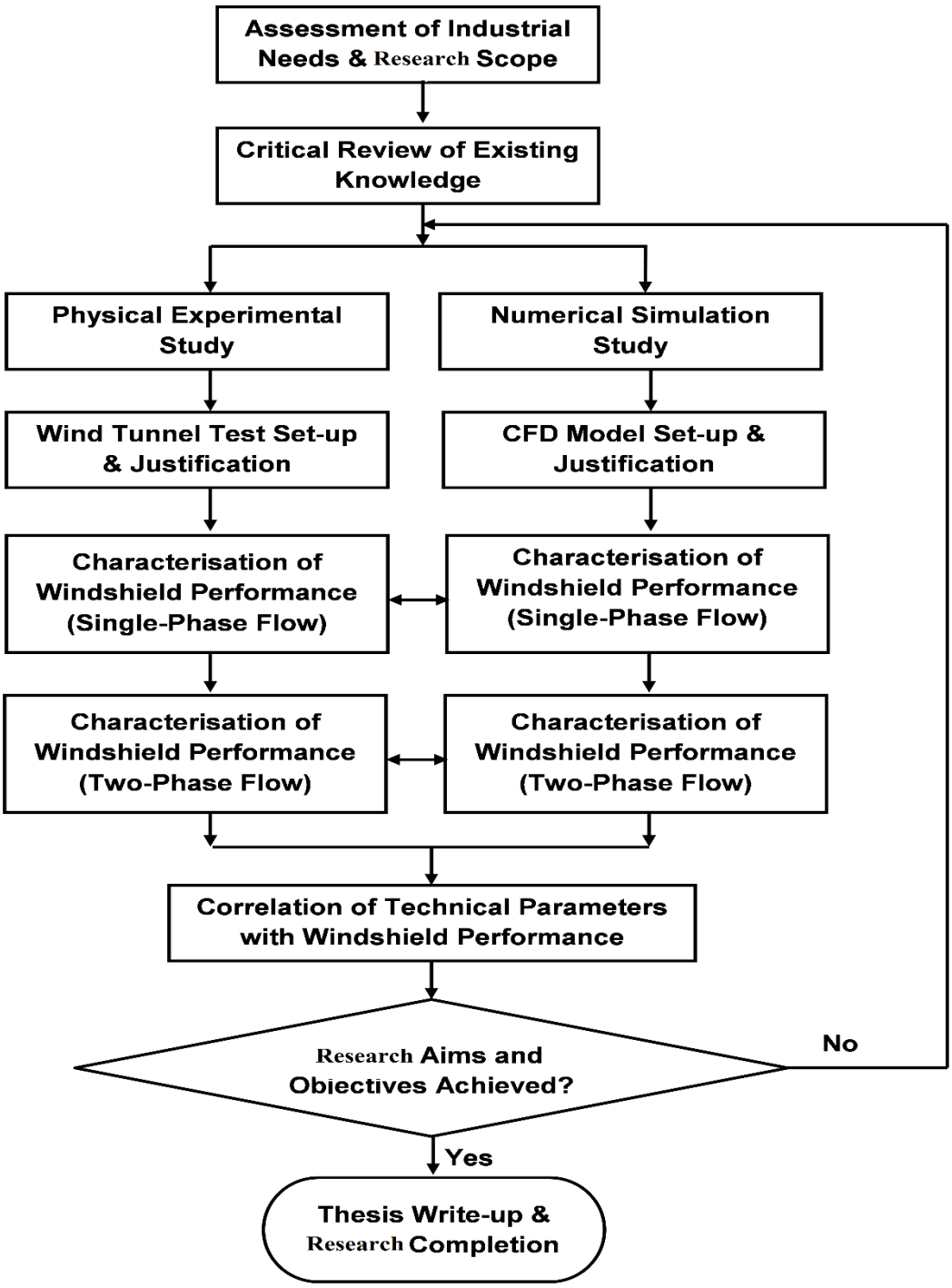

Figure 3-1: Flowchart of the research methodology of the thesis.

Existing knowledge and research methods will be critically assessed through a comprehensive literature review. Detailed investigations on the effect of key technical parameters on the performance of the porous fence will be carried out in the combined experimental and numerical studies. The optimal design and application of snow fences differs from those of wind fences, i.e. the optimal porosity of snow fences is usually required greater than that of wind fences, and snow fences are usually installed with a bottom gap from the grounds that wind fences are not. Since snowdrift are highly diluted in air in the cold and rather dry Cold Regions, it is reasonable to consider that the snow particles follow the airflow without influence, which implies that the two-phase snowdrift flow mainly affects the change of boundary condition, and the characteristic of airflow regime remains similar. As such, the present research will be carried out in two parts, which the characteristic of airflow regime around porous fences will be investigated under the condition of the single-phase airflow, while the behaviors of snowdrift movement will be studied under the condition of the two-phase snowdrift flow. Such a methodology will reduce a degree of the complexity in the research, and can bridge a systematical knowledge from the single-phase airflow to the two-phase snowdrift flow as a whole to evaluate the performance of porous fences in Cold Regions.

The research is focused on the issues where the knowledge gaps remain in the research field, and will be continued until the research aims and objectives have been achieved.

Chapter 4 EXPERIMENTAL STUDY

The wind tunnel experiment provided direct observation and measurement of the characteristics of flows around the testing porous fences in a controllable physical environment. The obtained experimental data covered three-dimensional velocity vectors, fluctuation of velocity vectors, turbulence kinetic energy, turbulence intensity, threshold wind velocity for snowdrift and height of snow deposition, etc. Visualization provided the motion of airflow and the movement of snow particles around the testing fences.

The experimental study consists of two parts. The performance of porous fences under single-phase airflow were investigated in the first part, and the performance of porous fences under two-phase snowdrift airflow were studied in the second part. The present experimental work was accomplished by the author together with his supervisor Dr Mohamad Mustafa and the members of the staff at Shinjo Cryospheric Environment Laboratory, Japan.

The experiment consists of the following tasks:

- Investigating the structure of airflow leeward of different porous fences;
- Investigating the influence of porosity on the performance of porous fences;
- Investigating the influence of the arrangement of porous holes on the performance of porous fences;
- Investigating the effects of the configuration of testing samples on their performance.
- Investigating the movement of windblown snow particles around different porous fences.

4.1. EXPERIMENT FACILITIES

4.1.1. The Environmental wind tunnel

The environmental wind tunnel as shown in Figure 4-1 is positioned in a cold room with controllable operation temperature from *-30* to *25°C*. It is a closed circuit flow type with a *1m*1m* rectangular cross-test section. The test section is *14m* long. Inlet wind velocity

varies from *0* to *20m/s*. The wind tunnel has been equipped with a movable traverse in three dimensions that enables to access measurement points in a great degree (about *60%* inner space of the wind tunnel). The wind tunnel also has a snow-feeding machine designed to control snow supply rate and develop a saturated saltation layer from the snow bed.

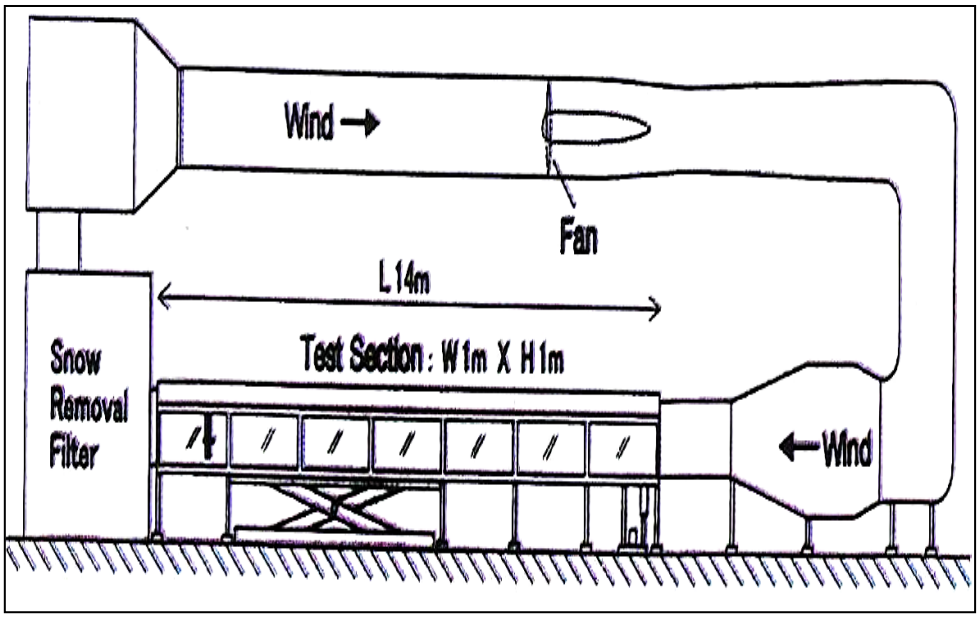

Figure 4-1: Sketch of the testing environment wind tunnel (image provided by the laboratory)

The great feature of the wind tunnel is that it has a large span of the test section with adjustable floor, which enables the tunnel to simulate various Atmospheric Boundary Layers (ABLs) in need. With its length, it can produce wall-bounded fully developed turbulent airflow with a nominal thickness in the range of *0.5-1.0m* at an ambient wind speed of about *10m/s*. This is consistent with other researchers' finding that a working section length between four and five boundary layer heights is adequate to produce a fully developed turbulent flow (Cermak, 1984) (Counihan, 1969). Detailed ABL consideration of the present experiment is presented in Section4.2.

4.1.2. Preparation of testing samples

To fulfil the above tasks, six types of the testing samples have been selected. All of which were provided by the IKM dsc AS and are the commercial products applied in Norway.

Figure 4-2 shows the photos of some of the testing samples. Details of the sample arrangements are presented in Table 4-1.

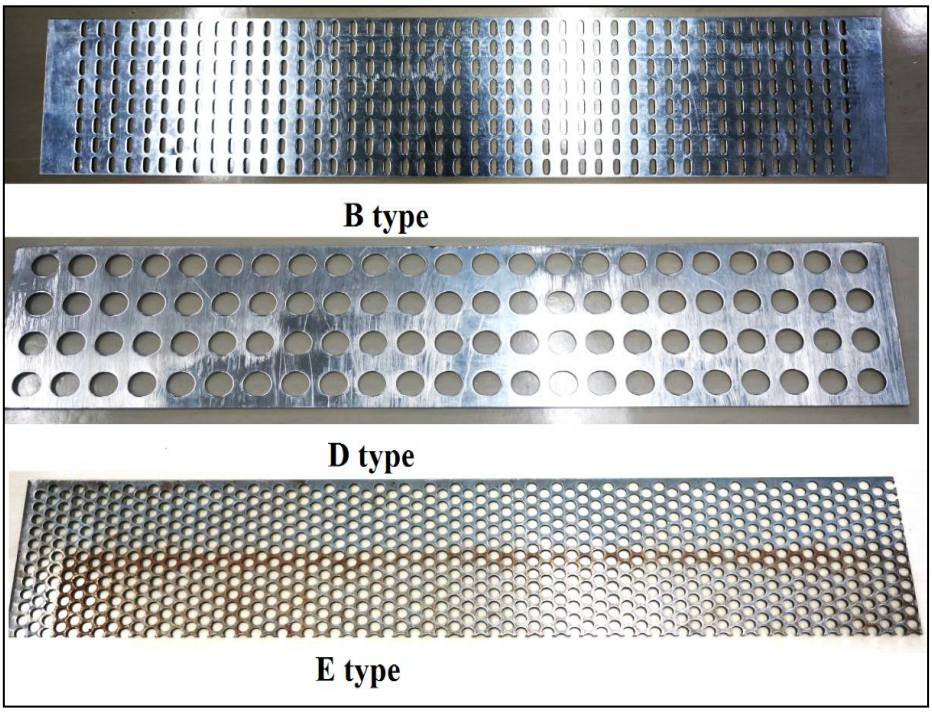

Figure 4-2: Part of the testing samples

Table 4-1: The configuration of the test samples

Sample type	Shape of hole	Porosity	Width*Height*Thickness (W*H*δ)	δ/H	W/H	Wind tunnel blockage
A	Oval	0.27	750*150*3mm	0.020	5.0	8.3%
B	Oval	0.27	750*200*3mm	0.015	3.8	11.0%
C	Oval	0.27	750*300*3mm	0.010	2.5	16.5%
D	Circle	0.35	750*200*3mm	0.015	3.8	9.7%
E	Circle	0.50	750*200*3mm	0.015	3.8	7.4%
F	Circle	0.35	750*150*3mm	0.020	5.0	7.3%

4.1.3. Instrumentation: ultrasonic anemometer (UA)

Ideally, the instruments should have properties such as high sensitivity, high accuracy, good quality of spatial resolution, large measurement range, and be non-intrusive to the airflow field. In this research, the experiment focused on the investigations of wind velocity field and structure of turbulence leeward porous fences.

Figure 4-3 shows the DA-650 UA model with TR-92T probe, manufactured by Kaijo Sonic Corporation, Japan. It allows measuring velocity vectors in three dimensions. On the balance of the cost and the capability, the UA can be justified as a suitable measuring instrument to fit this research.

The basic specifications of the UA are as follows:

- Measurement mode: Time sharing transmission/reception and switching type ultrasonic pulse emission
- Operation mode: Ultrasonic propagation reciprocal difference method
- Measuring range*: 0-20m/s*
- Accuracy of operation: *1%* or less
- Resolution: *0.005m/s* or less
- Repetition of measurement: *20* times per second
- Digital output: output mode- RS-232C
  Transfer speed: *9600*bps
  Transfer rate: *20*times per second
  Data form: ASCII (*6* bytes/measured vector)
- Measuring height: *40-440mm* (from the floor of the wind tunnel, due to the limit of its supporting traverse)
- Weight: *800g*

The three dimensional velocity vectors have been calibrated as follows:

1) $u_x = V_1 * 20$, where u_x is the longitudinal velocity (main direction) in *m/s*, and V_1 is the voltage of Channel 1

1) $u_y = V_2 * 5$, where u_y is the lateral velocity in *m/s*, and V_2 is the voltage of Channel 2
2) $u_z = V_3 * 5$, where u_z is the vertical velocity in *m/s*, and V_3 is the voltage of Channel 3

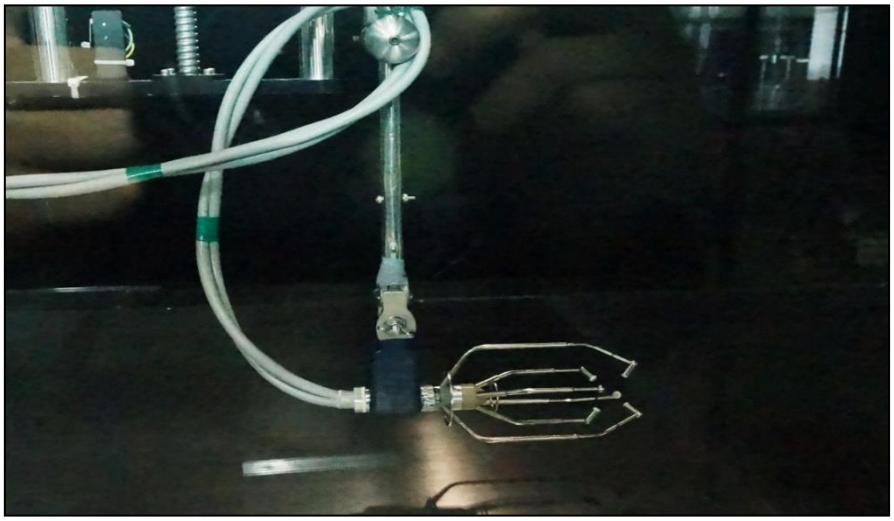

Figure 4-3: Picture of the UA

4.1.4. Laser Displacement Meter (LDM)

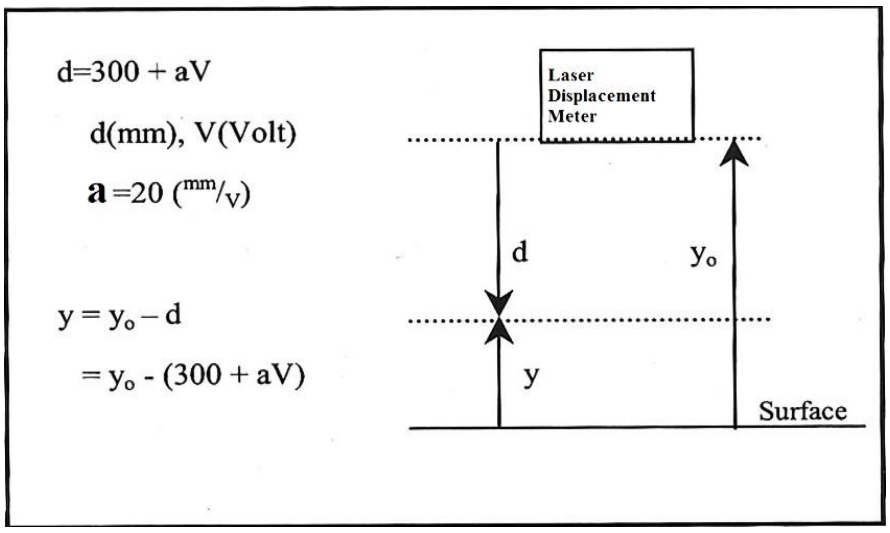

Figure 4-4: Work diagram of the laser displacement meter

The laser displacement meter has been used to measure the roughness of the snow bed before the fence in position and the depth of snow deposition after the fence in position.

Figure 4-4 shows the work diagram. The standard vertical measuring range is $300 + /-100mm$, and is equipped with an infrared laser beam with a measuring resolution of *50 μm*.

During the present experiment, y_0 was set to be *300mm*, as such, the depth of snow deposition was captures as:

$$y = -a * V \quad \textbf{Eqn.4-1}$$

where *y* is the depth of snow deposition, *a* is *20mm/voltage*, *V* is the voltage.

4.1.5. Snow-feeding machine

The snow-feeding machine is installed at the entrance of the test section shown in Figure 4-5. The configuration of its feeding bed is *a =770mm* and *b = 200mm*.

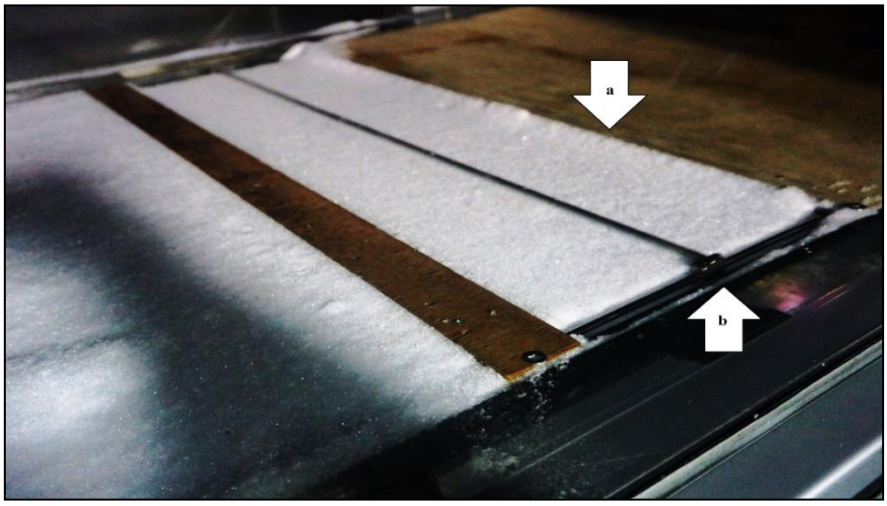

Figure 4-5: The snow-feeding machines

In this experiment, snow particles were supplied through a snow supply tank to the feeding bed. The stainless steel rod was in horizontally reciprocal movement at *0.5* second per iteration. The rate of snow supply could vary from *1%* to *100%*, where *100%* corresponds *3.55g/cm/s* in the present experiment. The snow-removing filter inserted at the end of the test section downwind collects Snow particles.

4.1.6. Other instruments during the test

The following are the other instruments employed during the experiments:

- Cold light laser sheet: for visualization
- High-speed video camera with tripod: capturing images during visualization
- Moisture molecule generator: producing seeding media for visualization
- Pitot static tube and Multi-tube manometer: for approaching wind velocity profile and boundary condition measurement
- Three dimensional movable traverse: support for measurement instruments (i.e. UA and LDM) with digital reading output
- Snow grinding and screening machine: for selecting proper snow particles

4.2. EXPERIMENT FOR SINGLE PHASE FLOW

4.2.1. Experiment set-up

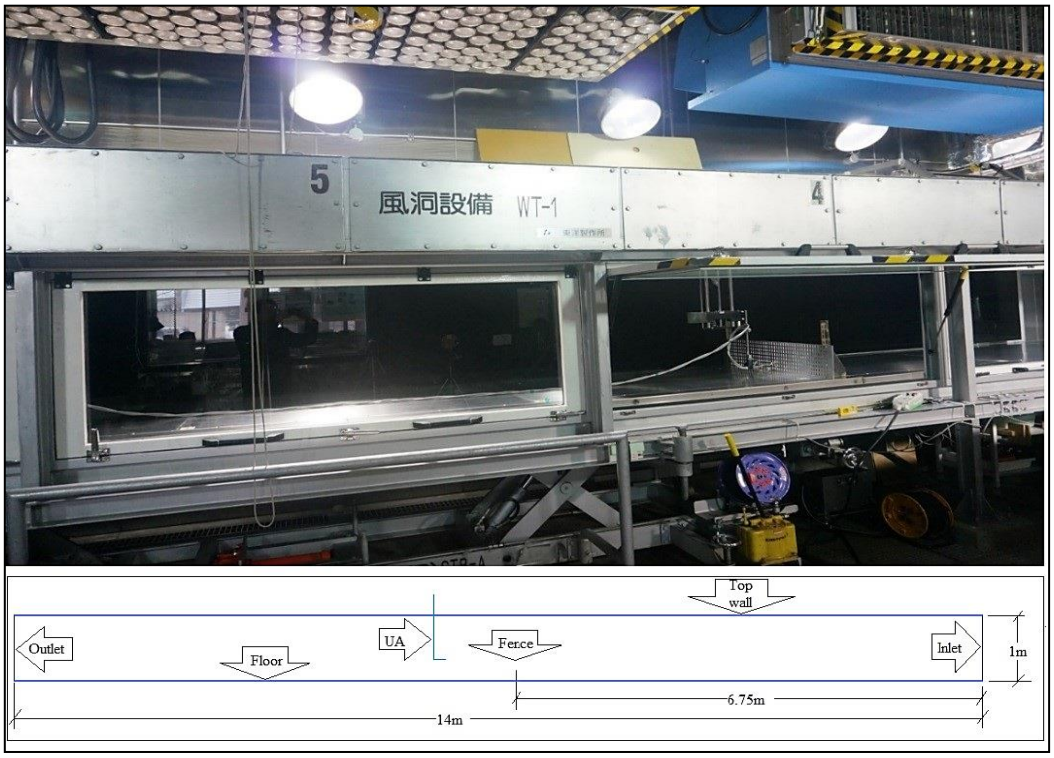

Figure 4-6: The experiment set-up

The experiment set-up is shown in Figure 4-6. The testing fence was installed at *6.75m* away from the leading edge of the testing section, and perpendicularly to the main flow direction. There were five types of fences (from fence A to E) being tested. The UA were

attached to a 3D movable traverse. The movement of the traverse were controlled by an electrical motor. The testing data yielded by the UA were automatically recorded onto a computer.

For each test, the experimental data was collected at the following positions:

- Longitudinal direction downwind: along the central line of the wind tunnel, taking positions downwind from the fence at *0.2m*, *0.6m*,*1.0m*, *1.4m*, *1.8m*,*2.6m*,*3.5m*,*4.5m* and *6.0m* , respectively;
- Vertical direction: at each longitudinal measuring point, taking a measuring height step of *60mm* that would create *8* vertical measurement points with the range of height from *40mm* to *440mm*, due to the restraint of the traverse moveable space;

Therefore, there would produce *72* data sets for each test.

The UA has capability to obtain 3D velocity vector data. During each measurement campaign, it was measured as a time duration of *10* seconds for the three velocity vectors (*u*, *v* and *w*) with a time resolution of *0.01s*. In other words, each wind velocity vector was obtained by taking the average of *1000* continuous values. These continuous values were regarded as instantaneous data and were saved as DAT file in the computer. Hence, the fluctuations of each wind velocity vector can be derived from the experiment.

The data were recorded as raw data for the wind velocity components on the *x*-, *y*-and *z*-axes (*u*, *v* and *w*) at all measurement positions. Positive *u* was defined for the longitudinal wind velocity component directed from upwind to downwind, positive *v* for the vertical wind velocity component directed from the wind tunnel floor to the top wall, and positive *w* for the lateral wind velocity component directed from right to left.

The variables to define the structure of wind flow regime around fences were calculated from the raw data as follows:

- Mean wind velocity vectors:

$$\bar{u}=\frac{\sum u_i}{N}, \bar{v}=\frac{\sum v_i}{N}, \bar{w}=\frac{\sum w_i}{N} \qquad \textbf{Eqn.4-2}$$

- Root-mean-square deviations of the longitudinal wind vectors σ_u:

$$\sigma_u = \sqrt{\overline{u'^2}} = \sqrt{\frac{1}{N-1}\sum_{i=1}^{N}(\bar{u}-u_i)^2} \quad \textbf{Eqn.4-3}$$

The vertical and lateral root-mean-square deviations σ_v and σ_w can be calculated in the similar way.

- The velocity magnitude U_m:

$$U_m = \sqrt{\bar{u}^2 + \bar{v}^2 + \bar{w}^2} \quad \textbf{Eqn.4-4}$$

- The turbulence intensity T_i:

$$T_i = \frac{\sqrt{\frac{1}{3}(\sigma_u^2 + \sigma_v^2 + \sigma_w^2)}}{U_m} \quad \textbf{Eqn.4-5}$$

where: σ_i is the root-mean-square deviation of the wind vector.

- The turbulent kinetic energy (*TKE*) *k* per unit mass:

$$k = \frac{1}{2}\left(\overline{u'^2} + \overline{v'^2} + \overline{w'^2}\right) \quad \textbf{Eqn.4-6}$$

where: $\overline{u'^2}$, $\overline{v'^2}$ and $\overline{w'^2}$ are the squared σ_u, σ_v and σ_w respectively.

For each test, flow visualization was conducted by using a high-speed camera to record images and videos. Moisture molecules (similar to fine water spray) as seeding materials were produced by a moisture molecule generator, and fed into the entrance of the test section through a hole in the wind tunnel floor. A cold light laser sheet covered the entire test section to make the motion of molecules more visible.

4.2.2. Investigation on wind velocity profiles under fence free condition

The approaching wind velocity profiles were investigated before the fence in position. The fully developed turbulent flow must be ensured at the fence position, which means

that the wind velocity will obey a logarithmic or a power-law profile at the position of the testing fence. The flow regime developed in the presence of the fence is formed by modification of the approaching flow. The approaching wind velocity profile and its correlated boundary condition are essential similitude parameters to be used in examining the results between numerical simulations and wind tunnel experiments.

The experiment is restrict to the low portion of the turbulent boundary layer in the low-speed environmental wind tunnel. With these considerations, the wind flow can be treated as an incompressible, logarithmic flow with negligible thermal impact and Coriolis Effect.

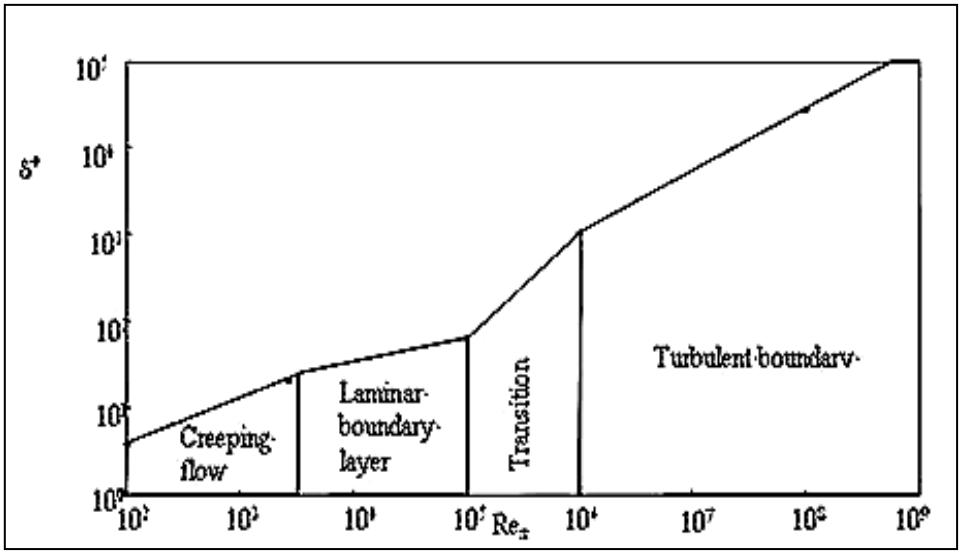

Figure 4-7: The four traditional regimes of flow past a flat plate (Trinh, 2010)

The boundary layer has significant impact on the approaching wind velocity profile. It is a layer adjacent to a surface where viscous effects are important. Air particles at a flat plate surface have zero velocity and act as retardants to reduce velocity of adjacent particles in the vertical direction. Similar actions continue by other particles until at the edge of the boundary layer where the velocity of these particles reaches *99%* of the free stream velocity. Reynolds number is used to characterize flow over a flat plate. The four typical regimes of flow past a flat plate are displayed in Figure 4-7, where δ^+ is the normalized thickness of the buffer layer (the time-averaged value of the wall layer thickness).

Since the thickness of the boundary layer varies between laminar and turbulent flow, it is important to distinguish the category of flow by checking on the Reynolds number. The longitudinal distance from the leading edge of the test section to the testing fence in the present experiment was *6.75m*. Using this distance as the reference length and the operation temperature at *5°C*, the Reynolds number Re can be calculated as the following:

$$Re = U_{free} * L/v_k \quad \textbf{Eqn.4-7}$$

where: U_{free} is the free-stream velocity, L is *6.75m* of the reference length, and v_k is $1.4 * 10^{-5} m^2 s^{-1}$.

The results of Re at the fence position under different velocities are given in Table 4-2. As per criterion shown in Figure 4-7, the airflow is turbulent for all test velocities. Based on Re, the thickness of boundary layer δ_T at the fence position can be estimated using Eqn.4-8 and are also given in the Table 4-2.

$$\delta_T = (0.382 * L)/R_e^{0.2} \quad \textbf{Eqn.4-8}$$

Table 4-2: The calculated Reynolds number and thickness of boundary layer

Velocity	8m/s	10m/s	15m/s
Re (*10^6)	3.86	4.82	7.23
δ_T (m)	0.13	0.12	0.11

During the experiment, a Pitot static tube was attached to the traverse at the central line of the wind tunnel at a distance of *6.75m* from the leading edge of the test section. The Pitot static tube was connected to a Multi-tube manometer (filled with coloured water). By moving the traverse at *5mm* step height in a range from *5mm* to *200mm* (in the direction from the wind tunnel floor up), a wind velocity profile in vertical direction could be obtained.

Three cases corresponding to inlet velocities of *8m/s*, *10m/s* and *15m/s* were investigated. The inlet velocities were maintained through the control system of the wind tunnel. As kinetic viscosity of air is affected by temperature, the experimental data were taken only

after the temperature inside the wind tunnel was to be stable. The inside temperature were monitored in each case. Table 4-3 lists the information of the experiment.

Table 4-3: The information of the experiment

Case	C1	C2	C3
Inlet velocity (m/s)	8	10	15
Step of height (mm)	5	5	5
Number of steps	40	40	40
Angle of the manometer(°)	25	25	25
Room temperature (°C)	5	5	5
Temperature inside the tunnel	5.4	5.5	6.1-6.3
Reference length (m)	6.75	6.75	6.75

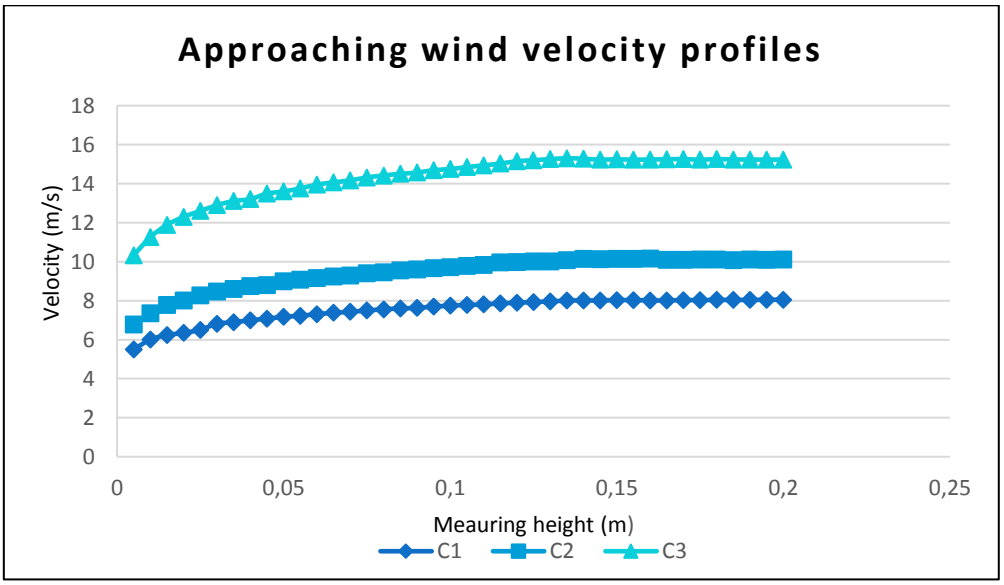

Figure 4-8: The approaching wind velocity profiles

The wind velocity profiles at the fence location are shown in Figure 4-8.

By comparing the results in Table 4-4 with those in Table 4-3, the measured thickness of boundary layer δ for each case is in good agreement with the estimated δ_T .

Table 4-4: The parameters from the experiment

Case	C1	C2	C3
δ (m)	0.125	0,113	0.105
α	0.1139	0.1199	0.1175
R^2	0.9968	0.9993	0.9989

Figure 4-9 shows the approaching wind velocity profiles at the fence position within the thickness of boundary layer, where Power (C1, C2 and C3) represents the trend lines derived from the experimental data. It can be observed that the trend lines were well fitted in power regression type, and the thickness boundary layer decreased with increasing approaching wind velocity.

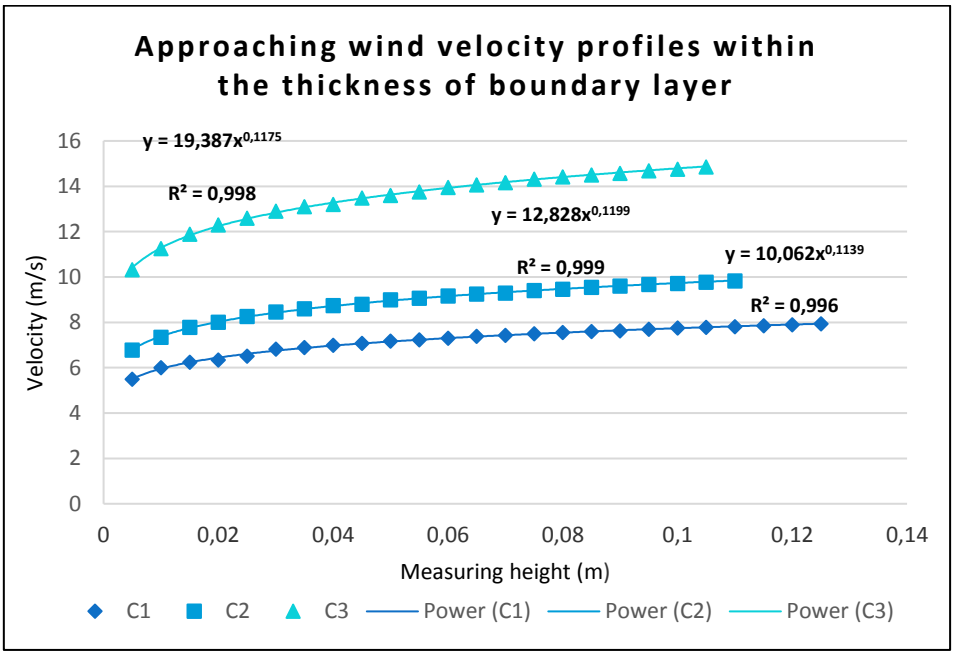

Figure 4-9: The approaching wind velocity profiles within the thickness of boundary layer

The exponent α and the *R*-squared value R^2 for each case are obtained from Figure 4-9 and presented in Table 4-4. The exponent α is the function of Reynolds number, and is

fitted to the intended smooth coastal boundary condition for each case shown in Table 4-5 (Davenport , 1967). The *R*-squared value of R^2 is the coefficient of multiple determinations for multiple regressions. The value of R^2 is always between *0* and *1*, where *0* indicates that the model explains none of the variability of the response data around its mean, while *1* indicates that the model explains all the variability of the response data around its mean. Generally, higher the value of R^2, the better the model fits the targeting data. It can be found that the power regression model was well fitted to the experimental data, since all of R^2 were close to *1*, that indicate the wind velocities within the range of the thickness of boundary obeyed the power law velocity profiles at the fence position.

Table 4-5: Power law exponent α for different terrain types based on Davenport's work

Typical Terrain Types	Power Law Exponent α
Costal & Open water	0.11
Natural snow surface	0.12
Rural	0.16
Forest	0.23
Suburban	0.24
Urban	0.40

To examine the power equations shown in Figure 4-9, *x* is expressed as a ratio of measuring height *h* and the thickness of boundary δ, and the power equations for each case can be written as follows:

- C1:

$$u_h = 10.062x^{0.1139} = 7{,}940 * (h/0.125)^{0.1139} \quad \textbf{Eqn.4-9}$$

- C2:

$$u_h = 12.828x^{0.1199} = 9{,}877 * (h/0.113)^{0.1199} \quad \textbf{Eqn.4-10}$$

- C3:

$$u_h = 19.387x^{0.1175} = 14.876 * (h/0.105)^{0.1175} \quad \textbf{Eqn.4-11}$$

The above equations are well fitted to the description of the power law velocity profiles within the thickness of boundary layer. It revealed that the wind tunnel has produced wall-bounded fully developed turbulent flow at the fence position.

4.2.3. Visualization of wind flow

Visualizations of wind flow were performed before the measurement of wind velocity field for each test. In this thesis, under inlet velocity at *10m/s*, airflow around the three types of fences are selected for the presentation. Figures 4-10, 11& 12are the airflow around the fence type B, D and E, respectively.

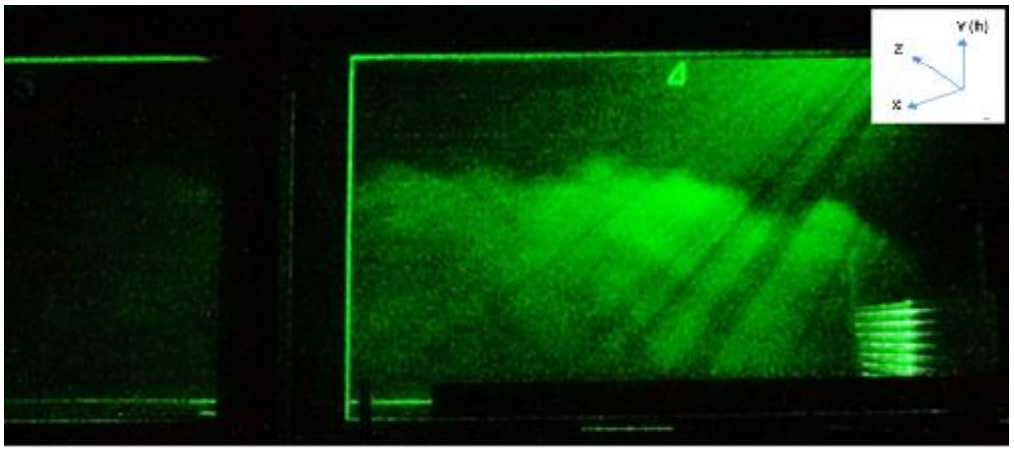

Figure 4-10: Visualization for B type fence

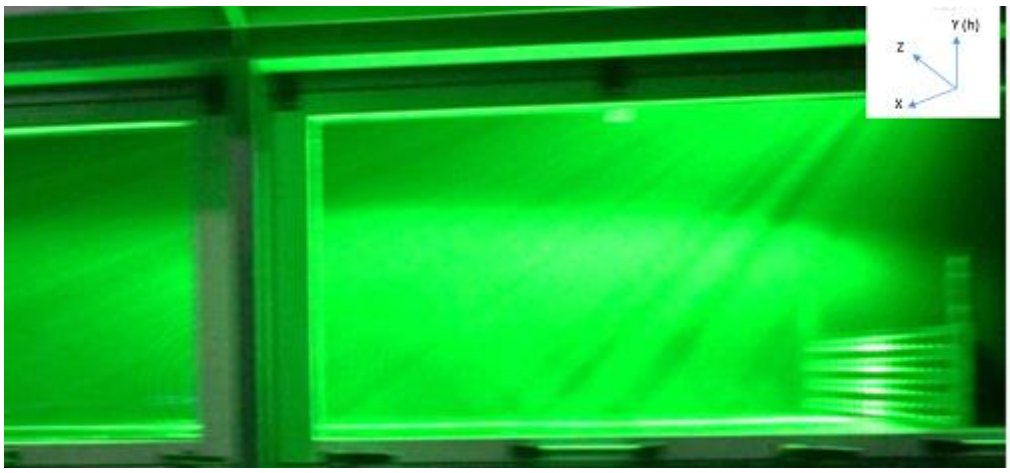

Figure 4-11: Visualization for D type fence

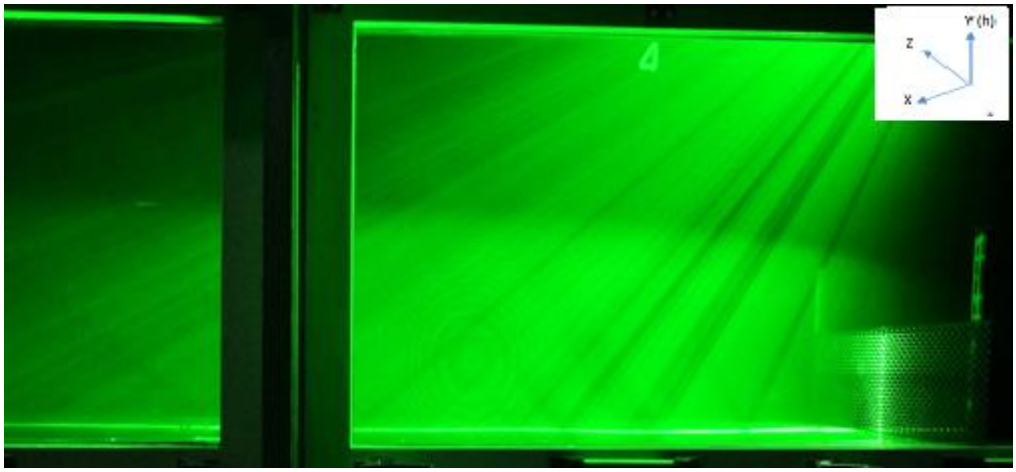

Figure 4-12: Visualization for E type fence

It can be observed that the B type fence has resulted in the strongest recirculating and separated airflow with clear reversal flow being observed. The D type fence had weak flow separation and reversal flow was hardly observed. The E type fence had no flow separation and the flow was dominated by bleed flow.

The visualization shows that porosity has significant influence on the structure of airflow behind porous fences. It also implies that there exists a critical porosity above which the airflow in the leeward is dominated by bleed flow and no flow separation occurs. In the present experiment, the critical porosity can be identified just above *0.35*. The visualization is in a good agreement with literature results that fence porosity in the range of *0.20-0.50* is considered to give noticeable changes of flow structures behind fences (Jensen, 1954) (Tani, 1958) (Raine & Stevenson, 1977) (Lee & Kim, 1999).

Other factors, such as approaching wind velocity, boundary condition, configuration of fence, porosity distribution and shape of hole, will influence the structure of airflow around fences. These will be discussed in details under four experimental cases listed in Table 4-6.

All of the data were obtained along the central line of the wind tunnel, where the y coordinate is 0mm. The arrangement of measurement points have been described in Section 4.2.1, except for the case A, where additional measurement points were added to increase the data resolution.

Table 4-6: The list of the study case scenarios

Case	Applied fences	Inlet velocity (m/s)	Target
A	B type	10	Study flow regime leeward fence with fine resolution
B	A Type	8, 10 &15	Study the effect of approaching velocities
C	A,B & C type	10	Study the effect of fence heights
D	B,D & E type	10	Study the effect of fence porosities

For the convenience of the comparisons, the following parameters are used in data presentations and discussions:

- Normalized velocity component by the correlated free stream velocity: u/U_{free}, v/U_{free}, w/U_{free} and U_m/U_{free}
- Normalized longitudinal distance x by the fence height H: x/H
- Normalized measuring height h by the fence height H: h/H

4.2.4. Case A: study of flow regime leeward the fence

All of the data sets in this section were the distributions of the wind velocities and turbulence along x-axis at different heights. The velocity components in three directions are displayed in Figures from 4-13 to 4-15. Figure 4-16 shows the velocity magnitudes.

Following observations have been made:

1) For the longitudinal velocity component u, the maximum positive u was *11.96m/s* at the position of $x/H = 3.0$ and $h/H = 2.2$, and the maximum negative one was *-1.52m/s* at the position of $x/H = 5.0$ and $h/H = 0.2$. Close to the fence at a height above 1.2H, u was accelerated due to the effect of the displaced flow passing over the fence. The presence of the negative u indicate that reversal flow occurred in the range of x/H from *3.0* to*7.0* and h/H from *0* to *0.7*. The reattachment length

for this fence is at least greater than *7H* observed in Figure 4-13. At the position of *x/H =27.5*, the flow appeared mainly affected by the internal boundary layer.

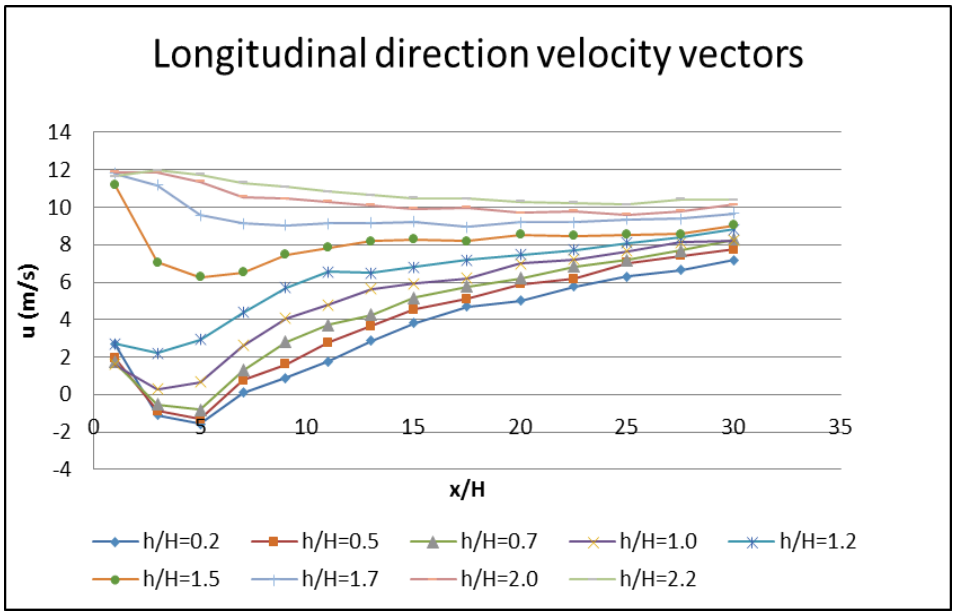

Figure 4-13: The *u* profiles for the case A study

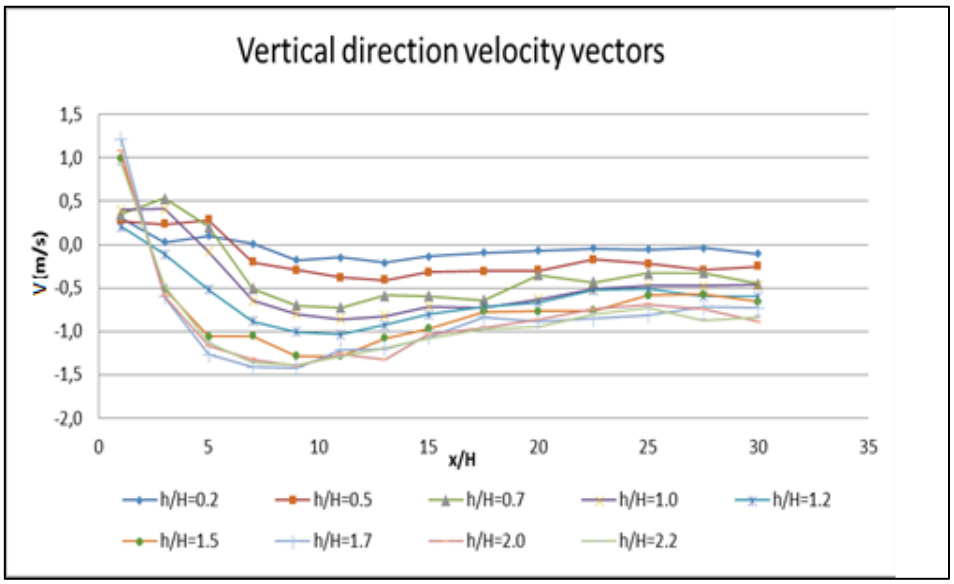

Figure 4-14: The *v* profiles for the case A study

2) For the vertical velocity component *v* shown in Figure 4-14, the maximum positive *v* was *1.214m/s* at the position of *x/H =1.0* and *h/H =1.7*, and the maximum negative one was *-1.423m/s* at the position of *x/H = 9.0* and *h/H = 1.7*.

In general, closer to the fence, the absolute values of v were greater. After the longitudinal distance of *20H*, v appeared to be stable. It indicates that the bleed flow passing through the fence and displaced flow developed v only at a certain distance (*20H* for this experiment). After that, v was recovered to the original nature of the flow.

3) For the lateral velocity component w shown in Figure 4-15, the maximum positive w was *0.425m/s* at the position of *x/H =7.0* and *h/H = 0.2*, and the maximum negative one was *-0.499 m/s* at the position of *x/H =7.0* and *h/H = 1.0*. The distribution appeared different from those of the other two components. It generally presented a vibrational manner, and the spectrum of the vibration decreased with increasing height and distance statistically. However, it can be noticed that the greatest spectrum occurred at the longitudinal distance of *x/H =7.0*. After the longitudinal distance of *11H*, w was still in vibration but in a narrow scale. Comparing its value with the significantly reduced effective area, it may conclude that w has minor impact on the performance of the fence in terms of velocity reductions and distributions.

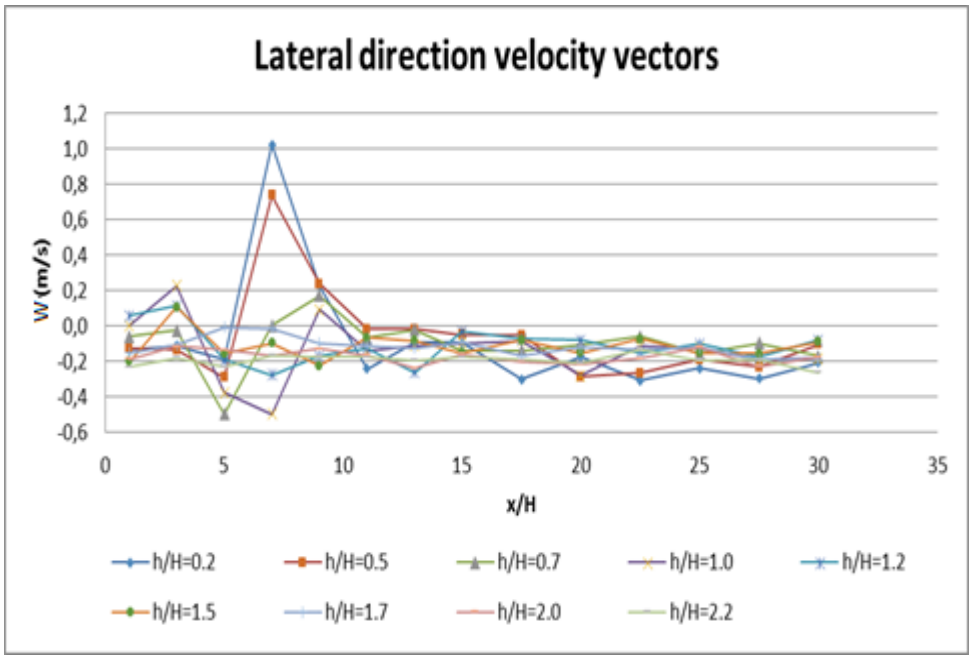

Figure 4-15: The *w* profiles for the case A study

4) When wind flow passes through and passes over the fence, it will create shear stresses in the porous zone and the edges of the fence, this will produce v and w, and transform a single flow into a three-dimensional flow. The shear stress only affects the flow in a certain region. Beyond which, the flow will be recovered to its original form. The value of w is in a one order smaller than the one of v in general, which may be negligible in the fence assessment and design. This explains the reason why majority of researchers took no account of w in their researchers (Yaragal, et al., 1977) (Dong, et al., 2010).
5) Observed from Figure 4-16, the fence has reduced wind velocities in the region with *x/H* from *0* to *27.5*, and *h/H* from *0* to *1.5*. If taking *40%* reduction of wind velocity as a criterion to evaluate the fence effectiveness, the effective shelter distance was $x = 15.0H$ for the height of $h/H = 1.0$ and $x = 9.0H$ for the height of $h/H = 1.2$. It also can be found that there is the similar distribution pattern between Figure 4-16 and Figure 4-13, which indicates that u is dominated in the structure of velocity leeward the fence. Study on the structure of velocity should take u of main concern.

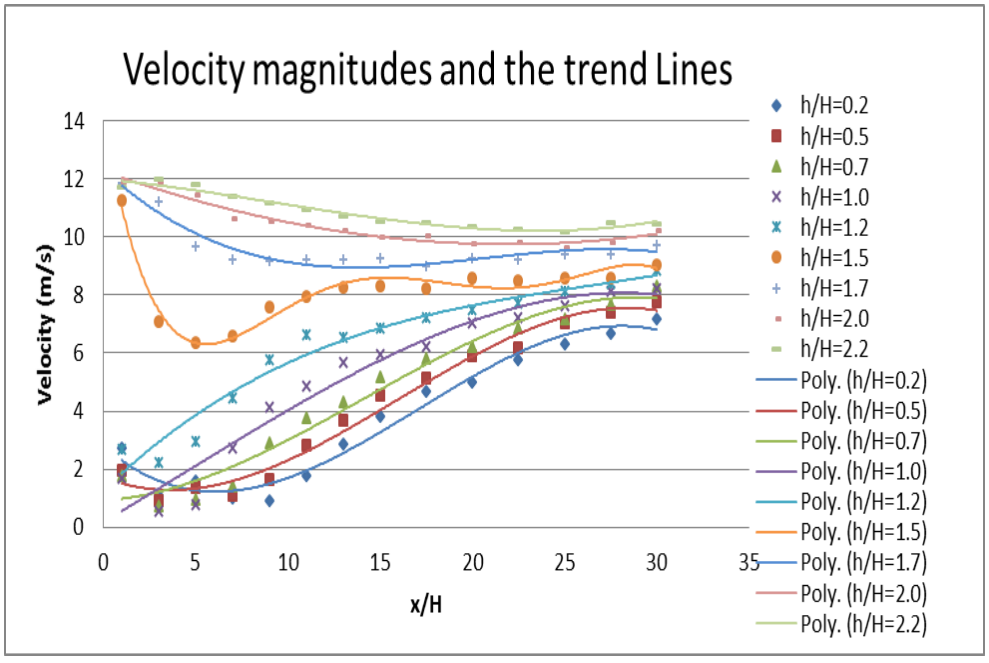

Figure 4-16: The velocity magnitudes and the correlated trend lines for the case A study

Porous fence will create significant turbulent flow downwind when its porosity is below the critical porosity. It is well acknowledged that turbulence will change flow structure in the domain and affect the effective shelter distance of the porous fence. It also has significant impacts on ventilation, visibility and sediment transport etc. The structure of turbulence leeward porous fences is therefore important to characterize the performance of porous fences.

In the present experiment, the data of turbulence intensity T_i and turbulent kinetic energy k were derived from the instantaneous velocity vector profiles. Figure 4-17 shows the distribution of T_i and Figure 4-18 presents the distribution of k leeward the fence.

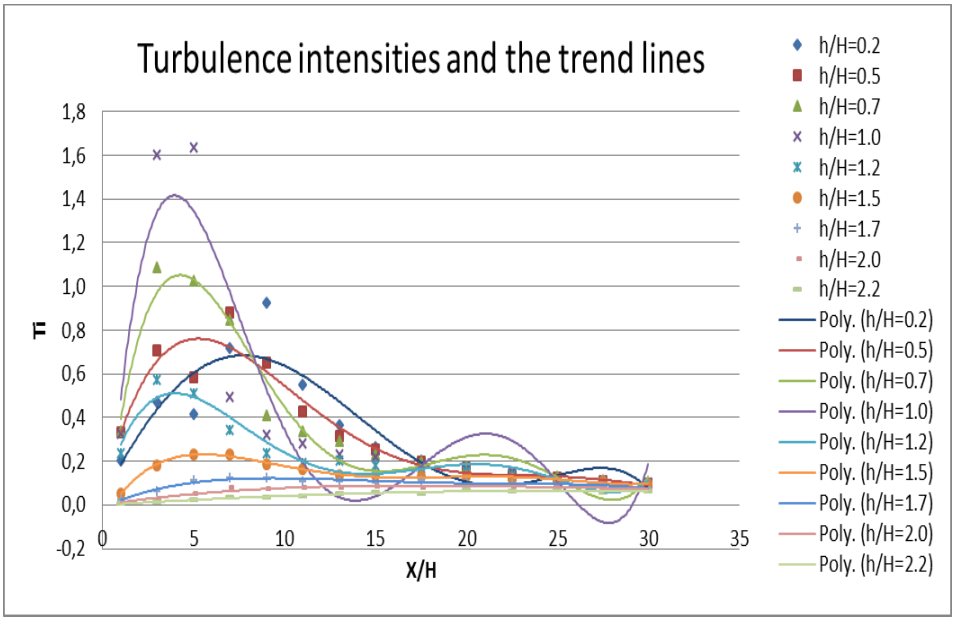

Figure 4-17: The turbulence intensities and the correlated trend lines for the case A study

Noticeable findings are summarized as follows:

1) For the turbulence intensity T_i shown in Figure 4-17, the maximum turbulence intensity was *1.637* at the position of *x/H = 5.0* and *h/H = 1.0*. Above the height of *h/H = 1.5*, the turbulence intensity appeared to be generally uniform with the value of *0.037*, which was in good agreement with the T_i for the free stream airflow in the case of fence free. It indicates that the fence created insignificant turbulence in the region where *h/H* greater than *1.5*. It has been observed that there were two peaks of the turbulence intensity for the *h/H =0.2* and *h/H =0.5* profiles,

indicating that there existed a wake zone in the region. It also can be found that the peak value occurred in the region of *x/H =3.0* and *h/H* from *0.5* to *1.5*. At *h/H =1.0*, the turbulence intensity developed quickly in the distance of *x/H* from *1.0* to *3.0*, and almost maintained the maximum value from *x/H =3.0* to *5.0*, and then decayed fast afterwards. In general, the region of *x/H* from *1.0* to *9.0* and *h/H* from *0.2* to *1.5* was the region with relatively strong turbulence.

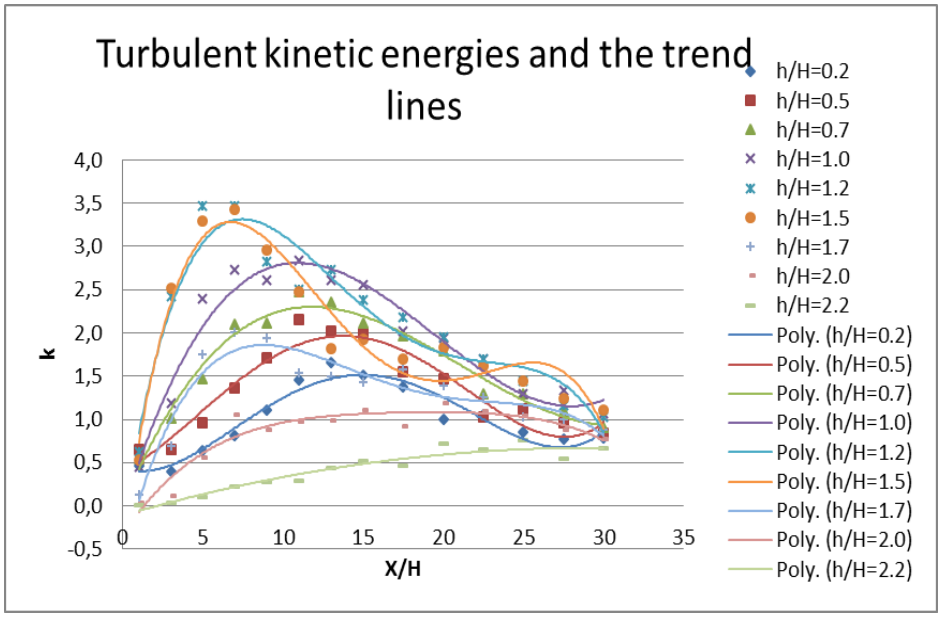

Figure 4-18: The turbulent kinetic energies and the correlated trend lines for the case A study

2) For the turbulent kinetic energy *k* seen in Figure 4-18, the maximum *k* was *3.463* m^2/s^2 at the position of *x/H =5.0* and *h/H =1.2*. It differed the position of the maximum T_i as T_i is associated both the *k* and the local velocity magnitude U_m.The relationship between T_i and *k* can be derived from Eqns.4-4, 4-5 & 4-6 and expressed as the following:

$$T_i = \sqrt{\frac{2}{3}k}/U_m \qquad \textbf{Eqn.4-12}$$

In general, *k* exhibited less dramatic trend if compared with T_i, and its dissipation range was longer than T_i's if compared with the leeward longitudinal distance. At the height of *h/H* from *0.7* to *1.7*, especially for *h/H* from *1.0* to *1.5*, greater *k* was

produced. It indicates that greater velocity fluctuations were created in the velocity acceleration zone where wind flowing over the fence.

Further, the U_m, T_i and k data were analysed using polynomial fitting as shown in Figures from 4-16 to 4-18. Table 4-7 lists the corresponding polynomial order and the R-squared value at each measuring height.

Table 4-7: The data collected from polynomial format

h/H	*Um* trend equation		T_i trend equation		*k* trend equation	
	Order	R^2	Order	R^2	Order	R^2
0.2	3	0.97	5	0.83	4	0.92
0.5	3	0.98	5	0.92	4	0.90
0.7	3	0.97	5	0.95	3	0.97
1.0	3	0.95	5	0.82	3	0.95
1.2	5	0.95	5	0.92	4	0.91
1.5	3	0.91	5	0.99	4	0.92
1.7	3	0.91	4	0.92	4	0.89
2.0	3	0.97	3	0.92	4	0.90
2.2	3	0.96	2	0.97	2	0.93

It can be seen from Table 4-7 that the 3-order polynomial equation fits well to the velocity magnitude, the 4-order polynomial equation does well to the turbulent kinetic energy. However the turbulence intensity needs to be described by the 5-order polynomial equation at least. The high order polynomial equation for describing the structure of turbulence in fact reflected the complex nature of turbulence. This implies that measuring turbulence is much harder than measuring velocity in the case of airflow around porous fences. Overall, the experiment has successfully captured the structures of velocity and

turbulence leeward the fence, which is in good agreement with the findings from the other researchers (Dong, et al., 2010) (Bradley & Mulhearn, 1983) (Cornelis & Gabriels, 2005).

4.2.5. Case B: effect of approaching wind velocity

In Cold Region like Tromsø in Norway, over the course of the year, typical wind speeds vary from *0m/s* to *9m/s*, and rarely exceeding *14m/s*. The annual wind speed in Tromsø is shown in Figure 4-19. The average daily minimum, maximum, and average wind speed is coloured in red, green and black, respectively.

In the experiment, the A type fence was selected to investigate its performance under different approaching wind velocities. The freestream velocity was designed at *8m/s*, *10m/s* and *15m/s* for each test, which is in the approximate wind speed condition in the wintry northern Norway. Accordingly, the measured variables were denoted as *1*, *2* and *3* to represent each test. For example, u_1 stands for the longitudinal velocity component under freestream velocity at *8m/s*, u_2 for the longitudinal velocity component under *10m/s*, and u_3 for the longitudinal velocity component under *15m/s*.

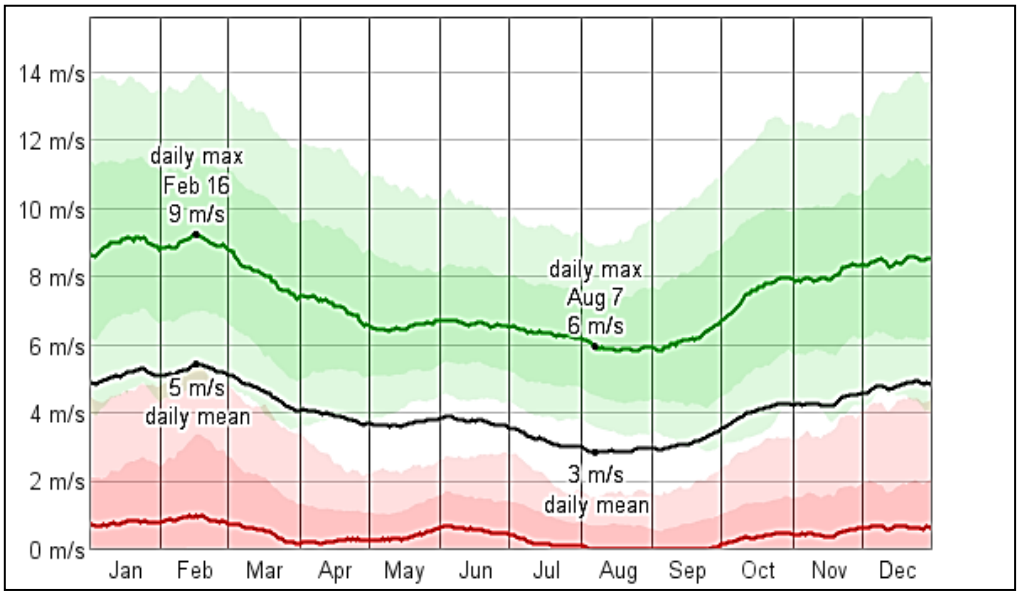

Figure 4-19: Annual wind speed in Tromsø, Norway (WeatherSpark, u.d.)

The experimental data profiles are presented in the form of XY scatter type chart, where the axis X is expressed as the measured variables of velocity or turbulence, and the axis

Y is expressed as the measurement height *h* normalized by the fence height *H*. The expressed velocity variables at the axis X have been normalized by the correlated inlet velocity

Due to large volume of the experimental data, the comprehensive testing data are presented in Appendix A. The normalized u profiles are show in App-Fig.1, the normalized v profiles in App-Fig.2, the normalized w profiles in App-Fig.3, the normalized velocity magnitude U_m profiles in App-Fig4, the turbulent intensity T_i profiles in App-Fig.5, and the turbulent kinetic energy k profiles in App-Fig.6.

The experimental data at *x=0.2m*, *1.0m*,*1.8m* and *3.5m* are selected to be presented in this section. At *x=0.2m*, vertex may involve and the position is very close to the fence. At *x=1.0m* and *1.8m*, reversal flow and the wake zone are in presence. At *x=3.5m*, the internal boundary layer mainly affects the airflow, and the airflow intends to be recovered to the flow with fence free. These positions generally capture the significant features of the structure of flow regime leeward the fence.

The discussions are as follows:

1) For the normalized u profiles shown in Figure 4-20, the u profiles appeared an almost identical trend at the same measurement positions. Although it can be observed that u increases with increasing the freestream velocity, the proportion was rather small. This reveals that the freestream wind velocity has minor influence on the structure of u in the tests.
2) For the normalized v profiles displayed in Figure 4-21, the v profiles appeared in a similar pattern at the same measurement positions. At the distance *x=0.2m*, the values of v were in positive. In the region *x* from *0.2m* to *1,0m*, below the height of *1.2H*, the values of v were positive, above the height, v negative. Away from the distance *x= 1.0m*, the value of v were all in negative and the absolute value was increased with the measuring height almost in a linear way, and significantly decreased with increasing the longitudinal distance of *x*. Overall, changing approaching velocity has limited influence on the structure of v.

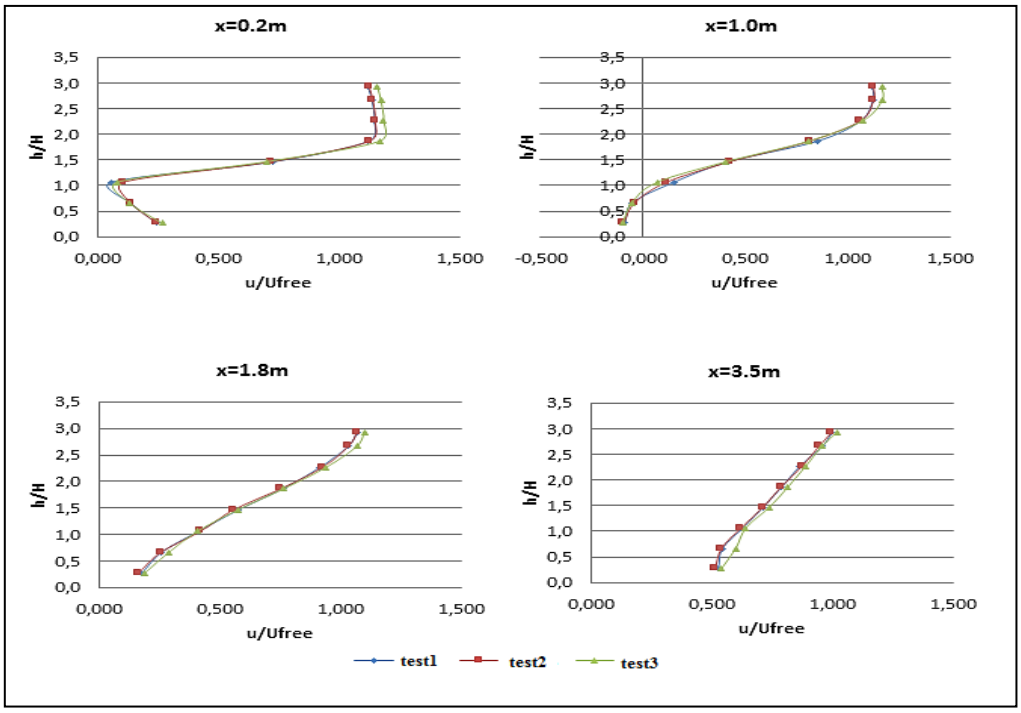

Figure 4-20: The u profiles at different x-positions for the case B study

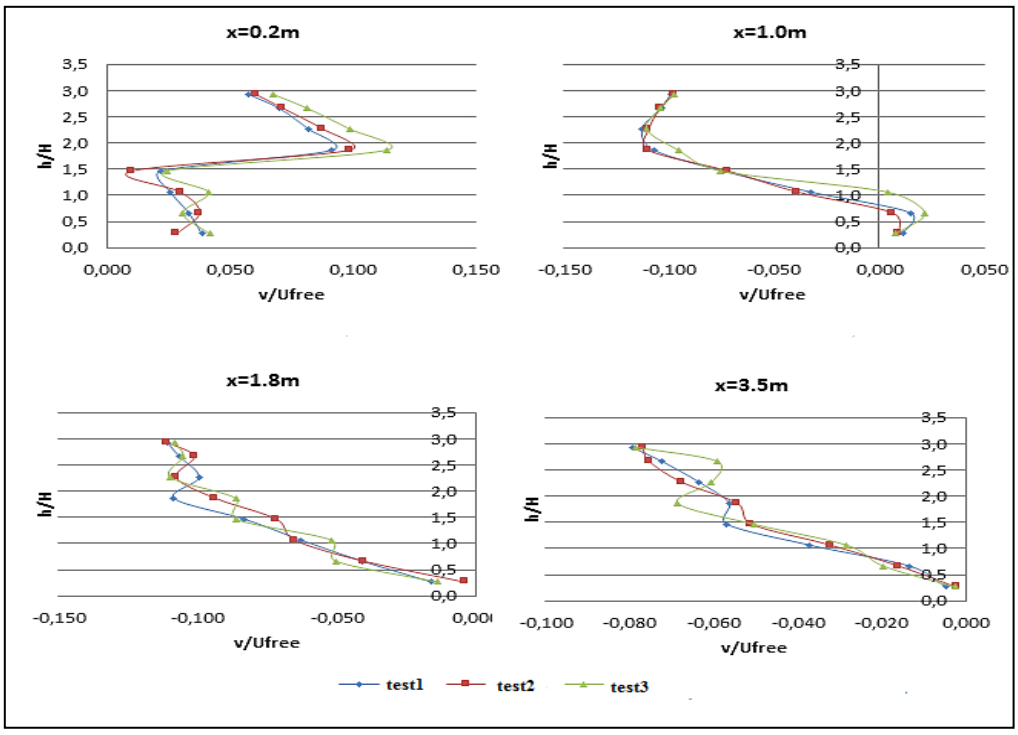

Figure 4-21: The v profiles at different x-positions for the case B study

3) For the normalized *w* profiles presented in Figure 4-22, the *w* profiles appeared an approximate vibration manner, and such a feature was more evident to be found at *x=0.2m* (close to the fence) and at *x=3.5m*. The positive values of *w* can be found in the region of x from *0.2m* to *2.6m* and y from *0.5H* to *2.0H* (see App-Fig.3), beyond which the values of *w* appeared to be negative. It appeared that *w* were more sensitive to the change of the approaching wind velocity than *v*. However, proportionally the change was insignificant.

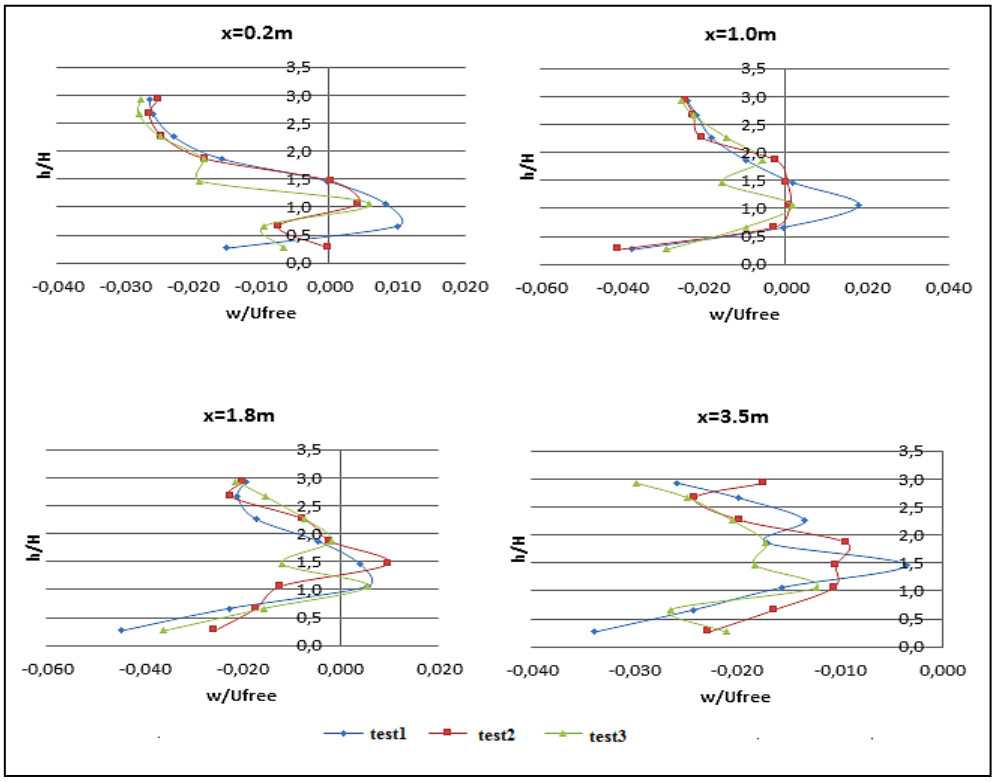

Figure 4-22: The *w* profiles at different x-positions for the case B study

4) The normalized velocity magnitude profiles shown in Figure 4-23 were very similar to the normalized *u* profiles, apart from there was no negative values appeared in the normalized velocity magnitude profiles. This is due to the nature of velocity magnitudes. This similarity also indicates that the *u* component plays the dominant part in the structure of wind velocity leeward the fence. This again reveals that the freestream velocity has little influence on the structure of wind velocity leeward the fence.

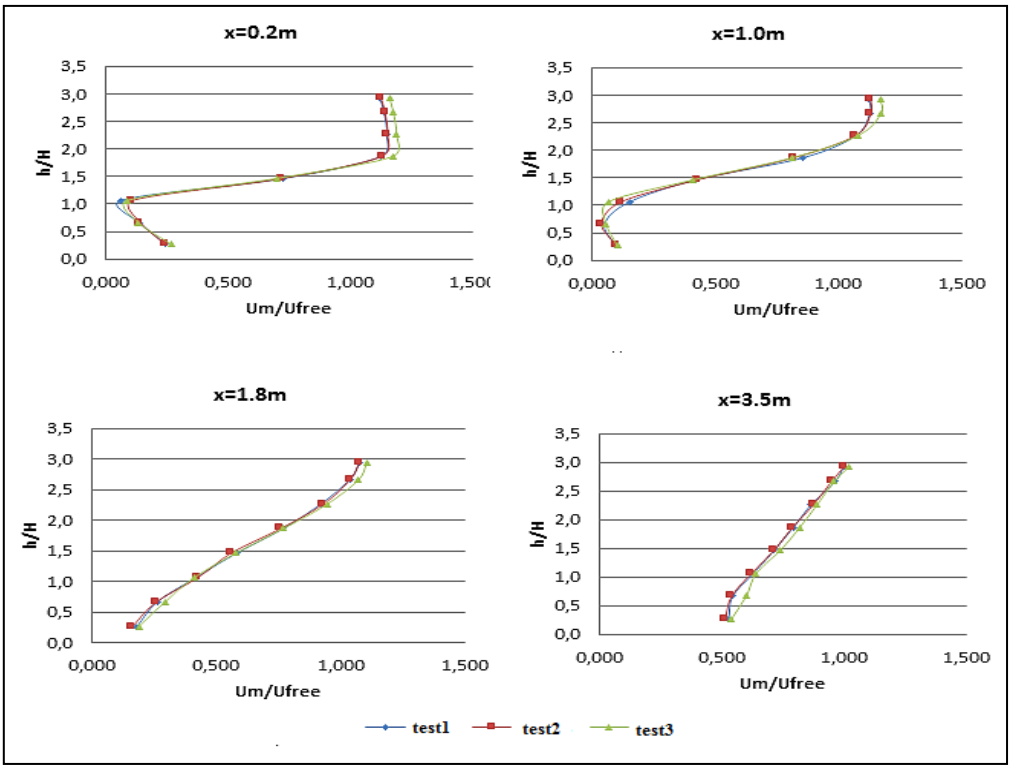

Figure 4-23: The velocity magnitude profiles at different x-positions for the case B study

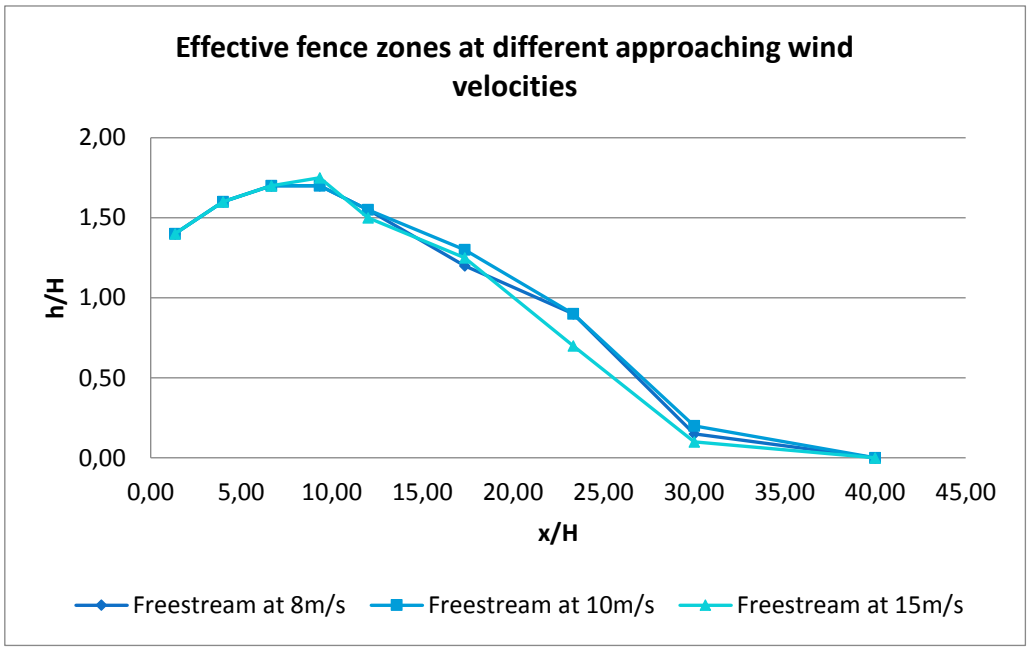

Figure 4-24: The effective fence zones at different approaching wind velocities for the case B study

Figure 4-24 shows the effective fence zone under these three different freestream wind velocities when taking *40%* reduction of the freestream velocities as the criterion to evaluate the effectiveness of the fence. The axis X is the ratio of longitudinal distance *x* to the testing fence height *H*, and the axis Y is the ratio of the measuring height *h* to the testing fence height *H*. It can be found from Figure 4-24 that, at the inlet wind velocity of *15m/s*, the effective fence zone appeared to be a little narrowed. This indicates that the increase of the freestream wind velocity might result in a reduction of the fence effective zone. It has however had little impact on the size of the fence effective zone considering the measurement errors in the experiment.

5) Both v and w components account very little to the local velocity magnitude. From *x=1.8m* downwind, the $u$components appeared all in positive values, the v components were all in negative values, and majority of the w components appeared in negative values. This consistence in the velocity component directions indicates that the reversal flow might not occur or at least became very weak.

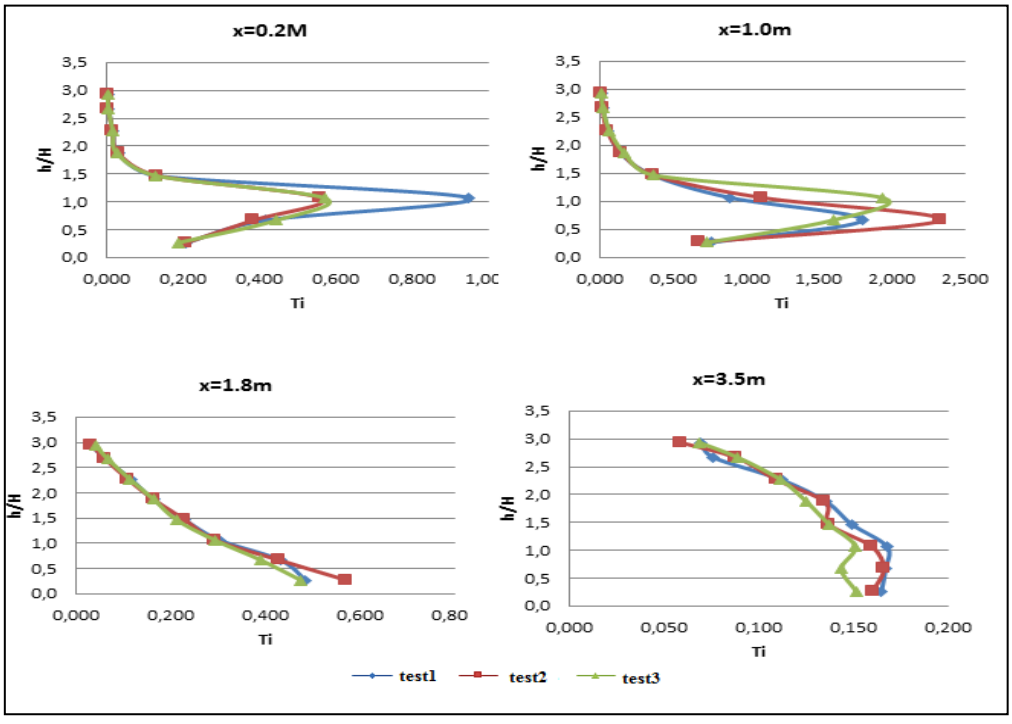

Figure 4-25: The turbulence intensity profiles at different x-positions for the case B study

The approaching wind velocity has had more influence on the structure of turbulence than on the structure of velocity (see App.Fig.5 and App-Fig.6). It can be seen from Figures 4-25 &26 that the turbulence intensity decreased with the increase of the freestream velocity, while the turbulent kinetic energy shows otherwise. Within the region *x=1.0m (6.7H)*, the turbulence intensity increased with the measuring height up to *0.7H*.For the measuring height between *0.7H* and *1.1H*, the maximum turbulence intensity occurred. Above which, the turbulence intensity decayed almost at the same rate. Away from *x=1.0m*, the turbulence intensity decreased with the increase of the measuring height. At *x=6.0m*, the turbulence intensity was recovered to the level of the fence free condition. The turbulent kinetic energy reached the peak value in the height range from *1.0H* to *1.5H*, which is higher than the height range for the turbulence intensity. In general, these three different approaching wind velocities affected the structure of turbulence only in the region of x from *0* to *6.7H* and y from *0* to *1.5H*.

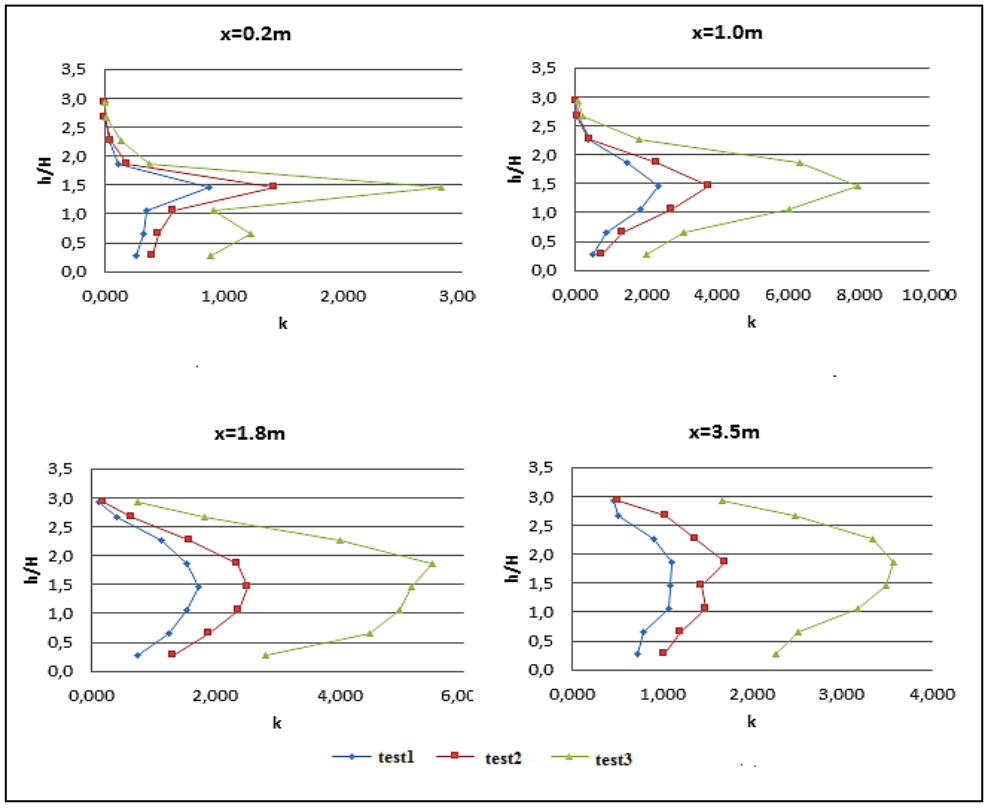

Figure 4-26: The turbulent kinetic energy profiles at different x-positions for the case B study

Overall, these three different approaching wind velocities have had no significant impact on the structure of leeward flow regime. It also shows that velocity profile alone is not sufficient to describe the structure of leeward flow behaviour, as the structures of turbulence can be different even if the structures of velocity are almost identical.

4.2.6. Case C study: effects of fence heights

To investigate the effect of fence height on the porous fence performance, fences of the same design parameters apart from the fence height were tested under the freestream wind velocity of *10m/s*. The A, B and C type fences selected for the experiment are of the height of *0.15m*, *0.20m* and *0.30m*, respectively. The corresponding results are denoted with subscripts 1, 2 and 3 for the tests of the A, B and C type fence accordingly, which is the same way applied in Section 4.2.5.

Due to large volume of the experimental data, the comprehensive testing data are presented in Appendix B. The normalized u profiles are show in App-Fig.7, the normalized v profiles in App-Fig.8, the normalized w profiles in App-Fig.9, the normalized U_m profiles in App-Fig10, the turbulent intensity T_i profiles in App-Fig.11, and the turbulent kinetic energy k profiles in App-Fig.12.

Similar to Section 4.2.5, the experimental data at *x=0.2m, 1.0m,1.8m* and *3.5m* are selected to be presented in this section.

The following are the discussions based on the experiment:

1) For the u components shown in Figure 4-27, it can be seen that higher fence height had better performance in terms of reduction of u. At *x=0.2m*, there was no negative u occurred for all fences. At *x=1.0m*, u was negative for all of the fence; At *x=1.8m*, the u components appeared to be positive for all of the fences. It appeared that the negative u components most likely occurred below fence height in the longitudinal distance *x* from *2* to *6* times of fence height, which indicates that reversal flow likely appeared below fence height. It also can be found that the increase of fence height does not proportionally increase the size of negative u zone.

2) For the v components as presented in Figure 4-28, negative v components appeared all the time except at the location of *x=0.2*. In general, increasing fence height produced greater v components downwind.

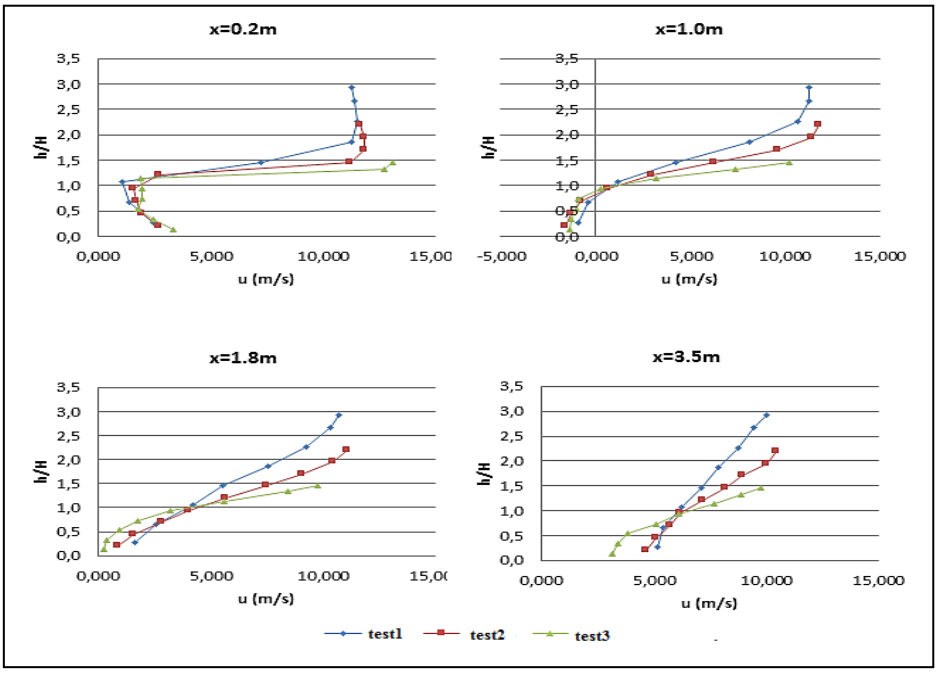

Figure 4-27: The u profiles at different x-positions for the case C study

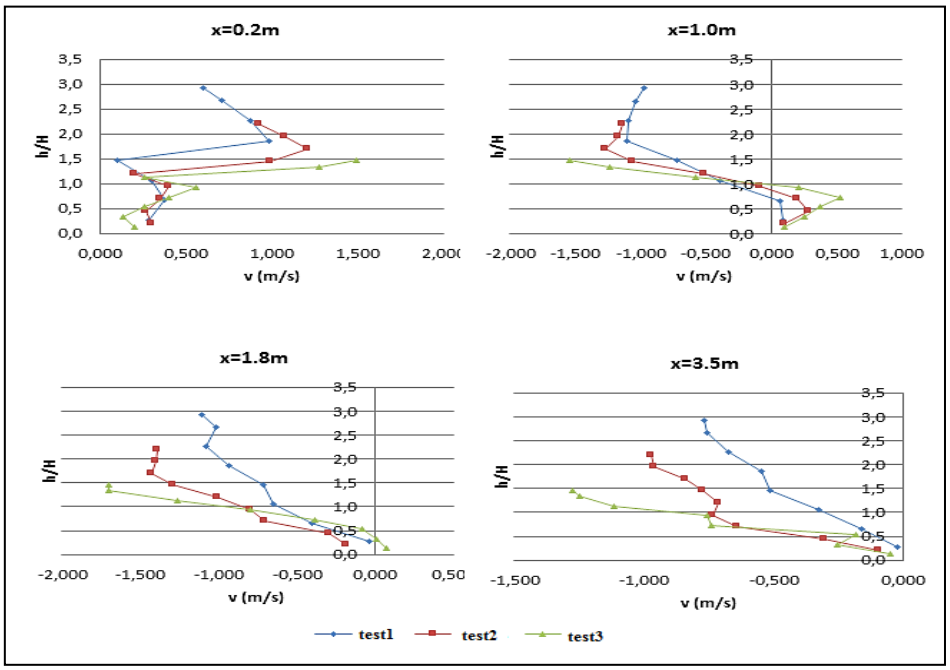

Figure 4-28: The v profiles at different x-positions for the case C study

3) For the *w* components shown in Figure 4-29, away from the fence, *w* was developed to be negative value. Increasing fence height resulted in the *w*components increased. The change is however very small if compared it with the local velocity magnitude.

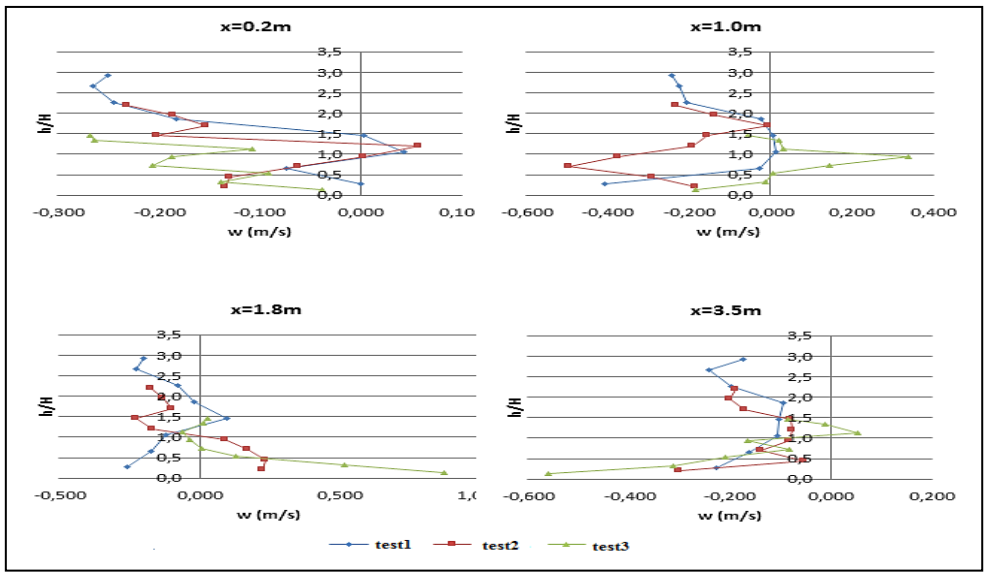

Figure 4-29: The *w* profiles at different x-positions for the case C study

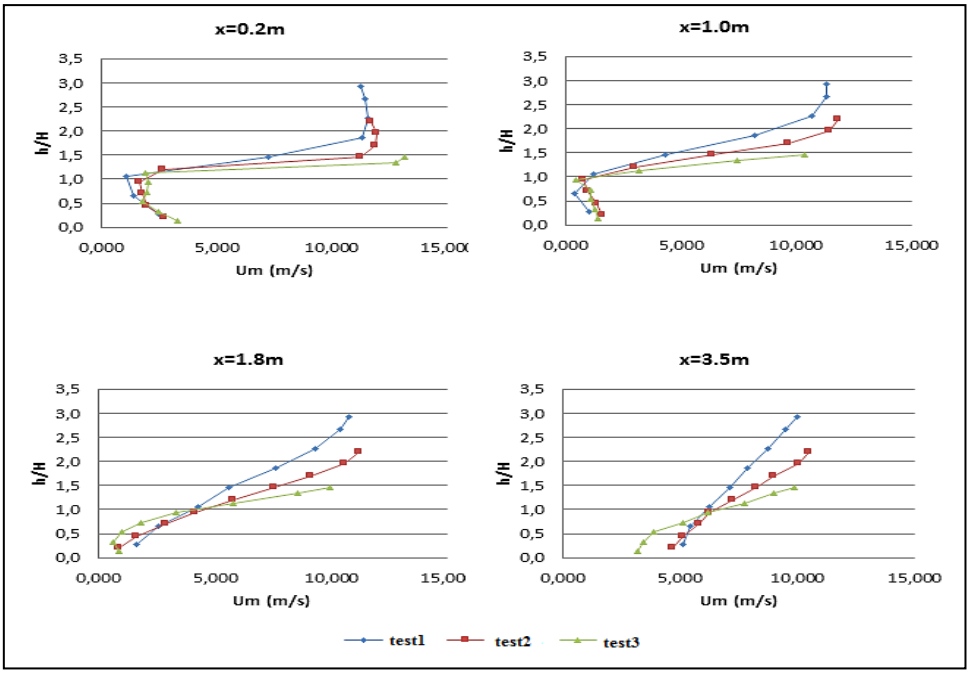

Figure 4-30: The velocity magnitude profiles at different x-positions for the case C study

4) For the velocity magnitudes shown in Figure 4-30, it is evident that increasing fence height resulted in greater fence effective zone in terms of reduction of wind velocity. By taking 40% reduction of freestream wind velocity as a criterion to assess the effectiveness of the fence, and based on App- Fig.10, Table 4-8 listed the positions where the velocity is equal to 40% reduction of the freestream velocity for the testing fences. The values at the Axes of X and Y were normalized the longitudinal and the vertical measurement distance by the correlated fence height.

Table 4-8: The positions where the velocity as 40% reduction of freestream velocity

Fence Type x(m)	A			B			C		
	$H_1 = 0.15m$			$H_2 = 0.2m$			$H_3 = 0.3m$		
	X	Y		X	Y		X	Y	
	x/H_1	h/H_1	*h (m)*	x/H_2	h/H_2	*h (m)*	x/H_3	h/H_3	*H (m)*
0.2	1.33	1.40	0.21	1.00	1.30	0.26	0.67	1.20	0.36
0.6	4.00	1.60	0.24	3.00	1.40	0.28	2.00	1.30	0.39
1.0	6.67	1.70	0.26	5.00	1.45	0.29	3.33	1.30	0.39
1.4	9.33	1.70	0.26	7.00	1.45	0.29	4.67	1.20	0.36
1.8	12.00	1.55	0.23	9.00	1.25	0.25	6.00	1.20	0.36
2.6	17.33	1.35	0.20	13.00	1.00	0.20	8.67	1.00	0.30
3.5	23.33	0.90	0.14	17.50	0.85	0.17	11,67	0.80	0.26
4.5	30.00	0.25	0.04	22.50	0.40	0.08	15.00	0.55	0.17
6.0	40.00	0.00	0.00	30.00	0.00	0	20.00	0	0

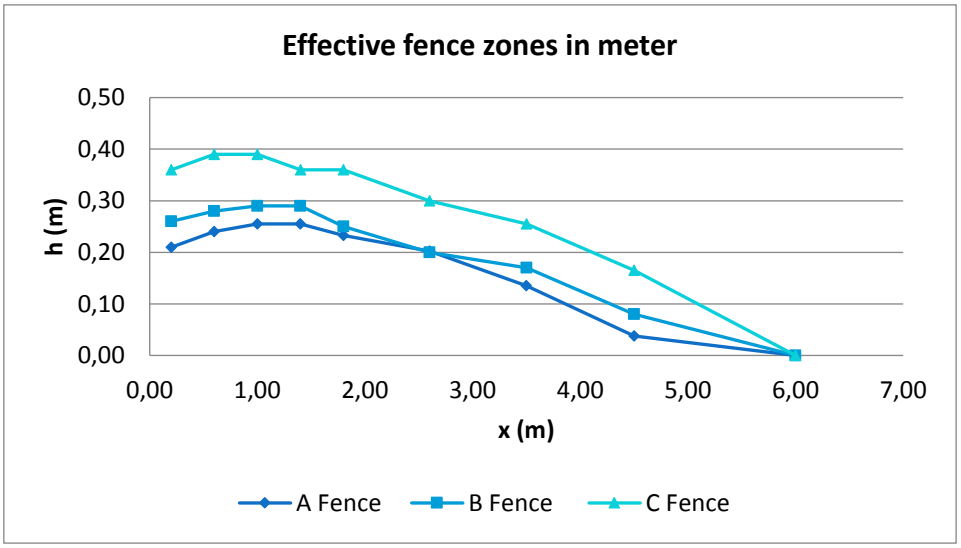

Figure 4-31: The effective fence zones in meter for the case C study

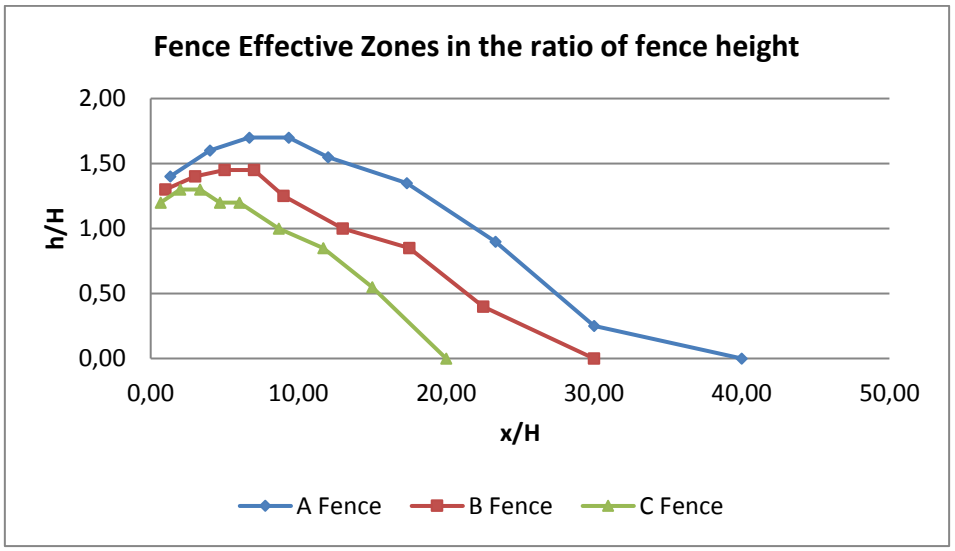

Figure 4-32: The effective zones in the ratio of fence height for the case C study

5) Figures 4-31 displays the size of the effective zones in meter, while Figure 4-32 shows the size of the effective zones normalized by the correlated fence height. Figure 4-31 shows that increasing fence height will increase the size of the fence effective zone accordingly. However, Figure 4-32 demonstrates otherwise. It reveals that increasing fence height will increase the physical size of fence effective zone. However, this increase is not proportional, especially for the

longitudinal shelter distance as shown in Figure 4-32. Hence, purely increasing fence height to reduce wind velocity is not an economic way.

6) For the turbulence intensities shown in Figure 4-33, lower fence height enhanced turbulence in the region closer to the fence. In the turbulence-intensified zone, turbulence increased with the increase of the height in the range from *0H to0.7H*, and reached a peak value in the range from *0.7H to1.0H*. The turbulence started to fade with further increase of the height. Above the height of *2.0H*, turbulence appeared to be recovered to the freestream feature. The maximum peak value was *2.117* created by the C fence at the position of $x=4.7H$ and $y=0.7H$ (see App-Fig. 11). In general, increasing fence height resulted in intensifying turbulence, and enlarged turbulence-intensified zone.

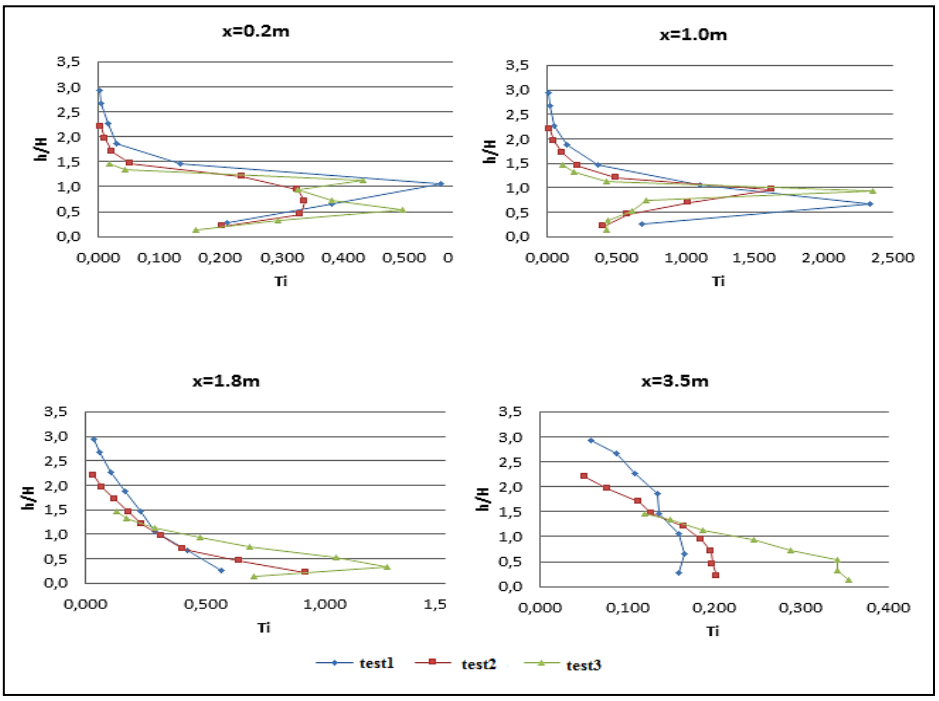

Figure 4-33: The turbulence intensity profiles at different x-positions the case C study

7) For the turbulent kinetic energies shown in Figure 4-34, close to the fence within the distance *x=1.0m*, lower height fence created more turbulent kinetic energies than higher height fence. After the distance *x=1.8*, higher height fence appeared to produce stronger turbulence kinetic energies, and turbulence kinetic energies started to be dissipated with x.

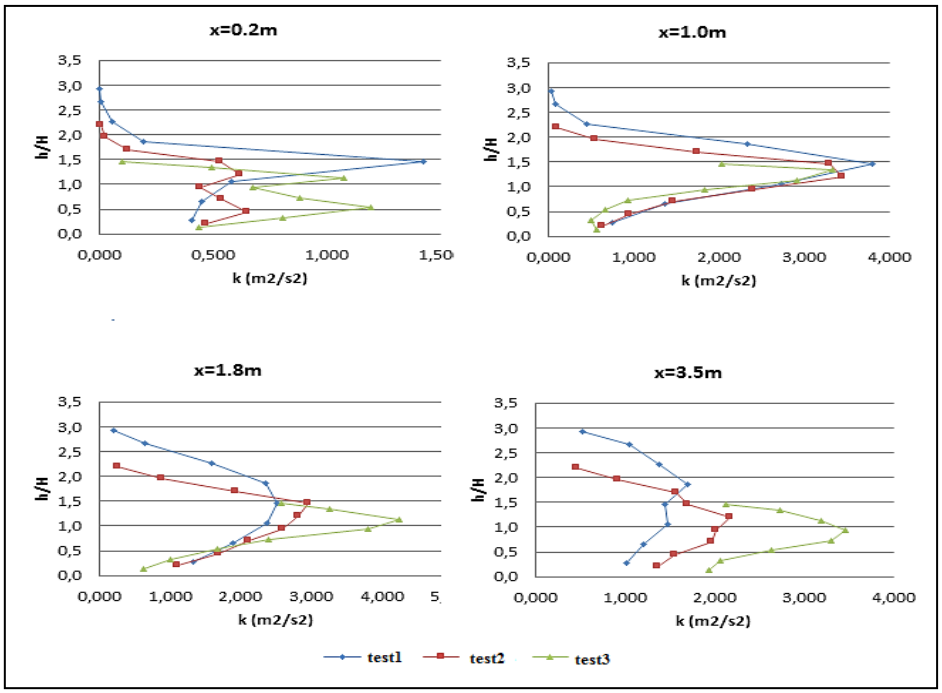

Figure 4-34: The turbulent kinetic energy profiles at different x-positions the case C study

It can be concluded that fence height has significant impact on the structures of wind velocity and turbulence leeward the fences. Increasing fence height will create more turbulent flow in general, and create larger size of fence effective zone leeward in terms of velocity reduction. However, purely increasing fence height to reduce wind velocity may not an economic way.

4.2.7. Case D study: effects of fence porosities

In this section, under the freestream velocity of 10m/s, the B, D and E type fences were selected to investigate their performance at different porosities, which were *0.27*, *0.35* and *0.50*, respectively. The corresponding results are denoted with subscripts 1, 2 and 3 for the tests of the B, D and E type fence accordingly, which is the same way applied in Section 4.2.5.

Due to large volume of the experimental data, the comprehensive testing data are presented in Appendix C. The normalized u profiles are show in App-Fig.13, the normalized v profiles in App-Fig.14, the normalized w profiles in App-Fig.15, the

normalized velocity magnitude U_m profiles in App-Fig16, the turbulent intensity T_i profiles in App-Fig.17, and the turbulent kinetic energy k profiles in App-Fig.18.

Similar to Section 4.2.5, the experimental data at *x=0.2m*, *1.0m*,*1.8m* and *3.5m* are selected to be presented in this section.

The discussions are as follows:

1) For the normalized u components shown in Figure 4-35, negative values of u only appeared in the B fence at *x=1.0m*. It generally appeared that

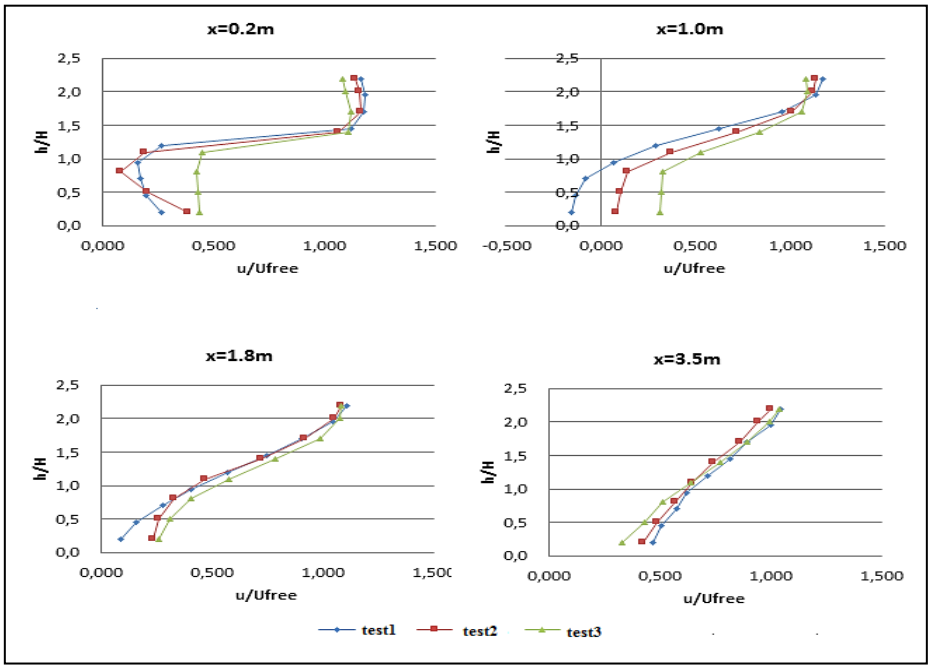

Figure 4-35: The normalized u profiles at different x-positions for case D study

lower porosity resulted in greater u reduction and large size of the fence effective zone. However, it was not the case at *x=3.5m*, where the E type fence had the greater u reduction. This may explain that fence with lower porosity will create more turbulent flow leeward, and velocity accelerations may be enhanced due to the comparatively greater blockage ratio in the cross-section, which affects the flow to be recovered to the flow with fence free at a longer distance. It also can be noticed that the performance was significantly deteriorated from the D fence to the E fence than from the B fence to the D fence, indicating the existence of optimum porosity.

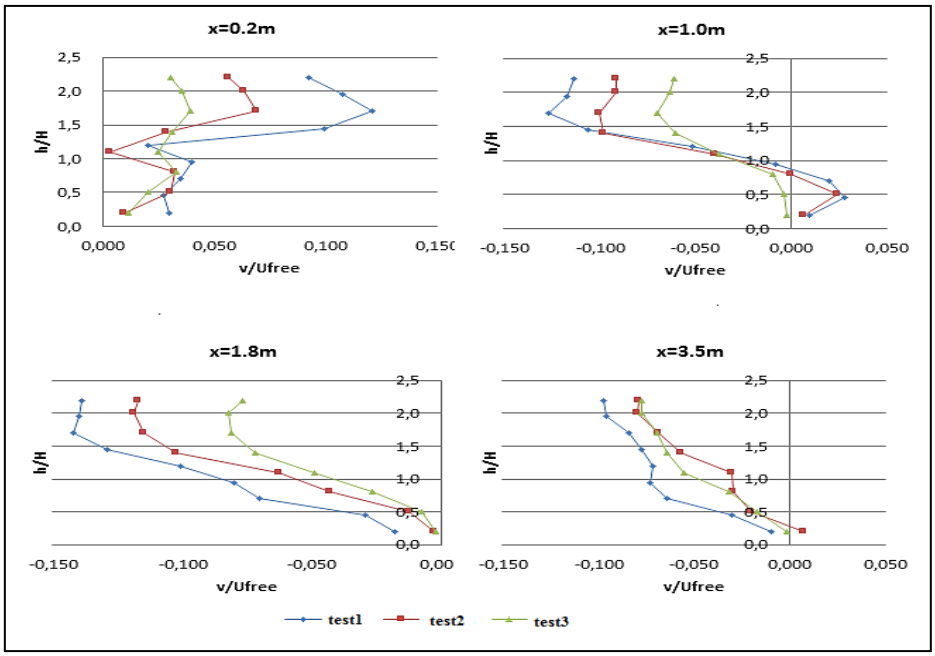

Figure 4-36: The normalized v profiles at different x-positions for the case D

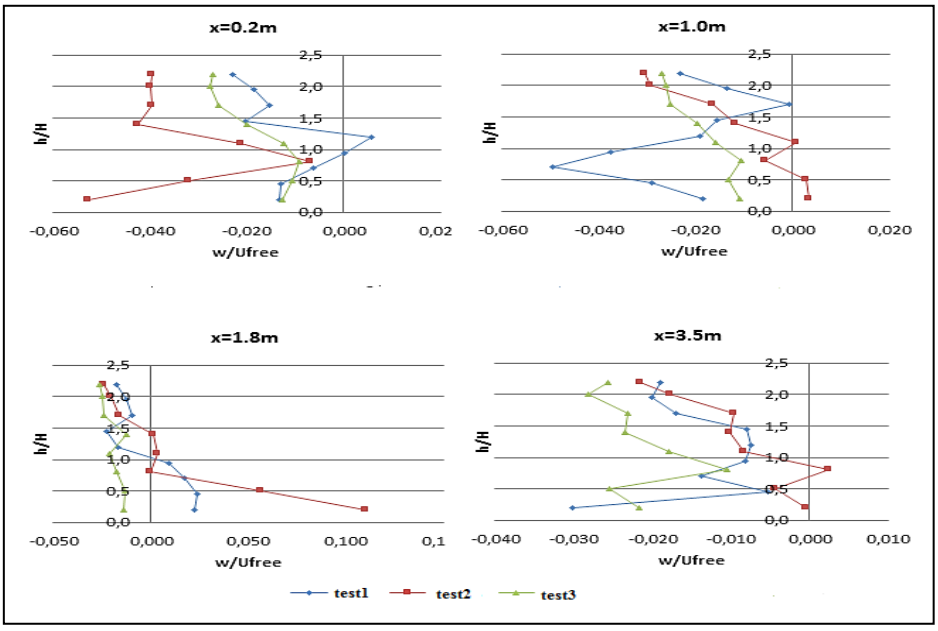

Figure 4-37: The normalized w profiles at different x-positions for the case D study

2) For the normalized v components presented in Figure 4-36, greater fence porosity resulted in weaker production of v and wider distribution area in general. All types

of the fences created negative values for the $v$components, except at $x=1.0m$, the B & D fences had positive values of v distributed below their fence height.

3) For the normalized w components shown in Figure 4-37, there is no positive $w$components for the E type fence. The vibrational feature were more evident with lowering porosity. This indicates that porosity has influenced the $w$components both on the values and distributions

4) At $x=1.0m$, the B type fence produced both of positive and negative values for the $u$components, and both of the B and D fence created both of positive and negative for the $v$components. However, the E type fence were consistent in the presence of one directional velocity components leeward. Since the w component has insignificant influence, it may ignore its impact on the structure of wind velocity. Therefore, it can be identified : the E type fence has not produce reversal flow downwind, the B & D type fences have created reversal flows in the regions around $x=1.0m$. Since u is dominant in determining the structure of velocity, the D type fence produced very weak reversal flow leeward as it has not produced co-existed negative and positive values of u.

   Overall, porosity has significant influence on these three velocity components in terms of velocity reduction and the behaviour.

5) Based on the normalized velocity magnitude data (see App-Fig.16), Figure 4-38 shows the effective fence zones assessed by the criterion of *40%* reduction of velocity, while Figure 4-39 displays the effective fence zones assessed by *60%*.

   The axis X is expressed as the effective shelter distance normalized by the fence height, and the axis Y is the effective shelter height normalized by the fence height. The area formed by the plotted cure and two axes is the effective zone. Compared Figure 4-38 with Figure 4-39, judged by *40%* reduction of velocity, the E fence had the greatest effective fence zone and the B fence had the smallest. While judged by *60%* reduction of velocity, the B fence created the greatest effective fence zone and the E fence produced the smallest. In general, increase offence porosity resulted in increasing the effective shelter distance while decreased the effective shelter height. The comparison also reveals that design of

optimum porosity should also consider the wind reduction criterion for the applications.

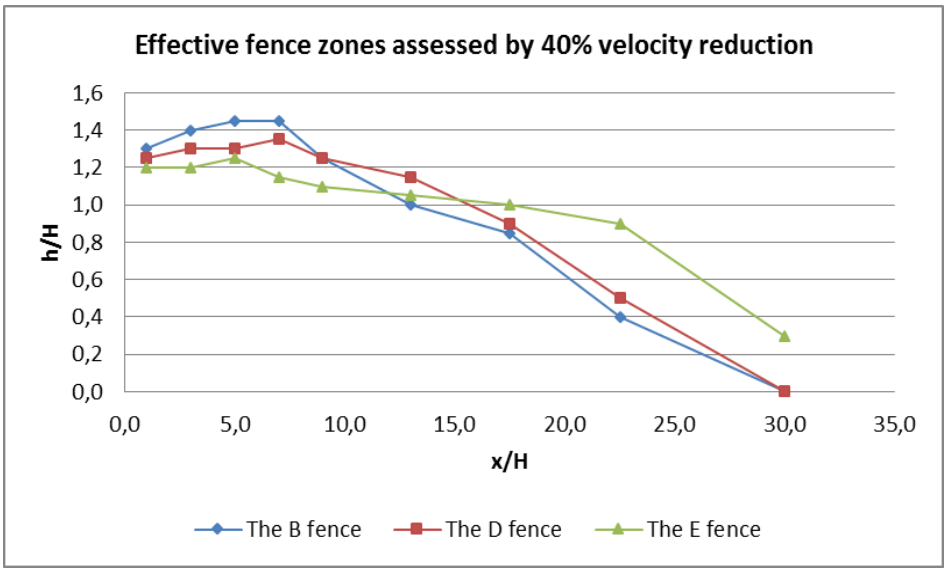

Figure 4-38: The effective fence zones by 40% velocity reduction criterion for the case D study

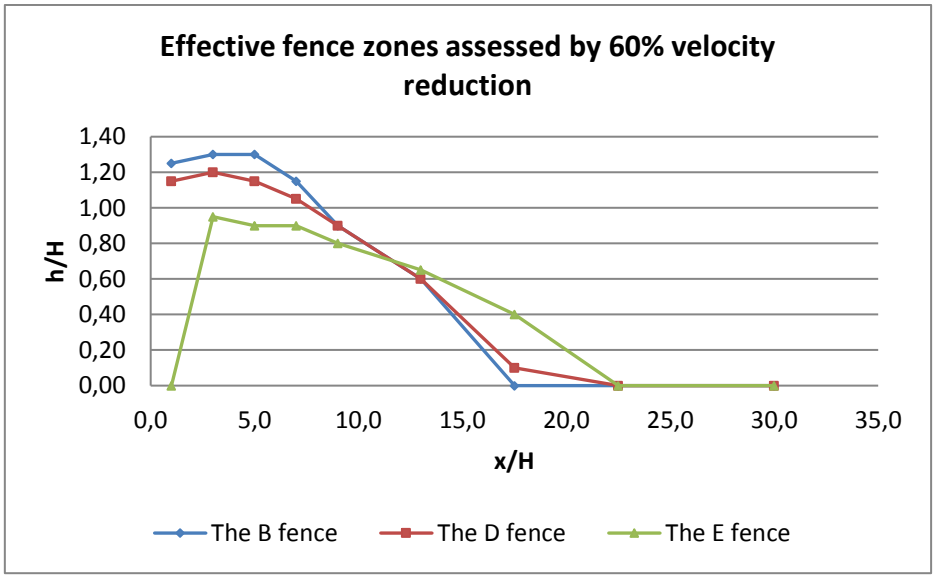

Figure 4-39: The effective fence zones by 60% velocity reduction criterion for the case D study

6) For the turbulence intensities shown in Figure 4-40, the B fence demonstrated the highest level of turbulence while the E fence had the lowest all the time except at the distance *x=0.2m*, where the D fence appeared the highest. Within the distance $x \leq 1.8m$, there was a distinguished peak value occurred at the height positon

around *0.5H* to *1H* for all of the fences, below which turbulence intensity increased with the increase of measuring height, and above which it decreased with the increase of measuring height. In the region where $h/H \leq 2$ or $x/H \geq 9$, the turbulence intensity for all of the fences appeared to be recovered to the flow with fence free. Overall, lower porosity creates stronger turbulence leeward the fence.

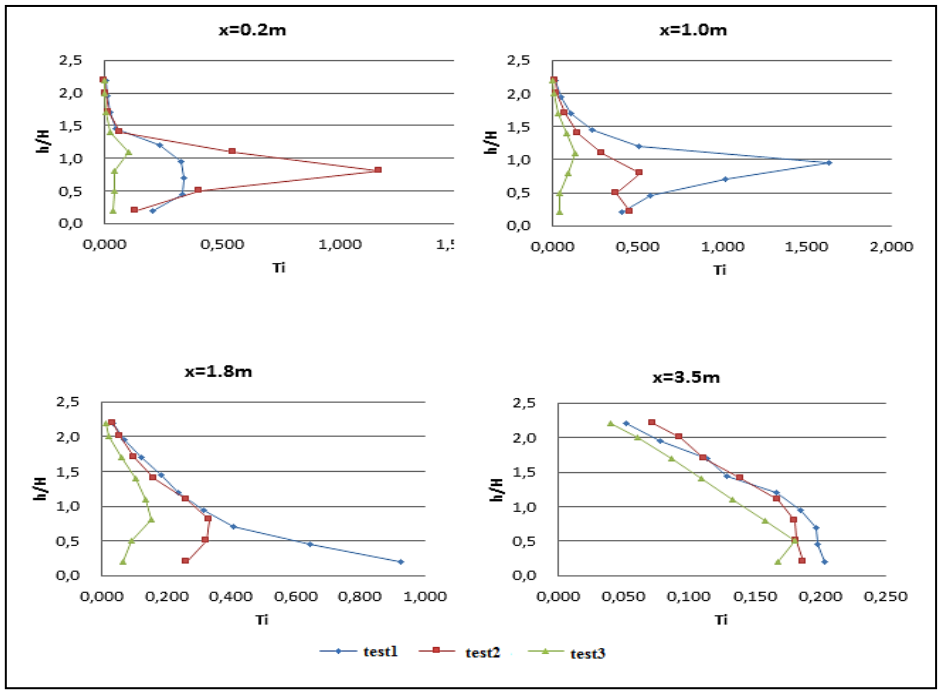

Figure 4-40: The turbulence intensity profiles at different x-positions for the case D study

7) For the turbulent kinetic energies presented in Figure 4-41, a peak value occurred at measuring height *h* between *1.0H* and *1.5H* all the time for all of the fences. It can be found that the position of peak value for the turbulent kinetic energy was higher than the position of peak value for the corresponding turbulence intensity. Lower porosity had greater turbulent kinetic energy in general.

The experiment reveals that lower porosity will create stronger turbulence and lower velocity behind the fence in general. It also has found that porosity has significant influence on the structures of velocity and turbulence, size of fence effective zone and the presence of reversal flow, etc.

The experimental results found the existence of optimum porosity. As the most important structural feature in the fence design, optimizing porosity of fence will offer the designed fence with optimal protection at the minimum cost. However, design of optimum porosity also needs to consider the wind reduction criteria for its applications. Optimizing porosity should also consider the effects of turbulence. Turbulence may affect comfortability, ventilation and visibility in a confined space, which should be considered in the fence design.

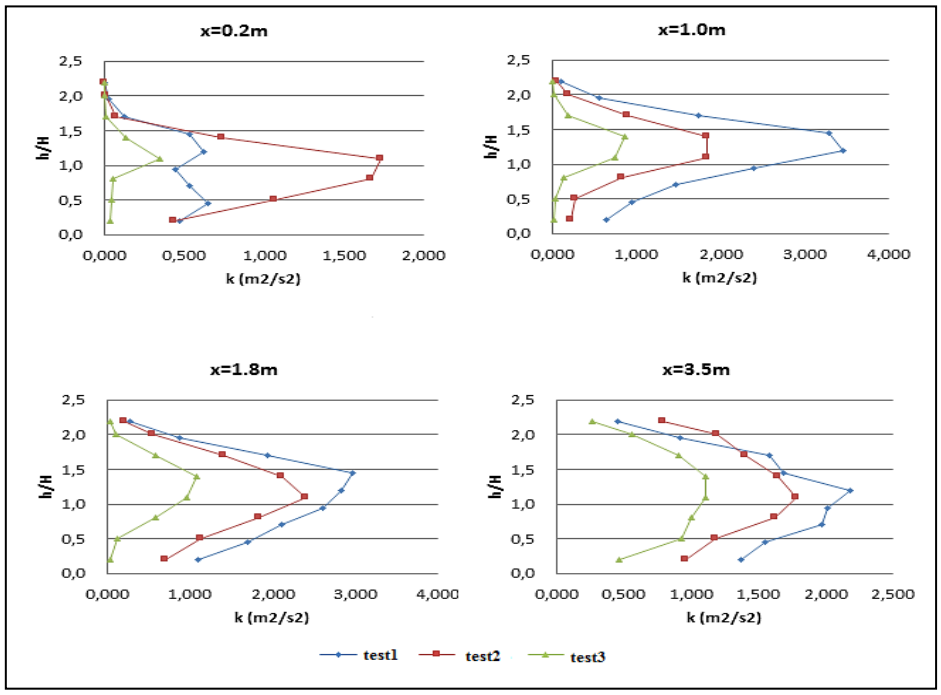

Figure 4-41: **The turbulent kinetic energy profiles at different x-positions for the case D study**

Overall, optimal fence design must optimize porosity of the fence based on understanding the structures of wind velocity and turbulence; neither the structure of flow velocity nor the turbulence field alone can provide sufficient information to the optimization.

4.3. EXPERIMENT FOR TWO-PHASE SNOWDRIFT FLOW

4.3.1. Experiment set-up

The experiment for two-phase snowdrift flow mainly focused on the investigation of the deposition of snow particles behind the fences at the freestream velocity of *8m/s*. The A,

B and F fences were selected with the aims to investigate the effects of fence height and porosity on particle transport. The movement of windblown snow particles were visualized and recorded by a high-speed camera during the tests. Before positioning the fences in the wind tunnel, the roughness of snow bed and the threshold wind velocity for snow particles were investigated.

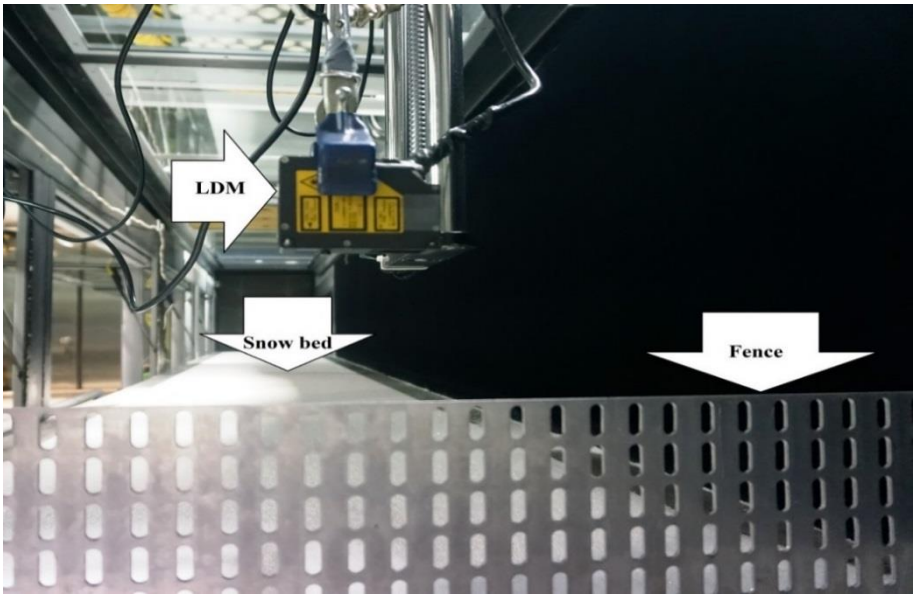

Figure 4-42: The experiment set-up

As the applied fences are not typical snow fences but are typical wind fences, the fences were placed in the snow bed with no bottom gap (a space between the snow bed and the bottom of the fence). This application differs for snow fences. Tabler (2003) suggested in his report that the optimum bottom gap of *10-15%* of the total fence height minimizes snow deposition close to the fence and easily traps the saltating particles near the ground.

The experiment set-up shows in Figure 4-42. The fence was placed at the distance of 6.75m away from the leading edge of the test section without a bottom gap to the snow bed. The LDM was attached to a movable traverse and maintained the position of *300mm* over the undisturbed snow bed.

The experimental procedures are presented as follows:

1) Preparation of low temperature environment for the wind tunnel: The cold room took *12* hours to cool down the experiment-required temperature of *-7°C*, where the wind tunnel is located.
2) Preparation of snow particles: The testing snow was local natural snow collected in the wintry season and was stored in a cold chamber at the temperature of *-7°C*. The experimental snow used a grinding machine to break it into particles. The snow was selected by applying a screener to ensure the equivalent diameter of snow particles equal to or below *2mm*. The density of these particles was checked by weighing *100* cubic centimetres of the snow particles. In this experiment, the density of these snow particles $\rho = 50.6g/100cm^3$ =506 kg/m^3.
3) Preparation of snow bed: The wind tunnel is designed to have a space of *14m* (length) * *0.77m* (width) * *0.05m* (depth) in its floor. The snow bed was formed to fill those selected snow particles into the space. To avoid loose snow particles in the snow bed, the snow bed was sintered by sprinkling water on the surface. After *15* minutes, running the wind tunnel at the freestream velocity of *8m/s*, the snow bed must be ensured no moveable snow particles on its surface. Otherwise, it would affect the accuracy for the late experiment.
4) Measurement of wind velocity profile and the roughness of snow bed: After the completion of snow bed, airflow with fence free were checked by a Pitot static tube manometer at the same procedure as the ones applied on the single airflow. Since it is not possible to make the snow bed completely even, the LDM measured the roughness of snow bed along the measuring lines and the data were recorded.
5) Preparation of the saturated snowdrift just above the snow bed: The assurance of a saturated snowdrift just above the snow bed is important to simulate saltating snow particles in the experiment, which can be accomplished by a snow-feeding machine supplying snow particles at the entrance of the test section. The screened snow particles were supplied from a snow supply tank to the snow-feeding machine. In the experiment, the Aeolian snow was supplied at a rate of *10%*, which corresponds to *0.355 g/cm/s*.
6) Measurement of threshold wind velocity: Threshold wind velocity is defined as the velocity at which snow particles start to move from the ground. In the

experiment, Aeolian snow was supplied at a rate of *10%* by the snow-feeding machine, and the fence was not in place in the wind tunnel. Carefully increasing inlet velocity with a fine step, the threshold wind velocity could be identified by careful observation at the point where the snow particles start to move. The threshold wind velocity was obtained from the averaged five testing data by repeating the same test at five times.

7) Measurement of the distribution of snow deposition: The distribution of snow deposition leeward of the testing fence was investigated combined with visual technique and measurement of snow depths. The transient movement of snowdrifts was visualized and recorded the images by a high-speed video camera. The depth of snow deposition was measured by the LDM. The first measurement point was *10mm* away from the fence, and then the measurement points took a step of *50mm* afterwards. At a time interval of *10*minutes, the wind tunnel stopped running and the depth of snow deposition was measured at each designated measurement point, then running the wind tunnel again. This procedure was repeated until it reached at a quasi-equilibrium snowdrift state. At equilibrium state, the combined wind resistance of the fence and snowdrift is at a minimum, the snowdrift is shaped so that the surface shear stress is uniform along the path of the air, and porous fence forms the deposited snow particles in an aerofoil shape leeward. The definition of the equilibrium snowdrift state is that snowdrifts are always streamlined and cease to grow. However, not all of snow particles are streamlined when the wind tunnel was projected by a porous fence. A completely equilibrium snowdrift state is therefore impossible to be achieved in the present experiments, However, a quasi-equilibrium snowdrift state can be achieved with the benefit of repeated measurements to verify that growth of deposition were stopped. In the experiment, the quasi-equilibrium snowdrift state was estimated at the time when an aerofoil-shaped snow deposition behind the fence was formed, and the crest of deposited snow almost ceased to grow (monitoring its position and height).

The snow bed, wind velocity profile and the roughness of snow bed must be checked again before carrying out another test.

4.3.2. Investigation of the parameters before the fence in place

Before the testing fence is in place, an undisturbed snow bed must be ensured, and the equivalent diameter and the density of the applied snow particles must be investigated. Apart from these, the following parameters must be investigated:

- Roughness of snow bed
- Wind velocity profile and thickness of boundary layer δ
- Aerodynamic roughness length z_0 and friction wind velocity u_*
- Threshold wind velocity u_t and threshold friction velocity u_{*t} for snow particles

The roughness of the snow bed was measured by the LDM at the designed measurement points. The data for each case are in Appendix D.

For the investigation of the wind velocity profile and the thickness of boundary layer at the fence position, the experimental procedure was the same as the one for the single-phase flow. At the freestream velocity of *8m/s*, the thickness of boundary δ was *0.128*. The wind velocity profile within the boundary layer was well fitted to a power regression as the following:

$$u_h = U_{free}\left(\frac{h}{\delta}\right)^{\alpha} = 8\left(\frac{h}{0.128}\right)^{0.121} \quad \textbf{Eqn.4-14}$$

Substituting a wind velocity, its corresponding height and z_0 into the logarithmic-law wind velocity equation, the friction wind velocity u_* was calculated as *0.30m/s*.

Based on the above calculations, the wind velocity profile within the thickness of boundary layer expressed in a logarithmic-law equation is written as the following:

$$u_h = \frac{u_*}{k} ln \frac{h}{z_0} = \frac{0.30}{0.41} ln \frac{h}{3.34*10^{-6}} \quad \textbf{Eqn.4-15}$$

where k is the von Karman's universal constant of *0.41*.

The threshold wind velocity u_t was experimented and was *6.4m/s* at which snow particle started to move. Under this velocity condition, revisited the testing domain, the wind

velocity profile and the thickness of boundary layer δ were obtained. The wind velocity profile within the boundary layer expressed as a power-law equation is the following:

$$u_h = U_{free}\left(\frac{h}{\delta}\right)^{\alpha} = 6.4\left(\frac{h}{0.131}\right)^{0.12} \quad \textbf{Eqn.4-16}$$

Table 4-9: The summary of the key parameters of the initial experiment

Parameter	Nomenclature	Value
Freestream velocity (m/s)	U_{free}	8.0
Thickness of boundary layer (m)	δ	0.128
Power exponent	α	0.121
Aerodynamic roughness length (m)	z_0	$3.34e-6$
Friction wind velocity (m/s)	u_*	0.30
Threshold wind velocity (m/s)	u_t	6.40
Threshold friction wind velocity(m/s)	u_{*t}	0.24
Von Karman's constant	k	0.41

Calculated based on the logarithmic-law velocity equation, the aerodynamic roughness length z_0 is $3.59 * 10^{-6} mm$, and the threshold friction velocity u_{*t} is *0.24m/s*.

The wind velocity profile within the thickness of boundary layer expressed in a logarithmic-law equation is the following:

$$u_h = \frac{u_{*t}}{k}\ln\frac{h}{z_0} = \frac{0.24}{0.41}\ln\frac{h}{3.59*10^{-6}} \quad \textbf{Eqn.4-17}$$

A summary of the key parameters of the initial experiment is listed in Table 4-9.

It can be observed that the aerodynamic roughness length is rather small. The artificial snow bed affected the boundary conditions as it is close to the iced snow ground.

4.3.3. Visualization

Visualization was performed during each test. Both of photos and videos were recorded. It provided general information on the movement of snow particles and the development of snow deposition.

It took *30minutes* to reach a quasi-equilibrium snowdrift state for the A and F fence, and *60minutes* for the B fence. It appeared that reducing fence height resulted in less time to reach a quasi-equilibrium snowdrift state. The development of snow deposition behind the A fence were shown in Figures from 4-43 to 4-45. Figure 4-43 is the test at the first 10minutes. Snow particles were accelerated over the fence. Populated snow particles appeared just above the snow bed. These particles moved in a way of creeping or saltation and played significant parts to form snow deposition. Increasing the measuring height from the snow bed, snow particles were less populated and moved in a mode of saltation or suspension. This feature can be found in Figure 4-44, which was at *20 minutes*. Figure 4-45 is the picture taken at *30minute*s, which was regarded as the stage of the quasi-equilibrium snowdrift state, where snow particles drifted approximately following the streamlines, and were the least populated. In the regions just above or far away from the snow bed, the presence of snow particles was far to significance. The reason is that equilibrium snowdrift forms surface shear stress uniformed along the path of the air, and fence has the minimum resistance on snowdrifts, that results the minimum influence in Aeolian erosions.

The development of snow deposition around the fence can be categorized into three stages during the visualization:

- Initial stage shown in Figure 4-43: The presence of creeping and saltating snow particles were clearly visible and suspending snow particles could be observed too. Snow deposited in both sides of the fence. Behind the fence, a concave like a horseshoe started in shape. Circulating snow particles could be observed.
- Developing stage shown in Figure 4-44: Three modes of snow transport (creeping, saltation and suspension) were visible. A crest of snow deposition appeared and was growing. The horseshoe concave reduced in size and grew in

depth. The zone for circulating snow particles extended in the longitudinal direction.

- Equilibrium stage shown in Figure 4-45: It was hard to observe creeping and suspending snow particles. Snow particles appeared to drift in the downwind direction. Circulating particles were diminished. The deposited snow was shaped like an aerofoil and ceased growing.

Figure 4-43: Snow deposition behind the A fence during the first 10 minutes test

Figure 4-44: Snow deposition behind the A fence during the second 10 minutes test

Figure 4-45: Snow deposition behind the A fence during the third minutes test

The shape of snow deposition at the quasi-equilibrium snowdrift state for each test is presented in Figures from 4-46 to 4-48.

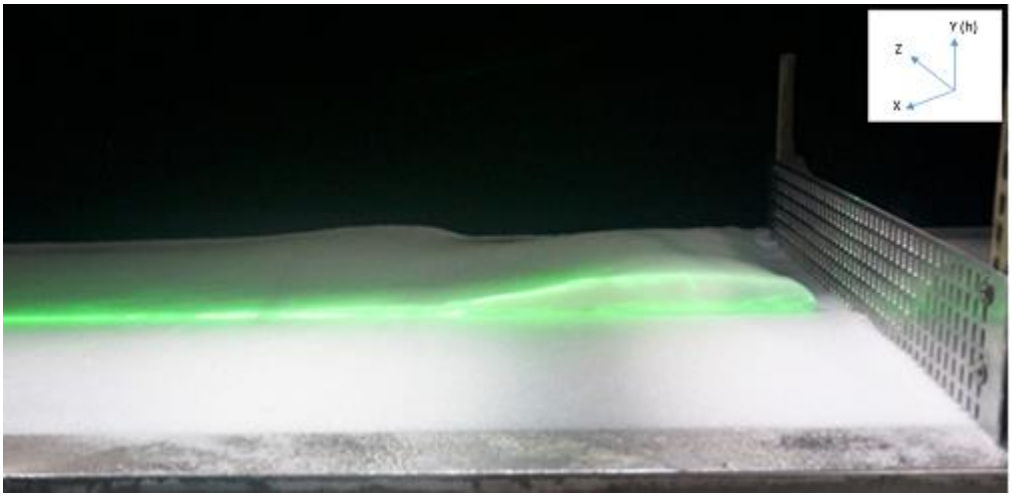

Figure 4-46: Shape of snow deposition at the quasi-equilibrium state around the A fence

The effect of fence height was investigated on the A and B fences seen in Figures 4-46 & 47. They have the same configuration except the fence height. The B fence is *50mm* higher than the A fence. The B fence has trapped more snow particles than the A fence did, and its crest of snow deposition was higher but was closer to the fence. The concave formed by the B fence was not in a horseshoe shape like the one by the A fence, and the shape of snow deposition appeared not so close to an aerofoil shape. The reason might be

that the quasi-equilibrium state was more difficult to be developed for the case of testing the A fence.

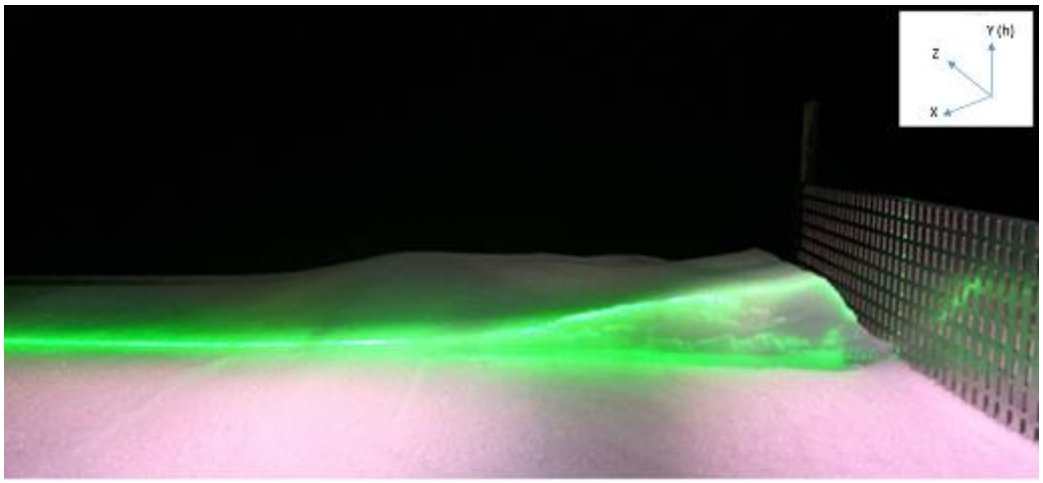

Figure 4-47: Shape of snow deposition at the quasi-equilibrium state around the B fence

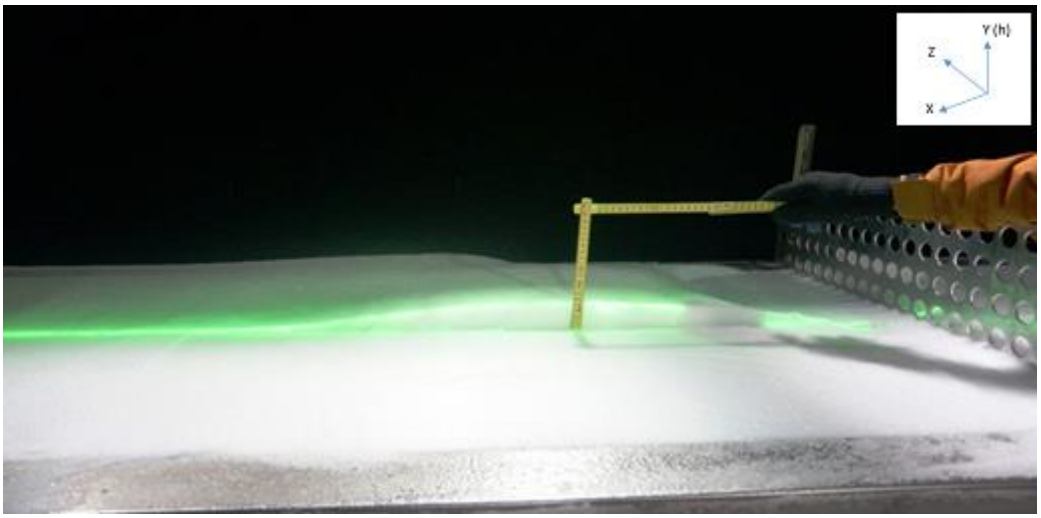

Figure 4-48: Shape of snow deposition at the quasi-equilibrium state around the F fence

The effect of fence porosity was investigated on the A and F fences shown in Figures 4-46 &4-48. Both of them have the same size but different porosities. The A fence has a porosity of *0.27*, and the F fence has a porosity of *0.35*. They all formed an aerofoil shape and a horseshoe shaped concave for deposited snow downwind. Compared with the F fence, the A fence trapped a relatively higher amount snow but in a shorter longitudinal distance from the fence position.

The visualization provided useful information with regard of the transient development of snow deposition and the movement of snowdrifts. It reveals that fence height and fence porosity have significant influence on the performance of the fences.

4.3.4. Investigation of fence performance by trapped snow

The development of snow deposition leeward of the testing fences presents in the Appendix D. The snow depths downwind were measured at a time interval of running the wind tunnel in*10minutes* until snowdrifts reached at a quasi-equilibrium state. App-Fig.19 is the development of snow deposition behind the A fence, App-Fig.20 for the B fence, and App-Fig.21 for the F fence.

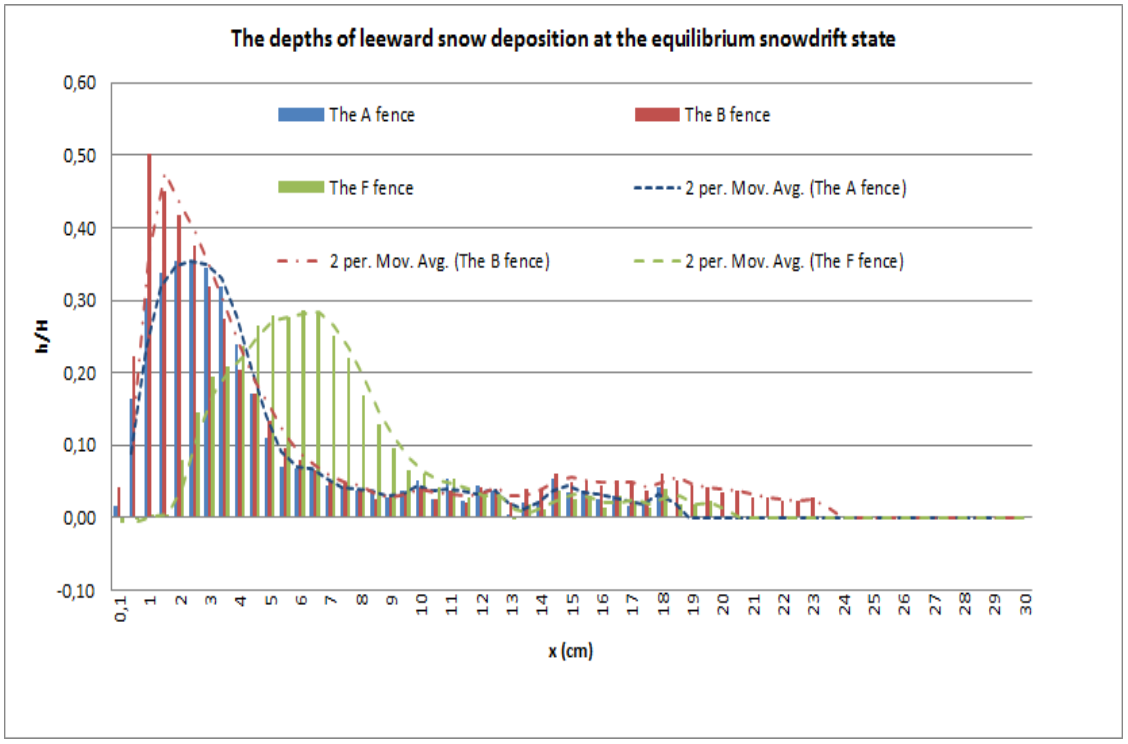

Figure 4-49: The leeward distribution of snow deposition at the quasi-equilibrium snowdrift state

At the state of quasi-equilibrium snowdrift, the distribution of snow depths along the central line for each testing fence is shown in Figure 4-49. The snow depths were adjusted with the consideration of the roughness of initial snow bed. The dash lines were formatted by two periods moving average regression. The axis Y was expressed as a ratio of the measuring height and the corresponding fence height.

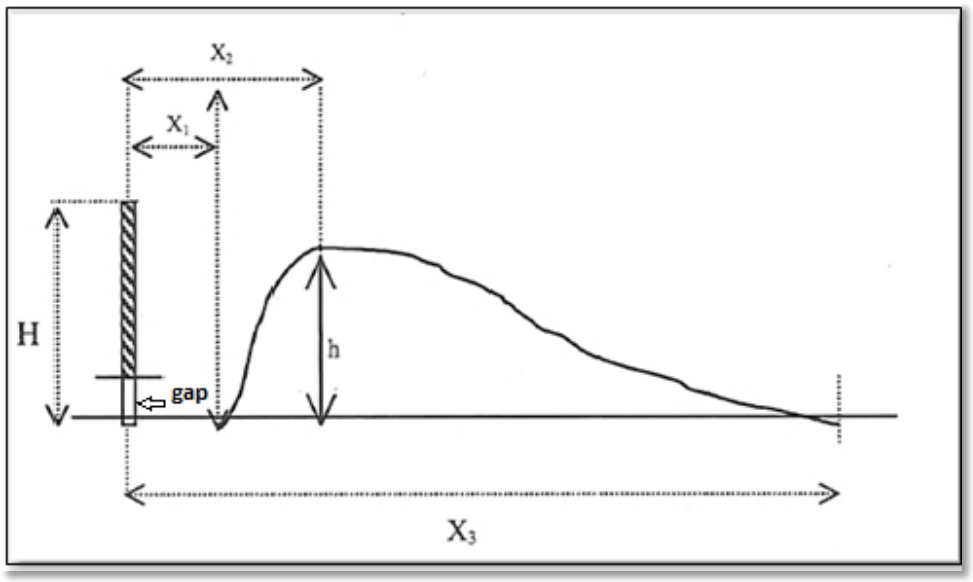

Figure 4-50: The parameters used to describe the shape of leeward snow deposition

Table 4-10: Physical parameters of the fence models and experimental results

Fence type	H (m)	β	$h_{b/H}$	h/H	X_1/H	X_2/H	X_3/H	A_d/H^2
A	0.15	0.27	0.00	0.35	0.06	1.70	12.33	0.18
B	0.20	0.27	0.00	0.50	0.05	1.70	11.80	0.16
F	0.15	0.35	0.00	0.29	1.30	4.00	13.50	0.19
Wyoming	3.80	0.50	0.15	1.20	0.00	6.00	34.00	21.50
Russian	0.10	0.66	0.05	0.27	2.61	6.56	17.16	N/A
Canadian	0.09	0.50	0.11	0.65	4.64	10.20	21.91	N/A
Japanese	0.18	0.16	0.20	0.69	2.40	3.32	10.16	N/A
Norwegian	0.10	0.30	0.10	0.89	1.24	4.07	14.84	N/A

The shape of snow deposition at equilibrium snowdrift state is important to evaluate the performance of the fence. It commonly takes the variables shown in Figure 4-50 to describe a cross-sectional shape of snow deposition. Apart from these, the area of cross-

sectional snow deposition A_d is used to evaluate the trap efficiency of the fence. The ratio of A_d/H^2 is commonly used to evaluate the trap efficiency of snow fences by many researchers (Tabler, 2003) (Liston & Sturm, 1998).

The detailed description variables are summarized in Table 4-10. X_1,X_2 , X_3 , h and the bottom gap h_b are all expressed as a ratio of the correlated fence height, and A_d is expresses as a ratio of H^2. β is the porosity of fence. Table 4-10 also includes the other researcher's work. The data of the Wyoming fence was obtained from the field experimental work (Tabler, 2003). The data, those of the Russian, Canadian, Japanese and Norwegian fence model, were experimented by other researchers in the same wind tunnel at Shinjo Cyrospheric Environment Laboratory, Japan (Gurer, et al., 2002).

The discussions are as follows:

1) From Figure 4-49, it is evident that the B fence created the largest physical area of deposited snow than the A and B fences did. However, if evaluated byA_d/H^2**,** the F fence was the best performer. It appeared that increasing porosity would elongate the length of deposition distance and reduce height of crest of deposited snow, and improved the trap efficiency of the fence. This founding was generally similar to the work done by other researchers in the same wind tunnel (experiments on the Russian, Canadian, Japanese and Norwegian fences). Fence with porosity in the range from *0.35* to *0.50* seemed more effective, above or below which the effectiveness of fence is to be compromised (Russian and Japanese fences).
2) In the experiments, increasing fence height appeared to increase the height of crest of deposited snow. However, the experimental results provided by Gurer, et al.(2002) did not prove it. Tabler believed that fence height is an important factor in snow fence design, and suggested that dimensions of snowdrifts are approximately proportional to fence height (Tabler, 2003). The proportion of fence height of the B fence to the A fence was *1.33*. The proportion of the deposited length of the B fence to the one of the A fence was *1.28*, which was close to the proportion of *1.33*. The proportion of the snow crest height from the B fence to the A fence was *1.90*, which is not close to *1.33*. Nevertheless,

the experimental results supported Tabler's finding that increasing fence height results in the increase of the size of snow deposition.

3) Table 4-10 shows that there is a big difference between field measurement and wind tunnel experiment. The ratio of h/H can hardly achieve to reach or exceed 1.0 in wind tunnel experiments (Gurer, et al., 2002) (Thordarson, 2002) (Sakamoto, et al., 2001), and so does A_d/H. Not like the behaviour of windblown snow deposited in natural environments, deposition of snow in wind tunnels is built up rather quick. Wind tunnel simulations of snow drifting resulted in marginal discrepancy with those correlative field measurement that have been recognized by the researchers. The most obvious difficulty is to scale a natural snow concentration profile in air down to the one in wind tunnel environment. White (1996) listed 15 criteria to satisfy the similarity requirements between natural snowdrift and wind tunnel snowdrift, which no one has done the job so far. It may say that wind tunnel simulations of snowdrift are indicative rather than verdicts.
4) The experiment placed the fences on the ground without the bottom gaps, as they were typical wind protection fences rather than snow fences. This is a different feature from the other wind tunnel experiments. For the design of snow fences, the bottom gap is usually required, since it can minimizes snow deposition close to the fence, and keeps saltating snow particles near ground where they can be more easily trapped. The result shows that snow deposited more closely to the fence than it did to the fences with bottom gaps seen in Table 4-10.
5) The depositions of snow shown in Figure 4-49 did not formed an aerofoil shape leeward, particularly for the B fence. These shape of snow deposition indicated that the equilibrium snowdrift state has not achieved at this stage. The experiments have found that identification of a quasi-equilibrium snowdrift state was not easy. The experiment also found that increasing blockage ratio led the difficulty to achieve equilibrium-snowdrift state insider the wind tunnel. The longest of testing time for the fence B and the best shape to close an aerofoil for

the fence F have indicated the effect of blockage to the snowdrift. Therefore, blockage must be justified.

The experiment found the limitations of experiment snowdrift under the wind tunnel environment. The design of snow fence is different from the design of wind fence. Nevertheless, porosity and fence height have significant influence on the performance for both wind fences and snow fences. It also can be found that purely increasing fence height is not an economic and efficient way for fence design. Optimum fence porosity is a positive way to achieve fence efficiency at a minimum cost. Undoubtedly, fence porosity is still the most important structural factor in snow fence designs.

4.4. EXPERIMENT UNCERTAINTY

Uncertainty in the experiment lies on two types of errors. One is precision error and another is accuracy error. Precision error is associated with the random error distribution associated with a particular experiment or even with a particular type of experiment. Accuracy error is the existence of systematic error associated with a flaw in the equipment or in the design of the experiment (Pugh & Winslow , 1966).

Errors of precision are probabilistic, which means that the actual value of some parameters is probably within a specified range. These errors can be reliably estimated by repeating measurements and usually quantified using the standard deviation formula or a *2/3* rule in a histogram (the famous Gaussian or bell-shaped curve). Errors of accuracy cannot be estimated by repeating the experiment with the same equipment. Unlike errors of precision, they shift the results in one direction. It is much harder to estimate errors of accuracy than errors of precision. A good experiment should minimize the errors of accuracy as possible as it can.

For wind velocity, turbulent intensity, turbulent kinetic energy and depth of deposited snow, data in the experiment were processed with the interest of two digits after the decimal. For the measurement position, the minimum reading was *1mm* due to the limitation of the traverse‘s movement.

4.4.1. Accuracy errors on the experiment design

The dominant errors associated with the experiment design are identified as follows:

- Intrusive measurement to disturb flow regime
- Difficulty in creating equilibrium snowdrift state

In the experiment, the Pitot static tube manometer was employed to investigate approaching wind velocity profiles and thickness of boundary layer, and the ultrasonic anemometer was used to investigate flow structures behind the testing fences. Both of these instruments were attached to the traverse in a domain, and their detect heads were kept as far away from the traverser as possible. However, it inevitably disturbed the flow regime that introduced errors in the experiment. Justification of such errors should employ more sensitive measurement instruments or apply non-intrusive measurement techniques.

It is not possible to achieve a complete equilibrium snowdrift state in the experiment as not all of snow particles are streamlined in the wind tunnel. Such a difficulty introduced errors in the identification of the comparing cases for the two-phase snowdrift experiments.

Justification of these errors is not included in this thesis.

4.4.2. Precision errors on the experimental operation

These errors are mainly associated with the wind tunnel, measurement instruments. The wind tunnel was examined by the investigations of approaching wind velocity profiles discussed in Section 4.2.2, which the wind tunnel had demonstrated its competence in developing wall bounded fully turbulent atmospheric flows. Measure instruments in this experiment were digitalized outputs with fine resolutions, which minimized reading errors caused by the operators. The possible error involved with the operators was the angle position for the UA, which must ascertain the detect head in a degree of $\pm 5°$ with the direction of main flow (x-direction). It was achieved during the experiment. Another possible error involved with the operators was the identification of equilibrium snowdrift state (a term of quasi-equilibrium snowdrift state is precise here). Such error has been reduced by repeating tests but could not be eliminated.

4.4.3. Accuracy errors on the experimental data

The dominant error is associated with the accuracy of the measurement equipment to velocity variables. The Pitot static tube manometer and the ultrasonic anemometer were employed to measure wind velocities during the tests. Both of them have an accuracy of *1%*. Wind velocities were measured both by the Pitot manometer and by the ultrasonic anemometer during running the wind tunnel with absence of the fences. The difference between them was in the range of *2.0%*. It is not a calibration but is worth to take a note.

In the experiment, velocity vector was measured by the ultrasonic anemometer and was independent from each other. It is already that the relative error σ for the instrument itself is *1%*. Therefore, the x-axial direction velocity vector u_i can be stated as:

$$u_i = u_i(1 \pm \sigma) = u_i\,(1 \pm 1\%) \qquad \textbf{Eqn.4-18}$$

Mean-squared deviation of the axial-x direction velocity vector $\overline{u'}$ can be stated:

$$\overline{u'^2} = \frac{1}{N-1}\sum_i^N(\bar{u} - u_i)^2\,(1 \pm 2\sigma)^2 = \frac{N(1\pm 4\sigma)}{N-1}\sum_i^N(\bar{u} - u_i)^2 = \overline{u'^2}\,(\,1 \pm \frac{4N\sigma}{N-1}) \qquad \textbf{Eqn.4-19}$$

where *N* is the total measuring times.

The above statements are applicable to the velocity vector v_i and $\overline{v'^2}$ in the y-direction and the velocity vector w_i and$\overline{w'^2}$ in the z-direction.

Substitute these velocity vectors into Eqn.4-6, error on turbulent kinetic energy can be calculated as:

$$k = \frac{1}{2}\left(\overline{u'^2} + \overline{v'^2} + \overline{w'^2}\right) = \frac{1}{2}\left(1 \pm \frac{12N\sigma}{N-1}\right)\left(\overline{u'^2} + \overline{v'^2} + \overline{w'^2}\right) = \left(1 \pm \frac{6N\sigma}{N-1}\right)k \qquad \textbf{Eqn.4-20}$$

Substitute Eqn.4-20 into Eqn.4-12, error on turbulence intensity can be figured out as well:

$$T_i = \sqrt{\frac{2}{3}\left(1 \pm \frac{6N\sigma}{N-1}\right)k} \Big/ U_m(1 \pm 3\sigma) = T_i\left[1 \pm \left(3\sigma \pm \frac{N\sigma}{N-1} + \frac{6N\sigma^2}{N-1}\right)\right]$$

Eqn.4-21

In the experiment, *N* is times of *1000*. As such, $\frac{N}{N-1}$ is close to *1*. Based on Eqns.4-20&21, the relative errors of k and T_i introduced by the UA itself can be calculated as follows:

$$\sigma_k = \pm\frac{6N\sigma}{N-1} \approx \pm 6 * 1\% = \pm 6\%$$

and

$$\sigma_{Ti} = \pm\left(3\sigma + \frac{N\sigma}{N-1} + \frac{6N\sigma^2}{N-1}\right) \approx \pm[3 * 1\% + 1\% + 6 * (1\%)^2]$$
$$\approx \pm 4\%$$

The above discussions reveal: for a given velocity measurement instrument, it will introduce four times of error of accuracy on turbulence intensity, and six times of error of accuracy on turbulent kinetic energy.

The experiment uncertainty has been discussed and analysed in this section. Justification of accuracy errors on the experimental design is the future research work, when the more advanced experimental facilities are available. Overall, the experimental results have qualitatively provided the analytical data to study the performance of porous fences. Errors in this experiment were in the tolerable range.

4.5. DISCUSSIONS

Various tests were performed in the experiment. The key factors influencing the performance of porous fences have been investigated. The discussions are presented as follows:

1) The investigation of structure of velocity and turbulence behind porous fences has been performed in the experiment. The longitudinal velocity component u that follows the main flow direction plays the dominant part in determining the

structure of velocity. The other two directional velocity components v and w only have noticeable presences in a certain region near the fence. The $w$component is the most insignificant one among the others, which may ignore its influence for the airflow around porous fence study. Turbulence was obtained based on the fluctuations of velocity components. Accordingly, strong turbulence was presented in the areas where strong fluctuations of velocity components occurred. The testing porous fences effectively reduced wind velocity and created turbulence in a certain region downwind. It is found that using *3*-order polynomial equation is well to describe the velocity magnitude, *4*-order polynomial equation for the turbulent kinetic energy, and at least *5*-order polynomial equation for the turbulence intensity.

2) The experiment has found that different approaching wind velocities have insignificant impact on porous fence performance.
3) Height of fence has significant impact on the structure of airflow behind fences. Increasing height of fence results more reduction in wind velocities and intensifies turbulence leeward the fence. Effective fence zone was examined two approaches: physical size based and normalized by fence height H based. It has been found that purely increasing height of fence is not an efficient and economic option.
4) Porosity has significant influence on fence performance in many aspects, i.e. reduction of velocity, production of turbulence, shelter distance, Aeolian erosion, visibility and ventilation. An optimal porosity design can achieve a good reduction on wind velocity with longer effective shelter distance at minimum cost.
5) For windblown snowdrifts around porous fences. Height of fence and porosity have significant impacts on the performance of snow fences. Such significance can be found from the present wind tunnel experiments and the field observations by other researchers. However, the size of snow deposition obtained from the wind tunnel experiments seems under-predicted. The reasons are the difficulties in satisfying similarity criteria and forming an equilibrium snowdrift state insider the wind tunnel.The wind tunnel experiments have revealed that the fence with porosity of *0.45* has greater trap efficiency than the others, which is close to the optimum porosity of *0.50* suggested by Tabler (2003).

Chapter 5 NUMERICAL STUDY FOR SINGLE PHASE AIRFLOW

Application of CFD technique in the porous fence research is extensive and the literature is rich. However, there remain various issues to be tackled in the future, particularly the difficulties in describing boundary conditions and weak sensitivity in simulating turbulence around porous fences. Therefore, physical experiments are indispensable. CFD simulation should demonstrate the assessment of numerical and physical modelling errors.

In the early stage, 2D CFD modelling was dominant in the fence research field. Starting from the late 1990s, 3D CFD modelling becomes a favorable modelling, due to the benefit of rapid development of computing and CFD techniques. The evident reason is that 3D CFD modelling can provide a comprehensive structure of airflow around porous fences within a calculation domain if the numerical model is sound, which will compensate the difficulty of providing a whole-flow field data for physical experimentation and 2D CFD modelling.

Both of 2D and 3D modelling have been conducted in the research work. Great attention has been paid on the 3D modelling. The followings are discussed and included in the chapter:

- Numerical model establishment, boundary condition considerations to the corresponding experiments, wall treatment, mesh sensitivity analysis, discretization schemes and convergence criteria;
- Assessment of numerical and physical modelling errors along with the justification of turbulence model selection;
- Demonstrations numerical post process on obtaining analytical and visual data within the entire domain;
- Effects of the arrangement of shape of porous holes on fence performance;
- Effects of non-normal wind loads on fence performance;
- Effect of fence surface shear and assessment on fence effective zone.

5.1. GEOMETRIC CFD MODEL TO THE CORRESPONDING EXPERIMENT

The geometric CFD model to the corresponding wind tunnel experiment was created by the following configurations:

- The configuration of the CFD domain was identical to the full span of the test section of the environment wind tunnel at Shinjo Cryospheric Environment Laboratory in Japan. Therefore, the size of the numerical domain for 2D model was *14m* long and *1m* high. For 3D model, it was *14m* long, *1m* wide and *1m* high.
- In the 2D model, the numerical fence model was treated as a porous jump discussed in Section 5.5.1. In the 3D model, the configuration of the numerical fence model was identical to the testing A fence, which was *0.75m* wide, *0.15m* high and *0.003m* thick, so did to the arrangement of porosity (same size, shape and distribution of holes). The area of single hole was $1.3e-06m^2$. The blockage of wind tunnel was *8.3%*. As the aspect ratio of fence thickness and fence height was *0.02*, the fence could be considered as a thin fence. The fence was allocated at the distance of *6.75m* from the leading edge of the test section, and was centered in the cross test section. This arrangement was the same as the one in the experimental test.
- The Cartesian coordinate system was allocated at the fence position followed by the right hand rule as shown in Figure 5-1, where the X-axis is directed from upwind to downwind. For the convenience of the comparisons, the setting of the coordinate system kept consistent for the experiments, 2D models and 3D models.

The purpose of doing so is to assess the reliability and credibility of the numerical modelling by comparing the numerical results with experimental results.

The geometric CFD model was created in the ANSYS FLUENT v14.0 workbench. The workbench allows creating design parameters for dimensions that is convenient to create new geometric models only by assigning new values into the design parameters, which is applicable to a wide range of cases.

In order to create the domain to an airflow domain, the fence for 3D model was treated as one of boundary walls. It was manipulated as follows:

- Frozen the fence;
- Selecting the fence as a tool body and the test section as a target body and then using "Boolean" function to subtract the fence from the test section, an airflow domain was then created.

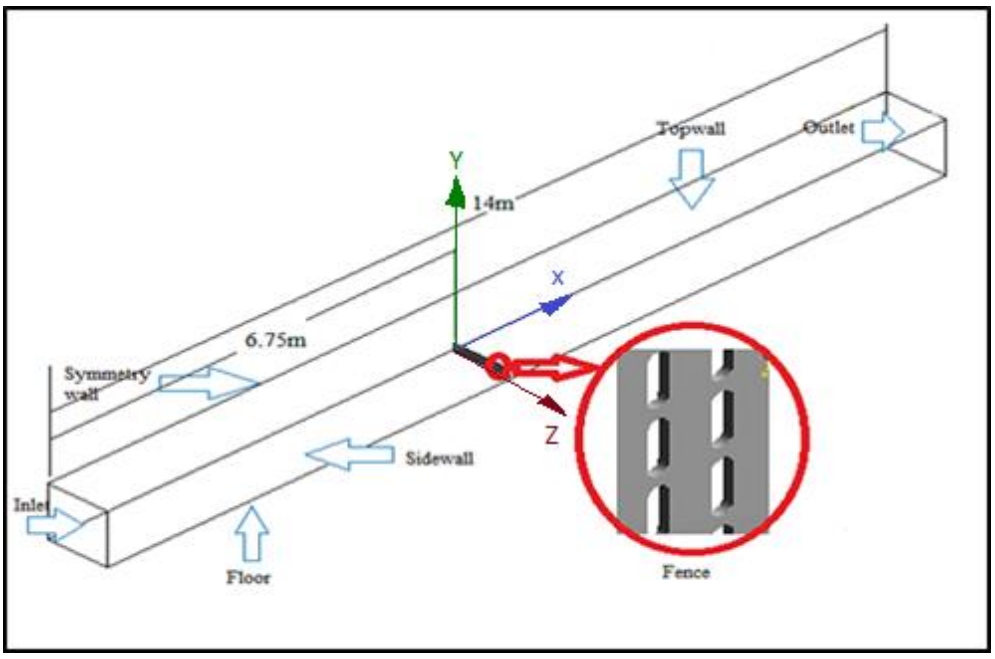

Figure 5-1: The geometric 3D numerical model

Figure 5-1 shows the created geometric 3D model. The numerical domain for 3D model was symmetrical to the XY-plane at *z=0m*. To save the future computing expense, the domain was reduced to half by applied "symmetry" tool in the workbench.

5.2. MODEL SENSITIVITY ANALYSIS

Model sensitivity analysis is important in numerical simulations. The values of model parameters, the computations, and the input values of variables are prone to many sources of numerical uncertainty. Therefore, the sensitivity of a model outputs to the perturbation in CFD simulations must be analyzed. Model sensitivity analysis may be performed on mathematical and computational models to determine the sensitivity of model outputs to

the uncertainty of input variables, computations, and parameter values (Campolongo & Braddock, 1999). By performing sensitivity analysis on an application, the insight of model stability is comprehended. If the results from the analysis are not stable, it needs to revise the designed computations.

There are generally two types of sensitivity analysis approaches:

- Mathematical sensitivity analysis: It is to compute partial derivatives of one or more outputs (called dependent variables) with respect to one or more inputs (called independent variables). Often it is expressed as system of equations, or commonly called as governing equations.
- Computational sensitivity analysis: It is calculated using numerical procedures based on computational approximations. Most of which use concepts of finite element methods in the calculation domain. Efficient computational model needs to be performed by recording the outputs at each calculating step to analyze the application. Often the numerical solutions need to be converged which is independent from the meshed elements. Solution convergence criteria and mesh independence study must be included in computational sensitivity analysis.

Except Detached Eddy Simulation (DES) and Large Eddy Simulation (LES), the governing equations for turbulent fluid flows in the CFD study are based on the Reynolds-Averaged- Navier-Stokes (RANS) equation, which describes time-averaged motion of fluid flow. The Reynolds averaged equation exhibits additional unknown variables (called Reynolds stresses), that need to be parameterized for the equation system to be closed and then solved. ANSYS FLUENT provides various turbulence models to address such closure problems on different applications. This sophisticated and powerful commercial available software has been widely accepted in the Wind Engineering industry (Blocken, 2014). As such, the model sensitivity analysis in this thesis focused on the discussions of turbulence model selection, convergence criteria and mesh independence.

5.2.1. Turbulence model selection

As discussed in Section 2.5.3, five RANS based two-equation turbulence models, named as the Standard k-ε, the RNG k-ε, the Realizable k-ε, and the Standard k-ω and the SST k-ω, are most applied and have been of great values in the research and industrial applications. Compared to the k-ε models, the k-ω models do not contain terms that are undefined at the wall in the equations, which can be integrated to the wall without using wall functions. Theoretically applying the k-ω models might result in better solutions for porous fence involved airflow study, as it is evident that such flows are often in the presence of flow rotation, separation, recirculation and strong adverse pressure gradients on the fence surface. In the fence research field, rich literature can be found for the CFD simulations with different k-ε models (Chen, et al., 2012) (Giannoulis, et al., 2010) (Santiago, et al., 2007) (Bourdin & Wilson, 2008). However, to the author's knowledge, it is few in the literature for the ones with different k-ω turbulence models.

As stated in ANSYS FLUENT Theory Guide (2009): "It is an unfortunate fact that no single turbulence model is universally accepted as being superior for all classes of problems. The choice of turbulence model will depend on considerations such as the physics encompassed in the flow, the established practice for a specific class of problem, the level of accuracy required, the available computational resources, and the amount of time available for the simulation." This fact is unfortunately true to the application of CFD techniques in the porous fence study. However, considerable research work has demonstrated that the two-equation based turbulence models have capabilities to achieve reasonable solutions, albeit no universal agreement on which of these turbulence models.

In this thesis, the above five turbulence models were assessed under the cases where the boundary conditions and computational procedures kept the same except the turbulence model. The assessment of turbulence model selection with respect to the present research will be discussed in the section 5.5.1. & 5.5.2.

5.2.2. Solution convergence criteria

The finite-volume method (FVM) is adapted in the present study, where volume integrals in a partial-differential-equation (PDE) that contains a divergence term. The numerical

solutions are calculated iteratively, since the turbulent flow poses highly nonlinear in nature. The solution convergence here was assessed by the following two criteria:

1) Scaled residual values

   Since the flow is steady and incompressible at low velocity, model of heat transfer is not considered in this thesis. The convergence of solutions was judged by the scaled residual values of continuity, three dimensional velocity components, *k* and epsilon. Additionally, the history of drag coefficient on the fence at longitudinal direction was monitored. The computations adapted single precision method with the segregated solver. Technically the residuals can drop as many as six orders of magnitude before hitting round off. In the practice, the convergence criteria of the scaled residuals was set below five orders except the scaled continuity residual below four orders. Additional iterations must be carried out if these scaled residuals reached the convergence criteria but the values were not steady. In the simulations, the calculation time to reach the convergence criteria increased in the sequence of the Standard *k*-ε, the Realizable *k*-ε, the Standard *k*-ω, the SST *k*-ω, and the RNG *k*-ε model. It implies that an appropriate turbulence model selection needs consider the computational cost.

2) Solution imbalances

   The present model will solve conservation equations within the computational domain, mass, momentum and energy must be conserved in the final solutions. As a numerical representation of a physical system, the CFD solution imbalance will never be exactly zero. However, the imbalances should be sufficiently small before considering the solution converged. In the present simulations, the mass flow rate at the velocity inlet and the pressure outlet has been examined, and the net mass rate was less than 10^{-4} *kg/s* for all of the cases, that can be considered that the solution imbalances reached convergence.

5.2.3. Mesh independence

A mesh that is too coarse may lead a numerical solution to reach the given convergence criteria, but may also result in truncation errors in CFD simulations. Mesh independence is that the numerical solution must be ensured to be independent of the mesh resolution. Any CFD simulation must conduct mesh independence before taking further actions. It is generally true that finer the computational mesh the smaller truncation errors in the numerical solution. However, an overly fine mesh will be costly in computational time and therefore is not necessary. An ideal mesh should be where a solution is just independent of it. A good quality of mesh should be efficient and economic which is as close to the ideal mesh as possible.

A successful mesh needs consider the selection of element type and mesh resolution. The presence of porous fence made the domain difficult to be constructed in structured grids. ANSYS FLUENT uses a cell-centered, segregated approach for solving on a collocated, unstructured grid. This feature is particularly suitable to solve flow problems in a 3D modelling without bearing excessive computational cost (minimizing quantity of elements to reduce computing time). In the present study, the region close to the wind tunnel floor was constructed by tetrahedron prism element and the rest by tetrahedron elements. Denser elements were constructed in the regions of near fence and floor. The detailed construction of mesh is presented as follows:

1) To ensure wall bounded fully developed turbulent atmospheric airflow in the domain, meshing with the first layer thickness of *0.1mm* was applied to the wind tunnel floor, and then inflated the layer to the maximum layers of *10* at the growth rate of *1.1*. Detailed boundary considerations will be discussed in Section 5.3.
2) In order to analyze the mesh independence, the Standard k-ε model with standard wall treatment was employed for the examination, where the boundary conditions and computational procedures remained in consistence.
3) The initial mesh guess: Using default mesh except changing the " Relevance Center" and "Smoothing" from "Coarse" to "Medium" in the "Sizing". This produced *0.38*million elements of the entire domain. The solution based on these elements was obtained.

4) The regions close to the wind tunnel floor and around the fence were of main concern in the simulation. In order to reduce the amount of element, Figure 5-2 shows the denser elements were created in the two dense element regions for 3D model. The configuration of the dense element region A was *14m* long, *1m* wide and *0.3m* high, and the configuration of the dense element region B was *1m* long, *1m* wide and *0.5m* high. The quality of meshed elements were changed by defining the sizes of elements in the two dense element regions and then influenced to the whole domain. This way made the mesh more effective and therefore reduced computational time considerably.

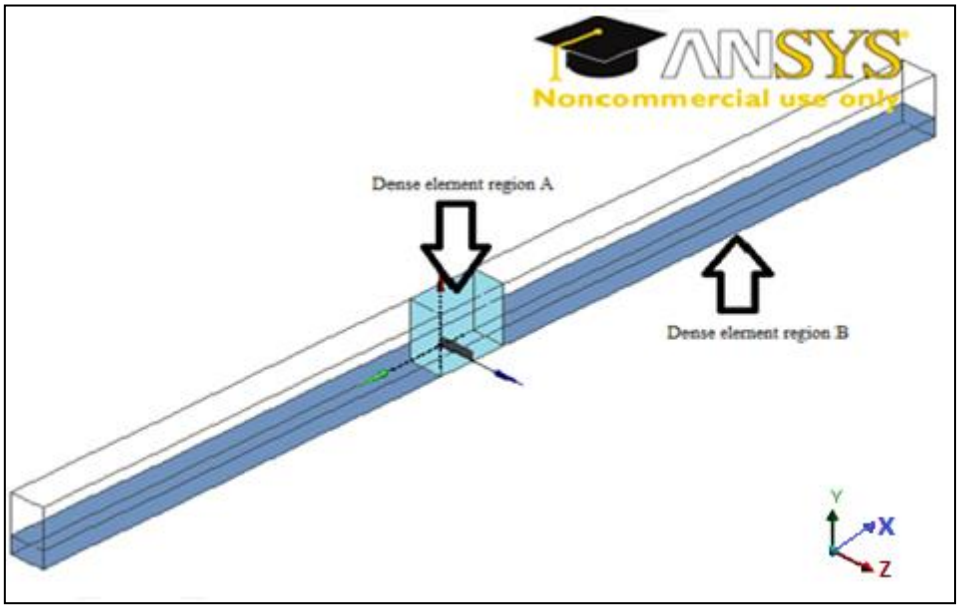

Figure 5-2: The dense element regions in the 3D domain

5) The second mesh guess: Increasing the quantity of meshed elements by a factor of *1.5*, the solution based on these elements was obtained, and then compared it with the one based on the initial guessed mesh. In the present work, the velocity magnitudes and turbulence intensity were selected as the comparing variables.
6) If the solution was quite different from the one based on the last mesh, increasing the quantity of meshed elements in the way as the step 5), until the solution was very close to the one based on the last mesh.

7) If the solution was very close to the one based on the last mesh, decreasing the quantity of meshed elements then compared two of the latest solutions.
8) Repeating the steps 6) and 7), the mesh independence in the present modelling was found.

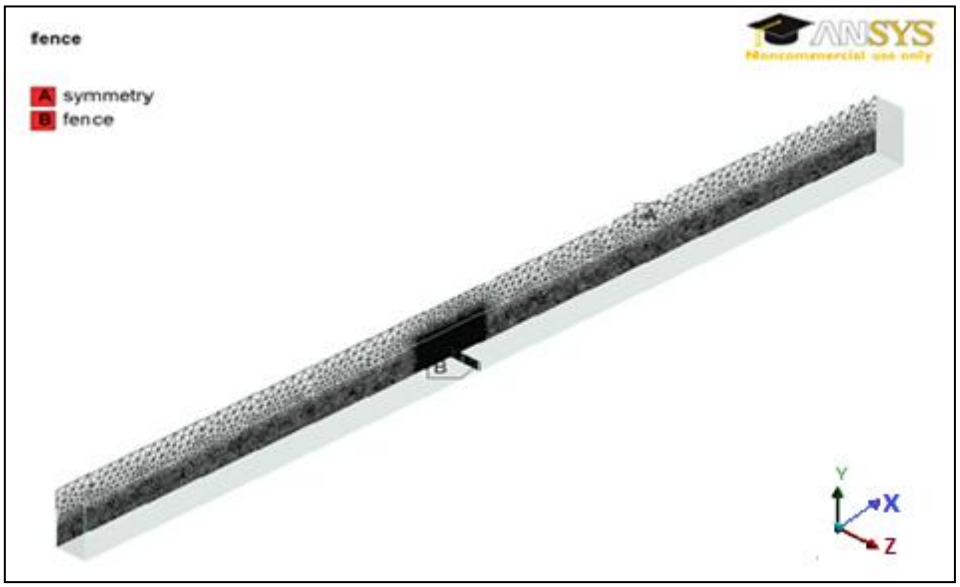

Figure 5-3: The distributions of mesh in the symmetry wall and the fence for the 3D model

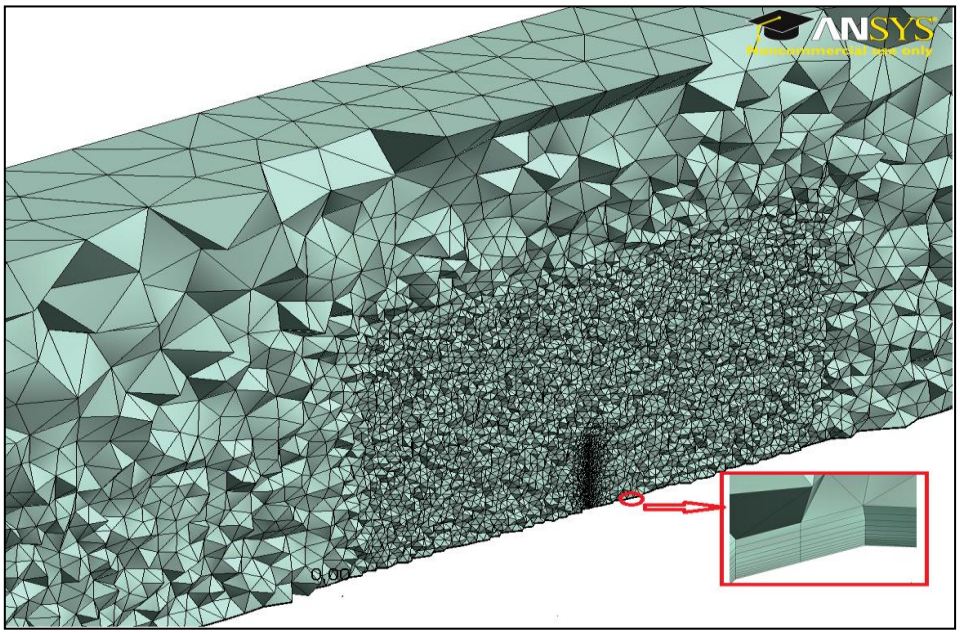

Figure 5-4: The detailed mesh in the near the fence and the floor for the 3D model

The identification of mesh independence was an extremely laborious task. The mesh with *1.5*million elements has made the solution independent from it in the present 3D modelling. The distributions of elements in the symmetry wall and the fence were shown in Figure 5-3, and the detailed mesh in the near the fence and the floor displayed in Figure 5-4.

Quadrilateral elements were applied in the entire domain in the 2D model shown in Figure 5-5. Since the fence was not physically modeled, the denser elements were arranged in the region close to the floor by applied the height of the first layer of 1mm with the bias factor of 1.2. The mesh with *0.28*million elements has reached the grid independence.

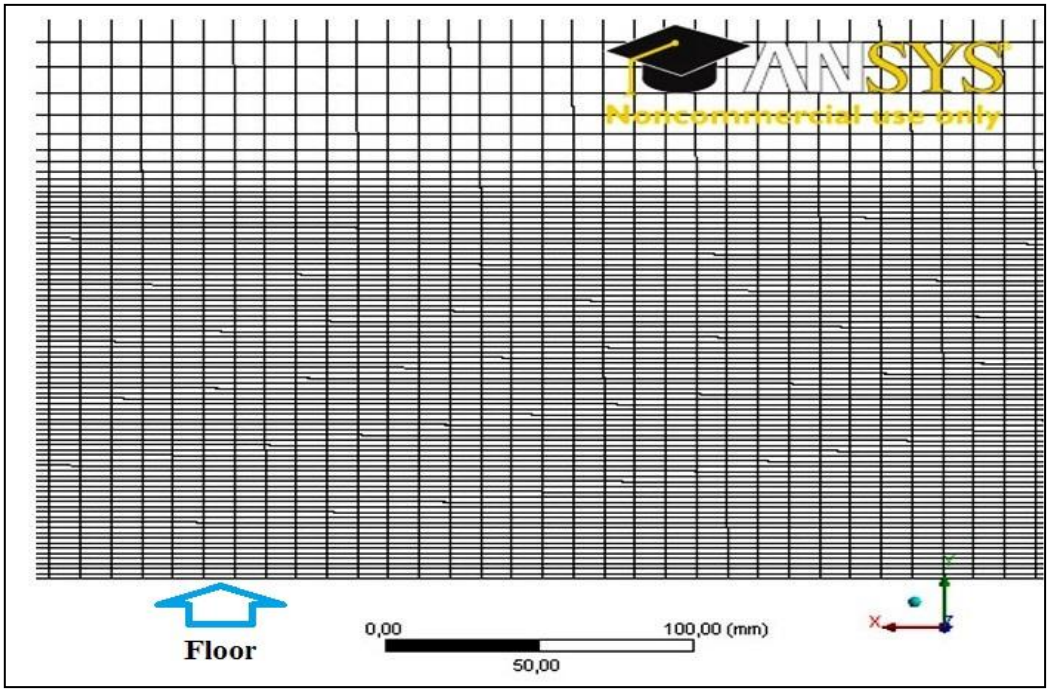

Figure 5-5: The mesh in the floor region for the 2D model

ANSYS FLUENT (ANSYS, 2011) recommends with regard of mesh quality that the minimum Orthogonal Quality should be greater than *0.1*, and the maximum skewness value should be less than *0.95*. The greater value of the Orthogonal Quality close to *1.0*, the better quality of the mesh. However, for the skewness value, vice versa. Table 5-1 lists the mesh metrics spectrum for the meshes of the CFD models. It shows that the quadrilateral elements in the 2D model have demonstrated the quality of the mesh

arrangement. Nevertheless, the elements in the 3D model have also shown the good quality in the mesh.

Table 5-1: The current mesh metrics and FLUENT recommendations:

Mesh metrics		2D model mesh	3D model mesh	FLUENT recommendations
Skewness value	Minimum	2.8e-05	5.0e-04	0
	Average	0.01	0.22	As possible as to 0
	Maximum	0.03	0.85	0.95
Orthogonal Quality	Minimum	1.0	0.48	0.1
	Average	1.0	0.87	As possible as to 1.0
	Maximum	1.0	1.0	1.0

5.3. CONSIDERATIONS OF BOUNDARY CONDITIONS

The testing fence was placed at the longitudinal distance of *6.75m* from the velocity inlet, which is equal to *45* times of the fence height. As such, wall-bounded fully developed turbulent atmospheric flow can be ensure at this position.

5.3.1. Velocity inlet

In order to assess the CFD modelling against the experimental results, the conditions of velocity inlet should be as the same to the ones in the experiment as possible. Since the inlet velocity was normal to the inlet boundary, the v and w components were zero. The velocity, turbulent kinetic energy, turbulent dissipation rate and specific turbulent dissipation rate for the velocity inlet can be determined as follows (ANSYS, 2009):

Within the thickness of the boundary layer δ:

$$u = U_{free}(y/\delta)^{\alpha} \qquad \textbf{Eqn.5-1}$$

Beyond the thickness of boundary layer:

$$u = U_{free}$$ **Eqn.5-2**

The turbulent kinetic energyk_{nw} is assumed to vary linearly from a near-wall value of:

$$k_{nw} = u_\tau^2/\sqrt{C_\mu}$$ **Eqn.5-3**

To a free-stream value of k_{inf}

$$k_{inf} = 0.002U_{free}^2$$ **Eqn.5-4**

The dissipation rate $\varepsilon$is:

$$\varepsilon = C_\mu^{3/4} k^{3/2}/l$$ **Eqn.5-5**

where l is the mixing length, and κ is the von Karman constant of 0.41. If $\kappa * y < 0.085\delta$:

$$l = \kappa * y$$ **Eqn.5-6**

else:

$$l = 0.085\delta$$ **Eqn.5-7**

The friction velocity $u_*$and wall shear $\tau_w$are formed as:

$$u_* = \sqrt{\tau_w/\rho}$$ **Eqn.5-8**

$$\tau_w = f\rho U_{free}^2/2$$ **Eqn.5-9**

The friction factor f is derived from the Blasius equation:

$$f = 0.045\left(U_{free}\delta/v\right)^{-1/4}$$ **Eqn.5-10**

The specific dissipation rateω is:

$$\omega = \varepsilon/k$$ **Eqn.5-11**

From the experiment, these variables were known: $U_{free} = 8m/s$, $\delta = 0.125m$, $\alpha = 0.1139$, $\kappa = 0.41$, $C_\mu = 0.09$ and $v = 1.7894e-05\, m^2/s$.

As such, the velocity, turbulent kinetic energy, turbulent dissipation rate and specific turbulent dissipation rate can be written in programming C language and compiled or interpreted into ANSYS FLUENT.

5.3.2. Pressure outlet

At the pressure outlet, the flow field variables were extrapolated from the adjacent interior cells and the normal gradient was vanished. The Gauge pressure was set to zero since the porous fence had no or very minor effect on the airflow at this position, where the freestream airflow was resumed. According to the characteristics of the wind tunnel, turbulence intensity in the freestream was *5%*. Both of the backflow turbulence intensity and the backflow turbulent viscosity ratio were set as *5%* in the simulation.

5.3.3. Wall and near-wall treatment

A no-slip condition was applied onto all of the walls in the domain. It is often called the Dirichlet boundary condition, and used almost universally in modelling macroscale of viscous flows in engineering. For viscous fluids at a solid boundary, the no-slip condition implies that the fluid will have zero velocity to the boundary. This assumption will cause the gradients of solution variables, especially the tangential velocity, are large. Thus, for CFD modelling of near–wall flows with no-slip condition on the walls, fine mesh resolution needs to be carefully arranged.

It is well acknowledged that the presence of boundary walls will affect turbulent flows significantly. Very close to the wall, viscous damping reduces the tangential velocity fluctuations, and kinematic blocking reduces the normal fluctuations. Due to the large gradients in the mean velocity producing turbulence kinetic energies in the outer part of the near-wall region, this will increase turbulence rapidly. Therefore, near-wall treatments for wall-bounded turbulent flows are essentially important to the fidelity of numerical modelling.

In the near-wall region, the solution variables have large gradients, and the momentum and other scalar transports occur most vigorously. Figure 5-6 illustrates the subdivisions of the near-wall region based on the experimental observations. Generally, the near-wall

region can be subdivided into three layers. The innermost layer is the viscous sublayer, where the flow is almost laminar, and the (molecular) viscosity plays a dominant role in momentum and heat or mass transfer. The outer layer is the fully turbulent layer, where turbulence plays a major part. Between these two layers, it is called as the buffer layer, where the effects of molecular viscosity and turbulence are equally important. y^+ is a non-dimensional wall distance for a wall-bounded flow defined as:

$$y^+ \equiv u_* y/v \qquad \textbf{Eqn.5-12}$$

where y is the distance to the wall, v is the local kinematic viscosity of the fluid, and u_* is the friction velocity at the nearest wall.

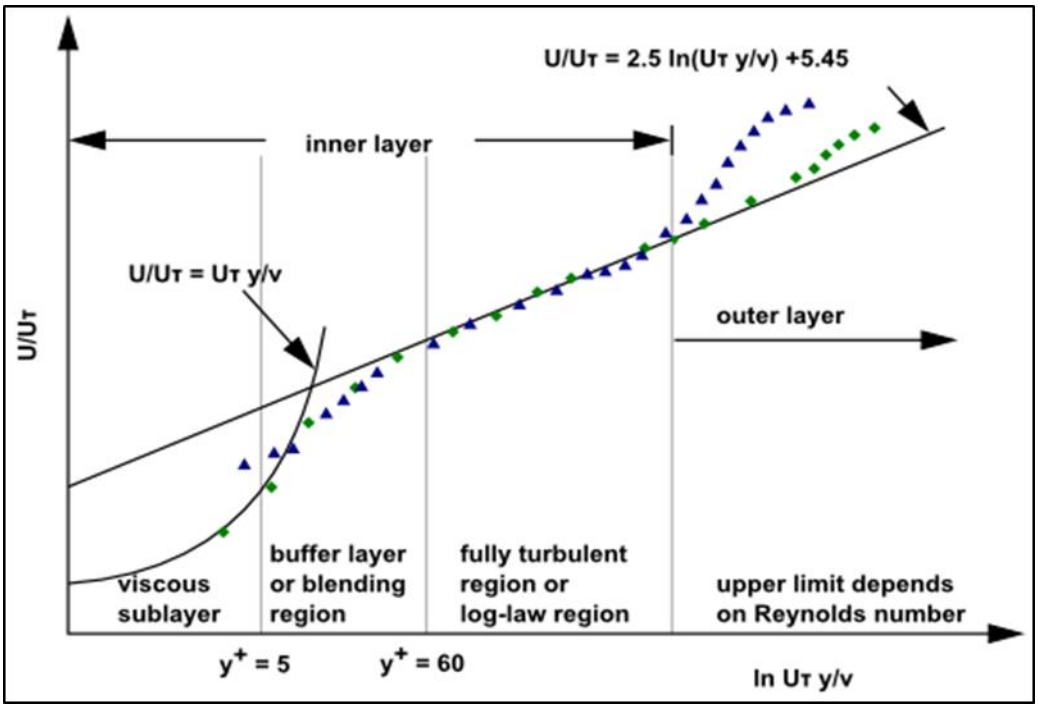

Figure 5-6: Subdivisions of the near-wall region (ANSYS, 2011)

y^+ is commonly used in the boundary layer theory in defining the law of the wall, and is also an important criterion for assessing mesh quality and selecting appropriate turbulence model. For near-wall modelling approach, the turbulence models are modified to enable the viscosity-affected region to be resolved with an appropriate mesh all the way to the wall, including the viscous sublayer. Therefore, y^+ must be carefully considered.

ANSYS FLUENT adapts semi-empirical formulas known as wall function approaches to bridge the viscosity affected region between the wall and the fully turbulent region. The benefit of these approaches is the significant reduction in mesh resolution that results in the reduction in computational time. For *k-ε* based turbulence model, ANSYS FLUENT offers five choices of wall-function, including the Standard Wall Functions, the Scalable Wall Functions, the Non-Equilibrium Wall Functions, the Enhanced wall Functions and the User-Defined Wall Functions. These wall functions comprise laws-of- the wall for the mean velocity or other scalars, and formulae for the near-wall turbulent quantities. The Standard Wall Function is a default option and works reasonably well for a broad range of wall-bounded flows. When encountered low-Reynolds number wall-bounded flows, usually the near-wall modelling approach combined with the adequate mesh resolution in the near-wall region, must be applied.

The Enhanced Wall Treatment is a two-layer approach that is integrated into the *k-ω* turbulence models and is recommended in the *k-ε* models too. This two-layer approach enhances the wall function by smoothly blending the logarithmic layer formulation with the laminar formulation.

y^+ for the Enhanced Wall Treatment requires the value in the range between *1*and *5*, and the value around *1* is more desirable. Values of 5 <$y^+ < 30$ must be avoided as it will gradually introduce unbounded errors in wall shear stress and wall heat transfer. (ANSYS, 2009) (Gerasimov, 2006).

In the present study, if taken $y^+ = 1$ as the desired value, the height of adjacent cell to the floor y was approximately *3.4e-05*. For 3D modelling with a porous fence in the presence, based on $y^+ = 1$ to construct the grid, the elements would skewed beyond the acceptable range if not marginally increase the quantity. Therefore, the y was estimated *1.0e-04*, which the $y^+$was approximated to *3*. This construction were applied to all of the turbulence models in the current study. The benefits of such construction of grid are as follows:

- Comparing the performance of each turbulence model under the same arrangement of grid;

- The *k-ω* models require $y^+ < 5$ as the Enhanced Wall Function was automatically integrated.
- The best practice for the Standard Wall Function is to locate each wall-adjacent cell's centroid within the viscous sublayer $y^+ < 5$ or the log-law sublayer $30 < y^+ < 300$ (Chmielewski & Gieras, 2013).
- The Standard Wall Function is a default option in *k-ε* models and works reasonably well for a broad range of wall-bounded flows. It is also a popular near-wall treatment in the porous fence study.
- Using the Standard Wall Function is quicker to get solutions and therefore saving computational cost, particularly those simulations in 3D modellings.

The detailed mesh is shown in Section 5.2.3.

Figure 5-7 shows the longitudinal distribution of y+ adjacent to the floor under the Standard k-ε turbulent model, and Figure 5-8 displays the longitudinal distribution of y+ adjacent to the floor under the Standard k-ω turbulent model. The structure of grid, the boundary conditions and computational procedures were the same.

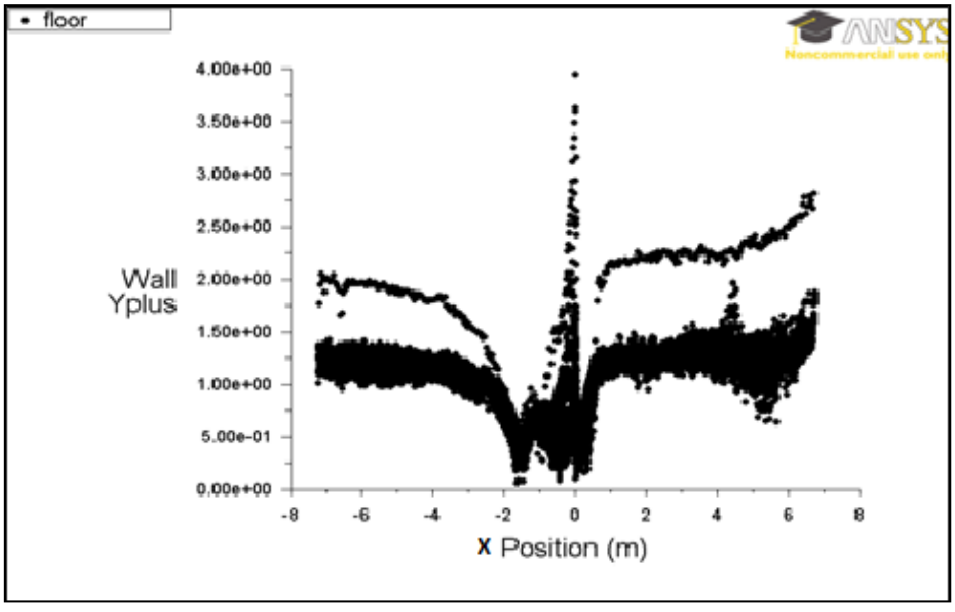

Figure 5-7: y+ adjacent to the floor under the Standard k-Epsilon model

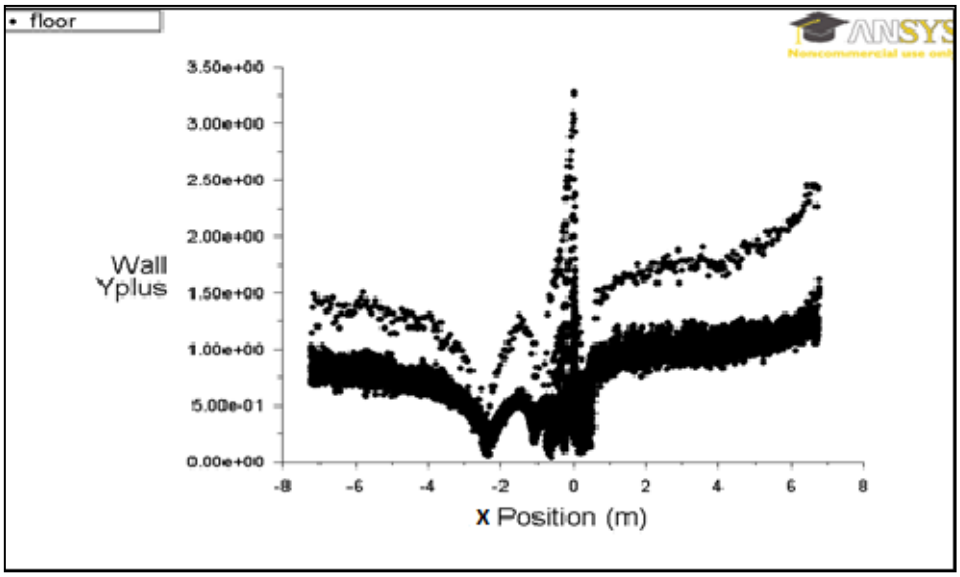

Figure 5-8: y+ adjacent to the floor under the Standard k-Omega model

It can be observed that both of y^+ were in the allowable region between *0* and *5*. The values of y^+ for the standard k-ω model were smaller than the ones for the Standard *k-ε* model. At the position $x = 0m$, both have the highest values. Between the fence effective region of $x = 6m$ and *0m*, the values of y^+ for both are close to *1*. Since the fence effective region is of most concern in the study, the results revealed that the quality of grids was sound.

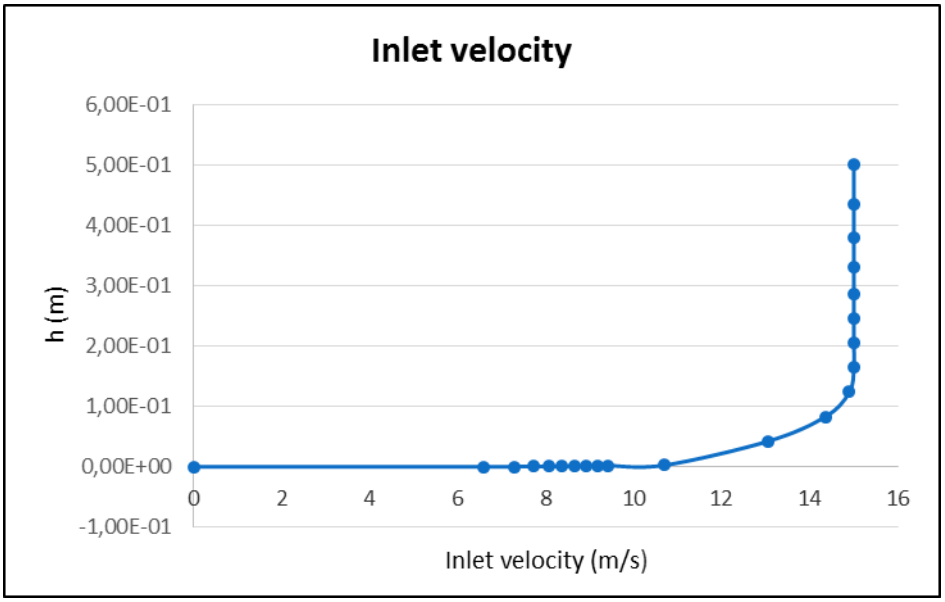

Figure 5-9: The inlet velocity profile produced by the Standard k- Epsilon model

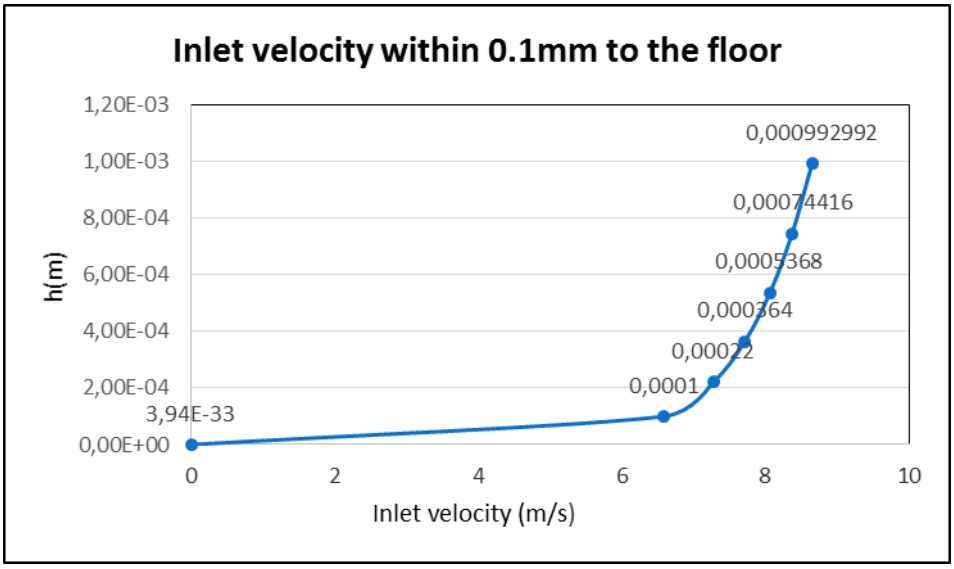

Figure 5-10: The amplified inlet velocity profile within 0.1mm to the floor

Figure 5-9 shows the inlet velocity profile produced by the Standard *k-ε* model (half of the wind tunnel height from the floor up), and Figure 5-10 is the amplified inlet velocity profile within *0.1mm* to the floor. It has clearly demonstrated the viscous sublayer, blending and log-law regions.

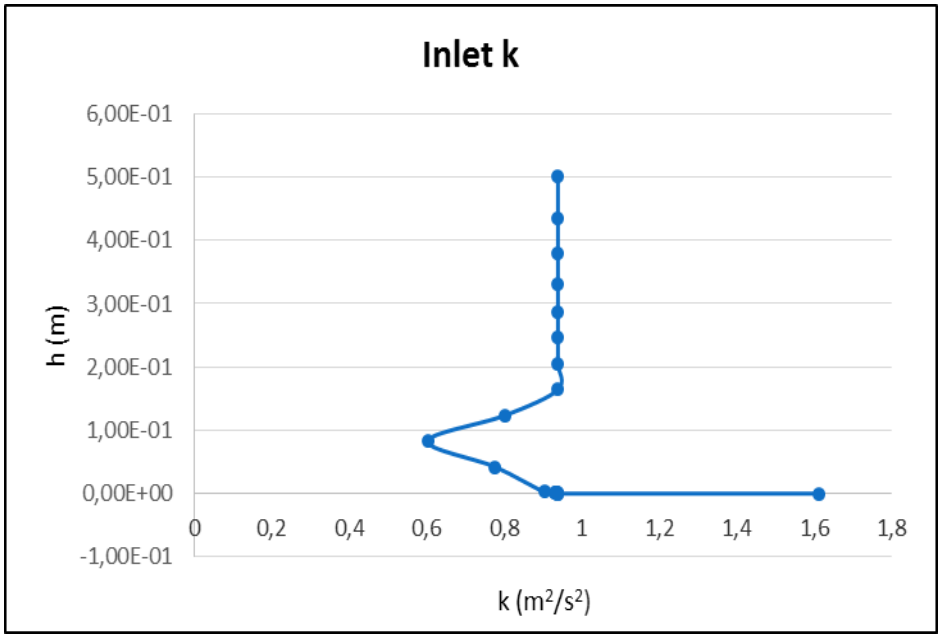

Figure 5-11: The inlet k profile produced by the Standard k-Epsilon model

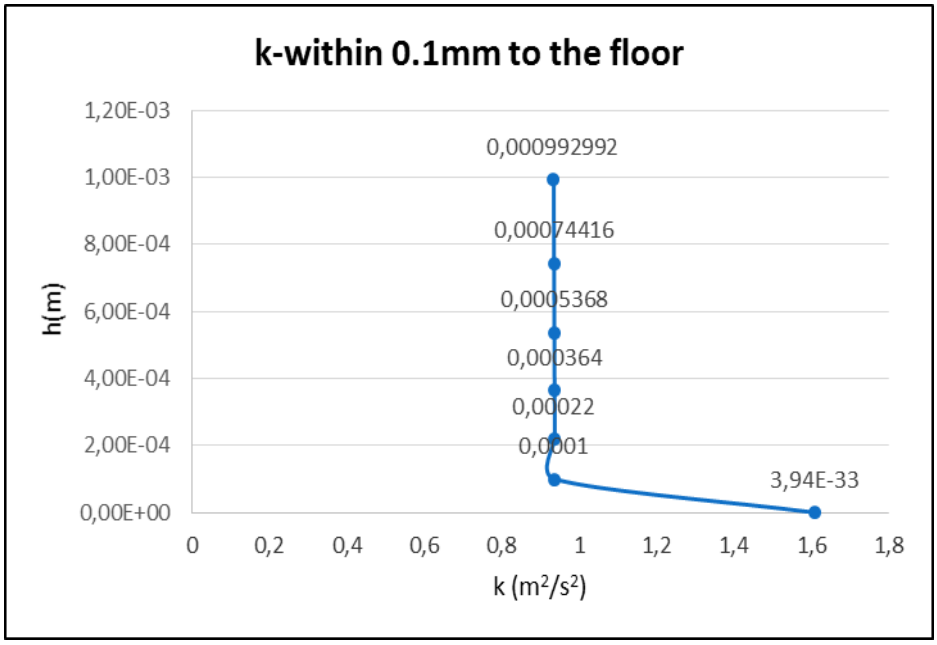

Figure 5-12: The amplified k within 0.1mm to the floor

Figure 5-11 is the inlet turbulent kinetic energy *k*, and Figure 5-12 is the amplified *k* profile within *0.1mm* to the floor. It can be observed that a peak value of *1.61* m^2/s^2 was appeared at the position where the flow separated from the floor, which was caused by the no-slip floor wall. After which, the *k* quickly reduced to *0.94*m^2/s^2 and almost kept this value until to *0.1mm* around, and then the value of *k* started to drop until at *83 mm* height. Between height of *83mm* and *160mm*, the k increased again. Beyond the height of *160mm*, the *k* maintained a constant value of *0.938*m^2/s^2. These features also reflected the effects of viscous sublayer, buffer layer and log-law region.

The inlet velocity and *k* profiles have also been checked on the other turbulence models. It was almost the same; the differences among them were only in the region very close to the floor (inner viscous sublayer).

The contour of du/dy in the symmetry wall is shown in Figure 5-13. The gradient of u along the vertical direction have been successfully captured within *10* prism layers in the near-wall region (floor). It demonstrated that the resolution of the boundary layer was in good quality.

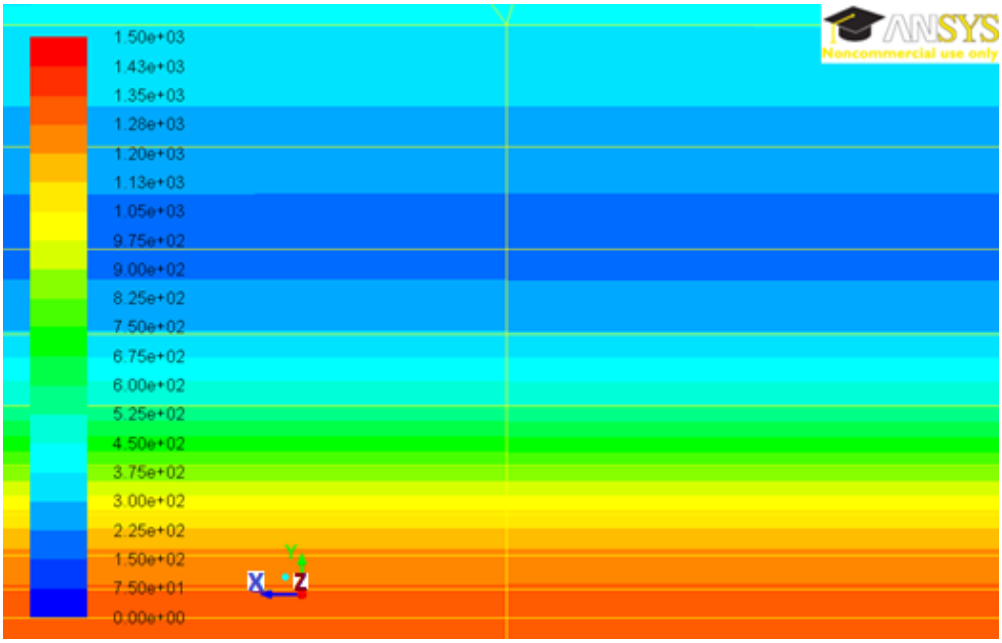

Figure 5-13: Contour of du/dy in the symmetry wall under the Standard k-ω model

5.4. CONSIDERATION OF SOLVER

The solution methods in the present study adapted SIMPLE scheme pressure-velocity coupling. The SIMPLE is an acronym for Semi-Implicit Method for Pressure Linked Equations. SIMPLE algorithm is a widely used numerical procedure to solve the NSE equations. It is a segregated solution method, which the velocity vectors and the pressure field are solved separately. Coupling between these field variables is achieved via velocity and pressure corrections. Hence, only the velocity correction is solved explicitly.

The spatial discretization only changed the momentum from the Second Order Upwind to the Frist Order Upwind, and the rest variables kept default.

No changes for Under-Relaxation Factors in the solution control. If there is a difficulty in solution convergence, consider to re-configure the solution control. It is however not a case for the present simulations.

The convergence criteria were assessed by monitoring the scaled residuals. Additionally, the history of drag coefficient in the longitudinal direction was monitored too. The detailed was discussed in Section 5.2.2.

The solution initialization run the hybrid method with *10* of iterations. After the solution converged, back to the solution methods, the Second Order Upwind discretization was applied to the variables of momentum, turbulent kinetic energy and specific dissipation rate.

Running calculations again, the ultimate solution must be obtained on the second Order Upwind discretization.

5.5. TURBULENCE MODEL ASSESSMENT

Appropriate selection of turbulence model is important to the numerical study on the performance of porous fences. Especially for the fences with low or medium porosity, where strong turbulence is in the presence. Both of 2D and 3D modelling have been performed in this thesis. By comparing the numerical results with the corresponding wind tunnel experimental results, the suitability of turbulence model to the present research has been assessed.

Focus was paid on the assessment based on the 3D modelling. For the 2D modelling, under the case of the freestream velocity of *8m/s*, the Standard *k-ε*, the Realizable *k-ε* and the Standard *k-ω* turbulence models have been employed. For the 3D modelling, apart from these three turbulence models, the RNG *k-ε* and the SST *k-ω* turbulence models were added to the assessment. Additionally, the 3D modelling has investigated the cases under the freestream velocity of *8m/s* and *15m/s*.

5.5.1. Turbulence model assessment by 2D modelling

2D CFD modelling airflows around porous fences was intensively employed at the early stage of the development of CFD techniques, and is still popular at the present (Liston , et al., 1993) (Packwood, 2000) (Huang, et al., 2012). The evident advantages are easy to construct models and considerably reduce the required elements, which quickly reach solutions and save computational expenses. Since the characteristics of the porous fence is not physically modelled, porous fence is usually treated as a pressure discontinuity surface by applying a porous medium condition (porous jump or porous zone), where

momentum is absorbed from the flow as a momentum sink expressed as the following (Bourdin & Wilson, 2008):

$$S_i = -\left(\frac{\mu}{\alpha}u_i + \frac{1}{2}C_2\rho|u|u_i\right) \quad \textbf{Eqn.5-13}$$

The first at the right hand side at Eqn.5-13 is the viscous loss term and the second is the inertial loss term, where $S_i$is equivalent to pressure gradient and the pressure drop is related to the porosity of the medium, α is permeability (m^2), and C_2 is inertial resistance (m^{-1}). The momentum sink term is therefore added to the RANS fluid flow equations.

In the present modelling, the fence was treated as a porous jump. This one-dimensional simplification was recommended by ANSYS FLUENT (2011). For turbulent flow around a perforated plate like planar porous fences, the viscous loss term can be neglected (Bourdin & Wilson, 2008). Hence, the face permeabilityα for the fence was assigned as *1e+20*m^2. C_2 was associated with the resistance coefficient or pressure loss coefficient k_r calculated as follows:

$$C_2 = k_r/\Delta m \quad \textbf{Eqn.5-14}$$

$$k_r = 0.52(1-\beta^2)/\beta^2 \quad \textbf{Eqn.5-15}$$

where Δm is the thickness of the fence, and β is the porosity.

Porous cells for a porous jump are treated as *100%* open to the domain, which differs the fact where the fence is only partially open to the flow. Presuming the flow rate unchanged with or without the fence, $u_{27\%open} = 3.7 * u_{100\%open}$.Hence, k_r needed to be adjusted as k_r':

$$k_r' = k_r * \left(u_{27\%open}^2/u_{100\%open}^2\right) \quad \textbf{Eqn.5-16}$$

The 2D domain was created the same as the arrangement of the wind tunnel experiment. The inlet velocity and turbulence profiles were derived from the wind tunnel experiment and compiled into the modelling in C programming. Detailed considerations of boundary condition have been discussed in Section 5.3.

Table 5-2 lists the calculated the variables for the porous jump (the fence), where α, Δm and C_2 are the input parameters for modelling the porous jump.

Table 5-2: The variables for the porous jump

Item	Unit	Value
Fence height *H*	*m*	0.15
Porosity		0.27
Fence thickness *Δm*	*m*	0.003
Pressure loss coefficient k_r		6.61
Adjusted pressure loss coefficient k_r'		90.67
C_2	m^{-1}	30224
Face permeability *α*	m^2	1e+20

The 2D domain was created the same as the arrangement of the wind tunnel experiment. The inlet velocity and turbulence profiles were derived from the wind tunnel experiment and compiled into the modelling in C programming. Detailed considerations of boundary condition have been discussed in Section 5.3.

The turbulence models of the Standard *k-ε*, the Realizable *k-ε* and the Standard *k-ω* were employed in the simulations. The positions of data acquisition were selected the same as the ones of the wind tunnel experiment.

Figures 5-14 to 5-16 shows the comparisons of velocity magnitudes between 2D simulations and the wind tunnel experiments, where the corresponding lines were at $x = 0.2m$, $1.0m$ and $3.5m$.

It can be seen that the predicted velocity magnitudes by 2D modelling were in good agreement with the experimental results. In the region of $x \leq 1.0m$ and $h/H \leq 1.0$, the Standard *k-ω* model seemed having better predictions than the others did. The 2D

modelling was not sensitive to the selection of turbulence model in terms of evaluation of the structure of wind velocity leeward the fence.

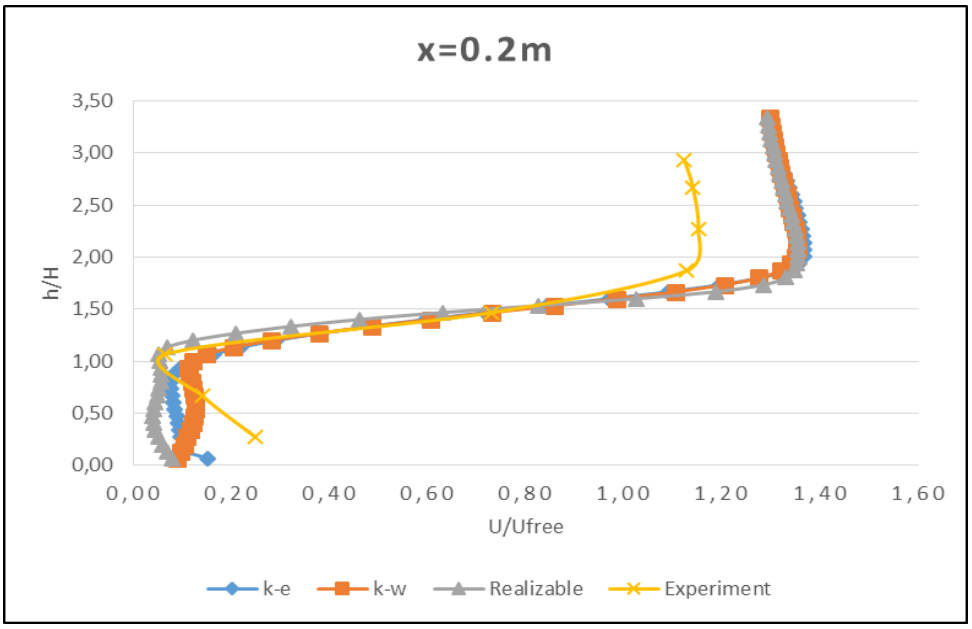

Figure 5-14: Comparison of velocity magnitudes at x=0.2m in the 2D modelling

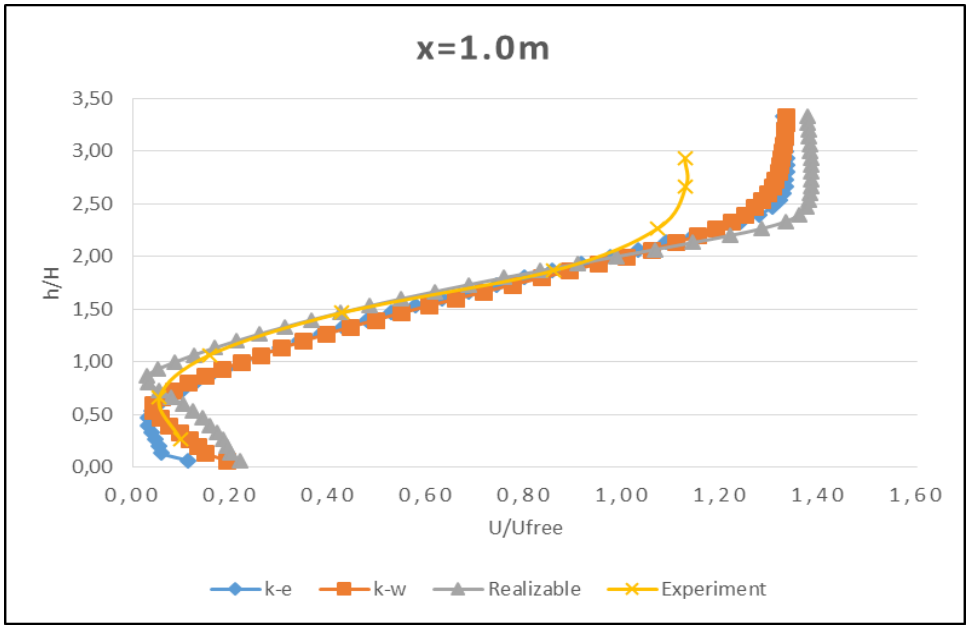

Figure 5-15: Comparison of velocity magnitudes at x=1.0m in the 2D modelling

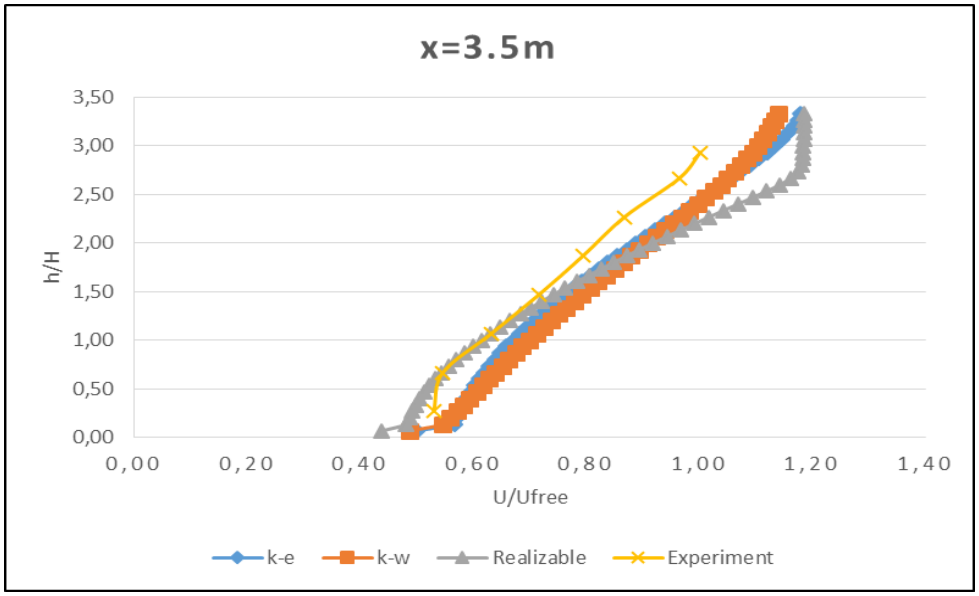

Figure 5-16: Comparison of velocity magnitudes at x=3.5m in the 2D modelling

The investigations of the turbulent kinetic energy k are presented from Figure 5-17 to Figure 5-19. The CFD results have over-predicted the values of k if compared with the experimental results, and the predictions on turbulence were sensitive to the selection of turbulence model. Comparatively, the Realizable k-ε model predicted the values closer to the experimental results.

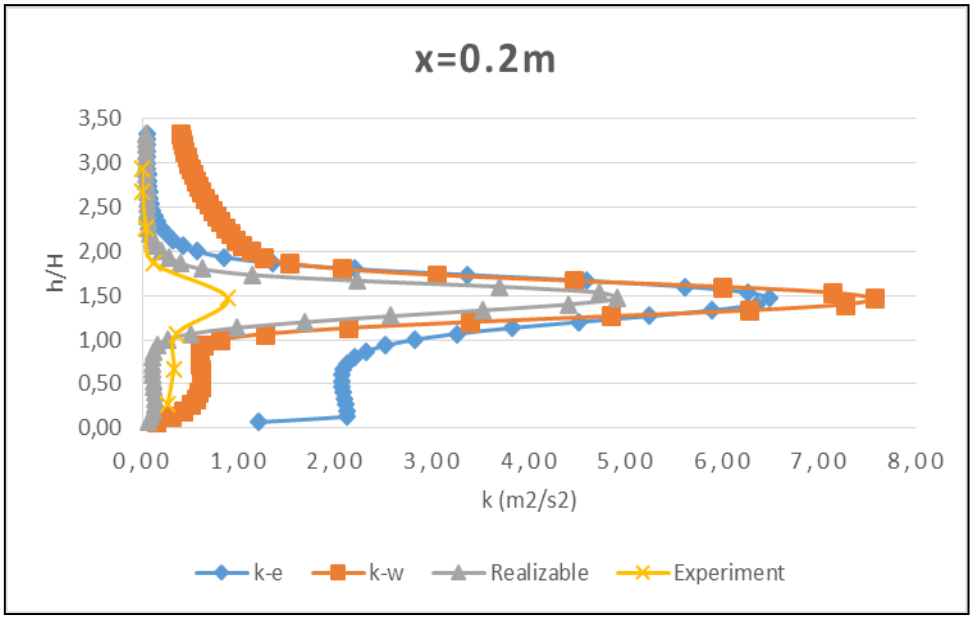

Figure 5-17: Comparison of turbulent kinetic energies at x=0.2m in the 2D modelling

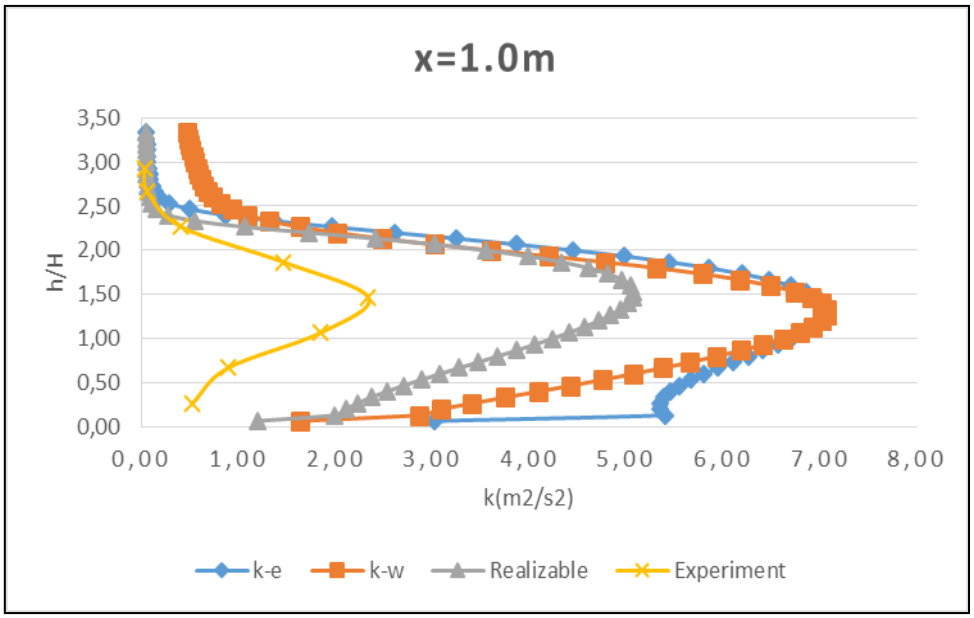

Figure 5-18: Comparison of turbulent kinetic energies at x=1.0m in the 2D modelling

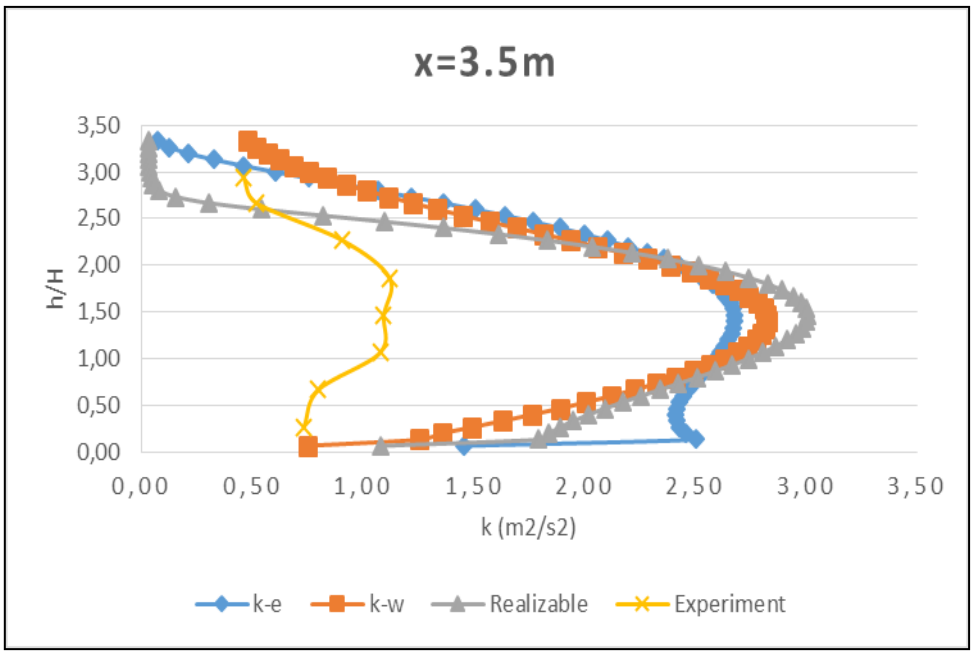

Figure 5-19: Comparison of turbulent kinetic energies at x=3.5m in the 2D modelling

Based on the above examinations, the discussions are as follows:

1) The velocity variables predicted by the 2D modelling were in good agreement with the experimental results. The prediction of the structure of velocity leeward

the fence was not sensitive to the selection of turbulence model. However, the turbulence predictions were sensitive to the applied turbulence models, and the values were over-predicted if compared with the experimental results.

2) It can be noticed that the Standard k-ω had better predictions for the velocities in the near fence region of $x \leq 1.0m$ and $h/H \leq 1.0$, and the Realizable k-ε predicted the turbulent kinetic energies closer to the experimental results.
3) The porous jump treatment for the fence had significantly reduced the required elements from *1.5* million for the 3D modelling to *0.28* million. The feasibility of such a treatment has been justified and proved by the wind tunnel experiment. The 2D modelling has greatly simplified the domain construction and saved computational cost. The 2D modelling has shown its strength on its applications.
4) The foreseeable disadvantage for the 2D modelling is unable to provide comprehensive information within the entire domain. I.e. the distributions of shear stress and pressure on the fence surface, and the three dimensional fence effective zone may be important in the fence study. Besides, the porous jump and porous zone treatments require empirical knowledge to define the input parameters during the simulations, and are limited to the applications in CFD modelling (ANSYS, 2011). All of which can be solved under 3D modellings.

5.5.2. Turbulence model assessment by 3D modelling

The 3D CFD model was constructed based on the corresponding wind tunnel experiment. The structure of grid kept unchanged in order to assess the suitability of the six turbulence models. The cases under the freestream wind velocity of *8m/s* and *15m/s* were selected for the assessment, where the Reynolds number was increased from *3.0e+06* to *5.7e+06* at the position of the fence.

For airflow from transition to fully developed turbulence over a flat plate, the value of the Reynolds number is about *2.0e+05* for a rough plate with a fairly high degree of turbulence at the inlet, and *3.0e+06* for a very smooth plate with a low level of turbulence at the inlet (John et al., 1988). The testing wind tunnel floor was a smooth flat plate with a low level of turbulence at the inlet. As such, the case under the freestream wind velocity of *8m/s* was approximately in the region where a fully turbulent flow was just developed;

while the case under the freestream wind velocity of *15m/s* was that a fully developed turbulence was maintained at the fence position. As such, the structure of the flow regime leeward the fence for these two cases might be different. The wind tunnel experiment has not captured such a difference. It is in the research interest to investigate the sensitivity of numerical simulations to such cases.

The examining data were taken at the lines corresponding to the ones in the wind tunnel experiment with the purpose of model assessment. $x = 0.2m$ was in the close fence region where vortex may involve, $x = 0.6m$, $1.0m$ and $1.8m$ were in the fence effective zone likely having reverse cells and wake flows, and $x = 3.5m$ was in the internal boundary layer affected region.

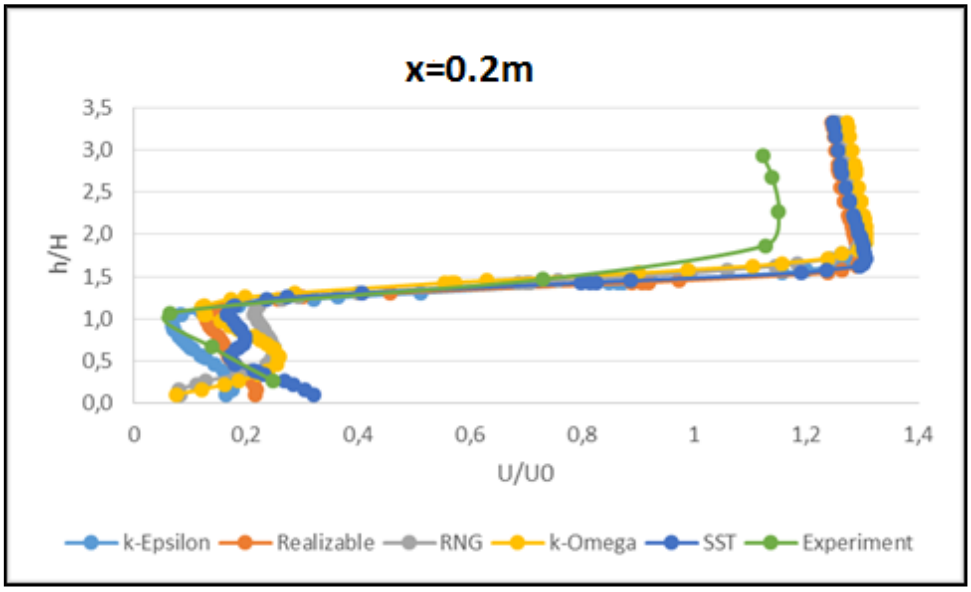

Figure 5-20: Comparison of velocity magnitudes at $x = 0.2m$ in the 3D modelling

In the convenience of comparisons, the presented figures were expressed as follows:

- Axis X: for velocity investigations, it was expressed as the ratio of the local velocity magnitude U and the free stream velocityU_0. For turbulence investigations, the local turbulent kinetic energy was targeted.
- Axis Y: it was expressed as the measuring height h normalized by the corresponding fence height H.

The comparisons of velocity magnitudes are presented from Figure 5-20 to Figure 5-24.The simulation results were in good agreement with the experimental results in general, particularly in the region where h/H > 1.0 and x/H >6.7. In the region of h/H< 1.0 and x/H=1.3, the Standard k-ε model performed the best among the others shown in Figure 5-20. In the region of h/H<1.0 and x/H=6.7, the Standard k-ε and RNG models under predicted the reductions of velocity shown in Figure 5-22. Beyond the region of x/H=12.0, the flow was mainly affected by the internal boundary layer shown in Figures from 5-23 to 5-24.

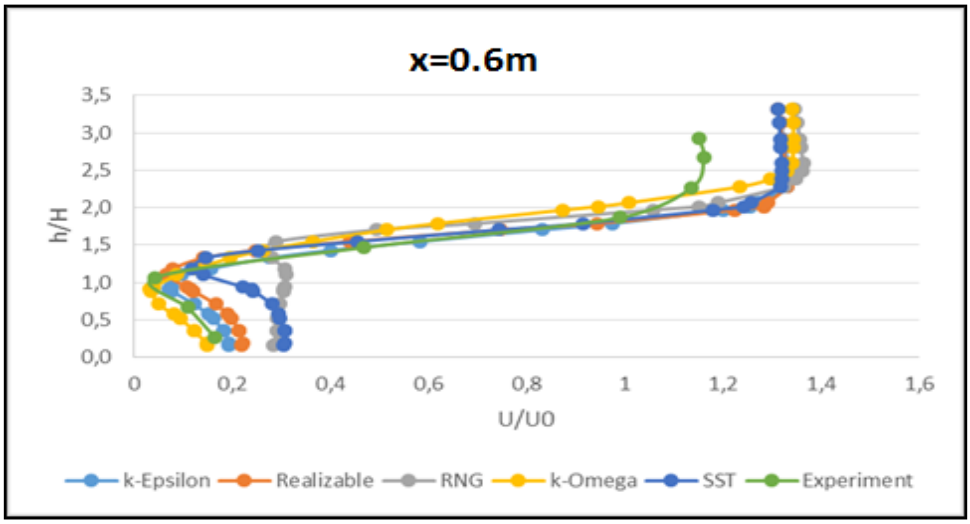

Figure 5-21: Comparison of velocity magnitudes at $x = 0.6m$ in the 3D modelling

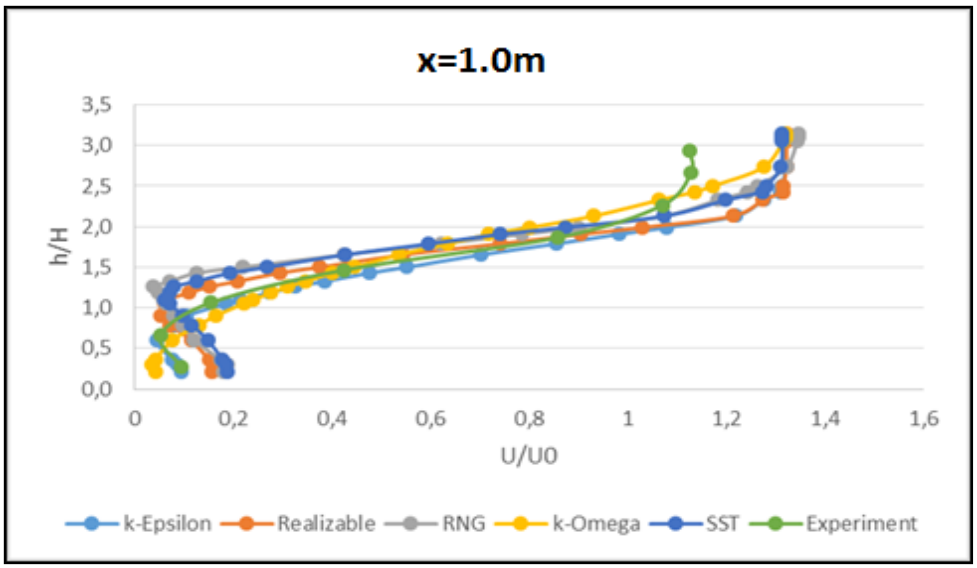

Figure 5-22: Comparison of velocity magnitudes at $x = 1.0m$ in the 3D modelling

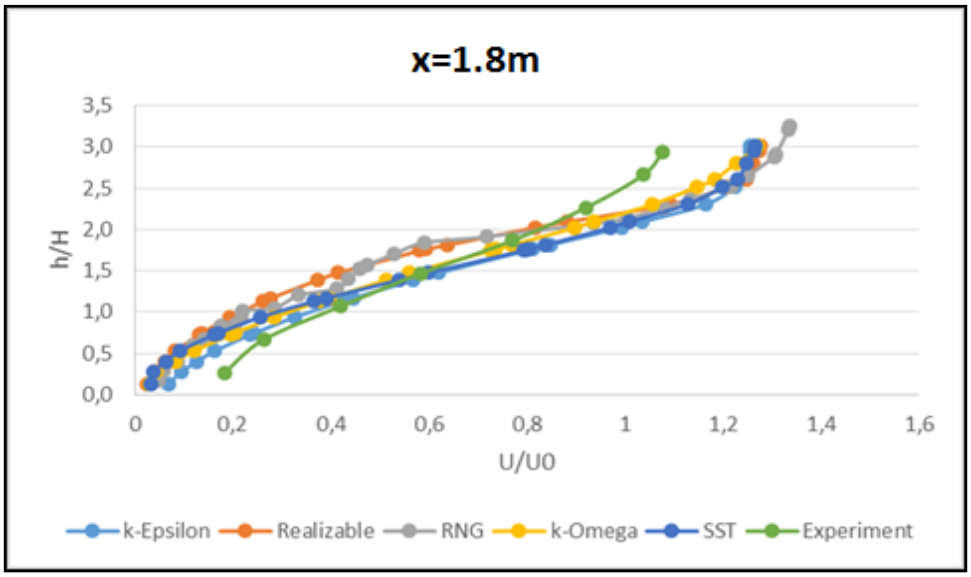

Figure 5-23: Comparison of velocity magnitudes at $x = 1.8m$ in the 3D modelling

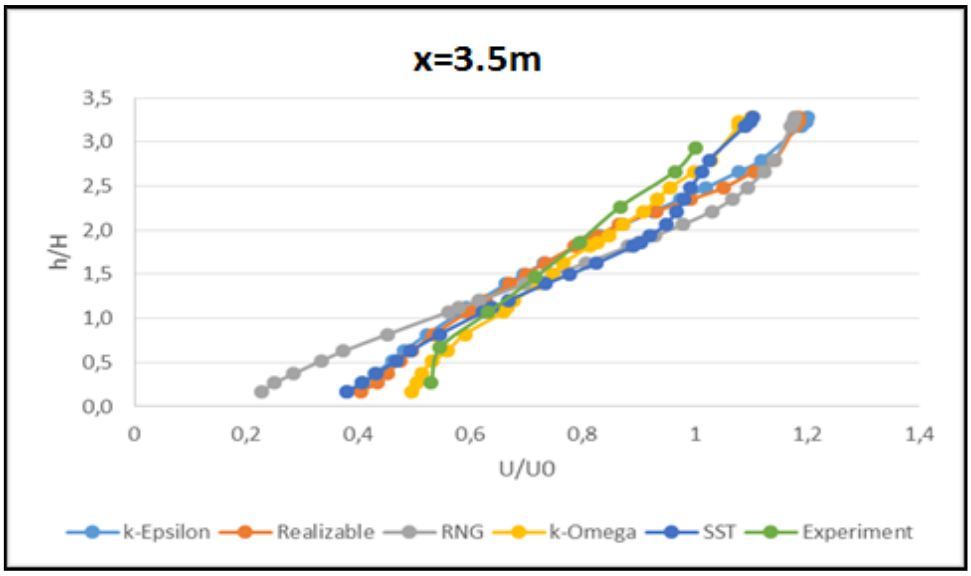

Figure 5-24: Comparison of velocity magnitudes at $x = 3.5m$ in the 3D modelling

In the near fence region shown in Figures from 5-20 to 5-22, there was a discrepancy among the models. Generally the models were under predicted the reductions of velocity except of the Standard *k-ω* model. The Standard *k-ω* model produced the closest data to the experimental one in such regions.

It can be observed that there was a difference between the experimental and numerical results in the region where $h/H > 2.0$, the values of experimental data appeared smaller.

This was because the top wall of the wind tunnel actually affected the flow that restrained the flow acceleration. In the simulations, the top wall was treated as a no-slip wall without fine mesh in place. Since the structure of flow within the effective fence zone was of main concern, such difference can be considered as acceptable.

Overall, the selection of turbulence model was not so sensitive to the prediction of wind velocities. In terms of velocity predictions, they were all applicable in the modelling. Comparatively, the Standard k-ω model performed the best among the others.

The comparisons of turbulence kinetic energy were displayed the Figures from 5-25 to 5-29.The numerical predicted turbulent kinetic energy appeared the similar pattern at each comparable line position to the experimental one. It increased the value from the floor and reached a maximum value in the region of $0.7 < h/H < 1.5$, after which its value started to drop, and beyond the region $h/H > 3.0$, the value closed to each other and appeared to be recovered to the flow with fence free. It can be observed that the stand *k-ω* model had the maximum value in the near fence region. Away from the fence, the maximum peak value could be produced by the other models. Compared with the experimental results, except the RNG model, all of the other models have over-predicted the values of turbulent kinetic energy.

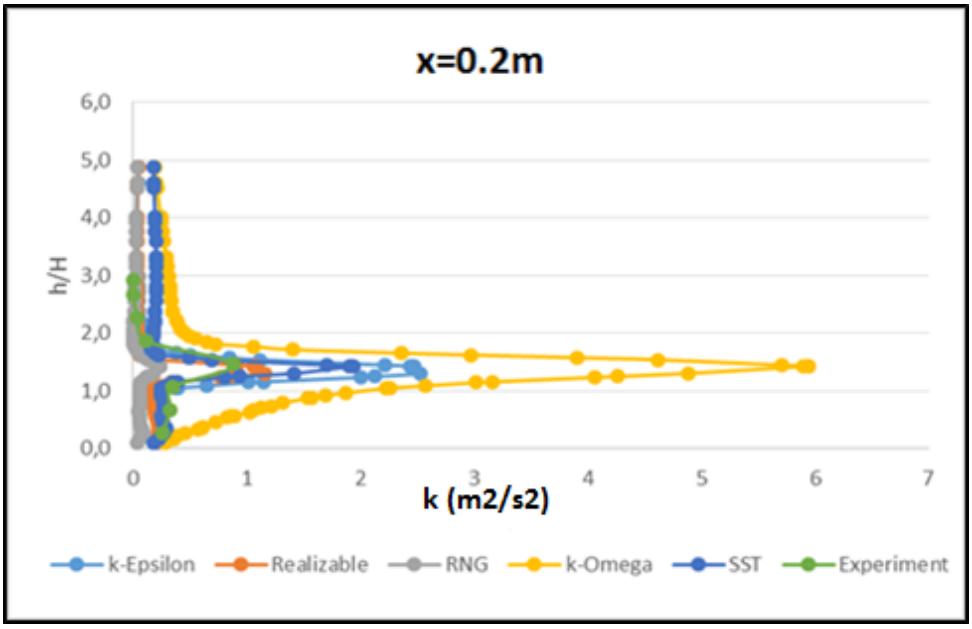

Figure 5-25: Comparison of turbulent kinetic energies at $x = 0.2m$ in the 3D modelling

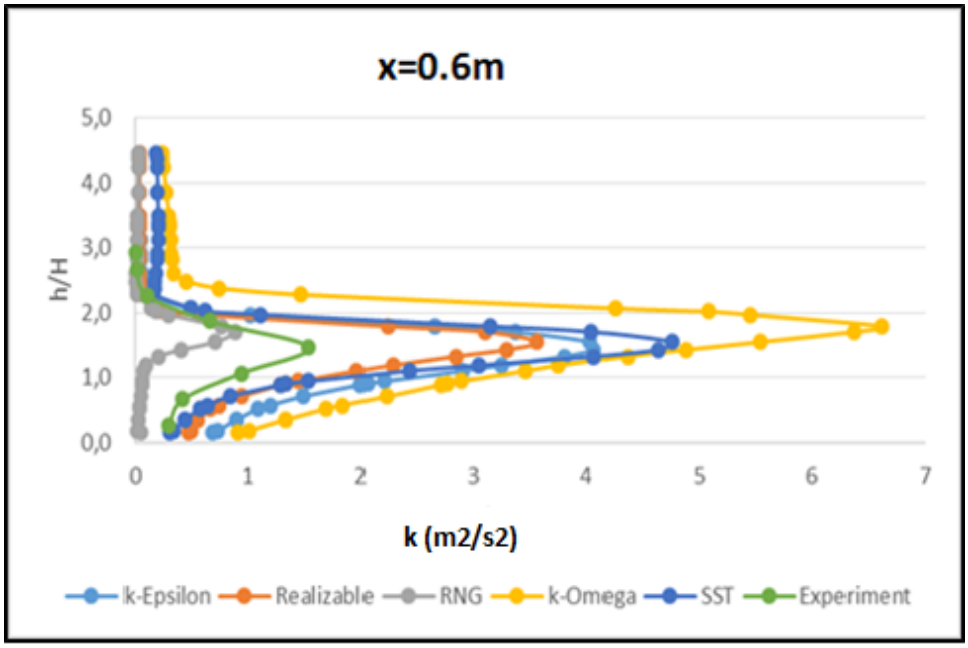

Figure 5-26: Comparison of turbulent kinetic energies at $x = 0.6m$ in the 3D modelling

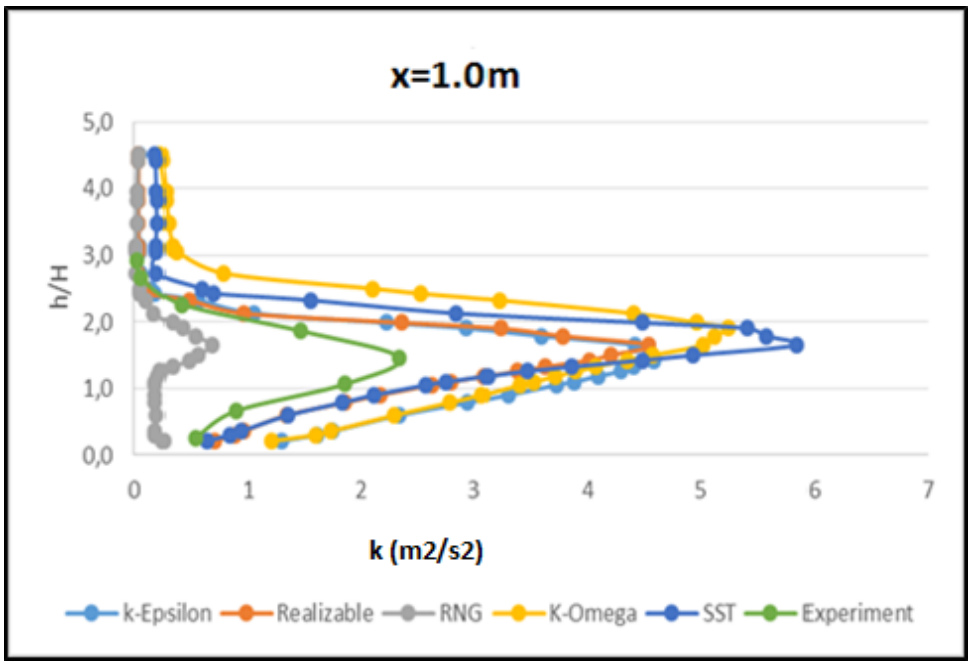

Figure 5-27: Comparison of turbulent kinetic energies at $x = 1.0m$ in the 3D modelling

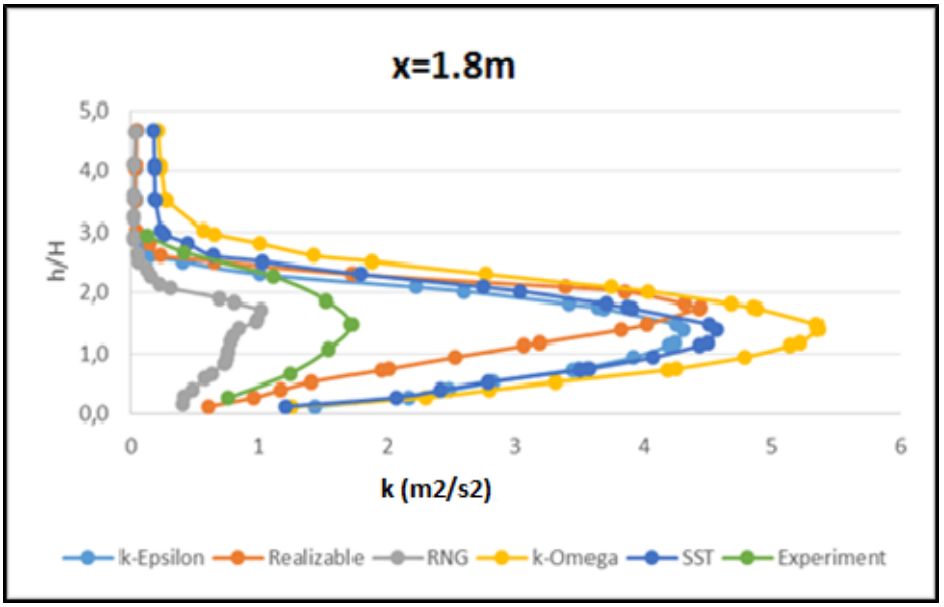

Figure 5-28: Comparison of turbulent kinetic energies at $x = 1.8m$ in the 3D modelling

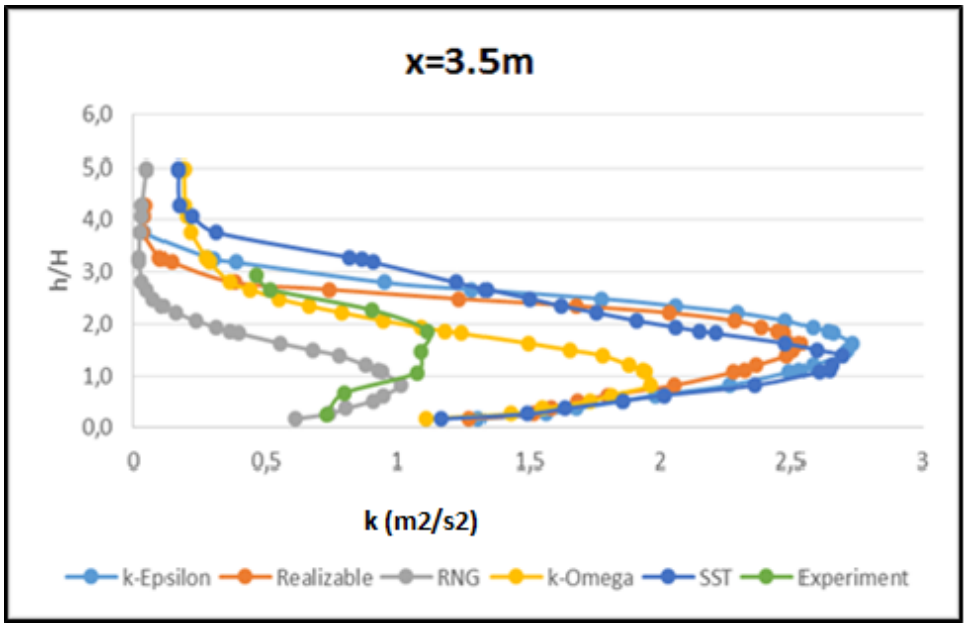

Figure 5-29: Comparison of turbulent kinetic energies at $x = 3.5m$ in the 3D modelling

None of the turbulence models has produced the turbulent kinetic energy in a very good agreement with the experimental results. However, the distribution patterns were in similar manners. The simulations have revealed that the turbulence model selection is sensitive to the prediction in turbulence.

The comparisons have also made in the case under the freestream velocity of *15m/s*. The detailed are presented in the App-Fig. 22-23 in Appendix E. It shows the pretty same outcomes which discussed in the case of the freestream velocity of *8m/s*, except that the Standard *k-ω* model produced maximum peak values in all of the lines. The comparisons also reveals that the turbulence model selection was not sensitive to the approaching wind velocities.

Table 5-3: the assessment of the performance of turbulence models.

Turbulence Model	Velocity Prediction	Turbulence Prediction
Standard k-ε	Good	Over predicted
Realizable	Good	Over predicted
RNG	Applicable	Under predicted
Stand k-ω	Quite good	Over predicted
SST	Good	Over predicted

Table 5-3 lists the performance of turbulence models with regard of the current cases. In practice, the computational time for the turbulence model application increased in the order: the Standard *k-ε*, the Realizable *k-ε*, the Standard *k-ω*, the SST and the RNG *k-ε* model.

The 3D CFD modelling has successfully simulated the structure of wind velocity leeward the fence in good agreement with the experimental results. The Standard *k-ω* model performed the best among them, since it produced results close to the experimental ones in the near fence region. However, this 3D CFD modelling produced turbulent kinetic energy resulted in a marginal discrepancy with the experimental results, albeit the distribution patterns appeared similar. This outcome is in agreement with other researcher's founding that these turbulence models often result in over-predicting turbulence intensities and turbulent kinetic energies in the study cases (Bourdin & Wilson, 2008) (Chen, et al., 2012) (Chmielewski & Gieras, 2013) (Menter, 1994).

5.5.3. Summary and discussions

The two-equation based turbulence models have been assessed under the 2D and 3D modellings. The summaries are presented as follows:

1) Both of 2D and 3D modellings have revealed that the numerical prediction on velocity was not sensitive to the turbulence model selection, and were generally in good agreement with the corresponding experimental results. Comparatively, the Standard k-ω turbulence model had better predictions for the velocities in the close fence region for both the 2D and 3D modellings.
2) Both of 2D and 3D modellings have found that the numerical prediction on turbulence was sensitive to the turbulence model selection, and were generally over-predicted the values if compared with the corresponding experimental results. However, both of 2D and 3D modellings have demonstrated the distribution patterns of turbulence similar to the ones from the experiment. Comparatively, the Standard k-ω model for 3D modelling predicted the turbulent kinetic energies closer to the experimental results, which differed from the 2D modelling where the Realizable k-ε model appeared better.
3) The numerical predictions between the 2D and 3D modellings were close to each other. Both of them have shown the competence especially for the velocity prediction.

The numerical predictions on turbulence had a noticeable discrepancy from each other, and generally all of the applied turbulence models had over-predicted the turbulence if compared with the experimental results. The reasons may associate with the followings:

1) Errors on experimental data acquisition: the ultrasonic anemometer used in the experiment is an intrusive instrument, which would distort the wind field at the measuring points that induced the errors into velocity data. Although the ultrasonic anemometer enabled to measure three dimensional velocity vectors in a time series of *10* seconds with a time resolution of *100* Hertz, the produced data were still time-averaged that might be still insufficient to capture the complex

nature of turbulence. The turbulent kinetic energies from the experiment were calculated based on the measurement of velocity vectors. As discussed in Section 4.4.1.2, error of accuracy on turbulent kinetic energy is amplified six times big than the error on velocity.

2) Errors on CFD modelling: the CFD model has demonstrated a fine mesh resolution that has successfully captured the floor bounded flow in different sublayers. However, the boundary walls were applied by no-slip condition, which might introduce errors for the wall modelling. Particularly for the porous fence, the no-slip condition was not sufficient to model large gradients involved variables induced by considerable numbers of porous holes. It is better to assign a scalar wall function in such region in the future work.
3) The complex nature of turbulent flow: turbulent flow is a flow regime characterized by chaotic property changes, which includes low momentum diffusion, high momentum convection, and rapid variation of pressure and flow velocity in space and time. This complex nature results in the difficulties in experimental measurement and numerical modelling even today. The CFD modelling is governed by the RANS equations, which has limitations in describing the characteristics of turbulence.

Overall, both of the 2D and 3D models are applicable to the present study. On balance, the Standard k-ω model had better performance. As such, this turbulence model was employed in the following numerical investigations throughout the thesis.

5.6. DISCUSSIONS ON POST PROCESS

The post processes demonstrated here are derived from the simulations by the standard k-ω model, since it had better predictions in general as discussed in Section 5.4.

Figure 5-30 displays the contours of total pressure in the relevant planes. The top is the contour of total pressures in the symmetry wall, which demonstrated a low-pressure zone leeward the fence. The left under is the amplified contour of total pressure around the fence in the symmetry wall, where is in absence of the holes. The right under is in the

plane with *7.5mm* offset from the symmetry wall with the holes in the presence. It can be observed that the holes have mitigated the total pressure drop.

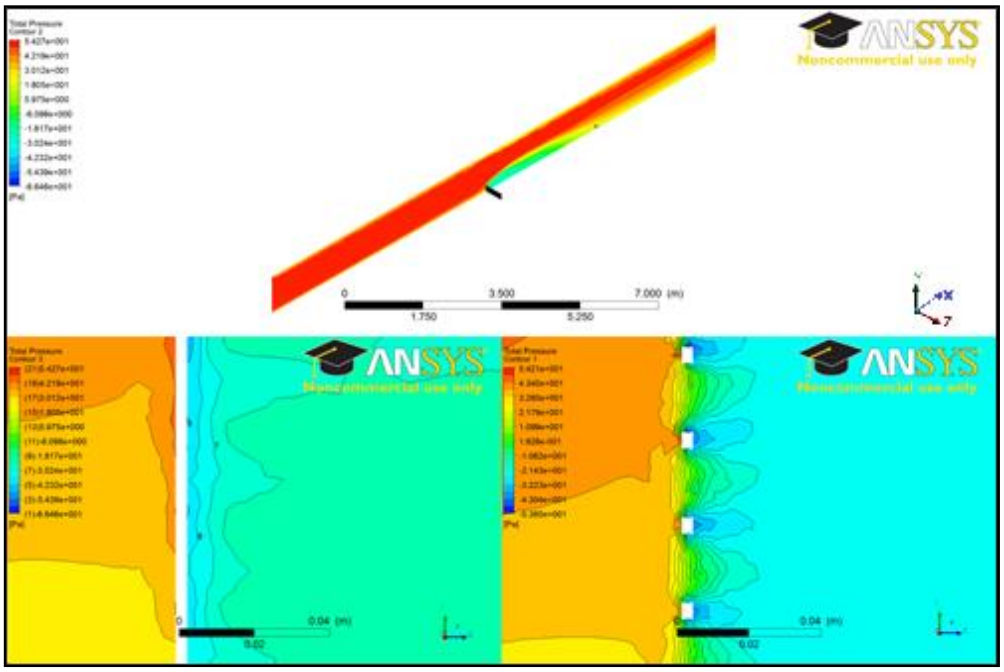

Figure 5-30: The contours of total pressure in the planes

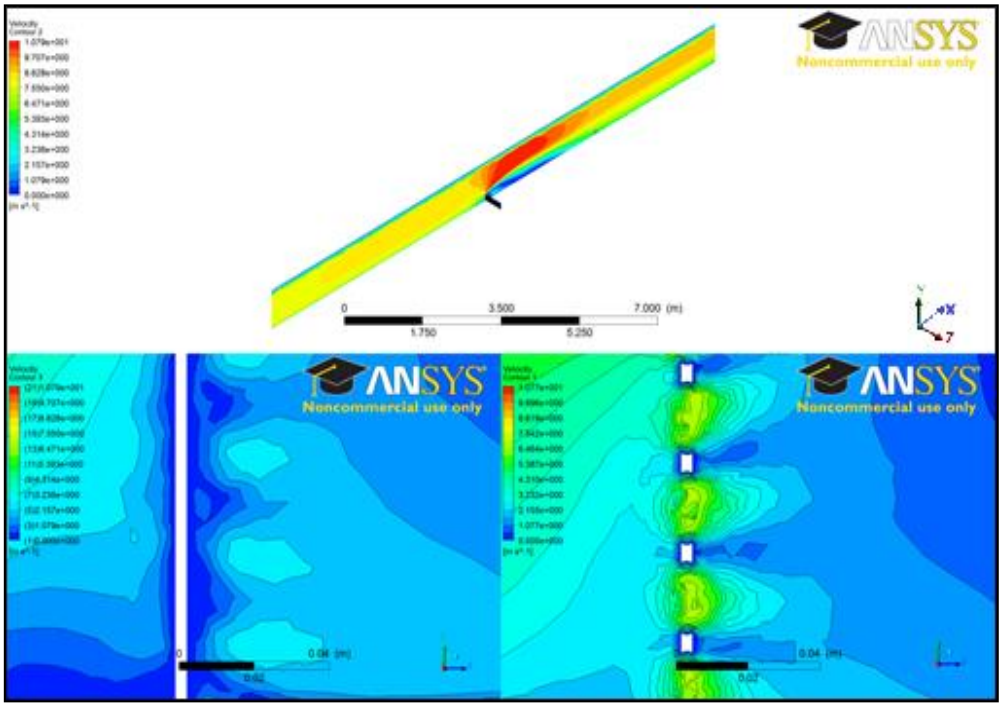

Figure 5-31: The contours of velocity in the planes

Figure 5-31 shows the contours of velocity magnitude in the planes. The top contour presents that the fence has created velocity reduction zones around the fence. Over the top edge of the fence, the velocity was accelerated and extended a certain distance leeward. The thickness of the fence is *3mm* that is quite thin, which can be considered the flow passing through the holes affected like by vena contracta, where velocities were noticeably accelerated in the region. However, it decayed quickly as well. Such bleeding flows were distinguishable in the very close fence region.

The porous fence has produced strong turbulent kinetic energies downwind shown in Figure 5-32. Inside the holes, the turbulent kinetic energy reached the highest level in the entire domain. On the contrary, the holes had limited impact on the local eddy viscosities, and a strong eddy viscosity zone was created approximately in the wake zone region seen in Figure 5-33.

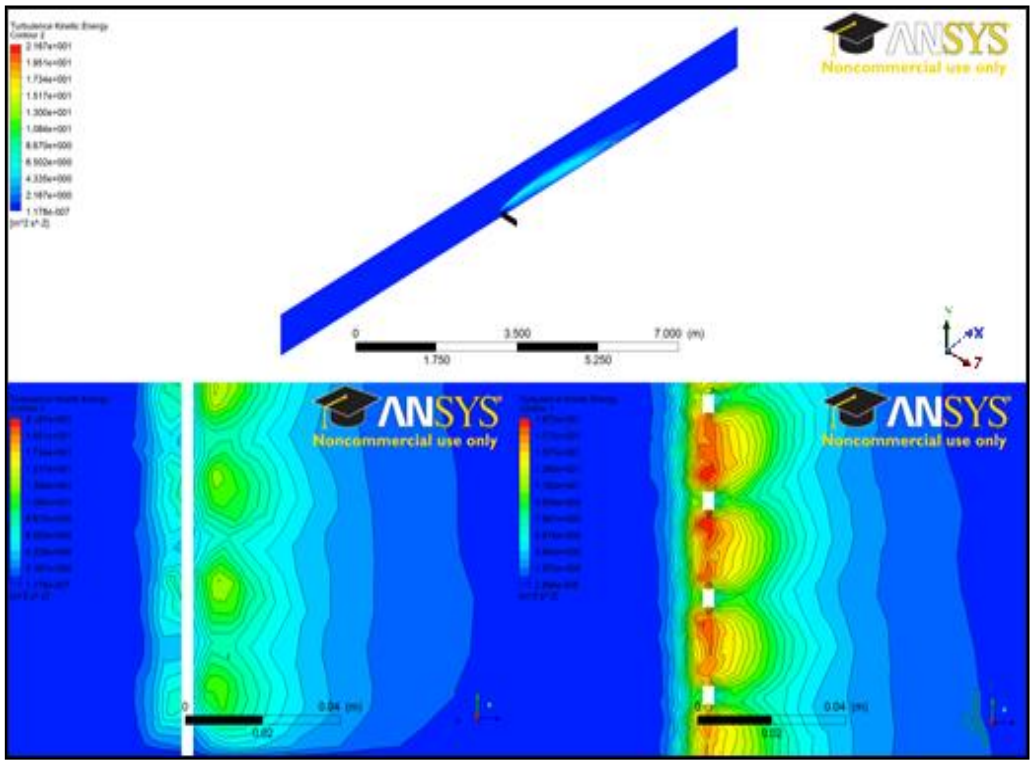

Figure 5-32: The contours of turbulent kinetic energy in the planes

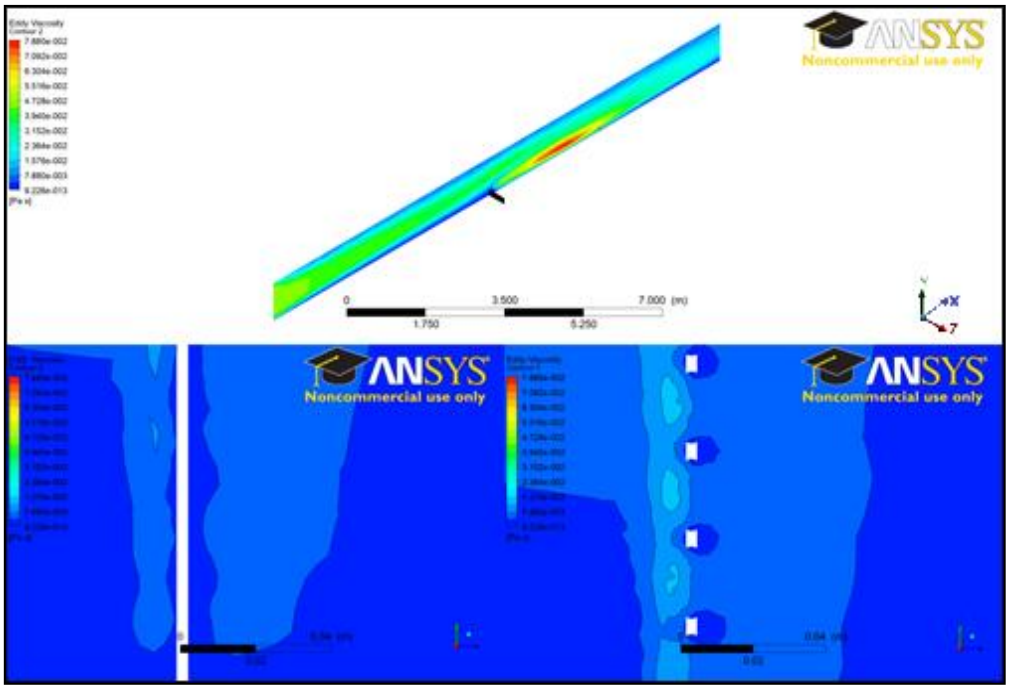

Figure 5-33: The contours of eddy viscosity in the planes

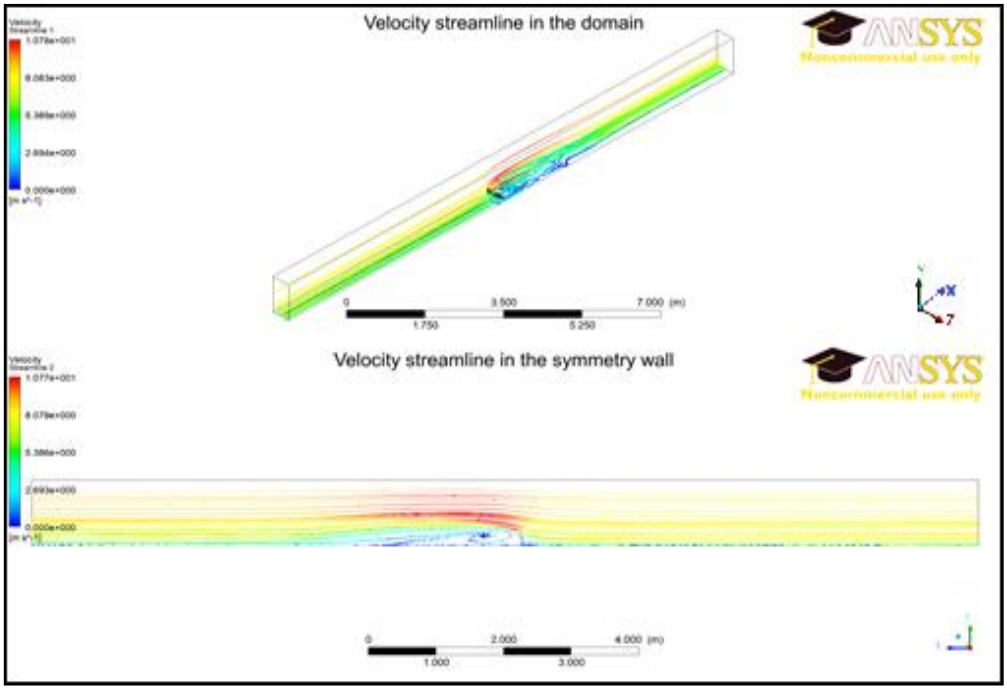

Figure 5-34: The velocity streamlines in the domain and in the symmetry wall

The post process enables to capture the streamlines at any of planes in the domain. Figure 5-34 presents the velocity streamlines, where the top is the velocity streamlines in the

entire domain, and the under is the velocity streamlines in the symmetry wall. This plot helps to understand in a form where the least resistance offered to the airflow. Flow circulations and a visual approximation of the fence effective zone can be found from the figure.

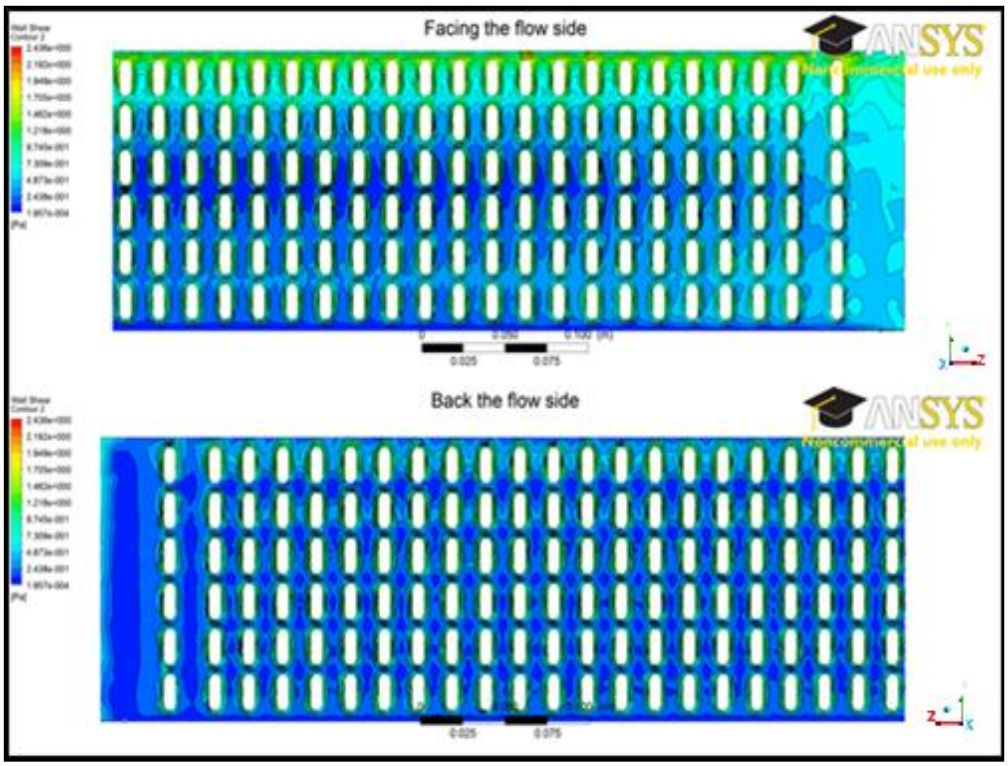

Figure 5-35: The contour of wall shear in the fence

The presence of considerable amount of holes in a porous fence will created a complex distribution of shear on the fence surface when encountered airflow. These shears result in producing large gradients to pressure, velocity and turbulence. It has been acknowledged that the distribution of fence shear is an important parameter in determining the feature of a porous fence. However, it has been a difficulty to be investigated by physical experimental techniques. It cannot be addressed under 2D CFD modelling too. The 3D modelling can provide such complementary information in detail. Figure 5-35 is the distributions of wall shear in two sides of the fence. It was observed that the front face presented far greater shear than the back face did. The value of shear was increased with the increase of the vertical height in the fence, which indicates that higher wind velocity encountered, higher wall shear created.

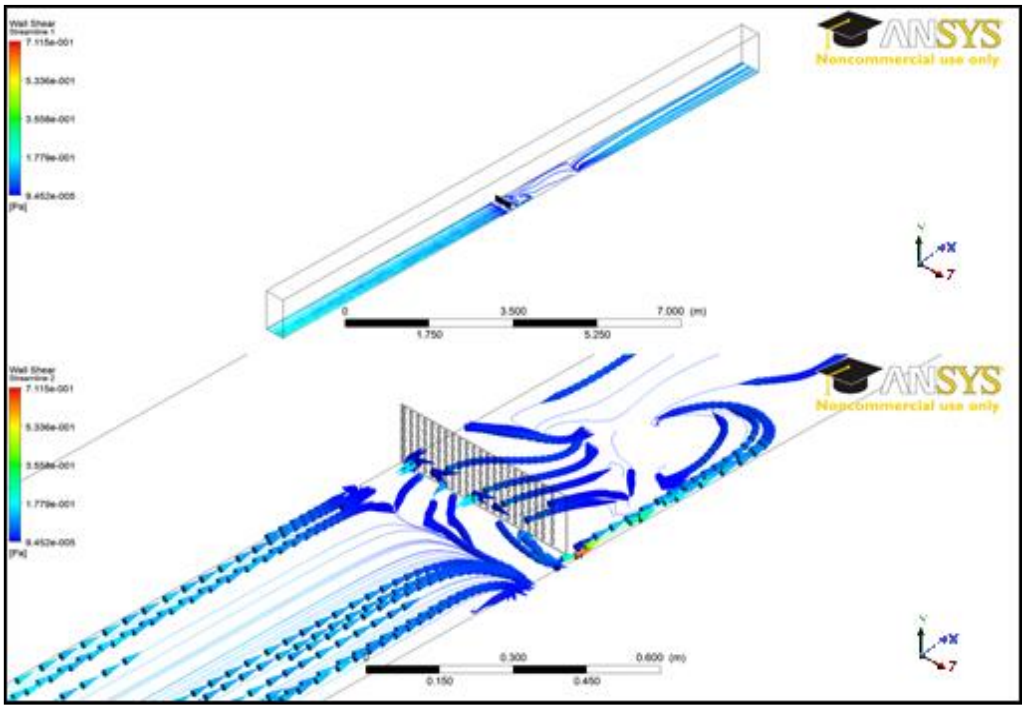

Figure 5-36: the streamline of wall shear in the floor

Close to the holes regions, higher wall shear was in presence. This founding suggests that the arrangement of holes in the near top edge of the fence may be considered in the fence designs.

A successful CFD modelling needs to provide correct information of wall shear distributions in a good resolution. This success has been demonstrated in Figure 5-36, where the top is the streamline of wall shear in the entire floor, and the under is an amplified one around the region where the fence is positioned. It can be observed that away from the fence, the wall shears were distributed evenly that were produced by the floor boundary layer. Near the fence region, the wall shears were affected by the floor and the bottom part of the fence, and the wind velocity had been greatly reduced, this resulted in reducing the values of shear and changing the pattern of shear distribution. It can also be noticed that the values of shear were increased in the region between the side edge of the fence and the sidewall of the domain; this was caused by the accelerations of the local velocity. The displayed streamlines of wall shear in the floor were in good agreement with the other CFD simulations. Modelling wall shears in the wall boundary layers is important to improve the accuracy in predicting structures of velocity and

turbulence, and is particularly important to model scaled CFD cases (the requirement of similitude). For modelling particle transport in wall-bounded flow, it is extremely import to obtain correct wall shears in a good resolution, since majority of such modellings are solved based on solving friction velocities that are derived from wall shears.

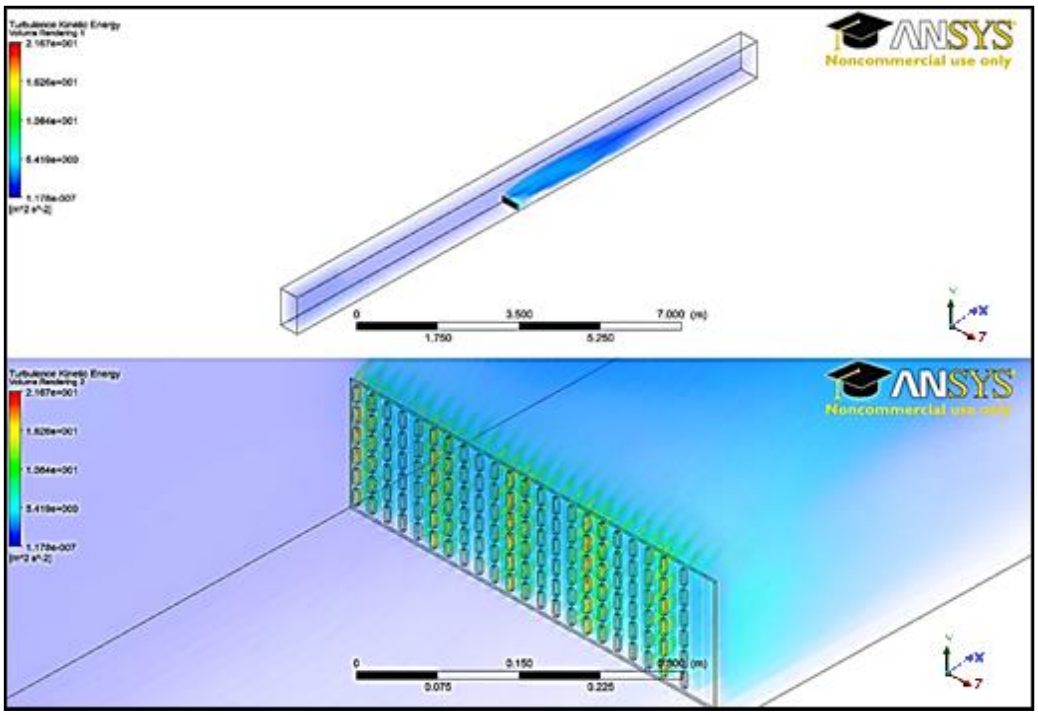

Figure 5-37: The volume render of turbulent kinetic energy in the domain

Figure 5-37 is the volume rendering of the turbulent kinetic energy in the domain. It was obtained with the resolution of *30* and the transparency of *0.2*. The volume rendering technique enables to visualize the CFD data for better understanding the processes in the simulation, and helps to assess the quality and efficiency of mesh. In Figure 5-37, the top shows that the concerned turbulent kinetic energies were captured in the effective element volumes. The under shows the changes of turbulent kinetic energies inside the holes captured in a good resolution. It also demonstrated that the elements with relatively large volumes have been arranged in the regions where the turbulent kinetic energy has trivial changes. The volume rendering has revealed that the current arrangement of mesh is sufficient and efficient.

Figure 5-38 demonstrates the contours of velocity magnitude and turbulent kinetic energy in the 2D modelling. These contours show the similar structures to the ones at the

symmetry wall in the 3D modelling. However, information of airflow insider the holes were unable to be delivered.

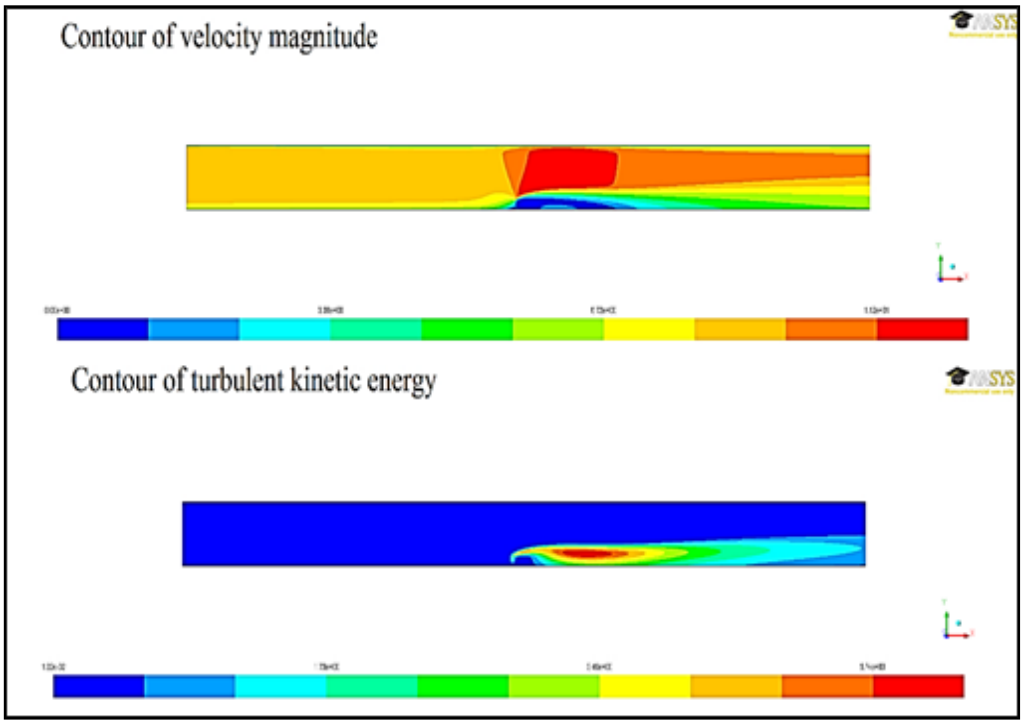

Figure 5-38: The contours of velocity magnitude and TKE in the 2D modelling

The post process has demonstrates its power and convenience in acquiring data in need. It can conduct graphic and numerical investigations at any position within the domain for the 3D modelling. It also can use the function calculator to obtain new variables, make tables and produce reports, etc. The discussions here are focus on the issues that are of main concern to the present research. The presented results have demonstrated the strength of the CFD modelling, especially for the 3D modelling.

5.7. INVESTIGATIONS ON EFFECTS OF THE ARRANGEMENT OF POROUS HOLES

Porous holes are the significant structural feature for porous fences. Rich literature can be found in the study of overall porosity. However, researches on the arrangement of porous holes, such as the effects of the size and shape of hole and the distribution of holes, are hardly to be found. Among the few, Davide et al (2013) have experimentally

investigated on the fences with circle or square shaped holes. His experimental results found that the effects of these two types of holes were negligible. Hagen & Skidmore (1971) reported that a porosity less than *0.4* near the fence top would cause excessive shear and turbulence, while low porosity near the bottom would create low pressure that induced a recirculation zone in the leeward area. Their comments were in agreement with the discussion on the distribution of fence wall shears in Section 5.5. Raine & Stevenson (1977) made a comment that the porosity of a shield should be increased from *0.0* at the base to *1.0* at the top, with an overall porosity between *0.2* and *0.3*. This comment was not supported by providing necessary scientific investigations. To the author's knowledge, there are no systematic physical experiments and no numerical simulations undertaken on these issues.

The numerical investigations on such issues have been carried out in this thesis. The standard *k-ω* turbulence model was employed in the simulations.

5.7.1. Investigations on the effects of shape of hole

Porous fences are commonly constructed with circle or oval shaped holes in the applications. For the point of view from engineering, this kind of design can avoid the presence of amount of angular corners in the fence. Sharp angular corners will create additional large gradients of shear, pressure around, which result in stress concentration, noise, vibrations, and intensify flow turbulent, etc. However, for some specific applications, porous fences may be constructed with holes formed by sharp corners. Such design is optimally to modify the structure of flow regime for special needs.

Figure 5-39 shows three types of shape of holes to be studied in the thesis, where the porosity was set at the value of *0.3* for all of them. Twelve holes were uniformly distributed and were located at the same central points. The height of hole is *50mm* for all of them too, that made the same local Reynolds number inside the holes if taking the height of hole as the reference length. This arrangement was to make the case as comparable as possible.

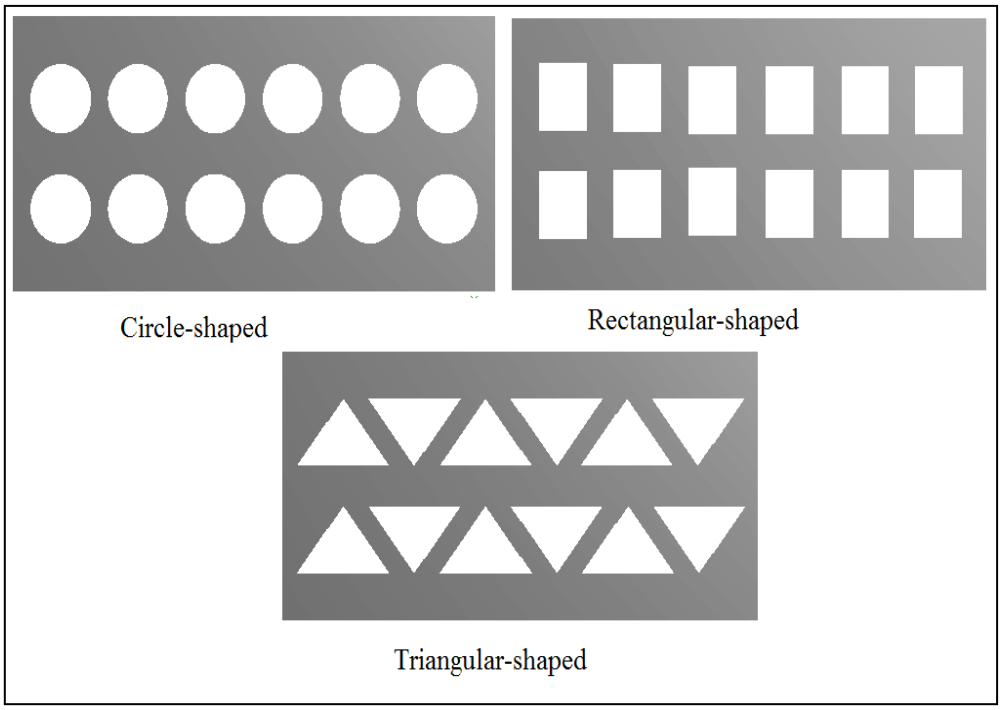

Figure 5-39: The testing fences with different shapes of holes

Triangular-shaped hole is usually to be avoided in the fence designs. The fence with triangular-shaped holes constructed here was to investigate how sharp angular corners affect the fence performance. The degree of the triangular was *52°*, *52°*and *76°*. The fourth fence was added to the investigation, where the angular corners were trimmed by a radius of *1mm*. The purpose of doing so was to investigate if the fence performance would be improved.

The configuration for all of the fences was *400mm* wide, *200mm* high and *3mm* thick. To minimize the effects of the boundary walls, the domain was constructed as *8.0m* long, *2.4m* wide and *1.2m* high. The fence was placed at the center of the cross section in the domain at a longitudinal distance of *3m* from the inlet, which was 15 times of the fence height. The distance between fence side edge and the domain sidewalls was *1.0m*, which was 5 times of the fence height. Such configuration was to reduce the effects of boundary walls at the minimum.

Mesh was adapted the same approach as the one discussed in Section 5.2.3. The first layer height to the floor was set at *0.1mm*, and then inflated to *10* layers with the growth rate of *1.1*.

To simplify the simulation, the inlet velocity was set at a constant of *10m/s* with *5%* of intensity and turbulent viscosity. The outlet was set the Gauge pressure of zero with *5%* of turbulent intensity and viscosity. The simulation was followed the same procedures discussed in Section 5.4.

The comparisons of velocity for each fence at the corresponding lines are presented in Figures from 5-40 to 5-44. In the near fence region of $h/H \leq 1.0$ and $x/H \leq 1.0$ seen in Figure 5-40, the fence with circle-shaped holes had the greatest velocity reductions among the others, and the fence with triangular-shaped holes was the least performer. In the region of $h/H \leq 1.0$ and $x/H \geq 1.0$, the fence with triangular-shaped holes became more obvious as the least performer among the others. However, the fences with circle and rectangular shaped holes have almost the same effects on the velocity reductions.

The fence after trimmed its angular corners has significantly improved its performance, which had almost the same performance as the fences with circle and rectangular-shaped holes did. Apart from in the region of $h/H \leq 1.0$ and $x/H \leq 1.0$, its performance seemed worsened shown in Figure 5-40.

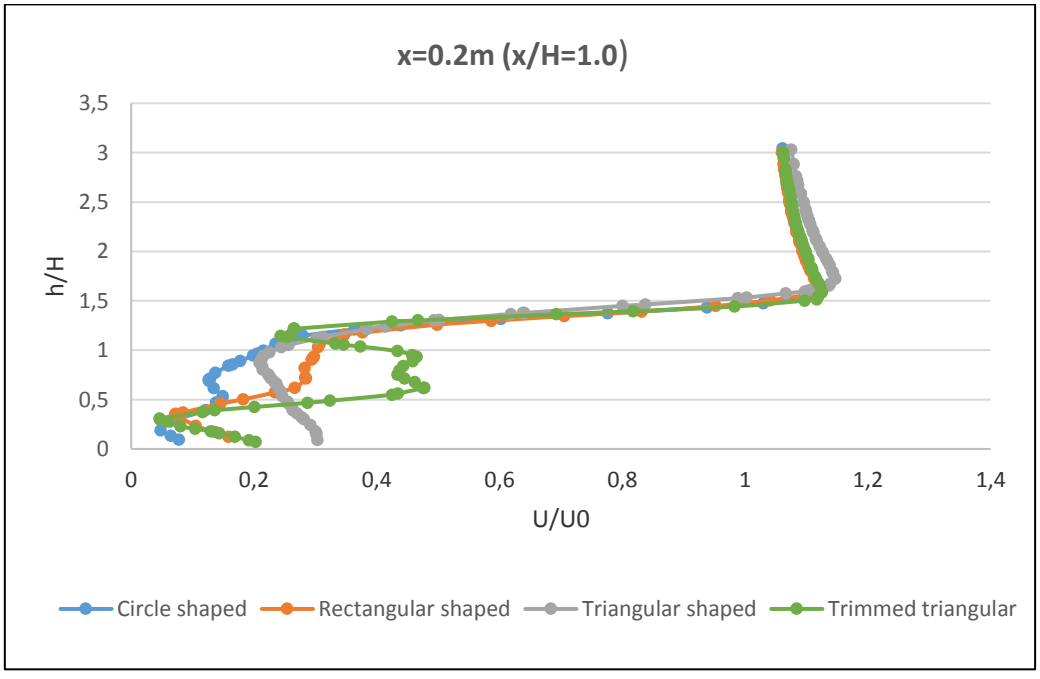

Figure 5-40: Comparison of velocity magnitudes at $x = 0.2m$ for study on shape of holes

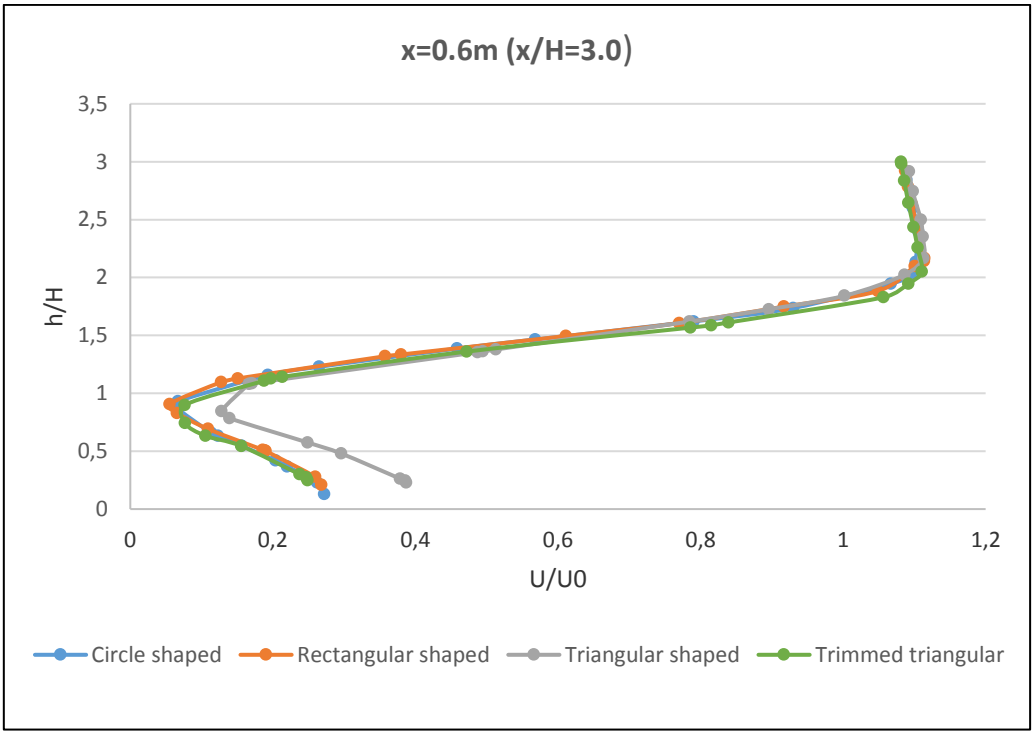

Figure 5-41: Comparison of velocity magnitudes at $x = 0.6m$ for study on shape of holes

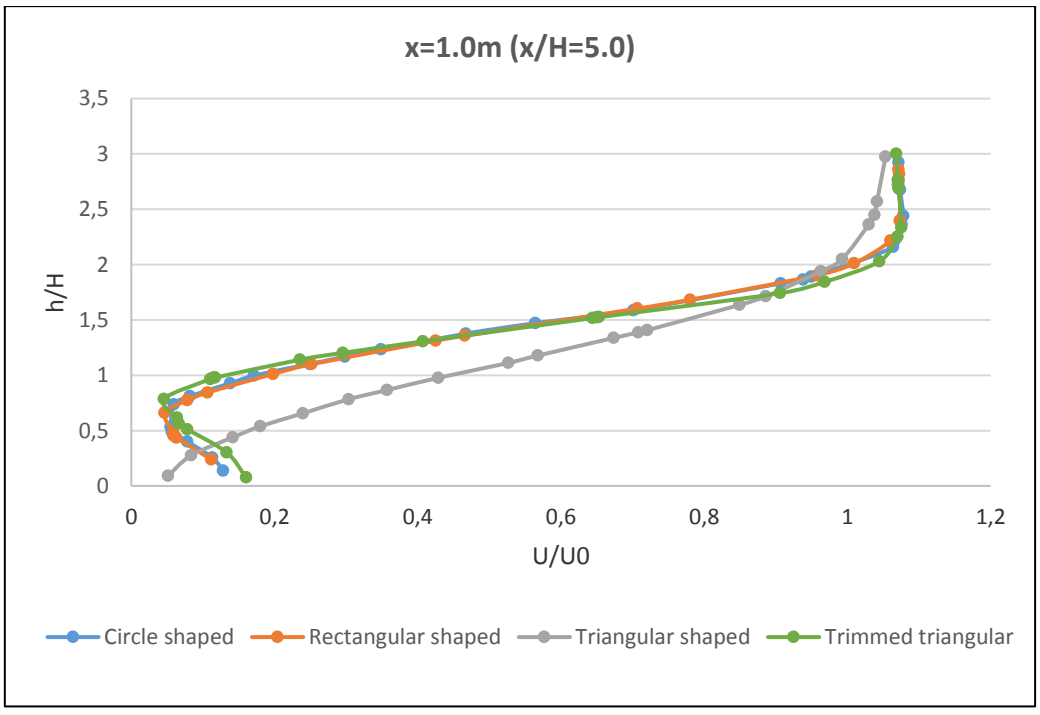

Figure 5-42: Comparison of velocity magnitudes at $x = 1.0m$ for study on shape of holes

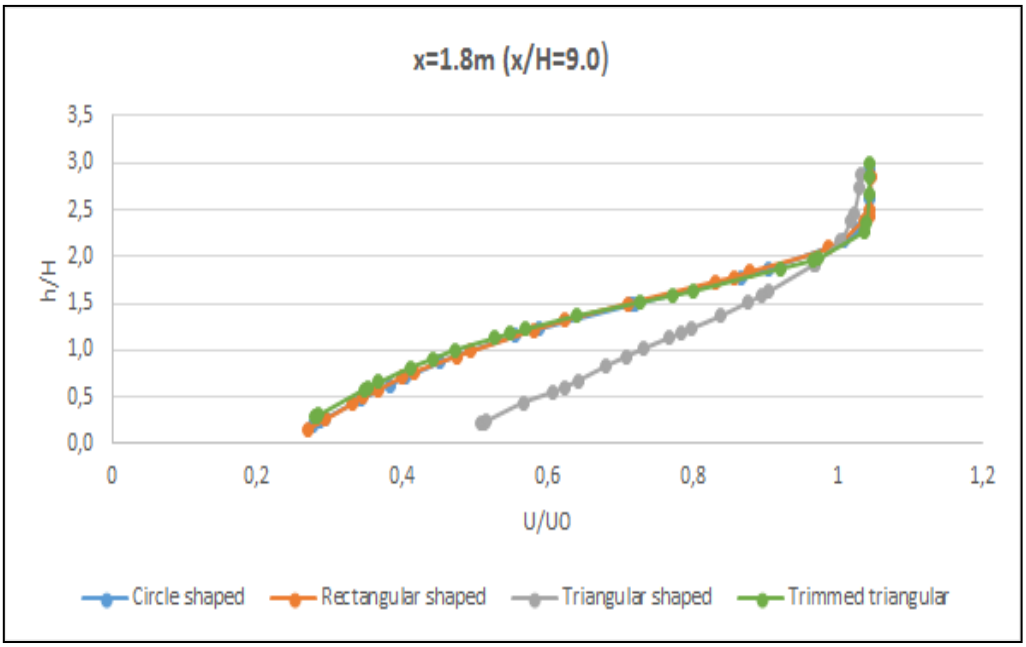

Figure 5-43: Comparison of velocity magnitudes at $x = 1.8m$ for study on shape of holes

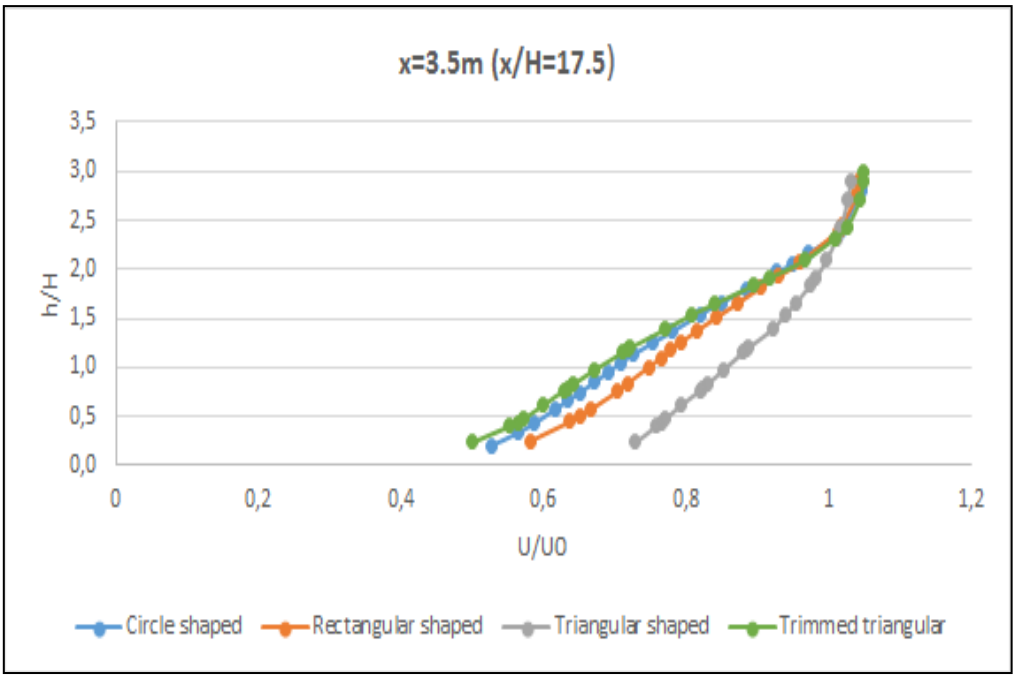

Figure 5-44: Comparison of velocity magnitudes at $x = 3.5m$ for study on shape of holes

The simulation found that the holes formed with sharp angular corners would greatly compromise the fence performance on velocity reductions and affected in a wide region shown in Figure 5-44. Significant improvement could be achieved by smoothing the

corners such as trimmed by a small radius. If the angle of the corners close to *90°*, the effects of corners could be diminished, as the fence with rectangular shaped holes had almost the same performance as the fence with circle shaped holes did.

Shape of holes has noticeable impact on velocity reductions for the fence only in the very near fence region shown in Figure 5-40. Beyond that, only the fence with holes formed sharp angular corners has been significantly affected in terms of velocity reductions.

Figures 5-45 to 5-49 presents the comparisons of turbulence intensity for each case at the comparing positions. The same to the velocity reductions, the fences with circle or rectangular had the turbulence intensity pretty in the similar structure except in the close fence region of $h/H \leq 1.0$ and $x/H \leq 1.0$. The fence with triangular shape holes created the least turbulent flow than the others except at $x/H = 3.0$ shown in Figure 5-47. On the contrary, the fence with trimmed triangular holes reduced the level of flow turbulence at $x/H = 3.0$ shown in Figure 5-46, and increased the level of flow turbulence in the rest regions. This demonstrated that smoothing sharp angular corners would increase the level of flow turbulent in general. It is understandable that sharp angular corners stagnated turbulence dissipation.

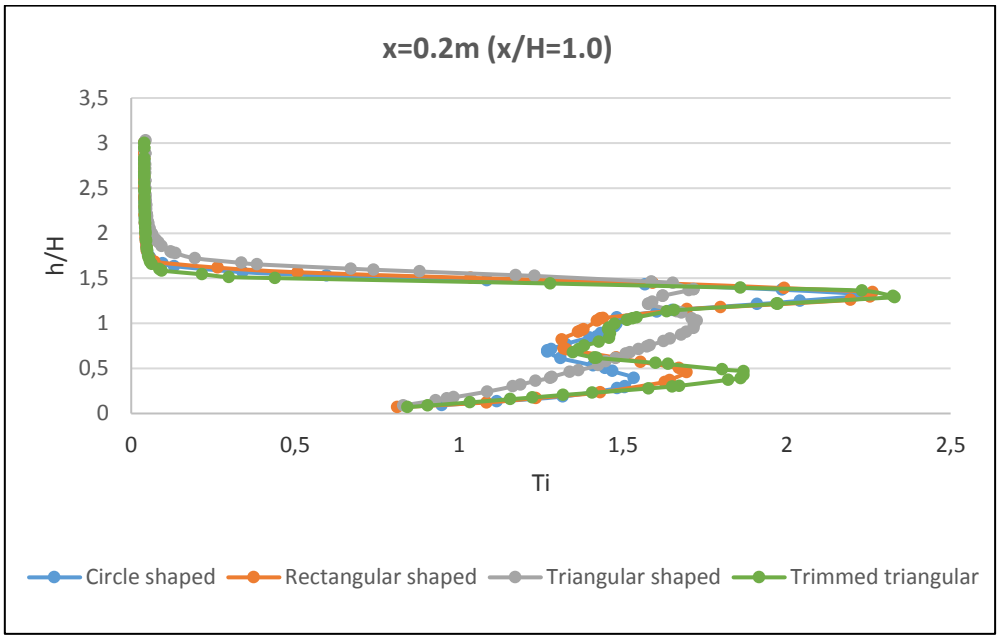

Figure 5-45: Comparison of turbulence intensities at $x = 0.2m$ for study on shape of holes

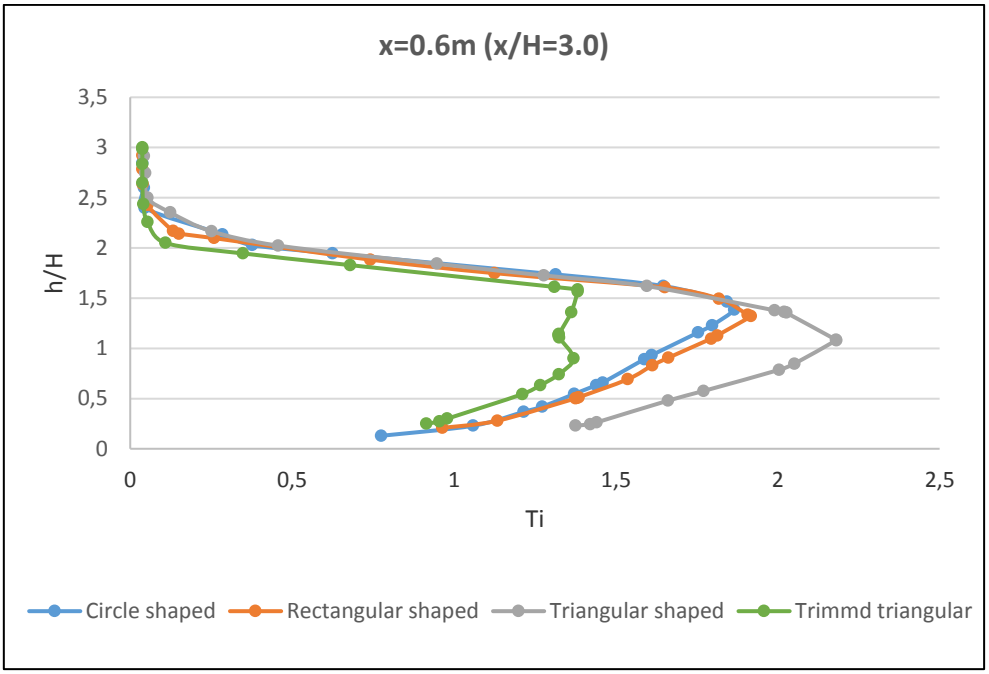

Figure 5-46: Comparison of turbulence intensities at $x = 0.6m$ for study on shape of holes

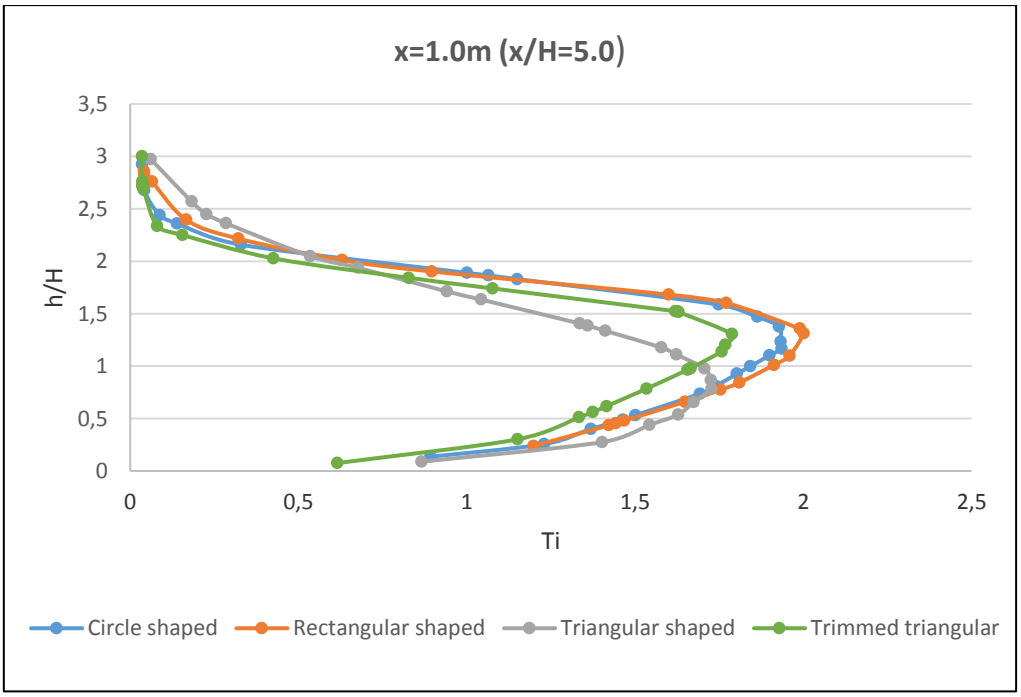

Figure 5-47: Comparison of turbulence intensities at $x = 1.0m$ for study on shape of holes

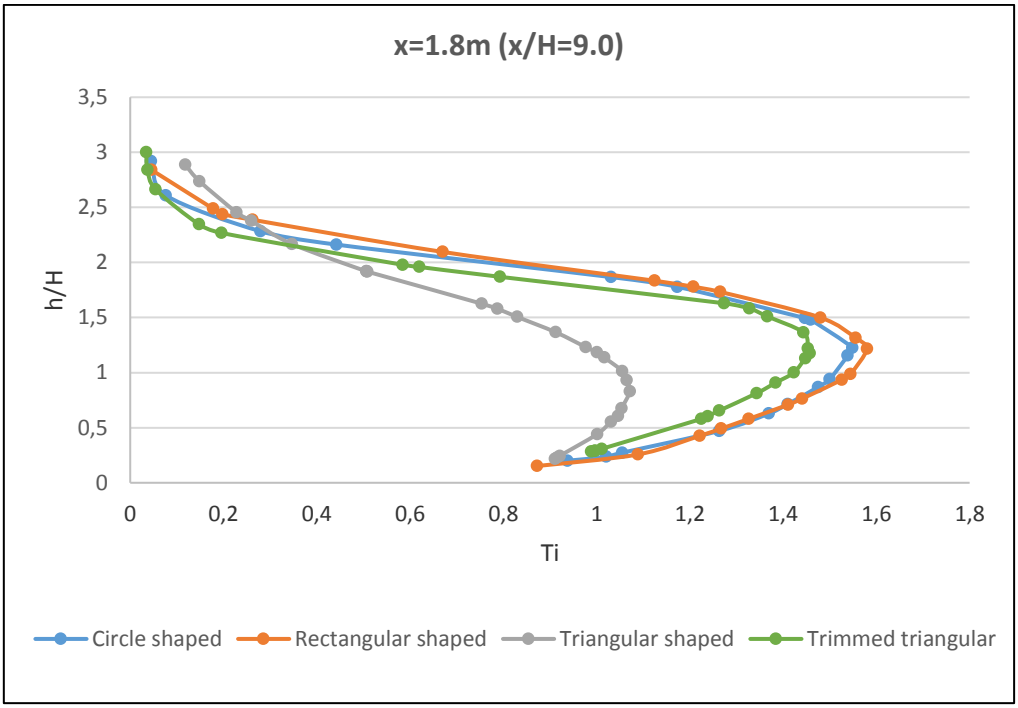

Figure 5-48: Comparison of turbulence intensities at $x = 1.8m$ for study on shape of holes

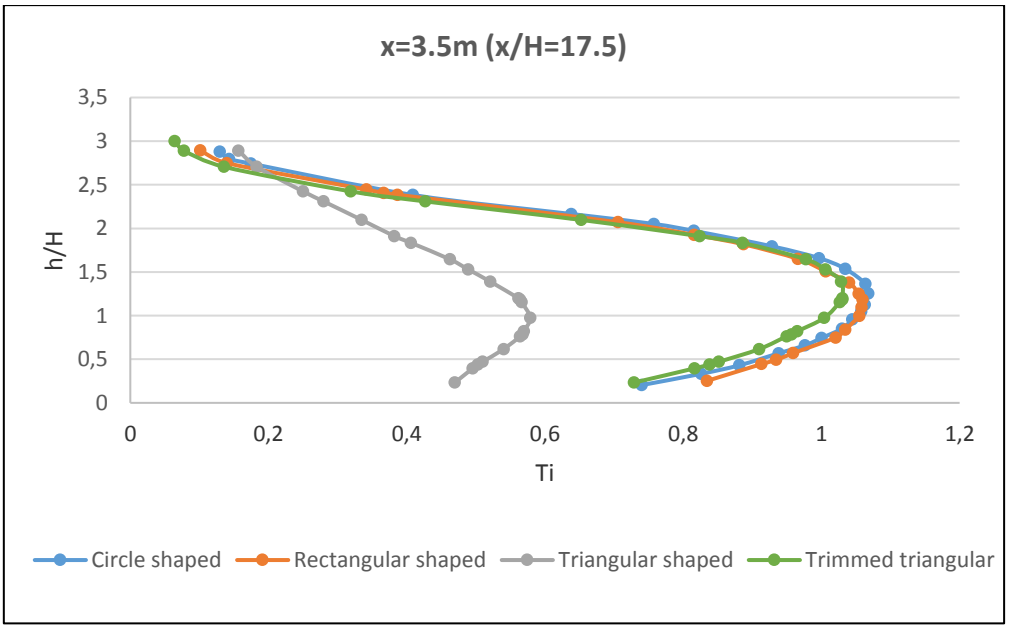

Figure 5-49: Comparison of turbulence intensities at $x = 3.5m$ for study on shape of holes

The simulation results revealed that shape of hole had noticeable impact on turbulent flow leeward the fences; particularly such impact was significant in the close fence region.

Beyond this region, the fences with circle or rectangular shaped holes had almost the same performance.

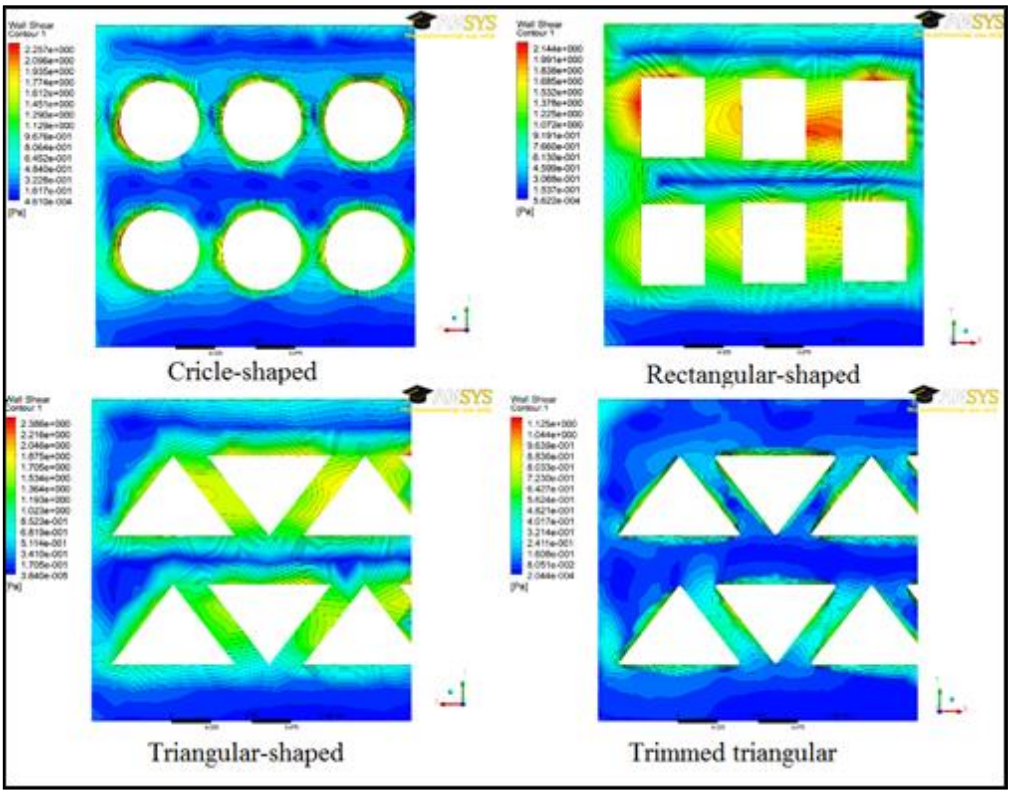

Figure 5-50: The distributions of wall shear stress on the facing flow fence faces (half of the fences)

Figure 5-50 shows the distributions of wall shear stress on the facing flow surfaces for the four fences. The presence of porous holes had created large gradients of shear on the fence surface. It can be observed that greater shears appeared at the regions near the top row of the holes, which indicates that higher velocity encounters, higher shear would be.

Table 5-4 summarized the maximum and the averaged shear stresses on the facing flow surface for each testing fence. The fence with triangular shaped holes had the greatest maximum shear stress on its surface than the others, the fence with circle shaped holes created the greatest averaged shear stress on the surface, and the fence with trimmed triangular shaped holes had the smallest values both in the maximum and averaged shear stresses. The reason is that the circumference of a circle was shortest among those of the other shapes for a given area, which could concentrate greater shear stress around; while the circumference of the trimmed triangular shaped was the longest, which reduced the

shear stress around. It indicates that the circumference of shape of hole affects the creation of shear stress on the surface. Smoothing sharp angular corners in the porous holes was effective to reduce the creation of shear stresses on the fence surface.

Table 5-4: The distributions of shear stress on the fence surface and reattachment lengths

Item	Circle	Rectangular	Triangular	Trimmed triangular
Maximum stress (Pa)	2.26	2.14	2.39	1.13
Averaged stress(Pa)	0.53	0.49	0.49	0.22
Reattachment length L(m)	1.33	1.37	1.21	1.43
L/H	6.65	6.85	6.05	7.15

For a wall-bounded flow, flow will separate from the bounded wall due to an adverse pressure gradient encountered as the flow expands downwind. This causes an extended region of separation flow, part of which separates the recirculating flow and divides the streamlines. The point where the dividing streamline reattaches to the wall is called as the reattachment point. Flow separation produces an increase in the flow losses, which is desirable for increasing the shelter distance for a porous fence. A fence with its porosity below the critical porosity (approximately in the range of *0.3-0.4*) will have significant effects on the flow separation. The longitudinal distance between the fence and the reattachment point is named as the reattachment length. It is an important parameter in determining the shelter distance for porous fences.

Dong et.al (2007) found in his wind tunnel experiments that the reattachment length varies as a function of fence porosity and approaching wind velocity, and the variation as a function of fence porosity is much more pronounced than that to the approaching wind velocity. His experiments revealed that the reattachment length decreased with increasing porosity from *0.1* to *0.2*. This finding indicates that maximizing wind reduction will sacrifice the effective shelter distance.

The reattachment point should be decided by examining the longitudinal velocity vector at ground level to identify the point where the longitudinal vector changes sign from upwind (negative sign) to downwind (positive sign), which is difficult to obtain from physical experiments. Physical experiments for the reattachment point usually takes the point (longitudinal velocity vector from negative to positive) in the downwind apex of the reverse cell, which is an approximate value (Dong, et al., 2007).

It is also a problem for numerical simulations to identify the position of the reattachment point, since the floor is usually treated as a no-slip condition wall which velocity vectors in the floor are computed as zero. However, when flow approaches the reattachment point, in both directions along the floor surface the shear stress should be zero. As such, the reattachment point actually can be captured without any approximation in CFD modelling, by the mean of identify the position where the shear stress is zero.

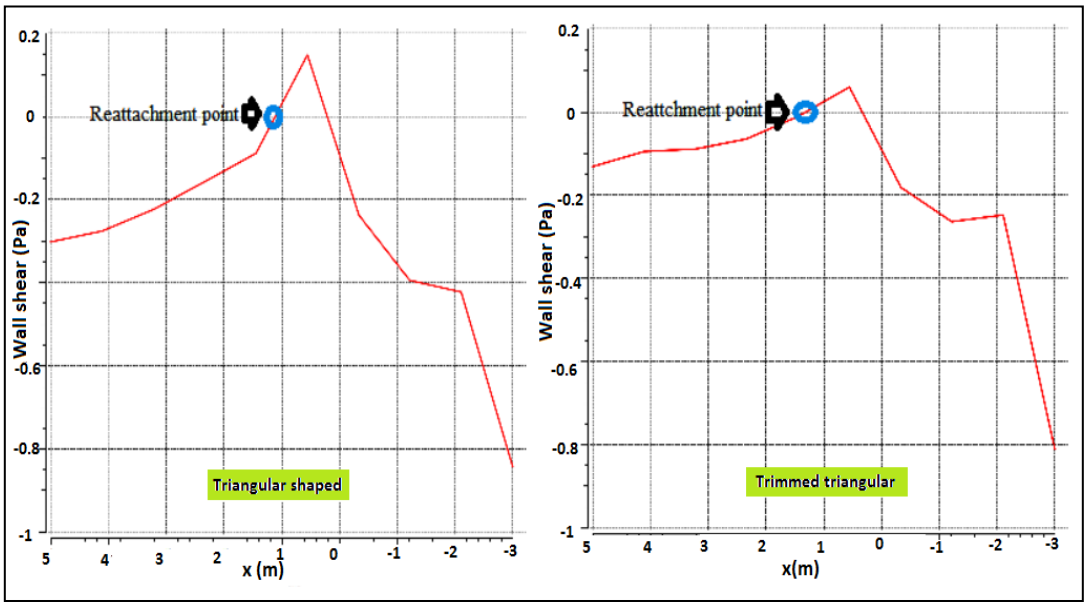

Figure 5-51: The x-direction shear stresses at the central line of the floor for the fence with triangular or trimmed triangular shaped holes

The longitudinal direction (x-) wall shear stress at the central line of the floor for the fence with triangular or trimmed triangular shaped holes is presented in Figure 5-51. The point highlighted in blue is the reattachment point where the shear stress is zero. It can be observed that the fence with trimmed triangular shaped holes produced more moderate

shear stresses around than the fence with triangular shaped holes did, and its reattachment length was longer too.

The detailed reattachment length for each case is concluded in Table 5-4. The reattachment length increased in the order from the fence with triangular shaped holes, the fence with circle shaped holes, the fence with rectangular shaped holes and the fence with trimmed triangular shaped holes. The simulations reveals that lower shear stress resulted in greater reattachment length, which implies that the reattachment length is associated with the distribution of wall shear stress.

The reattachment length for the testing fences was in the range from *6* to *7* times of the fence height, which was in agreement with Dong's experimental results (Dong, et al., 2007) if considering porosity increased from *0.2* to *0.3*. In his experiments, for the fence with porosity of *0.2* under the approaching wind velocity of *10m/s*, the reattachment length was *10.5* times of the fence height.

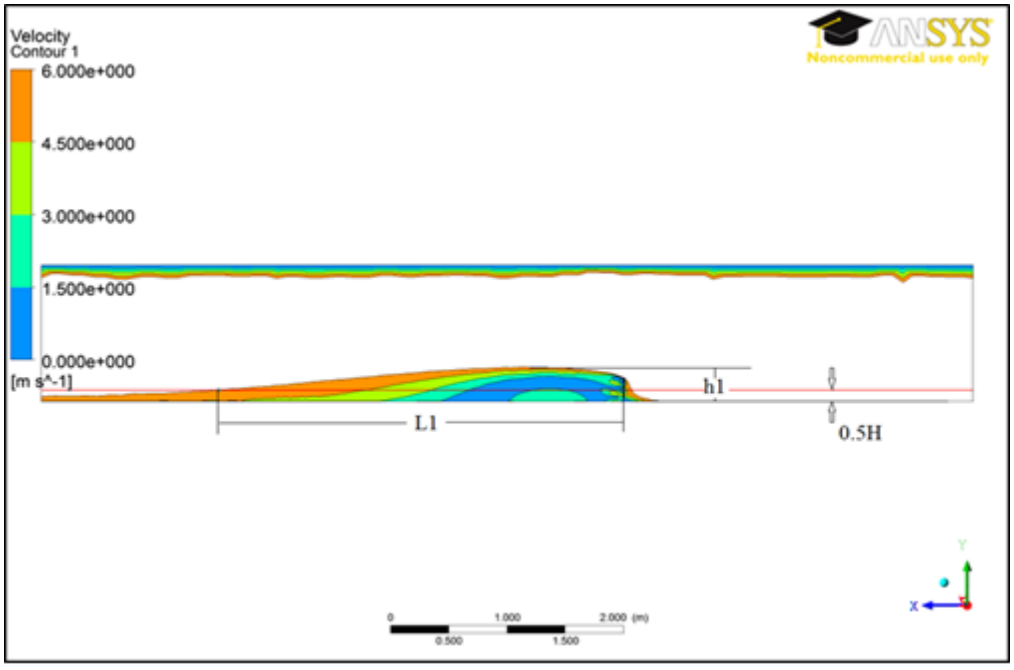

Figure 5-52: The effective fence for the fence with circle shaped holes in the symmetry

The definition of the fence effective zone (or the fence protection zone) is vague in the fence applications. Raine & Stevenson (1977) suggested that such zone should give a mean wind velocity reduction of *50%* up to *10H* downstream, *20%* up to *20H*

downstream, and a maximum reduction of *70-80% 1H-5H* downstream. These values were measured at half of the fence height.

In this thesis, the fence effective zone was assessed by *40%* of a mean velocity reduction, which the velocities on display were less or equal to *6m/s*. Figure 5-52 presents the effective zone for the fence with circle shaped holes in the symmetry plane. Figure 5-53 shows the effective zone for the fence with circle shaped holes in the cross section plane-1, which is at the distance of *9H* from the fence

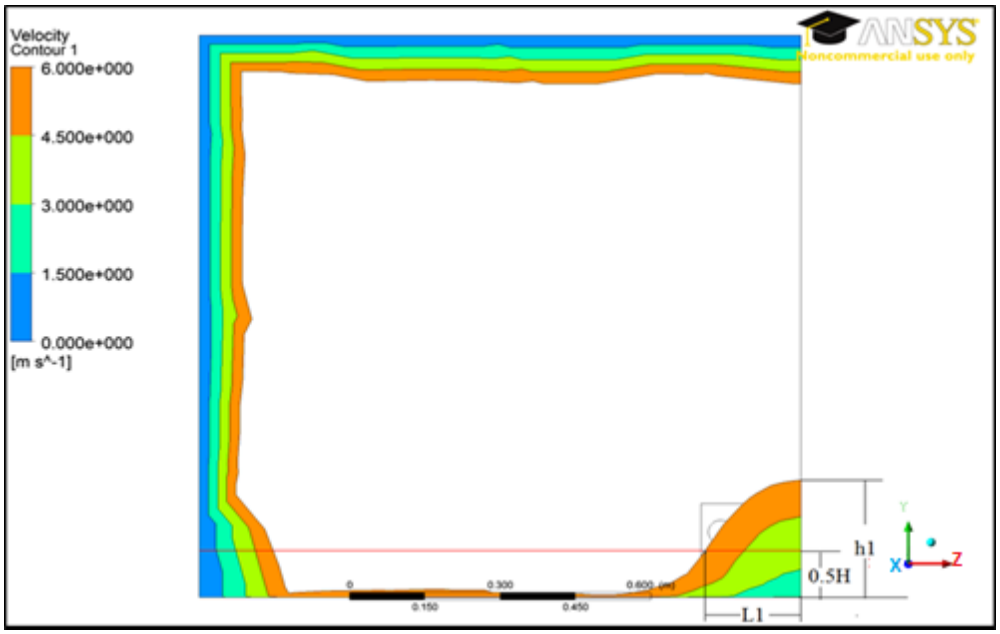

Figure 5-53: The effective fence zone for the fence with circle shaped holes in the plane-1

Table 5-5 is the summary of the effective fence zones for each fence in the symmetry plane and the plane-1.

From Table 5-5, the fences with circle shaped or rectangular shaped holes had the similar spectrum of the fence effective zone. The fence with rectangular shaped holes had the widest span in the plane-1 among the others. The fence with triangular shaped holes significantly reduced the spectrum of the effective zones both in the symmetry and in the plane-1. After trimmed the angular corners, the fence with triangular shaped holes has greatly increased the spectrum of the fence effective zone with the longest shelter distance in the symmetry. However, in the plane-1, its size was smaller than the ones created by the fences with circle or rectangular shaped holes. This finding was in consistence with

the one on the reattachment length, which again implies that the creation of fence effective zone is associated with the distribution of shear stress on the fence surface.

Table 5-5: Summary of the effective fence zones for each fence

Item	symmetry		Plane-1	
	L1/H	h 1/H	L1/H	h 1/H
Circle shaped	17.45	1.52	0.96	1.25
Rectangular shaped	17.31	1.52	1.01	1.25
Triangular shaped	9.35	1.47	0.27	0.53
Trimmed triangular shaped	19.30	1.48	0.89	1.22

Definition of the fence effective zone here was stricter than that of Raine & Stevenson (1977). The simulations found that the fences could be regarded as effective except the fence with triangular shaped holes. The results revealed that fence with sharp angular cornered holes would severely reduce the span of its effective zone and should usually be avoided in the fence designs.

The discussed fence effective zone did not take into account of the effects of turbulence in the regions where high level of turbulence may affect the healthy environment of the fence-confined space. Turbulence intensity induced by natural atmospheric flow hardly exceeds *0.8*. This is generally the upper limit of criterion for valuation of comfort rooms (Kovanen, K.; Seppanen, O.; Siren, K.; Majanen, A.;, 1989). Ideally a fence confined space should keep the inside turbulence intensity below this limit, consequently the porosity of the fence must be enough big to keep the bleed flow dominant. However, this will effectively reduce the span of fence effective zone both on velocity reduction and on shelter distance. Therefore, flows in the fence effective zones are usually in the presence of turbulence intensity higher than *0.8*. However, such evaluation has not found in other research work.

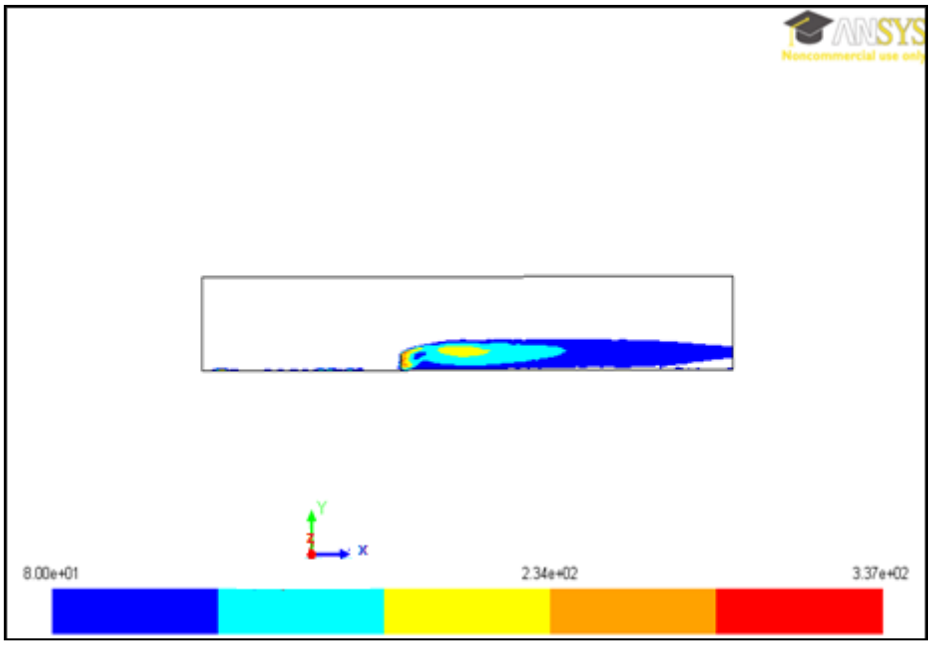

Figure 5-54: The contour of turbulence intensity greater than 0.8 in the symmetry

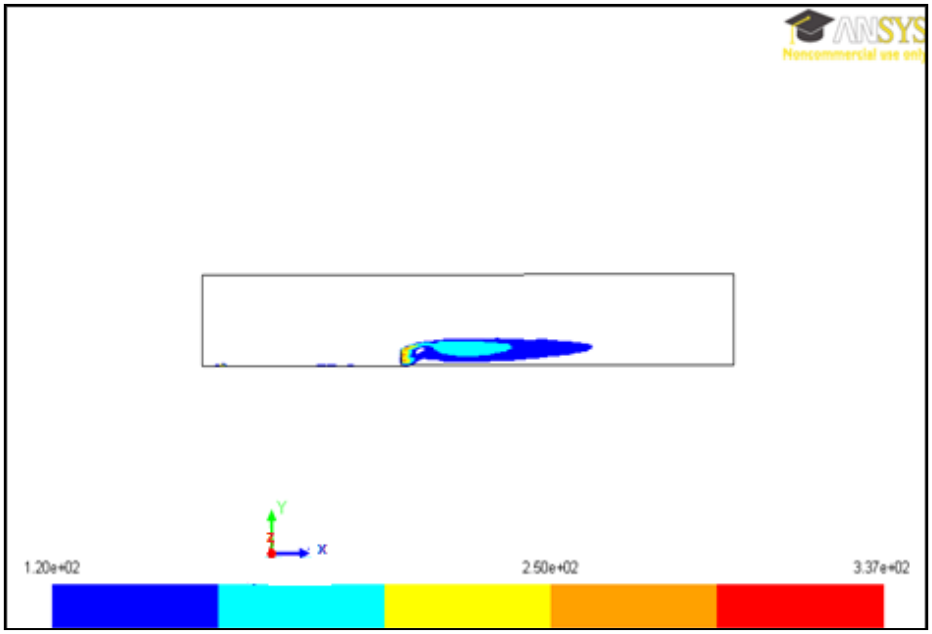

Figure 5-55: The contour of turbulence intensity greater than 1.2 in the symmetry

Figures 5-54 and 5-55 are the contours of turbulence intensity in the symmetry for the fence with rectangular shaped holes, where the turbulence intensity greater than *0.8* was plotted in Figure 5-54, and the turbulence intensity greater than *1.2* was plotted in Figure 5-55.

If considering desirable turbulence intensity below *0.8* in the fence effective zone, Figure 5-54 shows that there was almost no such space leeward the fence. However, if considering desirable turbulence intensity below *1.2*, Figure 5-55 demonstrates that there is a desirable space after the longitudinal distance of *12H* leeward the fence. Turbulence intensity should be expected to be higher in a porous fence confined space than an indoor environment.

5.7.2. Investigation on effect of the size of porous hole

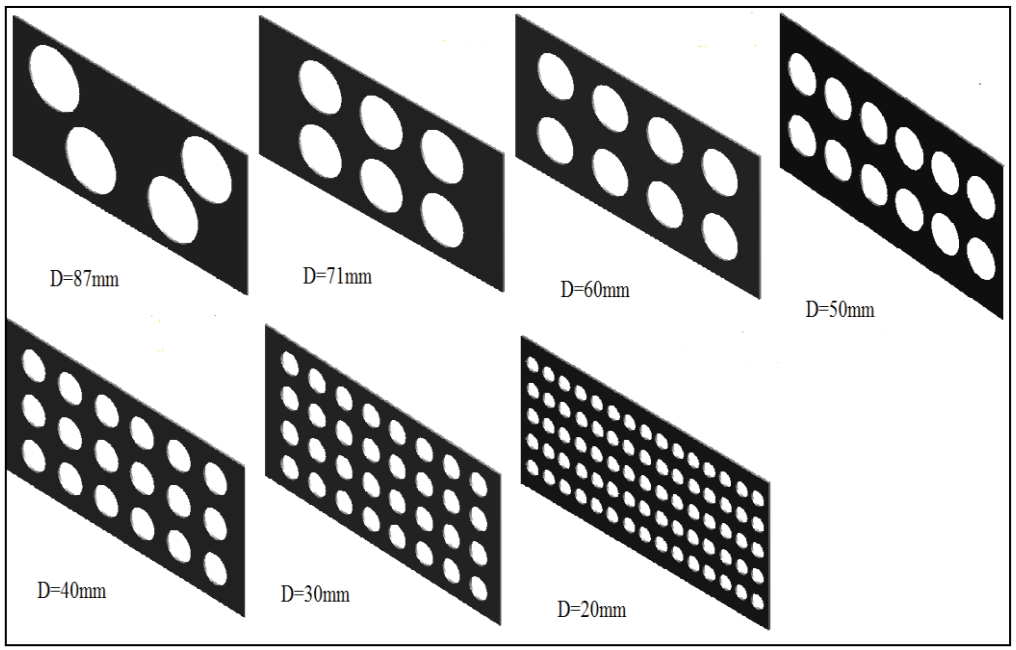

Figure 5-56: The fence models with porosity of 0.3

Considerable researches have revealed that the optimal porosity is in the range between *0.2* and *0.4* for tackling airflow problems. Porous holes without sharp angular corners has limited effects on the performance of the fence as discussed in Section 5.7.1. As such, the porosity of *0.3* with different circle shape holes was used to create the CFD fence models to investigate the effect of the size of holes.

The configuration of fence was *400mm* long, *200mm* high and *3mm* thick for all of the fence models. Figure 5-56 displays the seven testing fences. This arrangement actually consists of the changes of holes in the size and in the distribution.

The domain creation and the numerical procedures were the same as the ones in Section 5.7.1. Table 5-6 lists the elements applied to each case.

Table 5-6: Elements for grid independence

Fence	Elements for grid independence (million)
D=87mm	0.63
D=71mm	0.63
D=60mm	0.67
D=50mm	0.70
D=40mm	0.73
D=30mm	0.78
D=20mm	0.88

The detailed comparisons of the velocities and turbulence intensities for all of the seven testing fences are presented in App-Fig. 24-25 in Appendix F. Generally, the size of hole had noticeable impact on the performance of porous fence, particular in the region close to the fence. However, such impact did not act in a profound way. The simulation results revealed that the performance of the fences was not sensitive when the size of hole was in a certain range. Beyond the range, the fence acted noticeably differently, especially in the near fence region. Statistically, the sizes of hole with diameter of *3mm*, *4mm* and *87 mm* were the divisive points where the flow structure had noticeable changes. For better presentation, the following discussions were based on these three divisive cases, instead of presenting the data of all of the seven testing model. Figures from 5-57 to 5-60 are the comparisons of velocity magnitude at the corresponding position lines leeward the fences. Figures from 5-61 to 5-64 are the comparisons of turbulence intensities.

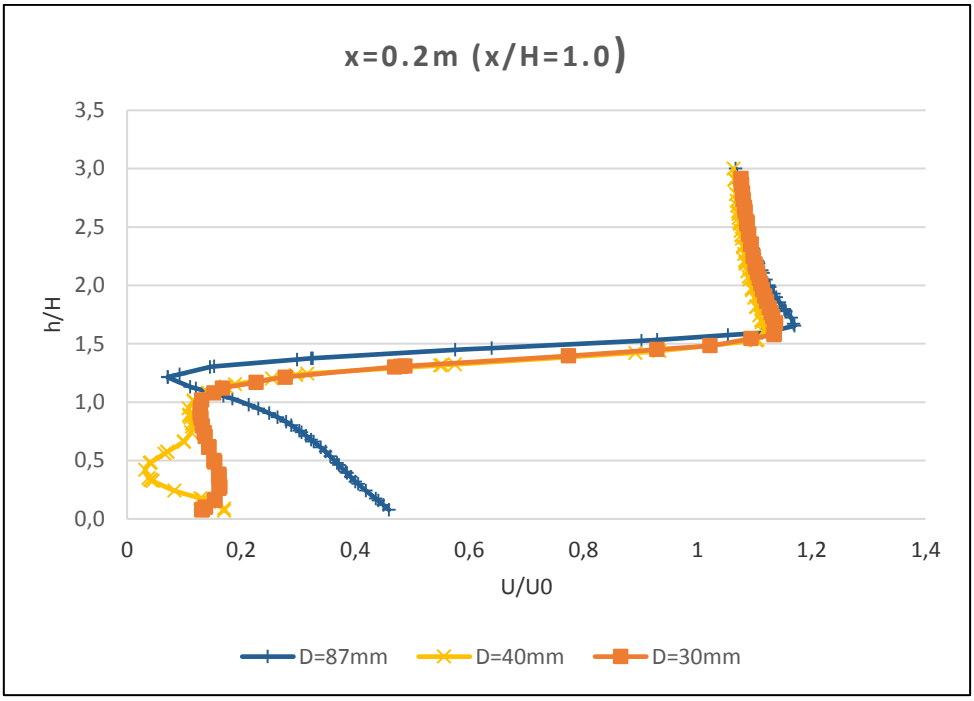

Figure 5-57: Comparison of velocity magnitudes at $x = 0.2m$ for the study on size of holes

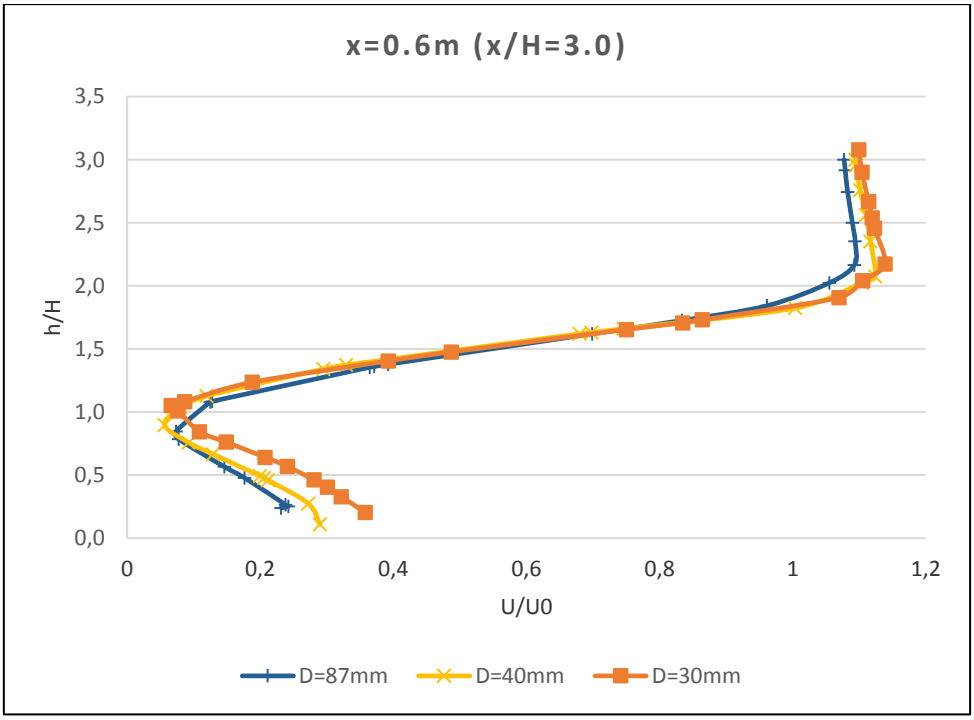

Figure 5-58: Comparison of velocity magnitudes at $x = 0.6m$ for the study on size of holes

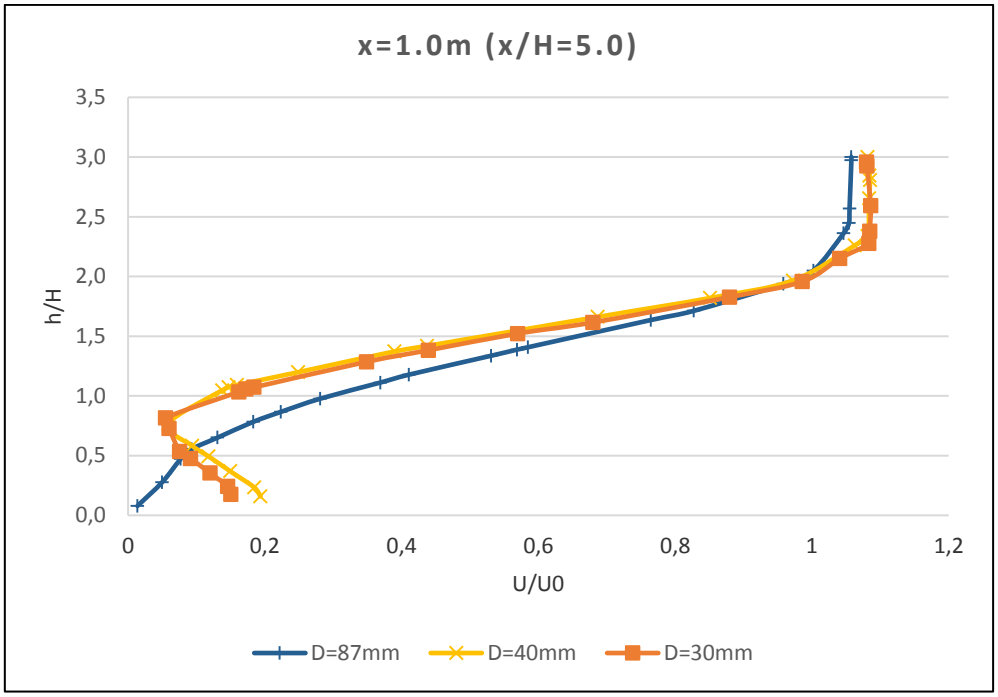

Figure 5-59: Comparison of velocity magnitudes at $x = 1.0m$ for the study on size of holes

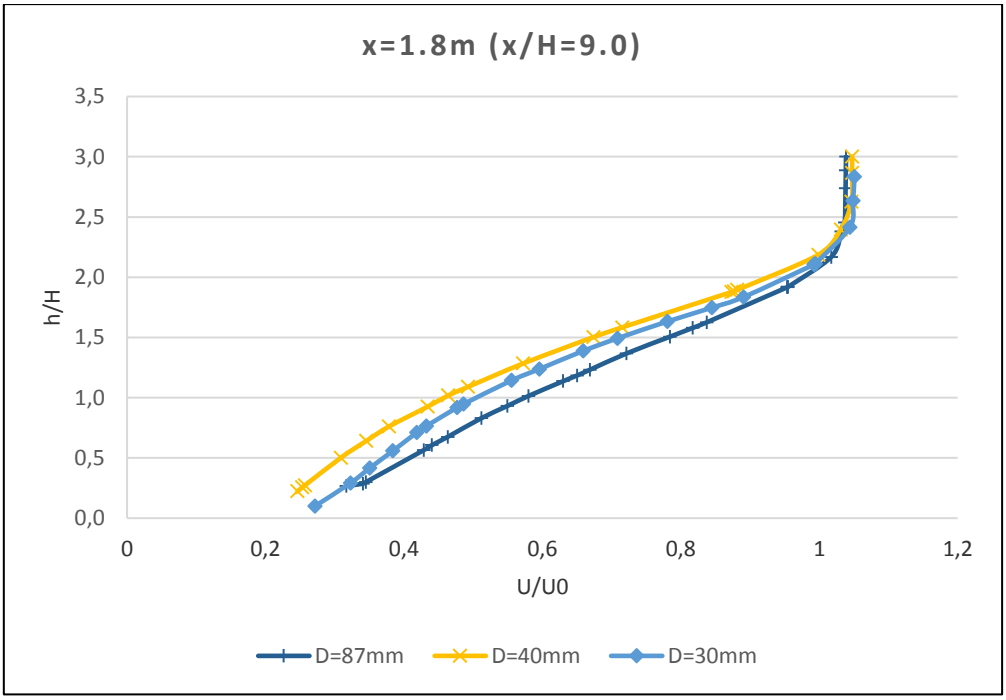

Figure 5-60: Comparison of velocity magnitudes at $x = 1.8m$ for the study on size of holes

In terms of velocity reduction, Figure 5-57 shows that the fence with the diameter of *40mm*holes performed the best, while the one with the diameter of *87mm*holes did the

least. It can be observed that size of hole had noticeable impact on the performance of fences particularly in the region within the fence height. The fence with the diameter of *30mm*holes was the least performer and the rest two acted quite similarly in Figure 5-58. The least performer changed to the fence with the diameter of *87mm* holes and the rest two acted quite similarly. In Figure 5-60, all of the velocity curves appeared in a similar trend with the values close each other at each comparable position. In this region, the effect of size of hole was insignificant.

It can be observed that the fence with the diameter of *87mm*holes actually weakened the velocity accelerations over the height of *2H*, which indicates that increasing size of hole might mitigate velocity accelerations over the fence. From the comparisons, the size of hole had noticeable impact on the performance of fences only in the region of $h/H \leq 1.0$ and $x/H \leq 5.0$. The fence with the diameter of *40mm*holes is the best performer in terms of effective reduction of velocity. The diameter below *30mm* or above *87mm* resulted deterioration in the ability of velocity reduction for the fences.

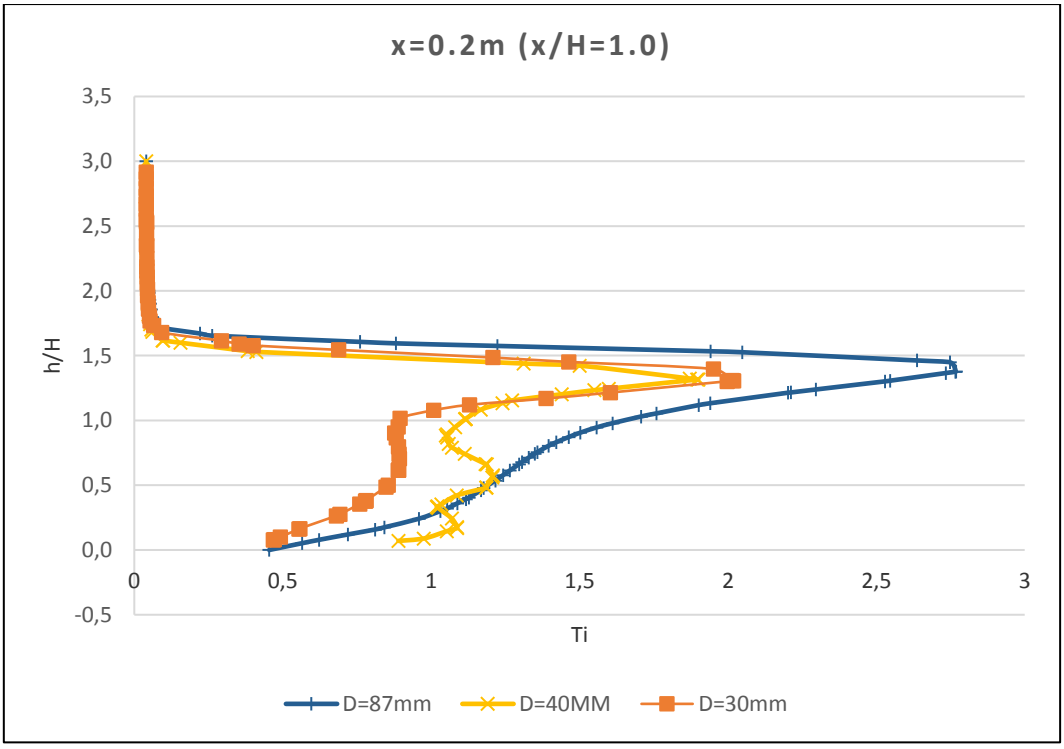

Figure 5-61: Comparison of turbulence intensities at $x = 0.2m$ for the study on size of holes

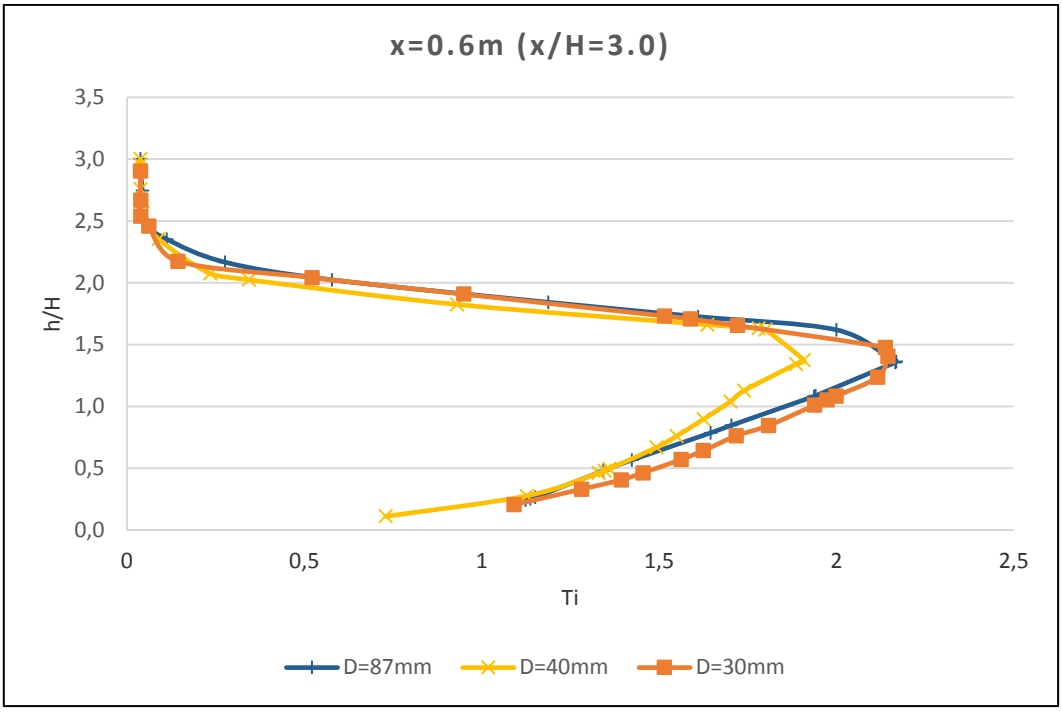

Figure 5-62: Comparison of turbulence intensities at $x = 0.6m$ for the study on size of holes

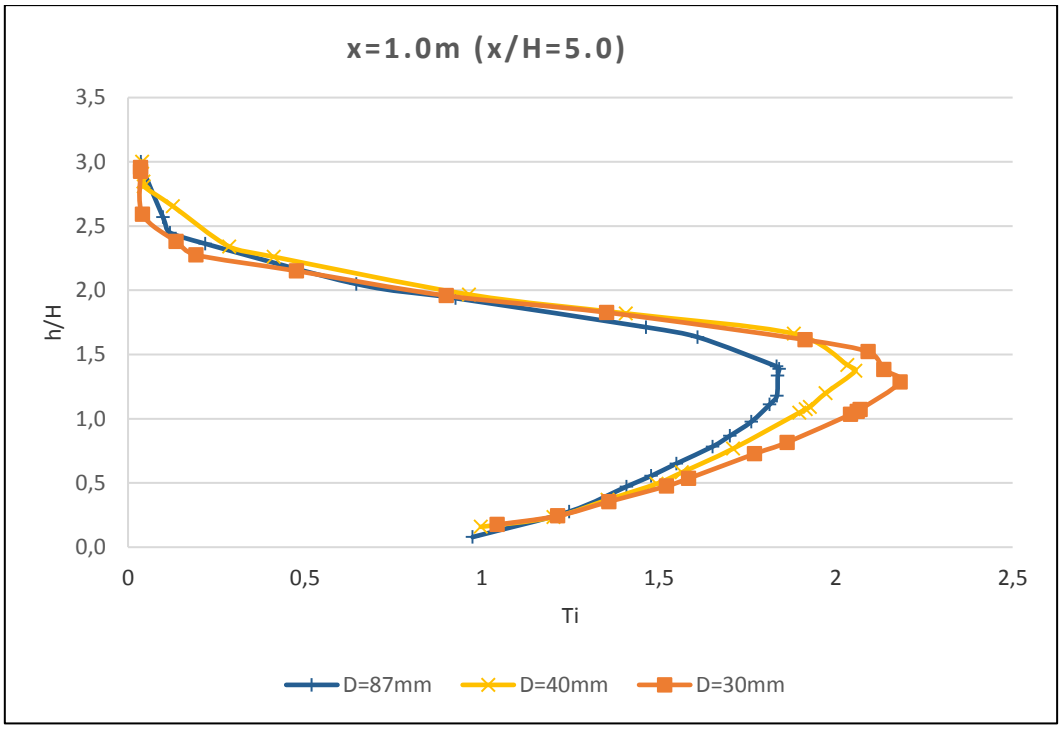

Figure 5-63: Comparison of turbulence intensities at $x = 1.0m$ for the study on size of holes

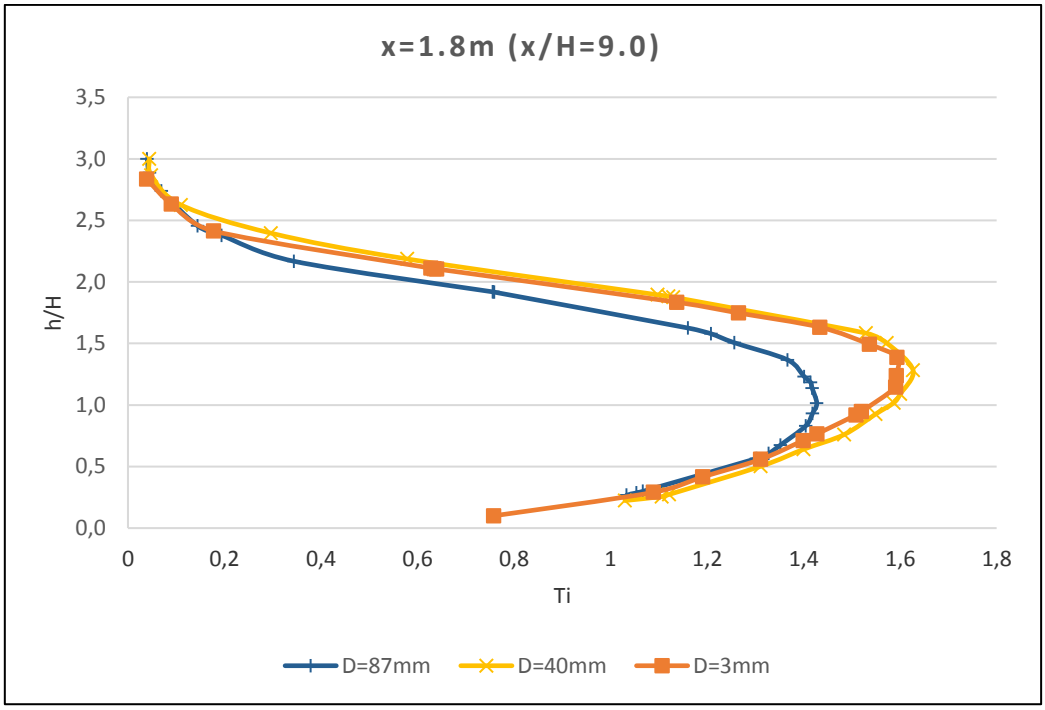

Figure 5-64: Comparison of turbulence intensities at $x = 1.8m$ for the study on size of holes

In general, larger or lower the diameter of hole at a certain value produced greater turbulence intensity in the near fence region shown in Figures 5-61and 62. However, away the distance of $x/H = 5.0$ from the fence, the fence with the diameter of *87mm* has created the least turbulent flow, and the one with the diameter of *30mm* had the highest level of turbulent flow shown in Figures 5-63 and 5-64. The results revealed that lower size of holes would enhance the flow turbulent with a greater span. The fence with the diameter of *40mm*holes generated a moderate turbulent flow among the others, as its maximum turbulent intensity was less than *2.0* in general.

Based on the numerical results, the size of hole has noticeable impact on the performance of fences in the near fence region. Statistically the fence with the diameter of *40mm*holes was the best performer among the others if assessed by velocity reduction and moderate turbulence intensity. It suggested the existence of an optimum range of the size selections, where the diameter below *30mm* and above *87mm* resulted deterioration in the effectiveness of the fence. It is however not a key factor influencing the performance of porous fence. If the near fence region is of concern, the size of shape needs to be considered.

The simulation also implied that the distribution of holes had insignificant impact on the fence performance, as the fences were intentionally created by different distributions of porous holes.

5.7.3. Summary

The numerical investigation on the effects of the arrangement of porous holes has been systematically conducted in this section. The summaries are as follows:

1) The fences with circle or rectangular shaped holes had almost the same performance. However, triangular shaped holes had significant negative effect on the performance of the fence. Great improvement for the performance could be achieved by the means of smoothing the sharp angular corners in the triangular shaped holes such as trimming with a small radius. It indicates that a fence with shape-cornered holes results in significant reducing its effectiveness. Such kind shape of hole should usually be avoided in the fence designs.
2) A novel approach was applied to investigate the correlation to the creation and distribution of fence surface shear, the reattachment length, and the size of fence effective zone. The Investigation found that the reattachment length and the size of fence effective zone were associated with the creation and distribution of fence surface shear, and reducing shear stress on the fence surface could improve the fence performance.
3) The size of hole had noticeable impact on the performance of fences only in the near fence region. There was a desirable size range of diameter of hole that was greater than *3mm* and less than *87mm*. In this desirable size range, the performance of fences was not sensitive to the selection of sizes. Out of this range, the size hole would have negative effects on the fence performance. Generally, size of hole is not an important factor to influence the performance of porous fences. However, for the case where the close fence region is of concern, designing size of holes may be important.
4) It is not realistic or at least not efficient to have turbulence intensities below *0.8* in the fence protection zone. However, high turbulent flow may affect the healthy

environment in a fence-confined space. Future work should take turbulence as an effective factor into defining effective fence zone.

5) Different distributions of holes have been intentionally configured in the testing seven fences. The numerical results implied that it was not an important factor influencing the performance of the fences.

The investigation provides recommendations to the optimal fence design: designing shape of hole should consider the creation and distribution of fence surface shear, the size of hole should be in the desirable range, and sharp angular corners in porous holes should usually be avoided. However, a degree of sharp angular corners in holes may be considered in the fence design when the low level of turbulent environment is required.

5.8. INVESTIGATION ON THE EFFECT OF NON-NORMAL WIND LOADS

In the real word, it is not realistic to expect that fences encounter flow in the normal direction all time. In fact, natural wind keeps changing its direction with time. However, for a certain location, statistically natural wind comes a certain degree of direction more often than the other degrees of direction. This suggests that allocating fences in a specific area should take considerations of such statistic degree of wind direction for maximizing their performance. Physical experimental investigations related to this subject can be found in Richards & Robinson (1999) and Briassoulis, et al. (2010). Numerical investigations on this subject are comparatively new.

Wind loads on a panel can be written as the following:

$$F = \frac{1}{2} c_d A_{ref} \rho U_{ref}^2 \qquad \textbf{Eqn.5-17}$$

where F is the force on the panel, A_{ref} is the reference area where the wind loads are applied, U_{ref} is the wind velocity at a reference height, and ρ is the density of air. c_d is the aerodynamic force coefficient (or drag coefficient), which is dependent on the shape and material of the panel. Letchford (2001) performed wind tunnel experiments to investigate c_d for elevated permeable and impermeable panels, where the dependence of

c_d on the geometric characteristics of height, width and bottom gap has been studied. However, his study was focused on elevated impermeable and low porosity (less than *0.23*) panels. He proposed a correction factor for the low porous panel that was $1-\beta^{1/2}$.

When a porous fence encounters wind flow with an angle θ, where θ is the angle between the onset wind and a normal to the fence. It is foreseeable that the normal area of the fence is reduced by a factor of $\cos\theta$. Wind forces acting on the fence at such angle is split into a normal force due to the pressure difference and a frictional drag force parallel to the plane of the structure. Richards & Robinson (1999) suggested that the loss coefficient could characterize the wind loads on porous structures. The loss coefficient is described as a function of porosity and the construction of the fence. When porous structures are at an angle θ to the wind, the effective loss coefficient is reduced by a factor of $(\cos\theta)^2$.

In this thesis, the testing fence was the same as the fence with circle shaped holes in Section 5.7.2. So did to the configuration of domain. Since the domain was no longer symmetric due to the fence positioned with an angle θ to the cross section, the simulations were performed in the full domain instead of a half domain. There were six cases investigated, which were the fence at θ of *0°*, *10°*, *15°*,*30°*,*45°* and *60°*, respectively. The meshed elements were in the range around *0.85* million due to the position of the fence changed the structure of the domain slightly. The inlet velocity was at a constant of *10m/s*. All of the numerical procedures were the same as the one in Section 5.7.2.

5.8.1. Investigations of fence effective zone

The fence effective zone was defined as the region where the velocities have been reduced to *40%* of the inlet wind velocity, which the presented velocities were less or equal to *6m/s*. The comparisons were based on the plane-1 that was an XY plane at the center of the longitudinal cross section.

Figure 5-65 shows the fence effective zones at different angles of wind load. The fence effective zone was evaluated by the length of effective shelter distance of *L1* and the height of the crest of *h1*. It can be observed that non-normal wind loads on the fence has reduced the size of effective fence zone in the plane-1. Increasing the angle θ, the size of effective fence zone was reduced accordingly. Increasing θ from *0°* to *10°*, it immediately

reduced the shelter distance approximately to *30%*. From *10°* to *30°*, the shelter distance continued reducing but not in a dramatic way. After *30°*, the situation was dramatically deteriorated.

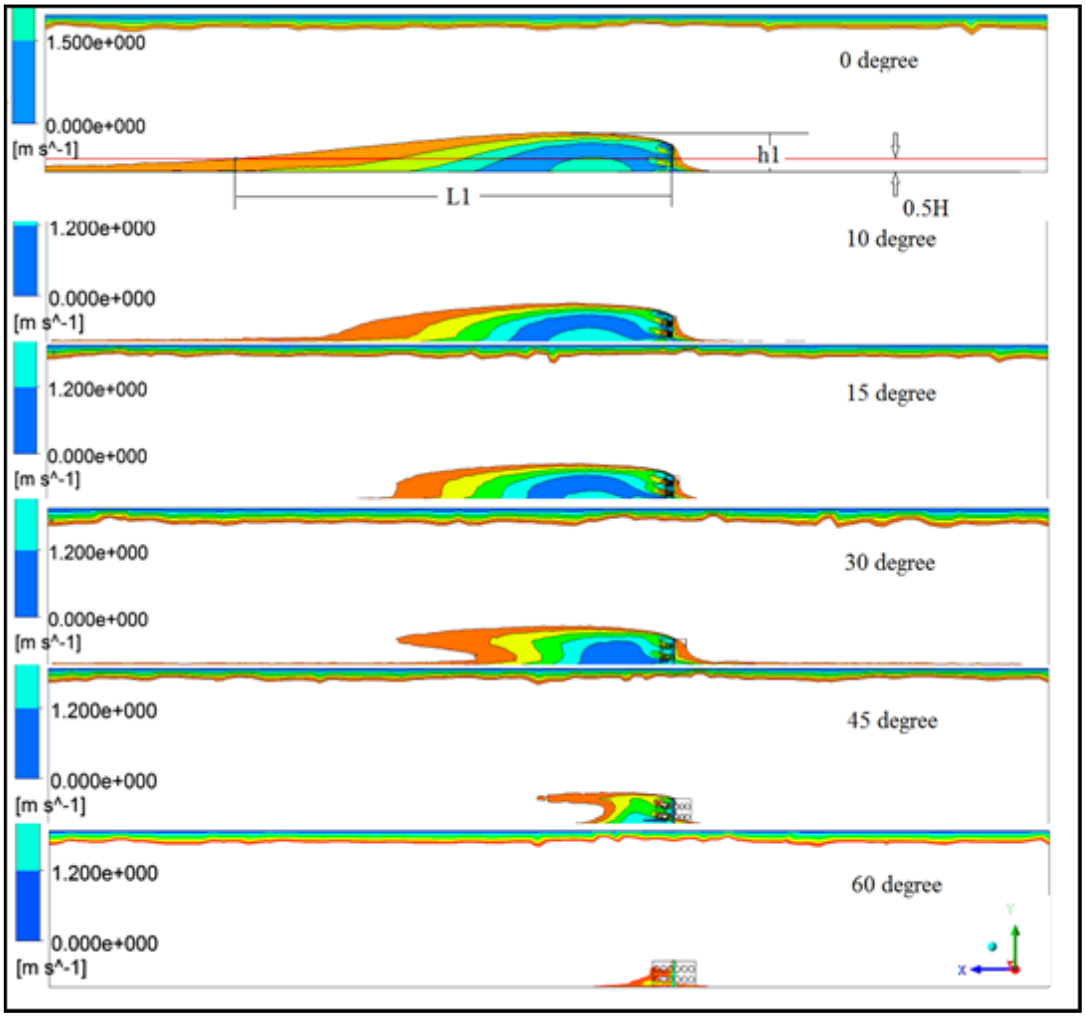

Figure 5-65: The effective fence zones at different angles of wind load

Further investigation on the effective fence zone was performed to offset the plane-1 to $z/H = 0.25$, *0.5* and *0.75*, respectively. The summary of the investigation is demonstrated in Figures 5-66 and 5- 67. The axis Y in Figure 5-66 was expressed as ratios of *L1/H*, and in Figure 5-67 as a ratio of *h1/H*. The axis X was expressed angle degrees for both.

Figure 5-66 shows the effective shelter distance decreased with the increase of the angle degree except in the region of the angle degrees between *0°* and *10°*. In the regions of the

planes at $z = 0m$ and $z = -0.05m$, the effective shelter distance appeared to be decreased, while at $z = -0.10m$ and $z = -0.15m$, it appeared to be increased. The maximum effective shelter distance was at $z = 0m$ with $\theta = 0$, which indicates that the maximum effective shelter distance was created by the fence encountered by *0°* degree wind load. It can be observed that the effective shelter distance was increased with the plane shifted away in the left from the position of $z = 0m$ except at $z = -0.15m$ at the angle degree of *60°*. This was due to the span of effective fence zones shifted to the left side. This also could be visualized from the streamline shown in Figure 5-68, which again demonstrated that it was more efficient to place fences normal to wind loads.

Both of Figures 5-66 and 5-67 revealed that the effective shelter distance dropped relatively slowly in the range from *10°* to *30°*. It was also true to the height of crest that was almost stable in this region shown in Figure 5-67. It was because that the height of crest was more associated with the fence height in the fence effective region. The results revealed that when wind loads at an angle greater than *45°*, it almost destroyed the effective fence zone. Therefore, Fences must be placed with an angle degree less than *30°* to the wind loads. It is preferable to be placed within *15°*.

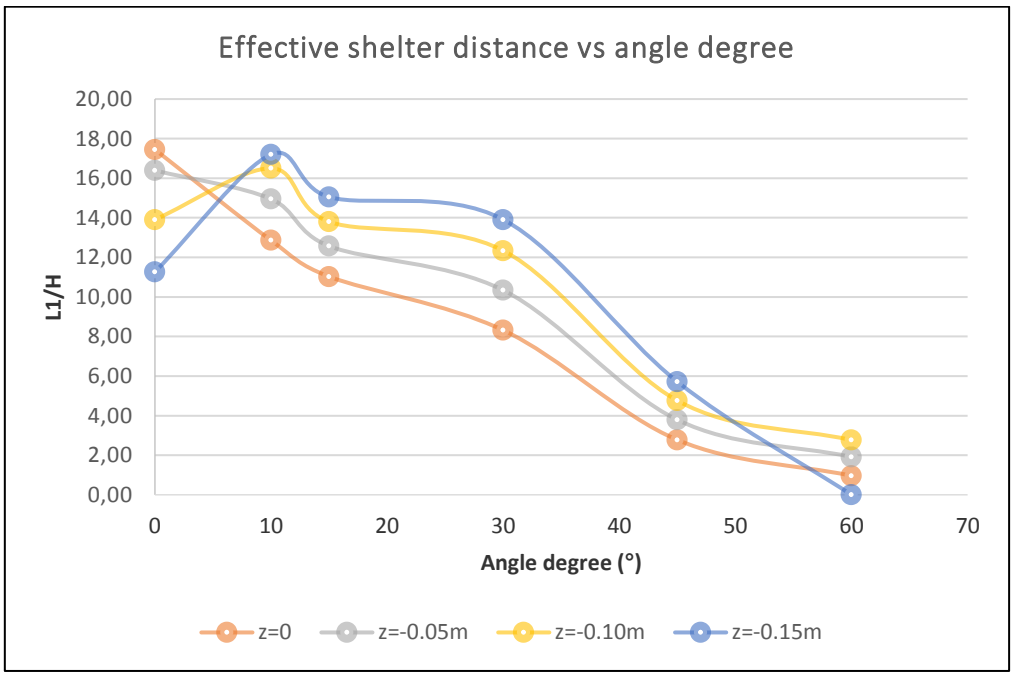

Figure 5-66: The effective shelter distance vs angle degree for the plane-1 at different z positions

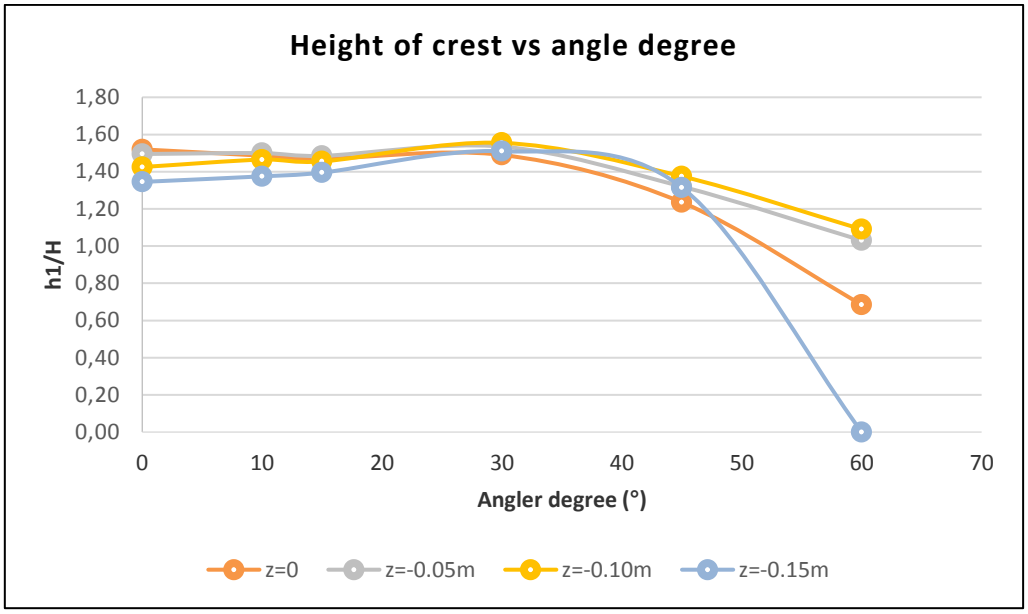

Figure 5-67: The height of crest vs angle degree for the plane-1 at different z positions

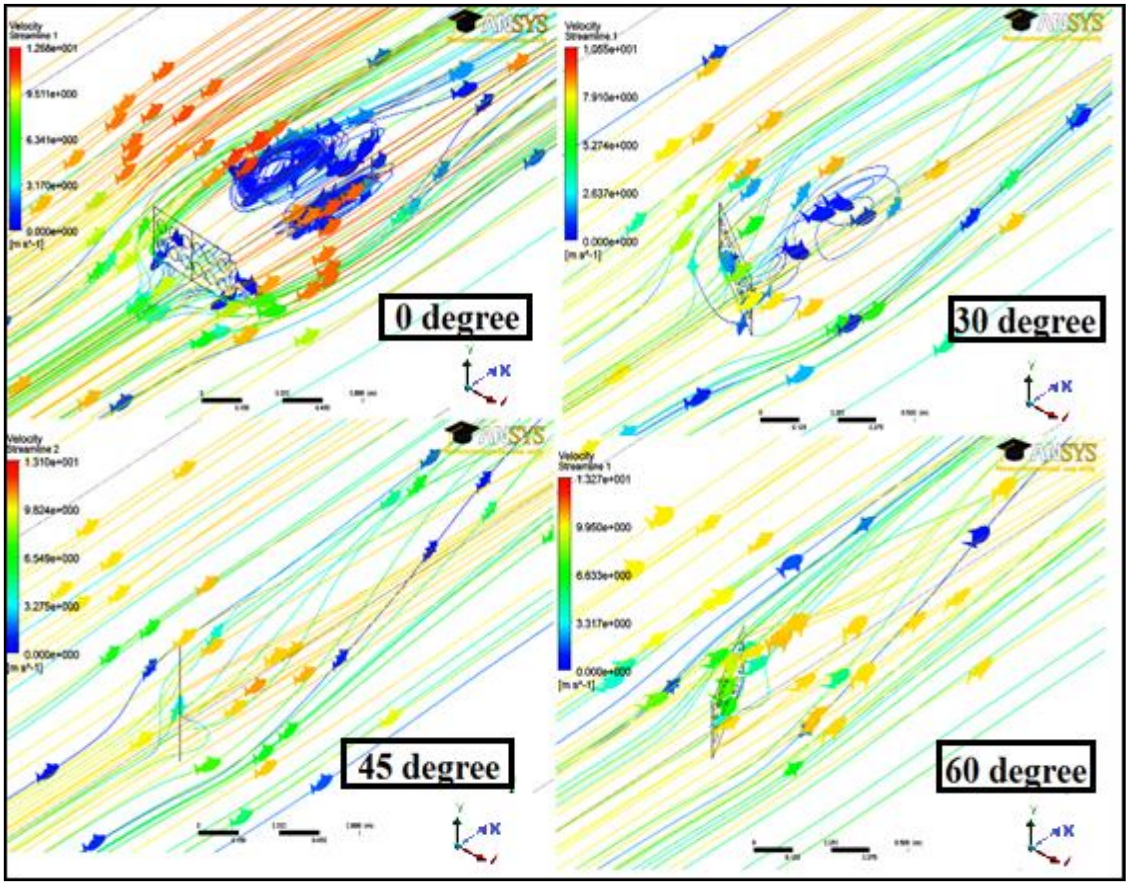

Figure 5-68: Streamlines around the fence at different angles of wind loads

Since the angle θ has effects on the area of normal fence and normal wind force, it is possible to describe the effective shelter distance as a function of $\cos^2\theta$. Figure 5-69 is the relationship of the effective shelter distance and $\cos^2\theta$, where the linearized trend lines were displayed. The linearized trend lines fit the data in the acceptable accuracy. As such, the effective shelter distance can be estimated by the following formula:

$$L1/H = a\cos^2\theta + b \qquad \textbf{Eqn.5-18}$$

where: *a* and *b* can be derived from the simulation data. In this case, *a* is in the range between *17.50* and *19.50, and b* in the range between *2.30* and *5.50.*

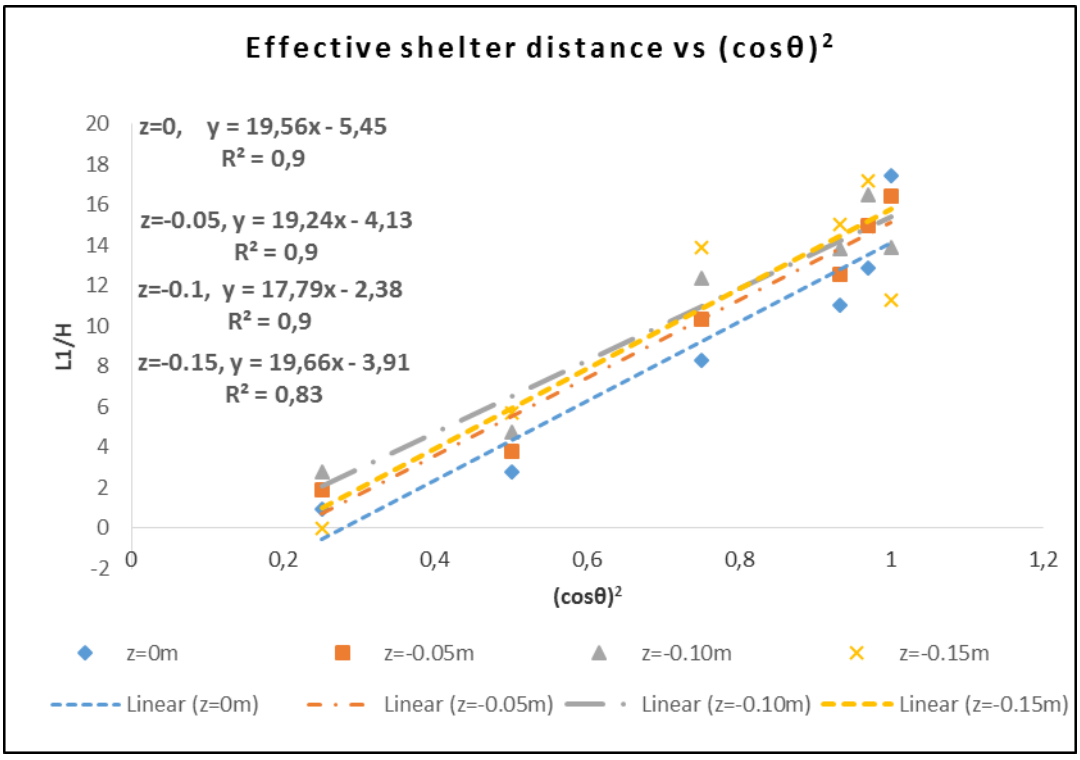

Figure 5-69: Linearized effective shelter distance vs $\cos^2\theta$

5.8.2. Investigation of wind loads on the fence

The wind-induced forces on the fence can be classified as two sources. One is the contribution of the net pressures named as the pressure force, and another is the viscous force that is proportional to the rate where the air velocity changes in space. The viscous

forces in the present case weights rather insignificantly. Therefore, the following discussions will exclude its effect.

Table 5-7 lists the three dimensional forces vectors and the drag coefficients vs different angles of wind load for the fence. Increasing the angles of wind load, z- axial force component was increased. Sensitive areas were in the ranges between *0°* and *10°* and *45°* and *60°*. At the angle of *60°*, the value of the z-axial force component was greater than the value of the x-axial force component. Due to the angles of wind load changing in the XZ-plane, which in fact were two dimensional, y-axial force component was created by the circle edges of holes encountered with the wind that could be neglected. The values of the x-axial force component and the drag coefficient were reduced with increasing the angles except in the range between *30°* and *45°* gone an opposite way. In the range between *0°* and *15°*, the x-axial force component and the drag coefficient appeared relatively stable, while at the angle of *60°*, both of them have been reduced to a significantly small value. Such phenomenon was similar to the findings in the investigation of effective fence zone. It indicates with the angle less or equal to *15°*, the structure of flow regime has not been affected pronouncedly. The structure of flow regime at the angle of 60° was almost destroyed.

Table 5-7: forces vectors and drag coefficients under different angles of wind load for the fence

Item	Force (N)			Normal drag coefficient
	X-	Y-	Z-	
0°	5.40	0.07	0.12	2.80
10°	5.09	0.07	0.88	2.73
15°	4.90	0.08	1.28	2.51
30°	2.79	0.05	1.55	2.01
45°	3.28	0.08	3.11	2.12
60°	1.96	0.07	3.17	1.15

In Figure 5-70, the data in the dash line were calculated by the normal drag coefficient at *0°* multiplied with a factor of $\cos^2\theta$. Good agreement could be found within the angle of *30°*, which was compatible to the finding of the other researchers (Richards & Robinson, 1999). However, out of this range, a jump of value appeared at *45°* in the simulation, and the normal drag coefficients were unlikely to be predicted by a factor of$\cos^2\theta$.

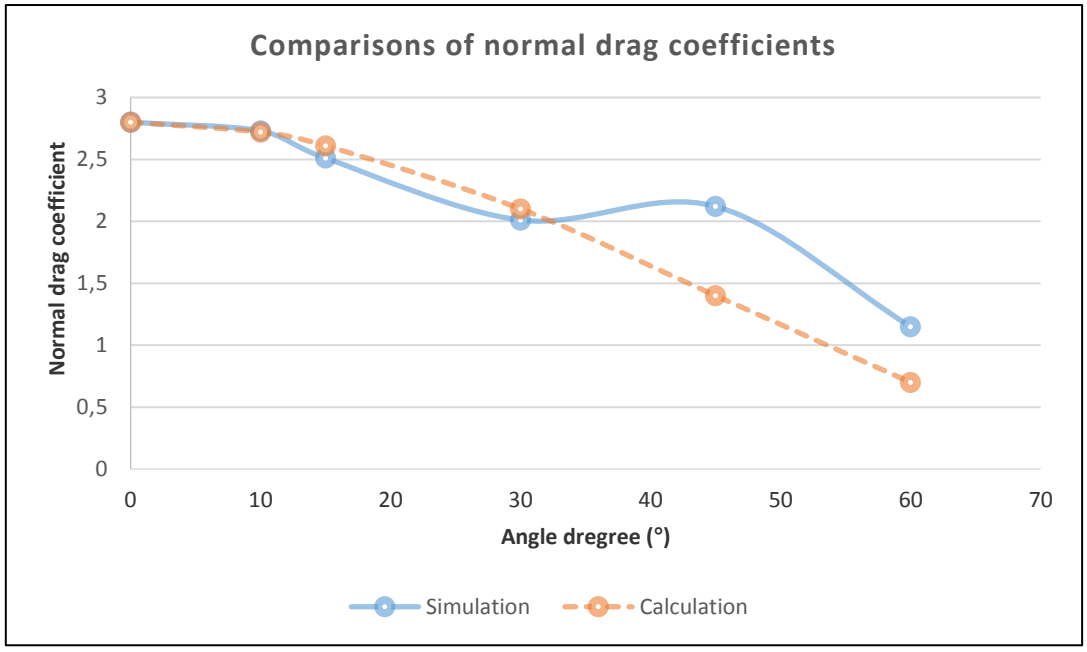

Figure 5-70: Comparisons of normal drag coefficient by simulations and calculations

It must be mentioned that the values of the simulated normal drag coefficient were higher than the ones from some physical experiments (Hagen & Skidmore, 1971) (Letchford, 2001) (Richards & Robinson, 1999). One reason is that those of physical testing fences were applied with higher porosity and different configurations, and the purposes of application were differed (i.e. Letchford's investigation on signboards and hoardings). Since drag coefficient is always associated with a particular surface area, especially a fence with porosity of *0.3* creates a structure of flow regime leeward the fence, which is usually more complex than the fence with lower porosity or higher porosity. Another reason may lie on the CFD modelling, as it was not sufficient to capture the mechanism of turbulence.

5.8.3. Summary

The investigations focused on the directions of wind loads influencing the fence effective zone and force components on the body of the fence. The summaries are presented as follows:

1) Non-normal wind loads to the fence reduced the fence effective zone. Within the range between *0°* and *30°*, the effective shelter distance was reduced comparatively slowly, after which, it was reduced dramatically. The height of crest almost maintained stable when the wind load angle within *30°*, noticeable reduction started from *30°*, and the reduction rate was increased with increasing the value of the angle. It was however less sensitive to the changes of angle than the effective shelter distance did, since it was more related to the fence height. Unlike the effective width of the fence was reduced with the increase of angle, the fence height remains unchanged.
2) Generally, the fence could remain effective when the angle of wind loads within *30°*. Beyond which, the effectiveness was deteriorated in a significant way. At *60°*, the fence effective zone could be considered to have been destroyed. Fences should be placed to encounter wind loads within the degree of angle no more than 30° in practice.
3) The effective shelter distance could be estimated in a linearized equation of $L1/H = a\cos^2\theta + b$ with regard of the changes of angle. However, this prediction should be limited to the angle of θ that was not more than *30°*.
4) Increasing the angle θ resulted in the increase of the lateral force component, and reductions of the normal force component and drag coefficient on the body of the fence except at *45°*, which the values of all of variables appeared higher than the ones at *30°*. Such a phenomenon was also observed from the other wind tunnel experiments (Richards & Robinson, 1999). Possibly the distribution of pressure drops changed its pattern in the range between *30°* and *45°*, since the fence effective zone has been dramatically reduced in this area too.
5) The normal drag coefficient could be described as a function of $\cos^2\theta$ within the degree angle of *30°*. This was coincidence with the effective shelter distance

where it could be estimated by $\cos^2\theta$ too. It might explain that the changes of θ mainly changed the normal fence width and distribution of forces, and the characteristics of flow regime were almost maintained.

6) The values of normal drag coefficient from the simulations were higher than the ones from some physical experiments. The main reason was due to the difference of the fence structures that leads different structures of flow regime. Another reason can be caused by the weakness in turbulence prediction for the CFD modelling itself.

5.9. DISCUSSIONS

The numerical study intentionally targeted the issues that a systematic research has not achieved today. It also is supplementary to the experimental investigation, as some of factors are unlikely to be investigated under the available experimental resources. Focus is paid on the 3D modelling. The discussions are presented as follows:

1) Single-phase airflow around the fence has been simulated in 2D and 3D models. Both of the 2D and 3D models have been evaluated against the corresponding wind tunnel experiments. Both of them have predicted the structure of wind velocity in good agreement with the experimental results. However, both of them have over-predicted the level of turbulence leeward the fence if compared with the experimental results. Overall, the models are applicable to the present research.
2) Six two-equation based turbulence models have been compared in the simulations. The selection of turbulence model was not sensitive to predict the structure of wind velocity; it however was sensitive to predict the structure of turbulence. It has been found that the Standard k-ω model had a limited improvement on the prediction of turbulence. As such, the Standard k-ω model was selected in the numerical simulations in this thesis.
3) Numerical investigation on the effect of shape of holes has found that the shape of holes has noticeable impact on the fence performance when the shape of holes are formed with sharp angular corners. The fences with circle or rectangular

shaped holes had almost the same performance; while the fence with triangular shaped holes had significant negative effect on the fence performance. Therefore, it should be avoided in the fence design. However, the fence with triangular shaped holes had statistically the lowest level of turbulence, which might be considered in the fence design where low level of turbulent environment was required. The fence with sharp angular corners in porous could be improved its performance by the means of smoothing the sharp angular corners in the holes.

4) A novel approach was applied to investigate the correlation to the creation and distribution of fence surface shear, the reattachment length, and the size of fence effective zone. The Investigation has found that the reattachment length and the size of fence effective zone were associated with the creation and distribution of fence surface shear. Reducing shear stress on the fence surface could improve the fence performance.
5) The numerical investigation has found that the size and distribution of porous holes had insignificant influence on the performance of the fences within the desirable size range. Out of this desirable size range, the fence performance was noticeably compromised. Hence, the desirable size range should be identified in the fence design.
6) Numerical investigation of the effect of non-normal wind loads onto the fences has found that the fence should be placed within the angle of $\theta \leq 30°$ to the wind load, where the effective shelter distance can be estimated in a linearized eqn.5-16, and the normal drag coefficient could be described as a function of $\cos^2\theta$. Beyond which, the fence performance was deteriorated in a significant way. To maintain the effectiveness of the fence, the fence should be positioned to encounter wind loads with the degree angle no more than *30*°, and preferably in the range with *15*°.

Chapter 6 NUMERICAL STUDY FOR TWO PHASE FLOW

In general, there are two fundamentally different theoretical approaches to study the dispersed phase (snowdrift) in two-phase flow (air-snowdrift): Lagrangian-Eulerian Model (Particle Tracking Model) and Eulerian-Eulerian Model (Continuum Two-Phase Flow Model). Lagrangian-Eulerian Model treats the fluid phase (air) as a continuum by solving the time-averaged Navier-Stokes equations, while the dispersed phase (snowdrifts) is solved by tracking a large number of snow particles through the calculated flow field. The Eulerian-Eulerian Model mathematically treats the two phases as interpenetrating continua. Air and snowdrift phases are considered as two equivalent sets of equations for the conservation of mass and momentum. It is often to simplify the model by assuming the snowdrift phase to be coupled with the airflow that reduces the total number of governing equations in the numerical modelling.

The advantage of the Lagrangian approach is that it can handle many physical phenomena to investigate the process of snow movement thoroughly. Whilst the perceived disadvantages is to simulate a large number of snow particle trajectories to satisfy the need of statistics, which consumes significant simulation time and possibly exceeds computer capacity. The Eulerian approach treats snow particles as a pseudo fluid solving both air and snow particles on the Eulerian reference frames. It has advantages of being computationally efficient when a large number of snow particles are assumed having the same physical properties. Its foreseeable disadvantage is not possible to model the movements of individual snow particles.

To evaluate the performance of porous fences on wind induced snow problems, the macro scaled snow movement is of main concern rather than the micro scaled snow movement. As such, the snowdrift transport CFD model in this thesis is based on the Eulerian-Eulerian approach. The models based on the threshold-friction-velocity theory and the mixture conservative snowdrift transport have been performed and discussed. Simplifications of the model with empirical knowledge and reasonable assumptions have also been discussed in this chapter.

6.1. EMPIRICAL KNOWLEDGE

The numerical simulations of windblown snowdrift around the fences were based on the empirical knowledge of Bagnold's threshold friction velocity theory (Bagnold, 1941). The correlative empirical knowledge has been discussed in Section 2.7.1. The empirical knowledge based parameters applied to the present model are included in Table 6-1.

Table 6-1: Parameters derived from the empirical knowledge and the wind tunnel experiment

Item	Unit	Experiment in Japan	The Other Cases
Temperature T	°C	-7	-7
Freestream velocity U_{free}	m/s	8.0	10.0
Effective bulk snowpack densityρ_p	kg/m3	506	450
Packed snow density ρ_{ps}	Kg/m3	910	910
Mean diameter of snow particle D_p	μm	110	110
Threshold friction velocityu_{*t}	m/s	0.24	0.18
Mean snow particle fall velocity w_f	m/s	0.43	0.43
Power law exponent α		0.13	0.15
Aerodynamic roughness length z_0	m	3.34E-6	5.00E-6
Thickness of boundary layer δ	m	0.128	10.00
Snow pack proportionality coefficient ρA		7.0E-4	7.0E-4
Maximum packing ratio of snow γ		0.62	0.62
Air density	kg/m3	1.31	1.31
Dynamic viscosity μ	Kg/m/s	1.69E-5	1.69E-5

6.2. SIMPLIFICATION AND ASSUMPTION

Windblown snowdrift transport through porous fences is multi-physics. The structure of wind flow, the property of air and snow particles, the interaction of air and snow particles, temperature, and the topology of the surrounding environment will have significant impact on the mechanism of snowdrift transport. It leads a difficulty to form a numerical model which comprehensively takes all of the mentioned factors into account, and could stretch or beyond the computational capacity. Reasonable simplifications and assumptions to the CFD modelling are essential in the industrial and scientific researches. The simplifications and assumptions to the current modelling are discussed as follows:

1) The snowdrift transport was studied on the macro-scale. Adhesion and cohesion of snow particles were not considered.
2) The surrounding temperature was at a constant of *-7°C*, which is an approximately averaged value applied to the wintry Arctic regions. Since the applied wind velocities were compatible to the atmospheric wind velocities within *20m/s*, the airflow can therefore be regarded as incompressible. Hence, temperature induced energy was not considered in the modellings.
3) The snow particles were assumed as spherical-shaped with a constant diameter. The sizes of natural snow particles vary from less than *100* microns for fractional particles to more than a centimeter for fresh snowflakes. However, in cold and rather dry environment, big snow particles are rapidly fractionated into small particles. It can be assumed that bigger snow particles are only in the presence at the very beginning in snowdrift transport, and their shapes are spherical with the same constant of diameters, that allows ignoring the orientation and eventual rotation of snow particles (Sato, et al., 2008). Snow bed is usually hardened by the shear stress induced by wind. Therefore, different densities of snow particles have been assigned for drifting snow and deposited snow particles. Detailed information is listed in Table 5-7.
4) Sublimation of snow particles was not included.
5) Snow particles start to entrain into airflow depending on the available turbulence kinetic energy. Suspended snowdrifts are elevated by the mean of turbulent

eddies. A highly anisotropic turbulence distribution is always presented in the airflow regimes behind a porous fence in the reality. However, the applied Standard k-ω model is assumed turbulence distribution as isotropic. This assumption might compromise the accuracy of snowdrift transport modelling in the thesis.

6) The mixture phase was treated as a highly diluted media, which the inter-particle collisions had negligible effects on the characteristics of air and snowdrift phases. This assumption entailed that there was minimal coupling between snow particles and the air, where the mean velocity and turbulence characteristics of the air phase were not disturbed by the snow particle phase. Therefore, the two-phase flow was considered only one-way coupled between the air and the snow particles, which the snow phase followed the air phase without influence. Natural snow volume fractions are typically around *0.1%* (Pomeroy & Gray, 1990). Considering the air-snowdrift mixture as a highly diluted continuum seemed acceptable in the current model.

The discussed simplifications and assumptions have reduced a great degree for essential factors in consideration. To succeed a CFD modelling as a suitable engineering tool, it is necessary to make a few of sacrifices in the form of simplifications and assumptions.

6.3. MULTI-PHASE MODEL SELECTION

There are three different the Eulerian-Eulerian Model available in ANSYS FLUENT: the volume of fluid (VOF), the mixture and the Eulerian models. The differences of these models are as follows:

- The VOF Model: It is a surface-tracking technique applied to a fixed Eulerian mesh for two or more immiscible fluids, where the position of the interface between the fluids is of interest. A single set of momentum equations is shared by the fluids, and the volume fraction of each of the fluid in each computational cell is tracked throughout the domain.

- The Mixture Model: It treats the fluids as interpenetrating continua, and solves for the mixture momentum equation and prescribes relative velocities to describe the dispersed phases.
- The Eulerian Model: It is the most complex models among the others, and solves a set of momentum and continuity equations for each phase. Coupling is achieved through the pressure and interphase exchange coefficients. The manner in which this coupling is handled depends on the type of phases involved.

Appropriate model selection results in better interpretation of simulated physics and low computational expenses. The VOF model has deficits in modelling for flows in which the phases mix or separate, that is insufficient to model snowdrift transport in saltation and suspension. Hence, the applicable multi-phase model here falls to the mixture and the Eulerian models.

6.3.1. Stokes number

For systems with intermediate particulate loading, estimating the value of the Stokes number helps to select the most appropriate model. The Stokes number S_t is the ratio of the particle response time τ_p and the system response time t_s. S_t, τ_p and t_s can be calculated by Eqns.2-52, 2-53 and 2-54, respectively.

The t_s must be considered at the stage of domain meshing by properly arranging the size of meshed elements. In the present modelling, the minimal t_s has been controlled in the range less than *1e-02*.

The $\tau_p$was calculated as *1.7e-02* based on the variables from Table 6-1. Therefore, overall S_t was much less than *1.0*. In the present modelling, finer elements were arranged in the regions close to the floor boundary and the fence, where the values of the characteristic length of the element were considerably small. However, in the regions insider the porous holes and around the edges of the porous fence (only applied to the 3D modelling), due to the accelerations of local velocity,, the vales of S_t might be greater than *1.0*. It can be considered as acceptable since such effects did not have significant impact on the macro-scaled snow transport behavior in the entire domain.

The discussed S_t indicated that the snow particle would follow the flow closely and therefore the mixture model was feasible to the present modelling. Compared with the applicable Eulerian model, it was less expensive and yielded solutions more stably.

6.3.2. Inter-particle space

Depending on the snow particle loading, the degree of interaction between the snowdrift and air phases can be evaluated by the parameter of inter-particle spaceL/D_p, which is (ANSYS, 2009):

$$L/D_p = \frac{\pi}{6}\frac{1+\vartheta}{\vartheta} \qquad \textbf{Eqn.6-1}$$

where: ϑ is the ratio of the volume fractions of snow particle and air, which takes the value of *0.1%* that is the typical natural snow volume fractions. The calculated L/D_p was about the value of *8.1*. Therefore, the snowdrifts could be treated as isolated. The air and snowdrifts were regarded as one-way coupled, where the air influenced the snow particles via drag and turbulence, but the particles had no influence on the air (ANSYS, 2009).

As such, the present multi-phase model could be further simplified as a one-way coupling mixture two-phase model.

6.3.3. Relative (slip) velocity and the drift velocity

The mixture model can be used to model air and snowdrift phases moving at different velocities but assuming local equilibrium over short spatial length scales. It solves the momentum, continuity for the mixture phase, and the volume fraction equations for the snowdrift phase. The relative (slip) velocities can be expressed as algebraic functions. When the relative velocity is equal to zero, the mixture model is reduced to a homogeneous air-snowdrift model.

In the present, the relative velocities and the drift velocities have been considered, since snow particles were slightly delayed to the carrier of air, and the gravity effected suspended snow particles falling to the ground. The relative velocity $\overrightarrow{u_{rel}}$in turbulent flows was given as (ANSYS, 2009):

$$\overrightarrow{u_{rel}} = \frac{(\rho_p - \rho_m) D_p^2}{18 \mu_a f_{drag}} \vec{a} - \frac{\eta_t}{\sigma_t} \left(\frac{\nabla \alpha_p}{\alpha_p} - \frac{\nabla \alpha_a}{\alpha_a} \right) \quad \textbf{Eqn.6-2}$$

where the first term at the right hand side is the velocity of the snow phase to the velocity of the air phase, and the second is a diffusion term due to the dispersion appearing in the momentum equation for the snowdrift phase. f_{drag} is the drag function taken from Schiller & Naumann (1933) and applied to spherical particles. $\vec{a}$ is the acceleration of snow particles. σ_t is a Prandtl/Schmidt number taken the value of *1.0* instead of the default value of *0.75* in ANSYS FLUENT. η_t is the continuous-dispersed fluctuating velocity correlation. The denote *p*, *m* and a represent snow phase, mixture phase and air phase respectively.

The snow particle drift velocity$\overrightarrow{u_{dr.p}}$ is connected to $\overrightarrow{u_{rel}}$ expressed as:

$$\overrightarrow{u_{dr.p}} = \overrightarrow{u_{rel}} - \sum_{k=1}^{n} c_k \overrightarrow{u_{ak}} \quad \textbf{Eqn.6-3}$$

where c_k is the mass fraction for any phase (*k*). Detailed calculations of the above variables can be found in ANSYS (2009).

Since air and snowdrifts were one-way coupled, the effect of snow particles on turbulence was neglected in the current modelling.

6.4. SNOW TRANSPORT MODEL

The snow transport was solved by partial differential equations for particle continuity and particle momentum, which could be expressed in a general form as the following (ANSYS, 2009):

$$\frac{\partial(\rho_p \emptyset_i)}{\partial t} + \frac{1}{V_f} \frac{\partial}{\partial x_j} \left(\rho_p u_j A_{fj} \right) = \frac{1}{V_f} \frac{\partial}{\partial x_j} \left[\Gamma_\phi \frac{\partial \phi_i A_{fj}}{\partial x_j} \right] + S_\phi \quad \textbf{Eqn.6-4}$$

At the left hand side in Eqn.6-4, the first is the terms of rate of change in ϕ, and the second is the term of convection. At the right hand side, the first is the diffusion term, and the second is the source term. ϕ is the solution variable to be solved. Γ_ϕ is the diffusion coefficient and S_ϕ is the source term. V_f and A_{fj} are dimensionless volume and area fraction varying between *0* and *1*.

Substituting the snow volume fraction α_p into ϕ_i, Eqn.6-4 becomes a mass flow rate equation for snowdrift phase. Rewriting the equation in the form as:

$$\frac{\partial \phi_s}{\partial t} + \frac{\partial \phi_s u_j}{\partial x_j} = \frac{\partial}{\partial x_j}\left[\frac{v_t}{S_{ct}}\left(\frac{\partial \phi_s}{\partial x_j}\right)\right] + \frac{\partial u_{rel}\phi_s}{\partial y} \qquad \textbf{Eqn.6-5}$$

where ϕ_s is named as snow drift density of $\phi_s = \alpha_p \rho_p$. x and y indicate variables in horizontal and vertical directions respectively. The first at the right hand side is the diffusion term that a Boussinesq approximation is used to translate the averaged turbulent scalar flux $-\overline{u_j' \phi_s'}$ into the averaged scalar concentration gradients of ϕ_s. S_{ct} is the turbulent Schmidt number assuming that turbulent diffusion flux of snow drift density has a similarity with momentum of flow. The second at the right hand side is the source term expressed the advection effect by the relative velocity effects. The relative velocity u_{rel} is calculated by Eqn.6-2. Since the air-snowdrift model was considered as a highly diluted one-way coupled mixture model, such assumptions were acceptable.

Further simplification on Eqn.6-5 can be made to substitute a constant value of snow terminal fall velocity w_f into u_{rel}, which expresses the advection source affected by gravitational sedimentation on snow particles.

Considerable researchers modelled snowdrift transport based on threshold-friction-velocity theory. They assessed deposition and erosion of snow particles based on Eqn.2-49 mostly in a steady or an equilibrium state (Wipperman & Gross, 1986) (Uematsu, et al., 1989) (Sundsbø, 1997).

The current model was to evaluate the snow transport rate in a saltation layer for ϕ_s in Eqn.6-5, where ϕ_s was solved without distinguishing between suspension and saltation layer. It differed from the similar model proposed by Tominaga et al (2006), where saltation and suspension of snow particles were modeled individually. Their model was found inabilities in predicting non-equilibrium flow fields such as flow around buildings. This also applies to flows around porous fences. As such, the present approach was expected to be better than assuming the equilibrium saltation layer in non-equilibrium flow fields.

The deposition rate Q_{dep} on the horizontal first layer adjacent to the floor boundary is considered as:

$$Q_{dep} = -\phi_s(w_f + v_{loc})\Delta x \Delta z \quad \textbf{Eqn.6-6}$$

where w_f here is taken a constant value seen in Table 6-1, and v_{loc} is the vertical direction velocity at the first layer adjacent to the floor.

The erosion or accumulation rate Q_{ero} is given as (Anderson, R.S.; Haff, P.K.;, 1988):

$$Q_{ero/acc} = -c_a \rho_{ps} u_* \left(1 - {u_{t*}^2}/{u_*^2}\right) \Delta x \Delta y \quad \textbf{Eqn.6-7}$$

where, $c_a$is a constant of *5.0e-04*. When ${u_{t*}^2}/{u_*^2} > 1$, erosion occurs, ${u_{t*}^2}/{u_*^2} < 1$, accumulation occurs, and ${u_{t*}^2}/{u_*^2} = 0$, neither erosion or accumulation occurs.

In order to make conservation of snow mass flow rate at the control volumes adjacent to the floor boundary layer, two conditions must apply to the diffusion term in Eqn.6-5:

- $\frac{v_t}{S_{ct}}\left(\frac{\partial \phi_s}{\partial x_j}\right) = 0$, when accumulation occurs; **Eqn.6-8**
- $\frac{v_t}{S_{ct}}\left(\frac{\partial \phi_s}{\partial x_j}\right) = \frac{Q_{ero}}{\Delta x \Delta y}$, when erosion occurs; **Eqn.6-9**

The net deposition rate Q_{tot} in a control volume is therefore as the following:

$$Q_{tot} = Q_{dep} + Q_{ero/acc} \quad \textbf{Eqn.6-10}$$

The depth of snow deposition per unit time $\Delta y/\Delta t$ can be calculated as:

$$\Delta y/\Delta t = Q_{tot}/(\lambda \rho_{ps}\, \Delta x \Delta z) \quad \textbf{Eqn.6-11}$$

The depth of snow deposition incremented at each time step can be expressed:

$$y_{n+1}^i = y_n^i + \Delta y_n^i \quad \textbf{Eqn.6-12}$$

The above equations were written in C programming and then compiled into the CFD simulation as the user subroutines. The increment of deposition depth scheme enabled to model the evolutions of snow deposition with each time or each iteration.

6.5. BOUNDARY CONDITIONS

Snow particles were considered to be transported over a wall-bounded fully developed turbulent atmospheric boundary layer. As such, the boundary conditions were similar to the discussions in Section 5.3. Apart from these, the inlet profile of snow concentration must be considered as follows:

- Saltation layer $0 \leq y \leq h_{sal}$: $\eta_r = Q_{sal}/h_{sal}\, u_p$;
- Suspension layer$y > h_{sal}$: $\eta_{sus}(y) = 0.8exp\left(-1.55(4.78u_*^{-0.544} - y^{-0.544})\right)$.

The inlet profile of snow concentration was based on the empirical knowledge written in C programming to be assigned to the computations.

6.6. CASE STUDY FOR WYOMING FENCE

Tabler (2003) reported field investigations on snow transport and deposition on Interstate Highway *80* in Wyoming with over *10* years' data collections. His report provided specific guidelines for designing structural and living snow fences to control blowing and drifting snow for drift-free roads. Many researchers implemented his field measurement data as benchmarks to examine their CFD snowdrift models (Alhajraf, 2004) (Sundsbø, 1997).

6.6.1. Tabler's field observation work

Tabler described snow deposition leeward a fence into four stages shown in Figure 6-1 (Tabler, 2003). The first stage is snowdrift growth, where snow particles passing through a fence encounter a zone of greatly diminished wind velocities and decreasing surface shear stress. This zone extends downwind for a distance about *7H*. Most particles that reach the ground come to rest and form a lens-shaped drift thickened in the middle as deposition continues. The second stage is the development of snow deposition due to the

drift adds significant resistance to the airflow. These two stages are represented by measurements from *1* to *3* in Figure 6-1.The third stage is characterized by snow filling the circulation zone as the depth of the downwind drift approaches its maximum represented by measurements from *4* to *6*, where a slip face is visible and the trapping efficiency remains relatively high. The fourth stage begins the deposition growth without a slip face or a circulation zone, and ends the cease of deposition growth despite of the continued influx of blowing snow (represented by the measurement of *7*). At this stage trapping efficiency declines rapidly and deposition is limited mainly to creeping and saltating particles. When the deposition ceases to grow, an equilibrium snowdrift state is achieved.

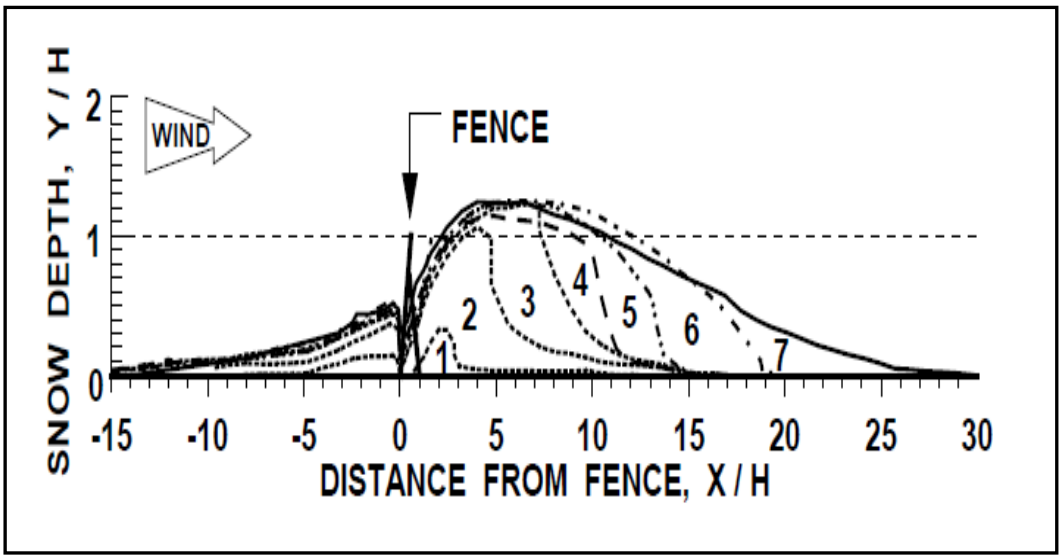

Figure 6-1: The development of snow deposition around a porous fence with 3.8m height and 0.50 porosity

Figure 6-2 shows the dimension of an equilibrium snowdrift formed by the Wyoming fence provided by Tabler (2003), where the fence is *3.8m* high with its porosity of *0.50*. A downwind inclination angle of *15°* layback is used in Wyoming fences, which has little net effect on trapping efficiency or snow storage capacity, and provides stability during construction and is easier for maintenance workers to clime the fences. It can be observed that porous fences form airfoil-shaped snowdrifts at the equilibrium drift state that offers a low resistance to the airflow, where the crest of deposition is at the position of *6H* away

the fence and *1.2H* high from the ground. Snow deposition occurs at the horizontal distances of 1*5H* upwind and *34H* downwind of the fence.

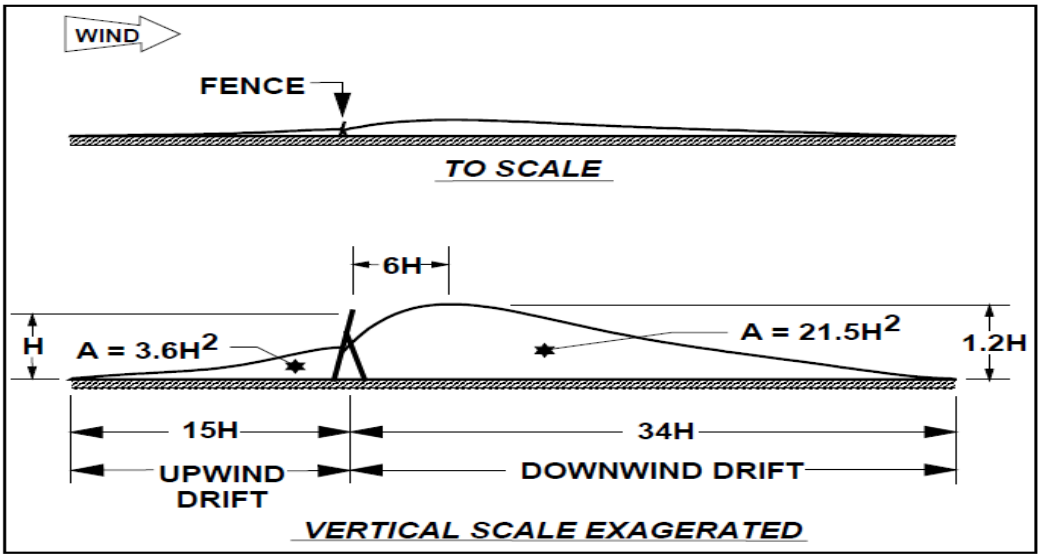

Figure 6-2: The dimensions of an equilibrium snowdrift formed by the Wyoming fence

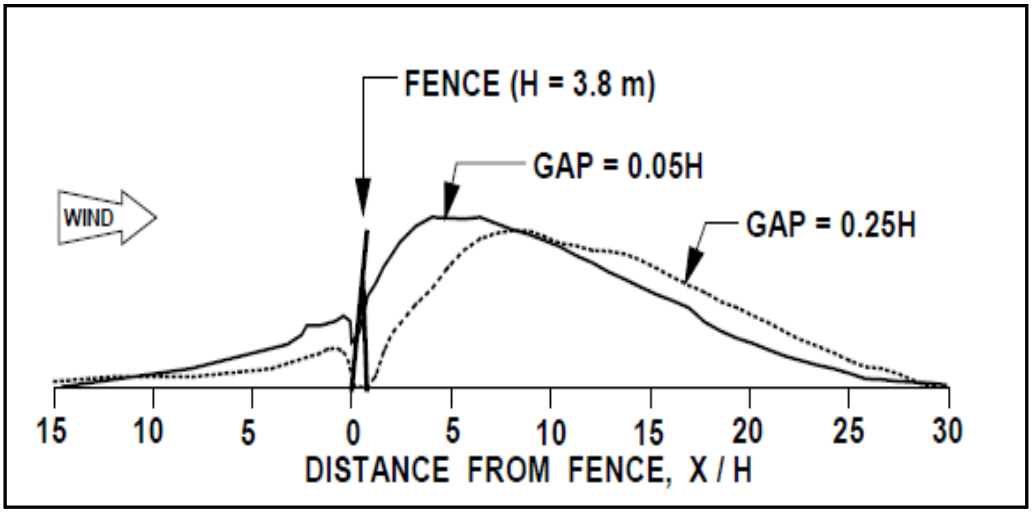

Figure 6-3: Comparison of drifts formed by two Wyoming fences having 0.05H and 0.25H bottom gaps respectively

One of significant features of snow fences that differs from wind fences is the bottom gap, defined as a space between the ground and the bottom of the fence. Such a bottom gap minimizes snow deposition close to the fence, and keeps the saltating snow particles near the ground to be more easily trapped. The optimum bottom gap is recommended to

be equal to *10-15%* of the total fence height (Tabler, 2003). Figure 6-3 is the comparison of snowdrifts formed by two *3.8m* height of Wyoming fences have *0.05H* and *0.25H* bottom gaps, respectively. Figure 6-4 is the effect of bottom gap on snow storage based on the field measurement (Tabler, 2003). It can be observed that the nose of the downwind drift is displaced farther downwind if the bottom gap is increased beyond the optimum range, and storage capacity of fence is reduced both on the upwind and downwind sides of the fence. However, the drift length almost remains unchanged.

Other structural factors such as porosity and height of the fence have profound impacts on the performance of fences to control snow transport, since these factors have great influences to form the structure of flow regimes around fences, which have significant effects on snow transport modes (creeping. saltation and suspension). The optimum porosity of snow fences is in the range between *0.40* and *0.50* (Tabler, 2003).

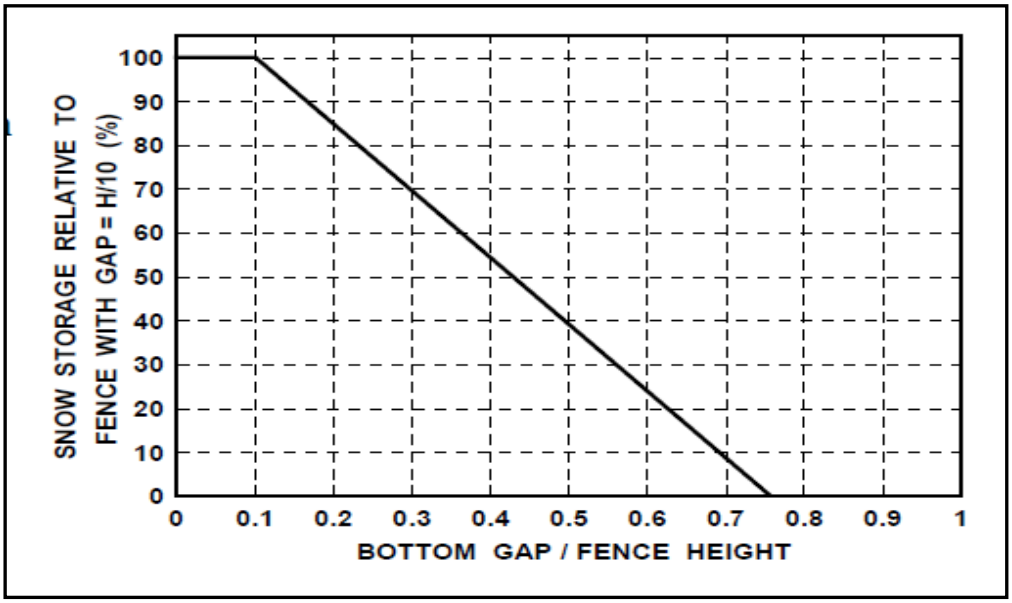

Figure 6-4: Effect of bottom gap on snow storage

6.6.2. 2D CFD modelling snowdrift around the Wyoming fence

The numerical simulation for snowdrift around the Wyoming fence was performed in 2D model. The domain is shown in Figure 6-5. The configuration of the domain was 200m long and 10m high. The Wyoming fence was 3.8m high and 0.04m thick, and with a downwind inclination angle θ of 15° layback. The fence was positioned at a distance of

40m from the inlet. The bottom of the fence was 0.5m away the ground making the bottom gap of 0.13H, which was in the optimum range from 0.1H to 0.15H (Tabler, 2003). The top wall was treated a symmetry wall.

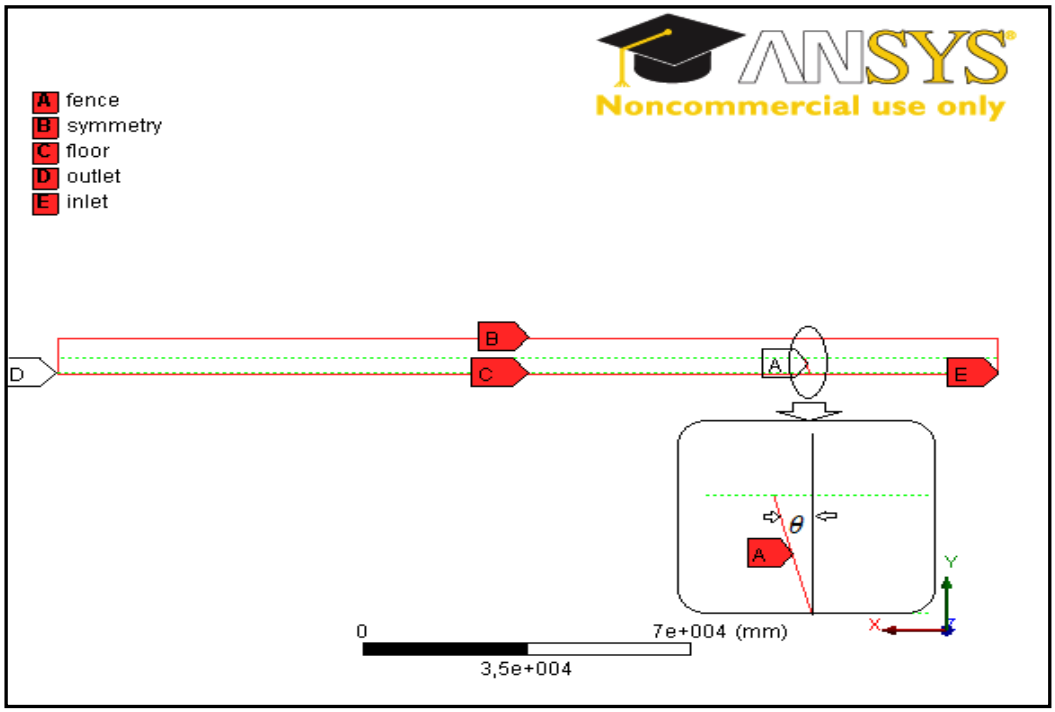

Figure 6-5: The 2D domain

The numerical simulation for snowdrift around the Wyoming fence was performed in 2D model. The domain is shown in Figure 6-5. The configuration of the domain was *200m* long and *10m* high. The Wyoming fence was *3.8m* high and *0.04m* thick, and with a downwind inclination angle θ of *15°* layback. The fence was positioned at a distance of *40m* from the inlet. The bottom of the fence was *0.5m* away the ground making the bottom gap of *0.13H*, which was in the optimum range from *0.1H* to *0.15H* (Tabler, 2003). The top wall was treated a symmetry wall.

The porosity β of the fence was *0.5* treated as a porous jump. The pressure loss coefficient $k_r$for the fence was estimated by the empirical relationship as the following (Reynolds, 1969):

$$k_r = 0.52[1 - (\beta \cos\theta)^2]/(\beta \cos\theta)^2 \qquad \textbf{Eqn.6-13}$$

Therefore, k_r was *1.74*. Porous cells for a porous jump were treated as *100%* open to the domain, which differed the fact where the fence was only partially open to flow. Presuming the flow rate unchanged with or without the fence, $u_{50\%open} = 2 * u_{100\%open}$.Hence, the k_r needed to be adjusted as:

$$k_r' = k_r * \left(u_{50\%open}^2 / u_{100\%open}^2\right) \quad \textbf{Eqn.6-14}$$

As such, $k_r' = 4k_r$ =6.96.

The pressure-jump coefficient C_2 was estimated as the following (ANSYS, 2011):

$$C_2 = (k_r' \cos\theta)/\Delta m \quad \textbf{Eqn.6-15}$$

where Δm is the thickness of the fence . Therefore, $C_2 = 168m^{-1}$.

For modelling a perforated plate under turbulent flow, the viscous loss term can be ignored (ANSYS, 2011). Consequently, the face permeability for the porous jump here was set as $1e + 20m^2$.

Denser elements were created in the regions close to the floor and near the fence. Such treatment was essentially to capture the movement of snow particles in the sensitive areas without scarifying excessive computational expense. Quadrilateral elements were applied in the entire domain. The mesh with *0.5million* elements has reached the grid independence.

Standard *k-ω* turbulence model was employed in the simulations. The set-up of boundary conditions have been discussed in Section 6.5. Snow precipitation and sublimation were not considered in the modelling. The snow phase and air phase were solved by a transient mixture Eulerian-Eulerian model, where snow particles followed airflow without influence (one-way coupled). The prediction of the rate of snow deposition or erosion was based on the particle convection-diffusion Eqn.6-10, and then solved by the means of coupled user subroutines at the first control volumes adjacent to the floor. The evolution of snow deposition was updated through a dynamic mesh technique, where the change in height of the cell vertices was calculated in Eqns.6-11 &6-12. The transient time scheme was evaluated by Eqns.2-52, 2-53 & 2-54. In the transient simulation, a total

time of *20* seconds with *500* iterations per second was applied. The empirical knowledge based parameters to be implemented in the modelling were included in Table 6-1.

6.6.3. Discussions

The discussions are presented as follows:

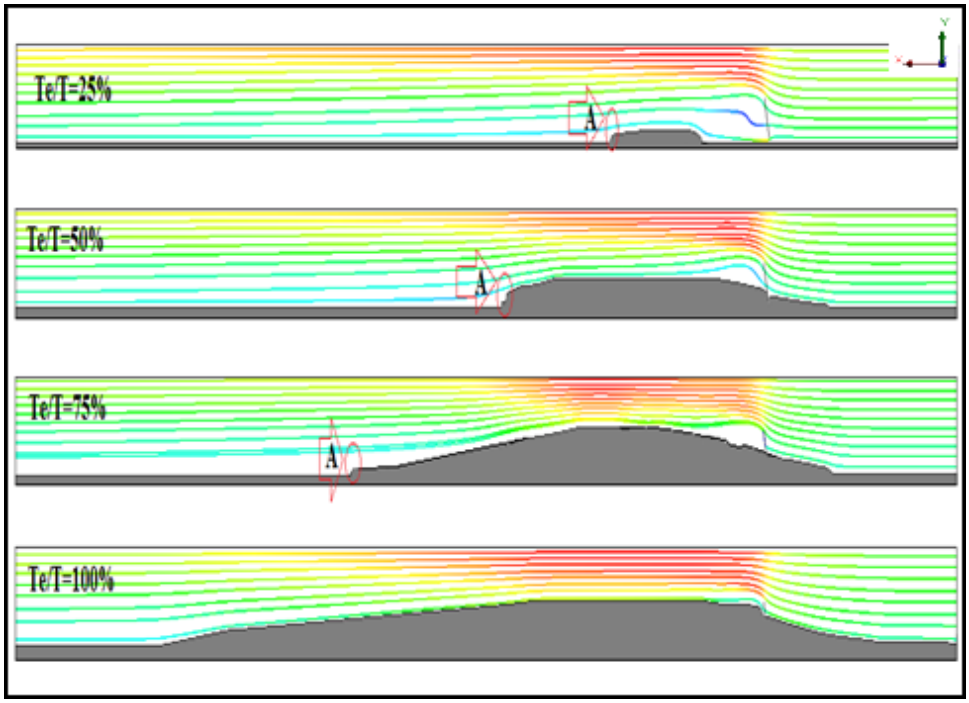

Figure 6-6: The evolution of snow deposition around the Wyoming fence with 0.13H bottom gap

1) The evolution of snow deposition around the Wyoming fence is presented in Figure 6-6, where the colored lines are the velocity magnitude streamlines within the domain, and the deposited snow is in grey. T represents the total simulation time, and T_e the current time stage. It can be observed that snow particles were first deposited at a distance of *3.7H* from the fence, then snow deposition was developed in both sides of the fence and elongated upwind and downwind sides. The velocity magnitude streamline kept changing due to the change of the floor boundary, which essentially changed the friction velocities in the control volumes adjacent to the floor and affected the transport rate of particles. At the first three stages, there existed a slip face marked the region of A in the figure, and the

velocity streamlines were separated in the regions of having a slip face and near the fence. At $T_e/T = 100\%$, the slip face was disappeared (no area A) and the velocity streamlines followed the shape of snow deposition. The trap efficiency of the fence was diminished and snow deposition almost ceased to grow. The equilibrium state of snowdrift was achieved at this stage, and a airfoil-shaped snow deposition pattern was formed.

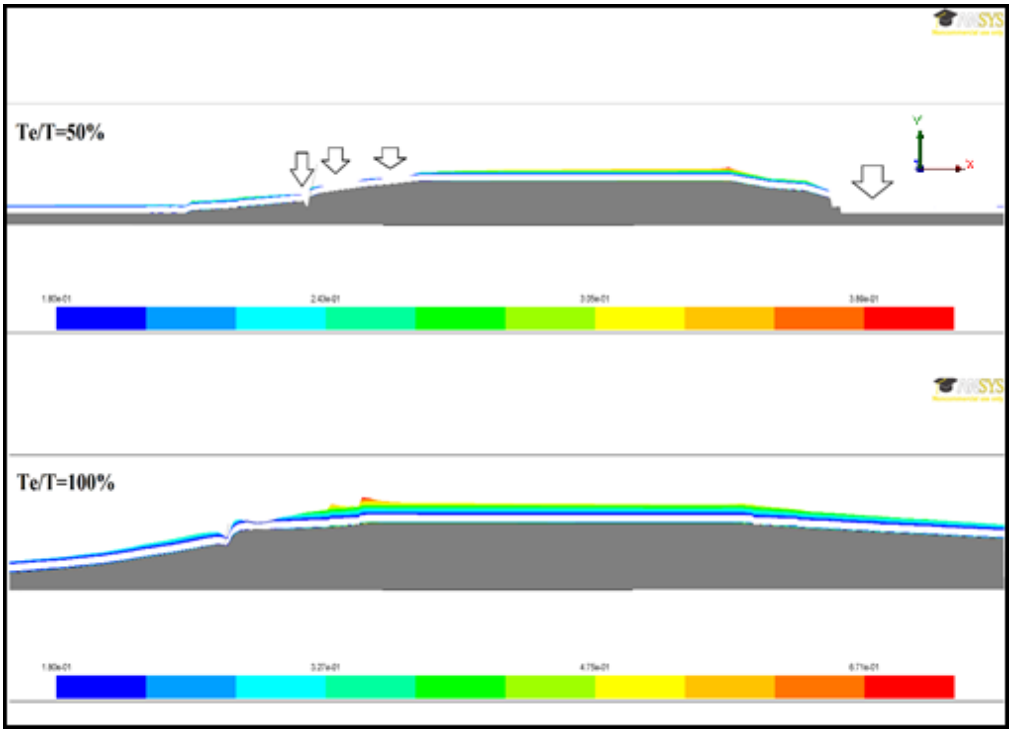

Figure 6-7: The friction velocity profiles at the snow ground at two stage of simulations, where the plotted values are greater than the threshold friction velocity of 0.18m/s

2) Friction velocity at snow ground is a vital parameter to determine the transport mode of snow particles. Figure 6-7 presents the friction velocities in the surface of snow ground at the stage of $T_e/T = 50\%$ and 100%, where those values greater than the threshold friction velocity of *0.18m/s* were plotted. For better presentation, the profiles were drawn by a scale factor of *3.0* projected in the Y direction. This arrangement enables to identify which regions snow particles will be eroded or deposited. At $T_e/T = 50\%$ stage, friction velocities were scattered in the near fence downwind region, and were disappeared in the slip face region,

which indicated that snow particles would continue to be deposited in these regions (pointed by arrows). At $T_e/T = 100\%$ stage, the friction velocity profile continuously covered the entire surface of snow ground, which indicated that snow deposition ceased to grow and the trap efficiency of the fence has diminished to the minimum. Hence, the equilibrium snowdrift state has been achieved. It also can be observed that the values of friction velocity generally increased with the development of snow deposition on the ground. This can explain that snow deposition will form a certain pattern under a certain circumstance.

3) The evolution of snow deposition for the Wyoming fence without a bottom gap is presented in Figure 6-8. At $T_e/T = 25\%$, snow particles were deposited immediately before and behind the fence. It appeared that there were two snow crests downwind the fence, which was affected by the circulating flows in the fence wake zone. Compared with the fence with a bottom gap, the pattern of snow deposition appeared noticeably different, and the trap efficiency of the fence at this stage was relatively higher. With the evolution of the simulations, deposited snow particles filled the gap between the two snow crests, since the dynamic meshed snow boundary kept modifying the structure of the flow regime, and the influence of circulating flows was weakening. The two snow crests were merged to one crest approximate at $T_e/T = 35\%$ stage. At the equilibrium snowdrift state, a airfoil-shaped snow deposition was formed and followed the velocity streamlines.

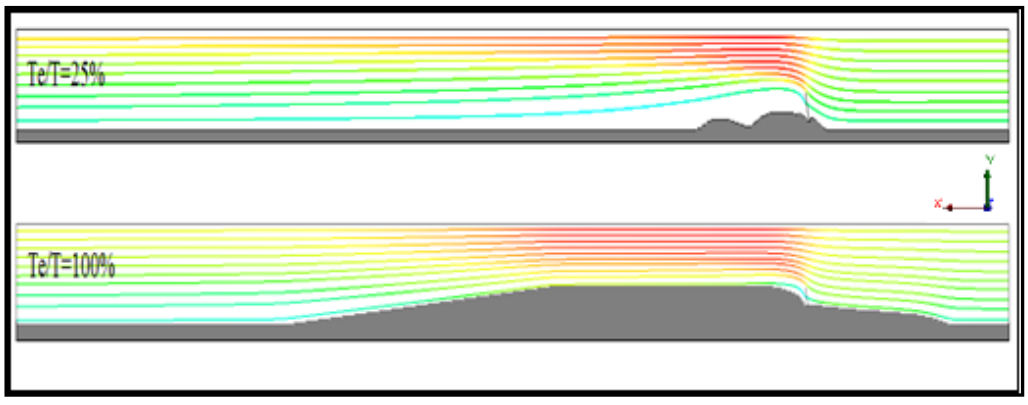

Figure 6-8: The evolution of snow deposition around the Wyoming fence without a bottom gap

4) The comparison of CFD simulations and field measurement is listed in Table 6-2. The CFD results have under-predicted the snow deposition area both in the upwind and in the downwind of the fence. The field measurement data included the effects of snow precipitation and sublimation under multi-directional wind attacks. The considerable long duration of the data collection also would harden the packed snow particles and iced the surface of snow deposition due to low temperature, which could significantly influence the snow particle transportations. In the CFD modelling, the precipitation of snow and sublimation have not considered, and wind driven was assumed in a single direction. The snow phase was simplified as one-way coupled to the airflow, which has over-estimated the momentums of airflow and therefore over-predicted the snow erosion rate. The CFD model may over-predict the turbulent kinetic energies and dissipation rates within the domain (discussed in section 5.5.1), which again might over-predict snow erosion rate. Additionally, in the reality, snowdrift through a projected object will never achieve an equilibrium state, where snow deposition can be diminished to a very low rate but cannot be ceased. All of which would under-predict the snow deposition rate.
5) The comparison of snow deposition around the fences with or without a bottom gap is also summarized in Table 6-2. Compared to the fence without a bottom gap, the downwind deposition length around the fence with a bottom gap of *0.13H* was increased from *26H* to *30.5H*. However, little changes in the position of snow crest and upwind deposition length. The bottom gap had significant influence on the distribution of snow deposition at the beginning and reduced its influence with time evolution shown in Figures 6-6 and 6-7. The comparison revealed that optimal bottom gap design would improve the trap efficiency of the fence mainly elongating the downwind snow deposition length. However, it was not a decisive factor to determine the performance of snow fences.

In general, the CFD results were in good agreement with the field measurement. The evolution of snow deposition around the fence was similar to the description made by

Tabler's observation (Tabler, 2003). The CFD model was able to simulate the modifications of snow ground and structure of flow regimes dynamically.

Table 6-2: Comparison of CFD simulation and field measurement

Item	Field measurement	CFD with bottom gap	CFD without bottom gap
Height of the snow crest	1.2H	1.05H	1.05H
Distance between crest and fence	6H	3.8H	3.7H
Upwind deposition length	15H	10H	9.5H
Downwind deposition length	34H	30.5H	26H

6.7. CASE STUDY FOR THE EXPERIMENTS IN JAPAN

Table 6-3: The input variables for porous jump

Item	Fence A	Fence F
Height of fence (m)	0.15	0.15
Porosity	0.27	0.35
Downwind inclination angle (°)	0	0
Thickness of fence (m)	0.003	0.003
Bottom gap (m)	0	0
Face permeability (m^2)	1e+20	1e+20
Pressure-jump coefficient (m^{-1})	30224	10122

Wind tunnel experiments for snowdrift around the porous fences have been performed at Shinjo Cyrospheric Environment Laboratory in Japan. The cases of snowdrift around the fences A and F were selected for the 2D CFD modelling. The domain was configured as the same arrangement for the wind tunnel experiment. The fences were treated as porous jumps. The input variables for porous jumps are listed in Table 6-3.

The comparisons between the CFD simulation and the wind tunnel experiment are summarized in Table 6-4, where the snowdrift was considered to reach an equilibrium state. The presented symbols were corresponded to the ones in Section 4.3.4.

Table 6-4: Summary of the CFD and experimental results

Item	Fence A		Fence F	
	Experiment	CFD	Experiment	CFD
h/H	0.35	0.85	0.29	0.85
X_1/H	0.06	0	1.30	0
X_2/H	1.70	3.15	4.00	3.30
X_3/H	12.33	19.50	13.50	24.50

The discussions are as follows:

1) It can be observed from Table 6-4 that the areas of snow deposition predicted by the CFD modelling were marginally greater than the ones obtained from the wind tunnel experiments. The CFD results were closer to the field measurement data presented in Table 6-2, which indicated that the wind tunnel experiments have under-predicted the areas of snow deposition. This was mainly due to the difficulties to meet the similarity criteria of snowdrifts between prototypes and wind tunnel experimental modellings (White, 1996). Apart from this, wind tunnel experiment usually requires a considerable short space of time to reach a quasi-equilibrium snowdrift state. In the present wind tunnel experiments, the quasi-equilibrium snowdrift states were achieved in *30* minutes, that differed from

nature snowdrift where a quasi-equilibrium snowdrift state might be achieves in days. This would also undermine the area of snow deposition around.

2) The CFD results show that snow particles were deposited immediate behind the fences, which was similar to the field observation. However, the wind tunnel experiments show that snow deposition occurred at a distance from the fences, and such distance was increased with the increase of the fence porosity (*0.06H* for the fence A and *1.30H* for the fence F). The reason was that insufficient similarity between prototypes and wind tunnel modellings affected the mechanism of snow transport modes, consequently insufficient snow deposition in the front of the fence resulted in a difficulty to bury the fence partially, due to the existence of wind velocities in this region. The quick response of wind tunnel modelling might also undermine snowdrift to be fully developed.
3) The snow crests were lower than the ones presented in Table 6-2. The reason was that the top wall was treated as a no-slip wall instead of a symmetry wall. This treatment increased the level of velocity accelerations in the top fence region, which increased the friction velocities and reduced the rate of snow deposition.

Both of the wind tunnel experiments and the CFD modellings revealed that the fence F created a larger area of snow deposition than the fence A did, and porosity affected snow deposition mainly on the downwind deposition length. The position of snow crest was not sensitive to the change of porosity. It can be observed that the fence F formed the snow deposition area close to the one for the Wyoming fence without a bottom gap. This indicates that the optimal porosity for snow fences is in the range between *0.40-0.50* (Tabler, 2003).

6.8. CASE STUDY OF 3D CFD MODELLING

The 3D CFD modelling performed here were based on the threshold-friction-velocity theory, which was focused on the investigations of snow deposition areas and snow transport rates on the snow ground at the first snow deposition stage. The evolution of snow deposition were not included in the study.

The arrangement of the investigating cases are listed in Table 6-5. For all of the cases, the domain was configured as *55m* long, *20m* wide and *5m* high. The fence for each case was placed at the longitudinal distance of *15m* from the inlet, and the porous holes were uniformly distributed and were circle-shaped with the same diameters. The top wall in the domain was treated as a symmetry wall. Such arrangement ensured that only the floor (ground) boundary had wall effects on the snow-particle-transport-modes around the fence.

Table 6-5: lists the arrangement of four cases

Item	Unit	Case A	Case B	Case C	Case D
Fence Height (*H*)	m	1.0	1.0	1.0	1.0
Fence Width (*W*)	m	2.0	2.0	2.0	2.0
Thickness of fence (*Δm*)	m	0.003	0.003	0.003	0.003
Porosity(*β*)		0.20	0.30	0.50	0.50
Bottom gap	m	0	0	0	0.10
Diameter of hole (*D*)	m	0.05	0.06	0.08	0.08
Inclination angle *(θ)*	°	0	0	0	15
Quantity of element	million	1.48	1.95	1.94	1.96

Since the domain was symmetric along the YZ-Plane at *x=0m*, mesh was only applied to half of the domain. The present study was of concerns for the first stage of snow deposition and snow transport rate around the fence, and the modification of the structure of flow regimes due to the changes of snow deposition on the ground was not considered. Therefore, the simulations were performed under a steady state. The aerodynamic roughness length z_0 for the floor was changed to *5e-6m* as a snow bed shown in Table 6-1.

The first stage of snow deposition was examined by the distribution of floor wall shear stresses, friction velocities, and the snow transport rates. The friction velocity was calculated by Eqn.5-8, and the snow transport rate was evaluated by Eqn.2-49. It must be noted that such an assessment was only considered snow erosion and deposition within the saltation layer and was based on the empirical knowledge of the threshold friction velocity theory.

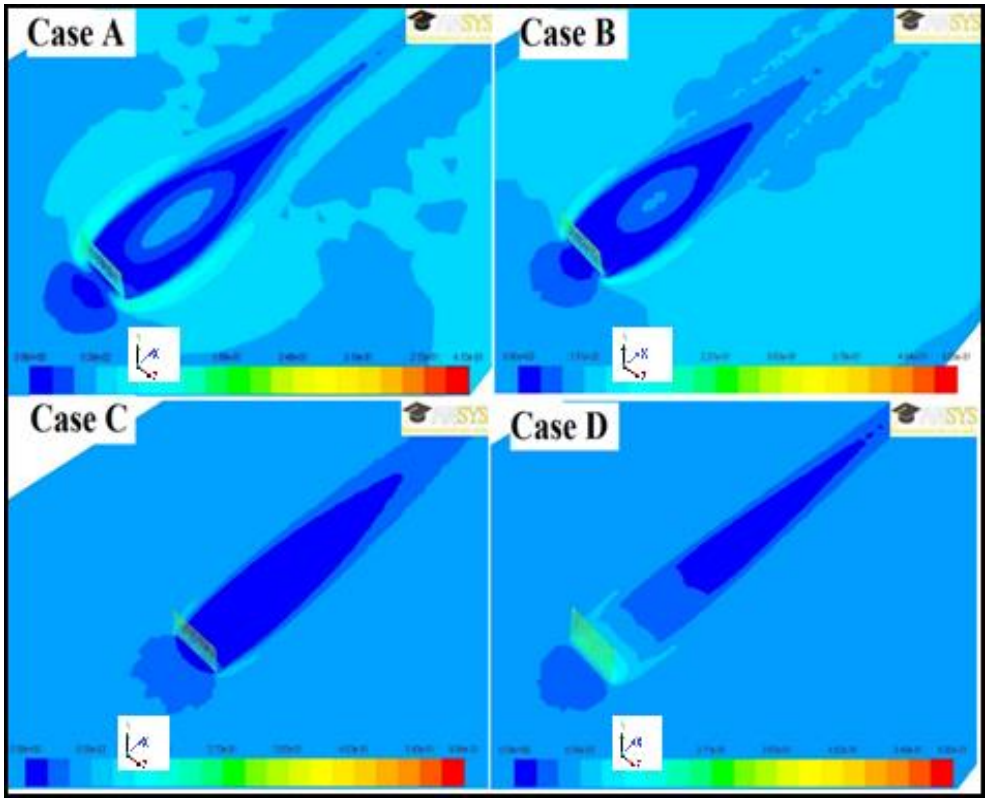

Figure 6-9: The distribution of shear stresses on the ground

The discussions are as follows:

1) The distribution of shear stresses on the ground for each case is displayed in Figure 6-9. It can be observed that higher wall shear stresses appeared in the regions of the fence edges, due to the accelerations of displacement airflow passing over the edges. The shear stresses were weakened and reduced the distribution regions with the increase of the porosities. Apart from the case D, low shear stresses were distributed right before and behind the fences. Behind the fences, the distribution patterns of the cases A and B appeared similar, where

lower shear stresses surrounding an oval-shape core region formed by relatively higher shear stresses. The size of the core region was reduced from the case A to the case B, and disappeared in the cases of C and D. It can be explained that such a core region was affected by the reversal and circulating flow due to the mechanism of airflow through fences with low or medium porosities. The distribution of shear stresses for the case D demonstrated a different pattern from the others, where higher shear stresses developed right behind the fence due to the accelerations of airflow between the ground and the bottom edge, and the lower shear stress region was offset at a distance of around *3.5H* from the fence. The different distribution patterns of shear stresses reveals that different arrangements of porosity and fence placements have significant impacts on snowdrift transport modes.

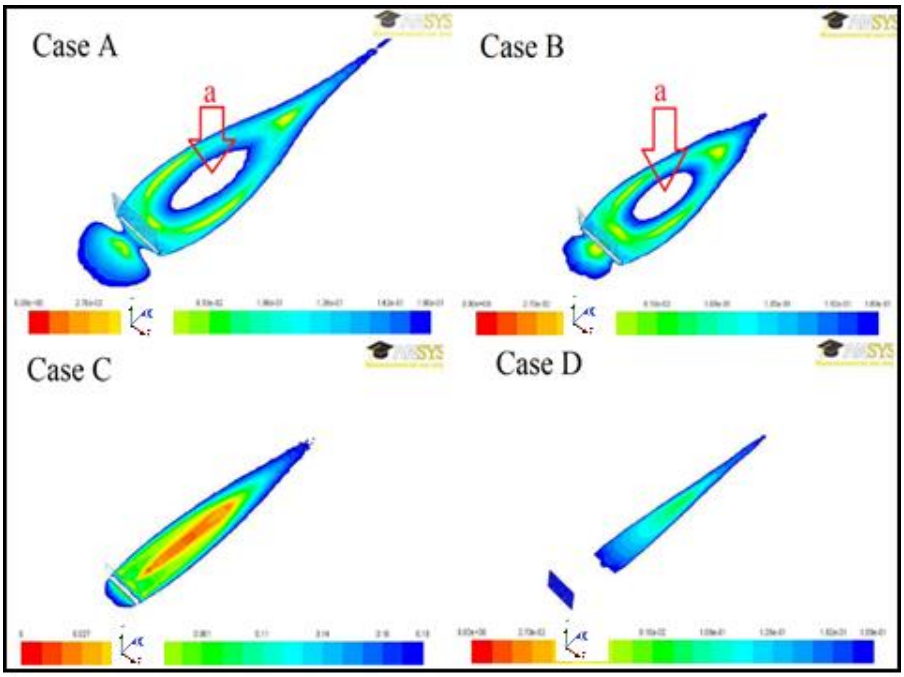

Figure 6-10: The distribution of shear velocities on the ground, where the plotted values not greater than 0.18m/s

2) The threshold friction velocity for snow erosion was assumed at *0.18m/s* in the present study. Figure 6-10 shows the distribution of shear velocities for each case, where the plotted values were not greater than the threshold friction velocity of

0.18m/s. The area of friction velocity before the fence was reduced accordingly with the increase of porosity. The cases A and B had a similar distribution pattern behind the fences, where lower friction velocities were developed surrounded an oval-shape core region (pointed by the red arrow of *a*), at which the friction velocities were greater than the value of the threshold friction velocity. It indicates that snow particles were firstly deposited surrounded the region *a*. It could be expected that there would be two snow crests developed before and after the region *a* at the first stage for the cases A and B.

The distribution of friction velocities for the case D appeared quite different from the others. The plotted friction velocities only appeared approximately at a distance of *2.5H* behind the fence. It can be observed that the position of snow deposition for the case D was farther away from the fence downwind than the others did. Similar to the case C, the lowest values of friction velocities occurred in the central area of the domain.

The investigation revealed that porosity had significant influence on the distribution of friction velocities around the fences; particularly the distribution pattern for fence with high porosity was quite different from the ones for fence with low or medium porosity. Placing a fence with a bottom gap and an inclination angle would affect the creation of friction velocities around, and the position of snow deposition was farther away from the fence than the others did.

3) Figure 6-11 presents the distribution of snow transport rate for each case, where the negative values refer to the snow deposition rate, while the position values refer to the snow erosion rate. For the cases of A,B and C, the highest erosion rate appeared in the regions of two side edges of the fence, which differed from the case D, where the highest erosion rate occurred under the bottom of the fence area. This was due to the accelerations of displacement airflow passing over the fence edges. The highest deposition rate appeared in the regions where the lowest friction velocities in the presence (pointed by the black arrows). The position pointed by the arrow 1 moved closer to the fence from the case A to the case B, and disappeared in the cases C and D, which indicated that snow deposition rate

before the fence was reduced with the increase of fence porosity. The arrows 3 and 4 appeared in the cases A and B, but disappeared in the cases C and D, which also implied that higher deposition rate intended to be concentrated in the central area of the domain when the value of fence porosity shifted from low or medium to high value. It can be observed that the distance between the arrow 2 and the arrow 5 was shortened with the increase of the fence porosity. This indicated that fence without a bottom gap would create two snow crests leeward the fence, in the central area of the domain at the first stage of snow deposition. The significance of these two crests was reduced with the increase of the fence porosity. There was only one snow crest for the case D, and the position of snow deposition occurred farther away from the fence than the case C did. This finding was coincidence with the ones revealed in the 2D snowdrift around the Wyoming fence in Section 6.6.

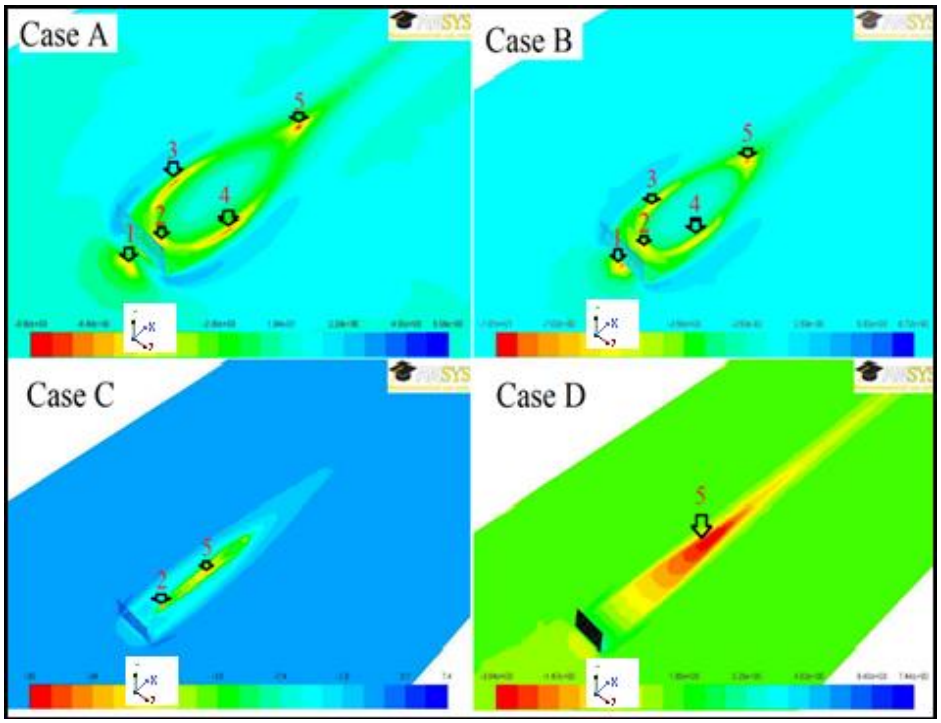

Figure 6-11: The distribution of snow transport rates

4) Figure 6-12 is the snow transport rate at the line A for each cases, where the line A is at the middle line on the floor across the entire domain in the longitudinal

direction. It can be observed that the case C had the greatest deposition rate, while the case D had the greatest erosion rate and the minimum deposition rate among the others. The cases A and B appeared a similar trend, where a peak of deposition rate before the fence and two peaks of deposition rate behind the fence. An erosion region was presented between the two peaks of deposition rate behind the fence. It differed from the cases C and D, which only created a single deposition area leeward the fence.

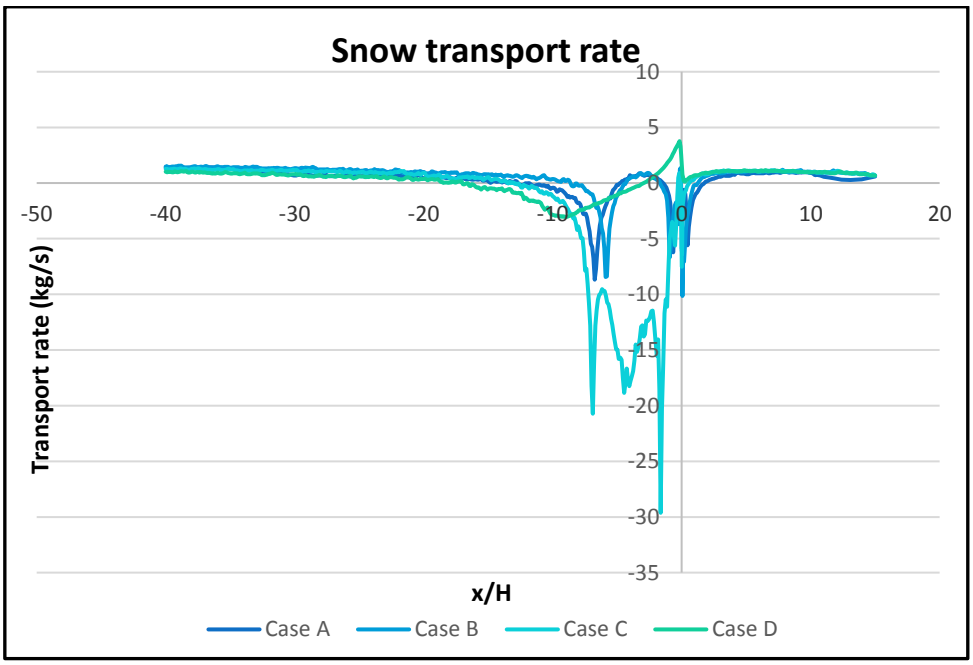

Figure 6-12: Snow transport rate at the line A

5) Table 6-6 summarizes the snow deposition area along the line A at the first stage. It can be observed that the case D had the longest deposition area among the others. However, if considered the snow deposition rate, the case C had the highest trapping efficiency. The case B had the smallest deposition area, which might indicate that increasing porosity in the low or medium porosity range did not mean significantly improving the trap efficiency of the fence. Figure 6-11 and Table 6-6 revealed that the optimal porosity of snow fence was in the range around *0.5*. Placing a fence with an optimum bottom gap with an inclination angle of *15°* increased erosion rate and reduced deposition rate leeward the fence at the first

stage, which effectively shifted the position of snow deposition farther away from the fence with a longer distribution. Consequently, snow deposition would be developed back forwards to the fence until the friction velocities at the fence bottom area have been modified below the threshold friction velocity, due to the evolution of snow deposition on the ground.

Table 6-6: The snow deposition areas for each case at the first stage

Item			Case A	Case B	Case C	Case D
Before fence (x/H)	Deposition area 1	From	0	0	0	0
		To	1.7	1.2	0.5	0
		Net	1.7	1.2	0.5	0
After fence (x/H)	Deposition area 2	From	0	0.2	0	3.0
		To	1.4	1.6	13.3	17.0
		Net	1.4	1.4	13.3	14.0
	Deposition are 3	From	4.8	3.8		
		To	12.6	9.5		
		Net	7.8	5.7		
Total deposition area (x/H)			10.9	8.3	13.8	14.0

The 3D modellings have demonstrated the features of snow transport around different fences at the first stage, which were quantitatively in good agreement with the findings from the 2D modellings discussed in Section 5.6 and the field experiments (Tabler, 2003). It has proved that the threshold friction velocity theory based model can be used to predict saltation snow transport under a steady or an equilibrium snowdrift state.

6.9. NUMERICAL UNCERTAINTY

The estimation of numerical uncertainty comes a need to establish the credibility of the numerical modelling. Verification and validation are the primary means to assess accuracy and reliability in CFD simulations. Verification is the assessment of the accuracy of the solution to a computational model by comparison with known solutions, which is primarily a mathematics issue. Validation is the assessment of the accuracy of a computational simulation by comparison with experimental data, which is however, a physics issue (Roache, 1998).

The present discussions of numerical uncertainty focus on the validation, which identification and quantification of the error and uncertainty in the conceptual and computational models, quantification of the numerical error in the computational solution, comparison between the computational results and the experimental data, are of major concern.

Errors associated with geometric constructions, mesh sensitivity analysis, convergence criteria, and consideration of solver have been discussed prior to the simulation. During the simulations, solutions have been discretized and converged, and there was no computer round-off error occurred. Additionally, the CFD simulations were performed under a sophisticated commercial software ANSYS FLUENT. Therefore, it can be regarded that such errors had minor impact on the numerical uncertainty.

The numerical predictions on the structures of wind velocity were in good agreement with the corresponding wind tunnel experimental results. However, the numerical modellings have over-predicted the level of turbulence if compared with the experimental results. This is due to the two-equation based turbulence models inadequately to describe the complex nature of turbulence mathematically.

The numerical predictions of windblown snowdrift around the fences were quantitatively in good agreement with the field measurement. However, the rate of snow deposition seemed to be under-predicted in the numerical simulations. The simplifications and assumptions in the snowdrift transport model were surely introduced numerical uncertainty. The applied turbulence model has over-predicted the level of turbulence,

which consequently under-predicted the rate of snow deposition due to over-predicted the rate of snow erosion in the modellings.

Although six different turbulence models have been tested in the numerical study with the Standard k-ω model shown a limited improvement, the uncertainty on numerical turbulence modelling is evident.

6.10. SUMMARY

Windblown snowdrifts around various porous fences have been numerically investigated by 2D and 3D modellings, and the results have been compared with the corresponding field and wind tunnel experimental results. The summaries are as follows

1) Numerical simulations of windblown snowdrifts around fences have been performed under the transient 2D snowdrift model. The evolution of snow deposition has been simulated by applying the dynamic mesh techniques. The distribution of snow deposition was quantitatively and qualitatively in good agreement with the field measurement. However, it was not so good in agreement with the wind tunnel experimental results. The agreement between the numerical predictions and field experimental results has revealed the incompetence of the wind tunnel to simulate snowdrift inside. It also implies that the numerical snowdrift modelling is an useful supplementary tool in the snow fence study.
2) The numerical snowdrift modelling has investigated the Wyoming fence with or without a bottom gap. At the equilibrium snowdrift state, it was found that the bottom gap had insignificant influence on the position of the snow crest and the upwind deposition length. However, it had extended the downwind deposition length at *3.5* times of the fence height longer than the one for the fence without the bottom gap. Placing A fence with the bottom gap was surely improved the trap efficiency. However, such improvement was evident only before the fence was buried by the snow particles, which implies the bottom gap has a limited improvement on the fence trap efficiency. .
3) It is worth noting that the patterns of snow depositions between the fences with or without the bottom gap were quite different at the beginning of the simulations.

For the fence without the bottom gap, snow particles were deposited immediate before and behind the fence, and there were two snow crests appeared in the leeward. For the fence with the bottom gap, snow particles were deposited at the distance of *3.7H* leeward away from the fence, and there was only single snow crest appeared. With the time evolution, such difference was visibly diminished.

4) The numerical simulations of Japan experiments found that porosity affected snow deposition mainly on the downwind deposition length. The position of snow crest was not sensitive to the change of porosity, which indicated that the position of snow crest was mainly affected by the fence height. It was also found that the trap efficiency was significantly improved with the increase of porosity from *0.27* to *0.35*. This explains that porosity is an influential structural parameter in determining the performance of snow fences.
5) The three dimensional snow deposition areas and snow transport rates at the first stage of snow deposition were investigated by a 3D model, which was based on the threshold-friction-velocity theory performed under a steady or an equilibrium snowdrift state. At the first stage, the snow deposition for the fences with porosity of *0.20* or *0.30* appeared to develop two-snow crests leeward the fence, while the fences with porosity of *0.50*, having or having not a bottom gap, only developed a single snow crest leeward the fence. This was coincidence with the finding from the 2D modelling. The numerical simulation also revealed that the optimal porosity for snow fence is in the range around *0.50*. Placing the fence with a bottom gap at an inclination angle of *15°* layback had the longest deposition length leeward the fence.

Overall, the numerical simulations were in good agreement with the findings from the physical experiments.

Chapter 7 CONCLUSIONS AND RECOMMENDED FUTURE WORK

The work in this thesis has reviewed the fundamental knowledge and techniques related to the evaluation of porous fence performance and the up to date research outcomes of the interactions among the porous fence, wind flow and snowdrifts. The correlations of the key technical parameters influencing the fence performance were investigated by using wind tunnel experimental and numerical techniques. The targeting environment is set intentionally comparable to the one in Cold Regions. The knowledge developed in this research can hence be used to the application and design of fences to Cold Regions.

Attentions have paid on the issues that a systematic research work has not been achieved today. New approach to study the effect of the creation and distribution of the fence surface shear has been applied in this thesis. The ultimate goal of this thesis is to provide novel and useful knowledge to the optimal fence design.

7.1. CONCLUSIONS

Based on the experimental and numerical studies, the conclusions can be drawn as follows:

1) Single-phase airflow and two-phase snowdrift airflow around the different porous fences have been investigated in the environmental wind tunnel. Important features of single-phase airflow and two-phase snowdrift airflow around the fences have been successfully investigated, and the results are generally in good agreement with the findings from the other researchers. The experiment has not only provided physical and useful information in the present work, but also has laid a foundation to carry out the numerical study.
2) The reliability and credibility of numerical modelling in this thesis have been assessed against the corresponding physical experiments. Both of 2D and 3D models have well predicted the structure of velocity around the fence. Both of them have predicted the similar structure of turbulence distribution but over-

predicted the level of turbulence around the fence, if compared with the corresponding experimental results. The applied numerical models are intentionally to reduce a degree of the complexity in the simulations, such as using porous jump for 2D model, using unconstructed elements for 3D model, and reasonably simplifying the two-phase snowdrift transport model, etc. All of which make it easier to construct the numerical models and quicker to reach numerical solutions at low computational cost. The numerical models have demonstrated the capability in the current research, and applicable to the optimal fence design.

3) The study has found that porosity is the most influential structural parameter affecting the performance of porous fences in many aspects. The velocity vector following the main airflow direction is dominant in determining the structure of airflow regime leeward a fence. Fence performance is not sensitive to the changes of approaching atmospheric airflow velocity. Fence height has significant impact on the fence performance. Bottom gap can improve snow fence trap efficiency. All of which are agreed with the findings from the other researchers, which also proves the research methodology in the thesis is sound.
4) Although the definition of fence effective zone is vague in the research field even today. The key factors influencing the fence effective zone have been investigated by evaluating the reduction of wind velocity leeward the fence in this thesis. Fence effective zone is not sensitive to the change of approach airflow velocity. Increasing fence height will increase the physical size of the fence effective zone but not proportional to the increase of the fence height, which implies that purely increasing fence height is not a economic way in the optimal fence design. Fence effective zone will be significantly reduced when the non-normal wind load at an angle is greater than $30°$ to the fence. Fence with the optimum porosity will effectively increase its effective zone. The study again reveals that optimal fence design must optimize the porosity. Optimal fence design should consider the evaluation of the fence effective zone.
5) Previous research work on the effects of the arrangement of porous holes is limited. Numerical investigation on this issue in the thesis has found that the distribution and size of holes have impacts on the fence performance only in the

close fence region. There is a desirable range of size of holes, which should be identifies in the fence design to maximize its performance. The shape of holes has noticeable negative effect on the fence performance when the sharp angular corners are in presence in the holes. A novel approach is applied to study the effect of the creation and distribution of the fence surface shear on the fence performance. Through which, it reveals that fence performance is associated with the fence surface shear, and reducing the amount of shear on the fence surface will generally increase the reattachment length and the shelter distance. The investigation reveals that the arrangement of porous holes has noticeable effects on the fence performance, especially when the close fence environment is of concern. Porous holes with sharp angular corners should be usually avoided in the fence design. However, if the environment is required to have low level of turbulent airflow, a degree of sharp angular corners should be considered in the fence design.

6) It is found that the Standard k-ω model had better predictions on the structure of airflow regimes especially in the fence effective zone, which differs from the majority of the other research employing the Standard k-ε model.
7) The numerical investigation of the effect of non-normal wind loads onto the fences is comparatively new to the research field. It has found that the fence should be placed within the angle of $\theta \leq 30°$ to the wind load, where the effective shelter distance can be estimated in a linearized eqn.5-18, and the normal drag coefficient could be described as a function of $\cos^2\theta$.
8) Differed from the majority of research work, the transient snow transport model considers the snow transport rate as a whole without distinguishing the rate in saltation and suspension layer. This approach has better predictions than those assuming the equilibrium saltation layer in non-equilibrium flow fields. The numerical simulations have found that the position of the snow crest is mainly determined by the fence height. Porosity and bottom gap mainly affect the downwind deposition length, which consequently improve the trap efficiency of the snow fence. The optimum porosity for snow fences is in the range from *0.4* to *0.5*, which is greater than the one for wind fences in the range from *0.25* to *0.35*.

9) The two-phase snowdrift modelling has found that two snow crests have been observed leeward the fence at the beginning of snow deposition, when the fence is placed without a bottom gap to the snow ground. This finding has not been stated in the other research work. The reason is that the other researchers studied the fence with a bottom gap to the snow ground, which the present study also reveals that there is only one snow crest developed under this case.
10) The wind tunnel simulation of snowdrift around the fences has marginally under-predicted the size of snow deposition. The incompetence of the wind tunnel experiment implies that the numerical modelling may play a more important part in the snow fence research, since the numerical predictions were quantitatively in good agreement with the field observations.

7.2. RECOMMENDED FUTURE WORK

The recommended future work is summarized as follows:

1) The current wind tunnel experiments used the ultrasonic anemometer to measure velocity vectors, which was intrusive to the flow field. This introduced errors in the experimental data. As discussed in Section 4.4, for a given velocity measurement, it will introduce *4* times of error of accuracy on turbulence intensity, and *6* times of error of accuracy on turbulent kinetic energy. This raises the experimental uncertainty especially for the accuracy of turbulence data. Future work should calibrate the intrusive measurement against the less or non-intrusive measurements such as PIV, and improve the accuracy of experimental data by employing more advanced measurement equipment. Field experiment should be engaged.
2) The present wind tunnel simulation of snowdrift around the fences only provided the indicative information in this thesis, which implies the necessity of the improvement in the future work.
3) The numerical study has found the inaccuracy on predicting turbulence. It has been widely recognized by many researcher that the two-equation based turbulence models have limitations on predicting turbulent flows, such as the turbulent flow developed by porous fences. Future work should improve the

accuracy of turbulence predictions. Model with large eddy simulation (LES) or Reynolds stress model (RSM) should be justified in the future work.

4) The current snowdrift transport model has produced promising results. However, reducing a degree of simplification and assumption to expand the current model for wider applications is the task for the future work.
5) The study has been found that the level of turbulence affects the performance of porous fence in many aspects. However, systematic justification of such effects has not included in this thesis. This was due to the lack of robust data and clear guidance available at the present. It can be expected to be achieved by improving the accuracy of the experimental and numerical predictions on turbulence in the future work.
6) Icing are a common phenomenon in the wintry Cold Regions. The effect of icing on the performance of porous fences is required in the future work.

REFERENCES

Abramovich, G., 1963. *Theory of Turbulent.* s.l.:MIT Press.

Alhajraf, S., 2004. Computational fluid dynamic modeling of drifting particles at porous fence. *Environmental Modeling and Software,* Volume 19, pp. 163-170.

Allori, D., Bartoli, G. & Mannini, C., 2013. Wind tunnel tests on macro-porous structural elements: A scaling procedure. *Journal of Wind Engineering and Industrial Aerodynamics,* Volume 123, pp. 291-299.

Alpman, E. & Long, L., 2005. *Separated turbulence flow simulations using a Reynolds sress model and unstructured meshes.* Reno, NV, s.n.

Anderson, R.S.; Haff, P.K.;, 1988. Simulation of eolian saltation. *Science,* Volume 241, pp. 820-823.

Andres , G., Wolfgang, F., Wolfgang, S. & Mathias, D., 2011. CFD modeling and validation of measured wind field data in a portable wind tunnel. *Aeolian Research,* Volume 3, pp. 315-325.

ANSYS, 2009. *ANSYS FLUENT 12.0 Theory Guide.* s.l.:ANSYS, Inc..

ANSYS, 2011. *ANSYS FLUENT user's guide.* s.l.:ANSYS, Inc..

Arendt, W. & Warma, H., 2003. Dirichlet and Neumann boundary conditions: what is in between?. *Evolution Equations,* Volume 3, pp. 119-135.

Australia, S., 1989. SAA Loading Code, Part 2: Wind Loads. In: *Australian Standard AS1170.2.* s.l.:s.n.

Bagnold, R. A., 1941. *The physics of blown sand and desert dunes.* London: Methuen.

Bang, B., Nielsen, A., Sundsbø, P. & Wiik, T., 1994. Computer simulation of wind speed, wind pressure and snow accumulation around buildings (SNOW-SIM). *Energy and Buildings,* Volume 21, pp. 235-234.

Barlow, J. B., Rae, Jr, W. H. & Pope, A., 1999. *Low-speed wind tunnel testing (Third edition).* New York: John Wiley & Sons, Inc.

Bates, R. & Bilello, M., 1966. *Defining the cold regions of the northern hemisphere,* Hanover, New Hampshire: Cold Regions Research and Engineering Laboratory.

Baumeister, T.; Marks, L.S.;, 1958. *Mechanical Engineers Handbook.* New York: McGraw Hill Book Co..

Beyers, M. & Waechter, B., 2008. Modeling transient snowdrift development around complex three-dimensional structures. *Wind Engineering and Industrial Aerodynamics,* Volume 96, pp. 1603-1615.

Blocken, B., 2014. 50 years of computational wind engineering: past, present and future. *Journal of Wind Engineering and Industrial Aerodynamics,* Volume 129, pp. 69-102.

Boldes, U., Colman, J. & Leo, J., 2003. About the penetration of a horizontal axis cylindrical vortex into the nearby downwind region of a vertical porous fence. *Wind Engineering and Industrial Aerodynamics,* Volume 91, pp. 859-872.

Bourdin, P. & Wilson, J., 2008. Windbreak aerodynamics: is computatinal fluid dynamics reliable?. *Boundary-Layer Meteorology,* Volume 126, pp. 181-208.

Bradley, E. & Mulhearn, P., 1983. Development of velocity and shear stress distributions in the wake of a porous shelter fence. *Wind Eng. Ind. Aerodyn.,* Volume 15, pp. 145-156.

Brennen, C. E., 2005. *Fundamentals of multiphase flow.* Cambridge: Cambridge University Press.

Briassoulis, D.; Mistriotis, A.; Giannoulis, A.;, 2010. Wind forces on porous elevated panels. *Wind Engineering and Industrial Aerodynamics,* Volume 98, pp. 919-928.

Campolongo, F. & Braddock, R., 1999. The use of graph theory in sensitivity analysis of model output: a second orfer screening method. *Reliability Engineering and System Safety ,* Volume 64, pp. 1-12.

Celik, I., Cehreli, Z. & Yavuz, I., 2005. Index of resolution quality for large eddy simulations. *Journal of Fluids Engineering,* Volume 127, pp. 949-958.

Cermak, J., 1984. Wind-similation critera for wind-effect tests. *Structural Engineering,* Volume 110, pp. 328-339.

Chanson, H., 2009. Turbulent air-water flows in hydraulic structures: Dynamic similarity and scale effects. *Environmental Fluid Mechanics,* Volume 9, pp. 125-142.

Chen, G., Wang, W., Sun, C. & Li, J., 2012. 3D numerical simulation of wind flow behind a new porous fence. *Powder Technology,* Volume 230, pp. 118-126.

Chmielewski, M. & Gieras, M., 2013. Three-zonal wall function for k-e Turbulence models. *Computational Methods in Science and Technology,* Volume 19, pp. 107-114.

Clifton, A. & Lehning, M., 2008. improvement and validation of a snow saltation model using wind tunnel measurements. *Earth Surface Processes and Landforms,* Volume 33, pp. 2156-2173.

Cornelis, W. & Gabriels, D., 2005. Optimal windbreak design for wind-erosion control. *Journal of Arid Environments,* Volume 61, pp. 315-332.

Counihan, J., 1969. An improved method of simulating an Atmospheric Boundary Layer in a wind tunnel. *Atmospheric Environment,* Volume 3, pp. 197-214.

Counihan, J., Hunt, J. & Jackson, P., 1974. Wakes behind two-dimensional surface obstacles in turbulent boundary layers. *Journal of Fluid Mechanics,* Volume 64, pp. 529-564.

Davenport , A., 1967. *The dependence of wind loads on meteorological parameters.* Ottawa, Canada, International Seminar on Wind Effects on Buildings and Structures.

Davide, A., Gianni, B., Claudio, M. & Lorenzo, P., 2013. Wind tunnel tests on marco-porous structural elements: a scaling procedure. *Wind Engineering and Industrial Aerodynamics,* Volume 123, pp. 291-299.

Decker, R., 1991. *Multiphase flows and the modeling of drifting snow.* Feb, 26-28, p.673-684, s.n.

Dong, Z. et al., 2010. A wind tunnel simulation of the turbulence fields behind upright porous wind fences. *Arid Environments,* Volume 74, pp. 193-207.

Dong, Z., Luo, W., Qian, G. & Wang, H., 2007. A wind tunnel simulation of the mean velocity fields behind upright porous fences. *Agricultural and Forest Meteorology,* Volume 146, pp. 82-93.

Dong, Z., Luo, W., Qian, G. & Wang, H., 2011. Evaluating the optimal porosity of fences for reducing wind erosion. *Sciences in Cold and Arid Regions,* Volume 3, pp. 1-12.

Dong, Z., Qian, G., Luo, W. & Wang, H., 2006. Threshold velocity for wind erosion: the effects of porous fences. *Environ Geol,* Volume 51, pp. 471-475.

Dong, Z., Wang, H. & Liu, X., 2002. Velocity profile of a sand cloud blowing over a gravel surface. *Geomorphology,* Volume 49, pp. 277-289.

Durand, Y. et al., 1999. A computer-based system simulating snowpack structures as a tool for regional avalanche forecasr. *Glaciology,* 45(151), pp. 466-484.

Fang, F. & Wang, D., 1997. On the flow around a vertical porous fence. *Journal of Wind Engineering and Industrial Aerodynamics,* Volume 67, pp. 415-424.

Gauer, P., 1999. *Blowing and drifting snow in Alpine terrain: a physically-based numerical model and related field measurements.* s.l.:PhD Thesis.

Gauer, P., 2001. Numerical modeling of blowing and drifting snow in Alpine terrain. *Glaciol.,* Volume 47 (156), pp. 97-110.

Gerasimov, A., 2006. *Modeling turbulent flows with Fluent.* s.l.:ANSYS, Inc..

Giannoulis, A., Mistriotis, A. & Briassoulis, D., 2010. Experimental and numerical investigation of the airflow around a raised permeable panel. *Wind Eng. Ind. Aerodyn.,* Volume 98, pp. 808-817.

Greeley, A.D.; Iversen, J.D.;, 1986. *Wind as a geological process,* Cambridge: Cambridge University Press.

Guan, D. et al., 2009. Variation in wind speed and surface shear stress from open floor to porous parallel windbreaks: A wind tunnel study. *Journal of Geophysical Research,* Volume 114, pp. 1-13.

Gurer, I. et al., 2002. *Comparison of the models of different types of snow fences in cold wind tunnel.* Sapporo, Japan, s.n.

Hagen, L., 1976. Windbreak design for optimum wind erosion control. *Proceeding of the Symposium: Sheltbelts on the Great Plains, Denver, CO.,* pp. 31-36.

Hagen, L. & Skidmore, E., 1971. Turbulent velocity fluctuations and vertical flow as affected by windbreak porosity. *Trans ASAE,* Volume 14, pp. 634-637.

Hargreaves, D. & Wright, N., 2007. On the use of the k-e model in commercial CFD software to model the neutral atmospheric boundary layer. *Journal of Wind Engineering and Industrial Aerodynamics,* Volume 95, pp. 355-369.

Heisler, G. & Dewalle, D., 1988. Effects of windbreak structure on wind flow.. *Agriculture. Ecosystems and Environment,* Volume 22-23, pp. 41-69.

Heller, V., 2011. Scale effects in physical hydraulic engineering models. *Journal of Hydraulic Research,* Volume 49, pp. 293-306.

Hirt, C., 1993. Volume-Fraction Techniques: powerful tools for wind engineering. *Wind Eng. Ind. Aerodyn.,* Volume 46 & 47, pp. 327-338.

Hoerner, S., 1965. *Fluid Dynamic Drag; Theoretical, experimental and statistical information, Hoerner Fluid Dynamics.* s.l.:s.n.

Holford, J. & Hunt, G., 2003. Fundamental Atrium Design for Natural Ventilation. *Journal of Building and Environment,* Volume 38, pp. 409-426.

Holmes, J., 1988. *Pressure and drag on surface-mounted rectangular plates and walls.* Auckland, s.n.

Hong, S.-W., Lee, I.-B. & Seo, I.-H., 2015. Modelling and predicting wind velocity patterns for windbreak fence design. *Journal of Wind Engineering and Industrial Aerodynamics,* Volume 142, pp. 53-64.

Huang, L., Chan, H. & Lee, J., 2012. A numerical study on flow around nonuniform porous fences. *Applied Mathematics,* pp. 1-12.

Ingham, D. & Pop, I. eds., 2005. *Transport Phenomena in Porous Media.* s.l.:Elsevier Ltd.

Jensen, M., 1954. *Shelter effect: Investigations into Aerodynamics of shelter and its effects on climate and crops.,* Copenhagen: Danish Tech. Press.

John, James E.A.; Haberman, William L.;, 1988. *Introduction to fluid mechanics (third edition).* Englewood Cliffs, New Jersey: Prentice Hall.

Judd, M., Raupach, M. & Finnigan, J., 1996. A wind tunnel study of turbulent flow around single and multiple windbreaks; Part I: Velocity fields. *Boundary-Layer Meteorology,* Volume 80, pp. 127-165.

Kim, H.-B. & Lee, S.-J., 2001. Hole diameter effect on flow characteristics of wake behind porous fences having the same porosity. *Fluid Dynamics Research,* Volume 28, pp. 449-464.

Kim, H. & Lee, S., 2002. The structure of turbulent shear flow around a two-dimensional porous fence having a bottom gap. *Journal of Fluids and Structures,* Volume 16, pp. 317-329.

Kind, R., 1990. Mechanics of aeolian transport of snow and sand. *Wind Engineering and Industrial Aero-Dynamics,* Volume 36, pp. 855-866.

Ki-Pyo , Y. & Young-Moon, K., 2009. Effect of protection against wind according to the variation porosity of wind fence. *Environ Geol,* Volume 56, pp. 1193-1203.

Kline, S. J., 1986. *Similitude and Approximation Theory.* New York: Springer-Verlag.

Kovanen, K.; Seppanen, O.; Siren, K.; Majanen, A.;, 1989. Turbulent air flow measurements in ventilated spaces. *Environmental International,* Volume 15, pp. 621-626.

Lamb, H., 1932. *Hydrodynamics (6th edition).* Cambridge: Cambridge University Press.

Launder, B., Reece, G. & Rodi, W., 1975. Progress in the development of a Reynolds-stress turbulent closure. *Journal of Fluid Mechanics,* Volume 68, pp. 537-566.

Launder, B. & Spalding, D., 1972. *Lectures in Mathematical Models of Turbulence.* s.l.:Academic Press.

Laurence, D., 2002. *Applications of Reynolds averaged Navier Stokes equations to industrial flows.* s.l., Introduction to Turbulence Modelling, von Karman Institute for Fluid Dynamics.

Lee, S. & Kim, H., 1998. Velocity field measurements of flow around a triangular prism behind a porous fence. *Wind Eng. Ind. Aerodyn.,* Volume 77/78, pp. 521-530.

Lee, S. & Kim, H., 1999. Laboratory measurements of velocity and turbulence field behind porous fences. *Wind. Eng. Ind. Aerodyn.,* Volume 80, pp. 311-326.

Lee, S.-J. & Park, C.-W., 1998. Surface-pressure variations on a triangular prism by porous fences in a simulated atmospheric boundary layer. *Wind Engineering and Indusrtrial Aerodynamics,* Volume 73, pp. 45-58.

Lee, S. & Park, C., 2000. The shelter effect of porous wind fences on coal piles in POSCO open storage yard. *Journal of Wind Engineering and Industrial Aerodynamics,* Volume 84, pp. 101-118.

Lee, S., Park, K. & Park, C., 2002. Wind tunnel observations about the shelter effect of porous fences on the sand particle movements. *Atmos. Environ.,* Volume 36, pp. 1453-1463.

Letchford, C., 2001. Wind loads on rectangular signboards and hoardings. *Wind Engineering and Industrial Aerodynamics,* Volume 89, pp. 135-151.

Li, B. & Sherman, D. J., 2015. Aerodynamics and morphodynamics of sand fences: A review. *Aeolian Research ,* Volume 17, pp. 33-48.

Linden, P., 1999. The Fluid Mechanics of Natural Ventilation. *Annual Review Fluid Mechanics,* Volume 31, pp. 201-238.

Liston , G., Brown, R. & Dent, J., 1993. A two-dimensional computational model of turbulent atmospheric surface flows with drifting snow. *Glaciology,* Volume 18, pp. 281-286.

Liston, G. & Sturm, M., 1998. A snow-transport model or complex terrain. *Glaciol.,* Volume 44 (148), pp. 498-516.

Liu, S. & Liu, S., 1991. *The atmospheric dynamics.* Beijing : Peking University Publishers.

Li, Y., 1999. Buoyancy-driven natural ventilation in a thermally stratified one-zone building. *Journal of Building and Environment,* Volume 35, pp. 207-214.

Masselot, A. & Chopard, B., 1996. *Littice gas modelling of snow transport by wind*, s.l.: University of Geneva.

McAneney, K. & Judd, M., 1991. Multiple windbreaks: an aeolean ensemble. *Boundary Layer Meteorology,* Volume 54, pp. 129-146.

Menter, F., 1994. Two-equation eddy-viscosity turbulence models for engineering applications. *AIAA,* 32(8), pp. 1598-1605.

Mulati, Y. & Norio, T., 2009. Effects of windbreak width in wind direction on wind velocity reduction. *Forestry Research,* Volume 20, pp. 199-204.

Naaim-Bouvet, F. & Martinez, H., 1998. Numerical simulation of drifting snow: erosion and deposition models. *Annals of Glaciology,* Volume 26, pp. 191-196.

Naaim-Bouvet, F. & Mullenbach, P., 1998. Field experiments on "living" snow fences. *Annals of Glaciology,* Volume 26, pp. 217-220.

Nalpanis, P., 1985. *Saltating and suspended particles over flat and sloping surfaces II: Experiments and numerical simulations.* s.l., University of Aarhus, Denmark, pp. 37-66.

Nemoto, M., Nishimura, K., Kobayashi, S. & Izumi, K., 2004. Numerical study of the time development of drifting snow and its relation to the spatial development. *Annals of Glaciology,* Volume 38, pp. 343-350.

Nield, D. & Bejan, A. eds., 2006. *Covection in Porous Media, Springer, 2006,*. s.l.:Springer.

Norwegian Ministry of Petroleum and Energy, 2011. *An industry for the future - Norway's petroleum activities,* s.l.: Norwegian Ministry of Petroleum and Energy.

Norwegian Oil and Gas Association, 2014. *Time for Consolidation - Business Trend Report,* s.l.: Norwegian Oil and Gas Association.

Otakeguchi, K. et al., 2012. *PIV analysis of gas-solid multiphase flow relevant to wind-blown sand: Simultaneous measurement of near-wall turbulent motions and instantaneous relative velocity.* Lisbon, Portugal, 16th Int Symp on Applications of Laser Techniques to Fluid Mechanics.

Owen, P., 1964. Saltation of uniform grains in air. *Fluid Mechanics,* 20(2), pp. 225-242.

Packwood, A., 2000. Flow through porous fences in thick boundary layers: comparisons between laboratory and numerical experiments. *Wind Eng. Ind. Aerodyn.,* Volume 88, pp. 75-90.

Park , C. & Lee, S., 2001. The effects of a bottom gap and non-uniform porosity in a wind fence on the surface pressure of a triangular prism located behind the fence. *Wind Engineering and Industrial Aerodynamics,* Volume 89, pp. 1137-1154.

Patton, E. G. & Shaw, R. H., 1998. Large-eddy simulation of windbreak flow. *Boundary-Layer Meteorology,* Volume 87, pp. 275-306.

Perera, M., 1981. Shelter behind two-dimensional solid and porous fences.. *Journal of Wind Engineering and Industrial Aerodynamics,* Volume 8, pp. 93-104.

Ping , L., Dong, Z. & Luo, W., 2013. The pressure-field characteristics around porous wind fences: results of a wind tunnel study. *Environ Earth Sci,* Volume 68, pp. 947-953.

Plate, E., 1971. The aerodynamics of shelterbelts. *Agricultural Meteorology,* Volume 8, pp. 203-222.

Polanco, G., Xu, Y. & Mustafa, M. Y., 2013. *Conceptual approach applied to experiments design for noise mitigation in porous panels used on oil and gas platforms.* Budapest, Hungary, 4th IEEE International Conference on Cognitive Infocommunications.

Pomeroy, J.W.; Male, D.H.;, 1992. Steady-state suspension of snow. *Hydrology,* Volume 136, pp. 275-301.

Pomeroy, J. & Gray, D., 1990. Saltation of snow. *Water Resour. Res.,* Volume 26 (7), pp. 1583-1594.

Pope, S., 2000. *Turbulent flows.* s.l.:Cambridge University Press.

Pugh, E. & Winslow , G., 1966. *The Analysis of Physical Measurement.* s.l.:Addison-Wdsley.

Raine, J. & Stevenson, D., 1977. Wind protection by model fences in simulated atmospheric boundary layer.. *Wind Engineering and Industrial Aerodynamics,* Volume 2, pp. 159-180.

Reynolds, A., 1969. Flow deflection by Gauze screens. *Mechanical Engineering Science,* Volume 11, pp. 290-294.

Reynolds, O., 1895. *On the dynamical theory of incompressible viscous fluids and the determination of the criterion.* London, s.n., pp. 123-164.

Richards, P. & Robinson, M., 1999. Wind loads on porous structures. *Wind Engineering and Industrial Aerodynamics,* Volume 83, pp. 455-465.

Roache, P., 1998. *Verification and validation in computational science and engineering.* Albuquerque, New Mexico: Hermosa Publishers.

Robinson, S. K., 1991. *Coherent motions in the turbulent boundary layer.* Hampton, VA, USA, NASA Langley Research Center.

Rosenberg, N., 1974. *Microclimate: The Biological Environment.* New York: Wiley.

Saif, A., Mohamed, A. & Alam, E. A., 2010. *Variable porosity wind fences to control aeolian sand transport.* s.l., Proceedings of ICFD 10: 10th International Congress of Fluid Dynamics.

Sakamoto, H., Moriya, M., Takai, K. & Obata, Y., 2001. Development of a new type snow fence with airfoil snow plates to prevent blowing-snow disasters: Part1, evaluation of performance by blowing-snow simulation in a wind tunnel. *Natural Disaster Science,* Volume 23, pp. 1-11.

Santiago, J., Martin, F., Bezdenejnykh, N. & Sanz-Andres, A., 2007. Experimental and numerical study of wind flow behind windbreaks. *Atmospheric Environ.,* Volume 41, pp. 6406-6420.

Sato, T., Kosugi, K., Mochizuki, S. & Nemoto, M., 2008. Wind speed dependences of fracture and accumulation of snowflakes on snow surface. *Cold Regions Science and Technology,* Volume 51, pp. 229-239.

Schiller, L. & Naumann, A., 1933. Über die grundlegenden berechungen bei der schwerkraftaufbereitung. *Vereines Deutscher Ingenieure,* Volume 77, pp. 318-320.

Schmidt, R., 1980. Threshold wind-speeds and elastic impact in snow transport. *Hlaciology,* Volume 26, pp. 453-467.

Seginer, I., 1972. Windbreak drag calculated from the horizontal velocity field. *Boundry-Layer Meteorology,* Volume 3, pp. 87-97.

Shao, Y., 2000. *Physics and modelling of wind erosion* , Dordrecht: Kluwer.

Shiau, B., 1998. Measurement of turbulence characteristics for flow past porous windscreen. *Journal of Wind Engineering and Industrial Aerodynamics,* Volume 74-76, pp. 521-530.

Shiau, B. & Hsu, S., 2003. Measurement of the Reynolds stress structure and turbulence characteristics of the wind above a two-dimensional trapezoidal shape of hill. *Journal of Wind Engineering and Industrial Aerodynamics,* Volume 91, pp. 1237-1251.

Shiau, S. & Kim, H., 1999. Laboratory measurements of velocity and turbulence field behind porous fences. *Journal of Wind Engineering and Industrial Aerodynamics,* Volume 80, pp. 311-326.

Skidmore, E. & Hagen, L., 1970. Evapotranspiration and the aerial environment as influenced by windbreaks. In: *Proceeding of Great Plains Evapotranspiration Seminar.* s.l.:Bushland, TX, Great plains Agricultural Council, Publication No.50., pp. 339-368.

Smagorinsky, J., 1963. General circulation experiments with the primitive equations. *Monthly Weather Review,* Volume 91, pp. 99-164.

Standards Norway, 2006. *Norsork Standard C-002, Architectural Components and Equipment,* s.l.: Standards Norway.

Subhas, C., Yaragal, H., Govinda, R. & K., K. M., 1997. An experimental investigation of flow fields downstream of solid and porous fences. *Wind Engineering and Industrial Aerodynamics,* Volume 66, pp. 127-140.

Sundsbø, P., 1997. *Numerical modelling and simulation of snow-accumulations around porous fences.* Banff, Alberta, Canada, s.n.

Synder, W., 1972. Similarity criteria for the application of fluid models to the study of air pollution meteorology. *Boundary Layer Meteorology,* Volume 3, pp. 113-134.

Tabler, R., 1980. Geometry and density of drifts formed by snow fences. *Journal of Glaciology,* Volume 26, pp. 405-419.

Tabler, R., 2003. *Controlled blowing and drifting snow with snow fences and road design,* s.l.: National Cooperative Highway Research Program, Transportation Research Board of the National Academies.

Tabler, R. & Schmidt Jr., R., 1986. *Weather conditions that determine snow transport distance at a site in Wyoming.* s.l., UNESCO/WMO Symposia on the Role of Snow and Ice in Hydrology Proceedings, pp. 118-127.

Takahashi, T. et al., 2002. Turbulence characteristics of wind over a hill with a rough surface. *Journal of Wind Engineering and Industrial Aerodynamics,* Volume 90, pp. 1697-1706.

Taniere, A., Oesterle, B. & Monnier, J., 1997. On the behaviour of solid particles in a horizontal boundary layer with turbulence and saltation effects. *Exp. Fluids,* Volume 23, pp. 463-471.

Tani, N., 1958. *On the wind tunnel test of the model shelter hedge.* s.l., s.n., pp. A.6.1-80.

Tani, N., 1958. On the wind tunnel test of the model shelter hedge.. *Bulletin of the National Institute for Agricultural Sciences*, pp. A.6. 1-80.

Telenta, M., Duhovnik, J., Kosel, F. & Sajn, V., 2014. Numerical and experimental study of the flow through a geometrically accurate porous wind barrier model. *Journal of Wind Engineering and Industrial Aerodynamics,* Volume 124, pp. 99-108.

Tennekes, H., 1973. The logarithmic wind profile. *Atmospheric Science,* Volume 30, pp. 234-238.

Thordarson, S., 2002. Wind tunnel experiments and numerical simulation of snow drifing around an avlanche protecting dam. *Environmental Fluid Mechanics,* Volume 2, pp. 265-289.

Tominaga, Y.; Mochida, A.; Yoshino, H.; Shida, T.; Okaze, T.;, 2006. *CFD prediction of snowdrift around a cubic building model.* Yokohama, Japan, s.n.

Tominaga, Y., Okaze, T. & Mochida, A., 2011. CFD modeling of snowdrift around a building: an overview of models and evaluation of a new approach. *Building and Environment*, 46(4), pp. 899-910.

Torita, H. & Satou, H., 2007. Relationships between shelterbelt structure and mean wind reduction. *Agricultural and Forest Meteorology,* Volume 145, pp. 186-194.

Townsend, A., 1956. The structure of turbulent shear flow. *Cambridge University Press*, p. 315.

Trinh, K. T., 2010. *Additive layers: an alternate clssification of flow regimes.* [Online] Available at: http://arxiv.org/ftp/arxiv/papers/1001/1001.1587.pdf

Uematsu, T.; Kaneda , Y.; Takeuchi, K.; Nakata, T.; Yukumi, M.;, 1989. Numerical simulation of snowdrift development. *Glaciology,* Volume 13, pp. 265-268.

Vafai, K., 2005. *Handbook of Porous Media.* Second Edition ed. s.l.:CRC Press.

Wakes, S., Maegli, T., Dickinson, K. & Hilton, M., 2010. Numerical modeling of wind flow over a complex topography. *Environmental Modeling and Software* , Volume 25, pp. 237-247.

Wang, H. & Takle, E., 1995. A numerical simulation of boundary-layer flows near shelterbelts. *Boundary-Layer Meteorology,* Volume 75, pp. 141-173.

Wang, H. & Takle, E., 1996. On shelter efficiency of shelterbelts in oblique wind. *Agricultural and Forest Meteorology,* Volume 81, pp. 95-117.

Wang, H., Takle, E. & Shen, J., 2001. Shelterbelts and windbreaks: Mathematical modeling and computer simulations of turbulent flows. *Annual Review Fluid Mechanics,* Volume 33, pp. 549-586.

Wang, N. & Hu, B.-G., 2012. Real-time simulation of aeolian sand movement and sand ripple evolution: a method based on the physics of blown sand. *Journal of Computer Science and Technology,* Volume 27, pp. 135-146.

WeatherSpark, n.d. *Average Weather for Tromsø, Norway.* [Online] Available at: https://weatherspark.com/averages/28894/Troms-Norway

White, B., Greeley, R., Iversen, J. & Pollack, J., 1975. Particle motion in atmospheric boundaary layers of Mars and Earth. *NASA Technical Memorandum,* Volume X-62, p. 463.

White, B. R., 1996. Laboratory simulation of aeolian sand transport and physical modeling of flow around dune. *Annals of Arid Zone,* Volume 35, pp. 187-213.

White, F., 1998. *Fluid Mechanics.* 4th Ed. ed. s.l.:Mcgraw-Hill.

Wilson, J., 1985. Numerical studies of flow through a windbreak. *Wind Eng. Ind. Aerodyn,* Volume 21, pp. 119-154.

Wilson, J., 1997. A field study of the mean pressure about a windbreak. *Boundary Layer Meteorol,* Volume 85, pp. 327-358.

Wilson, J. & Flesch, T., 1999. Wind and remnant tree sway in forest cutblocks. III. a windflow model to diagnose spatial variation. *Agricultural and Forest Meteorology*, Volume 93, pp. 259-282.

Wilson, J. & Mooney, C., 1997. Comments on "A Numerical Simulation of Boundary-Layer Flows Near Shelterbelts" by H. Wang and E. Takle. *Boundary-Layer Meteorology*, Volume 85, pp. 137-149.

Wilson, J., Swaters, G. & Ustina, F., 1990. A perturbation analysis of turbulent flow through a porous barrier. *Quarterly Journal of the Royal Meteorological Society*, Volume 116, pp. 989-1004.

Wilson, J. & Yee, E., 2003. Calculation of winds disturbed by an array of fences. *Agricultural and Forest Meteorology,* Volume 115, pp. 31-50.

Wipperman, F. & Gross, G., 1986. The wind induced shaping and migration of an isolated dune-a numerical experiment. *Boundary-Layer Meteorology,* Volume 36, pp. 319-334.

Yang, P., Dong, Z. & Qian, G., 2007. Height profile of the mean velocity of an aeolian saltating cloud: wind tunnel measurements by particle image velocimetry. *Geomorphology,* Volume 89, pp. 320-334.

Yaragal, S., Ram, H. & Murthy, K., 1977. An experimental investigation of flow fields downstream of solid and porous fences. *Wind Engineering and Aerodynamics,* Volume 1997, pp. 127-140.

Yeh, C. P., Tsai, C. H. & Yang, R. J., 2010. An investigation into the sheltering performance of porous windbreaks under various wind directions. *Journal of Wind Engineering and Industrial Aerodynamics*, Volume 98, pp. 520-532.

Yves, D., Gilbert, G., Laurent, M. & Javier, G., 2005. Improvement of a numerical snow drift model and field validation. *Cold Regions Science and Technology*, Volume 43, pp. 93-103.

Zaghloul , N. A., 1997. Sand accumulation around porous fences. *Environmental Modeling & Software*, Volume 12, pp. 113-134.

Zhang, N., Kang, J.-H. & Lee, S.-J., 2010. Wind tunnel observation on the effect of a porous wind fence on shelter of saltating sand particles. *Geomorphology*, Volume 120, pp. 224-232.

Zhuang, Y. & Wilson, J., 1994. Coherent motions in windbreak flow. *Boundary-Layer Meteorology*, Volume 70, pp. 151-169.

I. APPENDIX A: THE EXPERIMENTAL CHARTS FOR THE CASE B STUDY

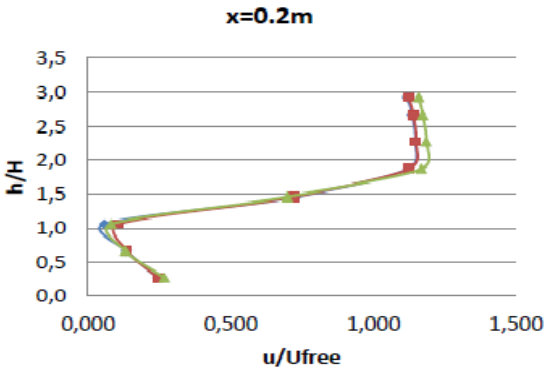

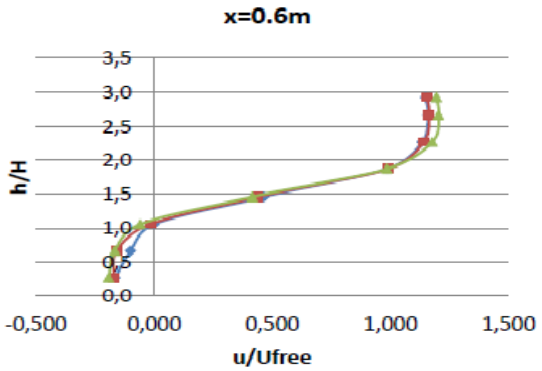

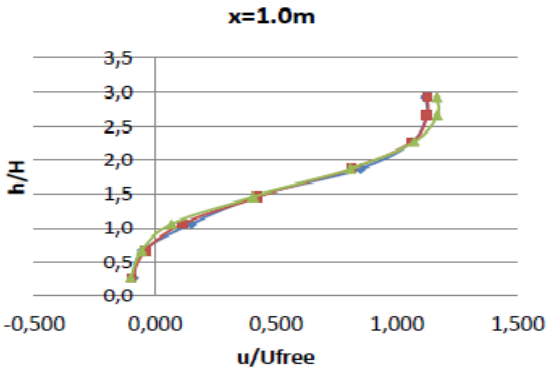

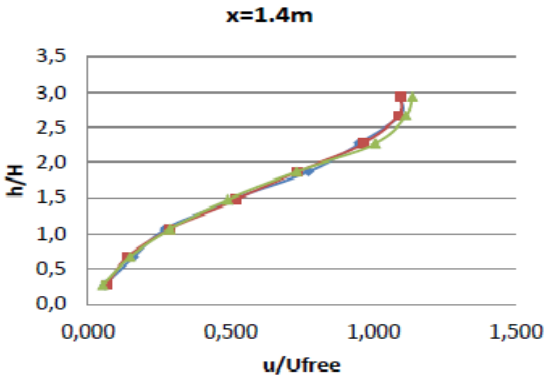

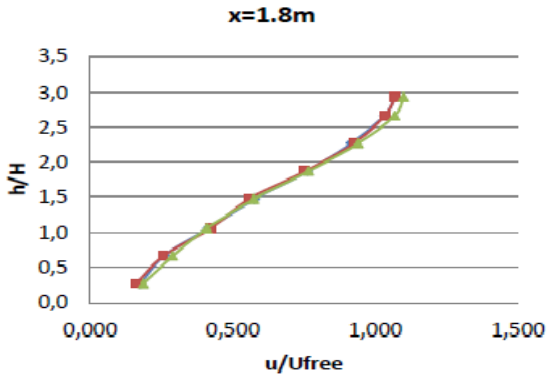

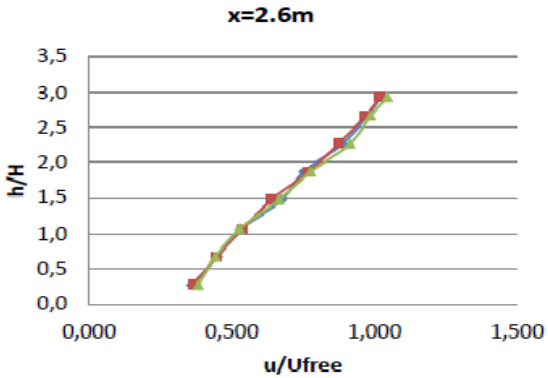

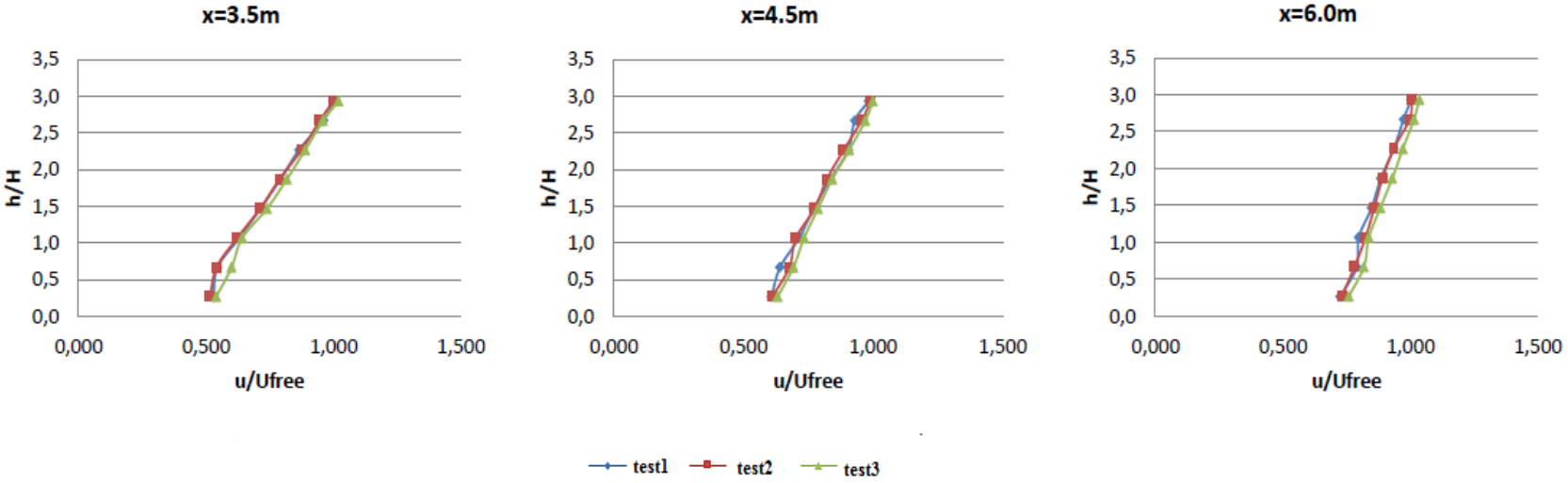

App-Fig. 1: The normalized u profiles at different x positions for the case B

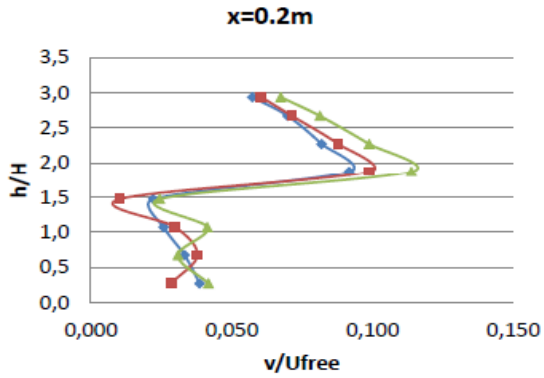
x=0.2m
h/H
3,5
3,0
2,5
2,0
1,5
1,0
0,5
0,0
0,000
0,050
0,100
0,150
v/Ufree

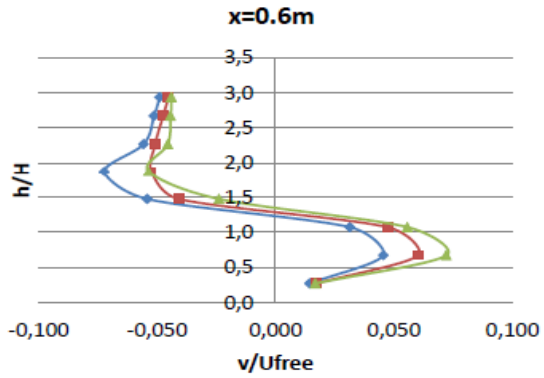
x=0.6m
h/H
3,5
3,0
2,5
2,0
1,5
1,0
0,5
0,0
-0,100
-0,050
0,000
0,050
0,100
v/Ufree

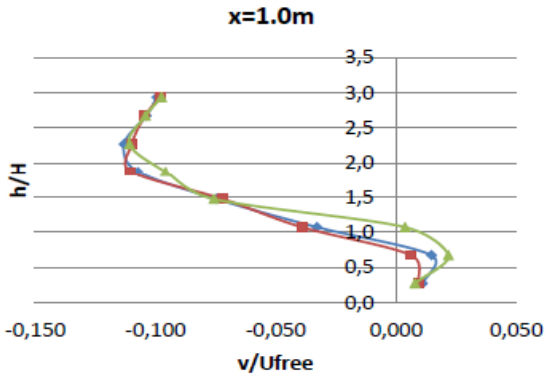
x=1.0m
h/H
3,5
3,0
2,5
2,0
1,5
1,0
0,5
0,0
-0,150
-0,100
-0,050
0,000
0,050
v/Ufree

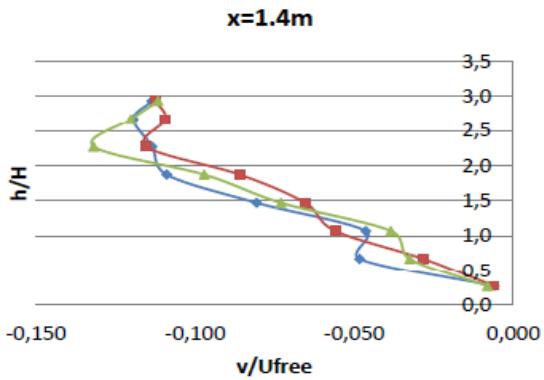
x=1.4m
h/H
3,5
3,0
2,5
2,0
1,5
1,0
0,5
0,0
-0,150
-0,100
-0,050
0,000
v/Ufree

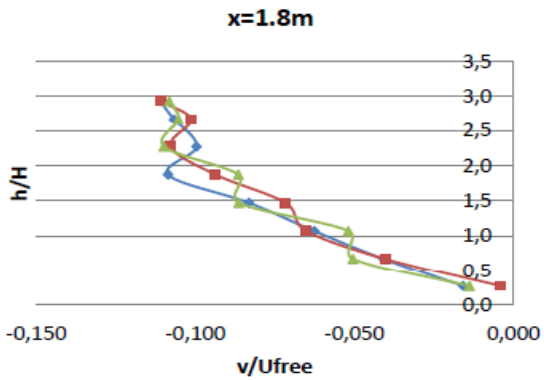
x=1.8m
h/H
3,5
3,0
2,5
2,0
1,5
1,0
0,5
0,0
-0,150
-0,100
-0,050
0,000
v/Ufree

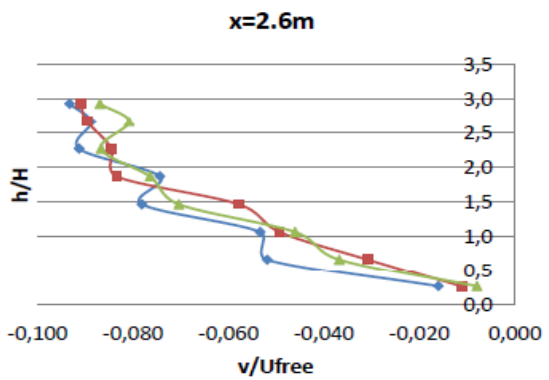
x=2.6m
h/H
3,5
3,0
2,5
2,0
1,5
1,0
0,5
0,0
-0,100
-0,080
-0,060
-0,040
-0,020
0,000
v/Ufree

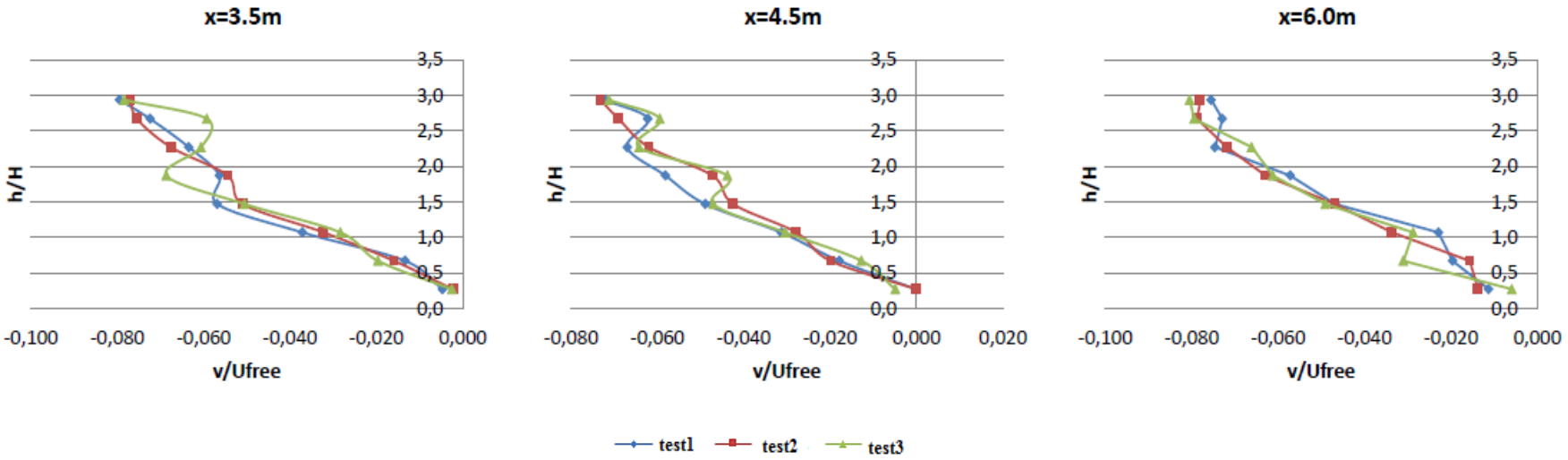

App-Fig. 2: The normalized v profiles at different x positions for the case B

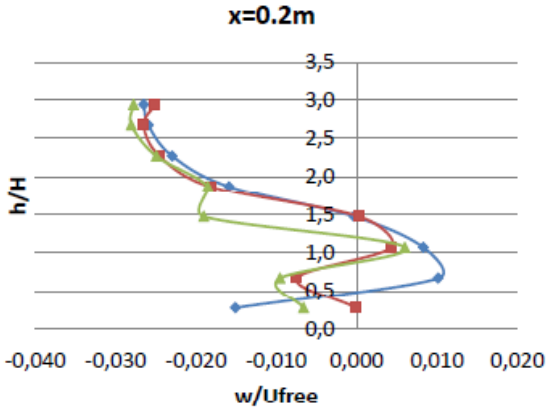
x=0.2m
h/H
3,5
3,0
2,5
2,0
1,5
1,0
0,5
0,0
-0,040 -0,030 -0,020 -0,010 0,000 0,010 0,020
w/Ufree

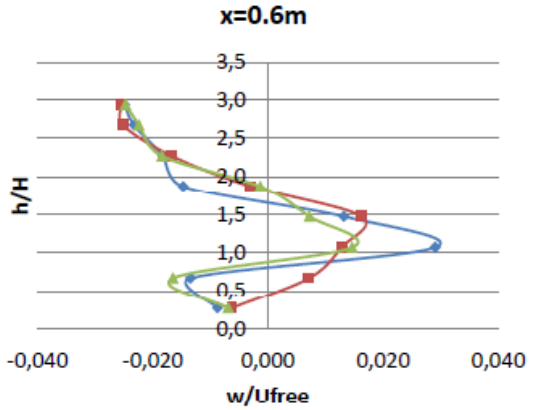
x=0.6m
h/H
3,5
3,0
2,5
2,0
1,5
1,0
0,5
0,0
-0,040 -0,020 0,000 0,020 0,040
w/Ufree

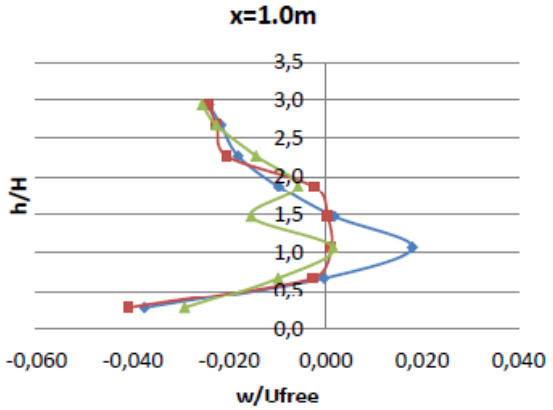
x=1.0m
h/H
3,5
3,0
2,5
2,0
1,5
1,0
0,5
0,0
-0,060 -0,040 -0,020 0,000 0,020 0,040
w/Ufree

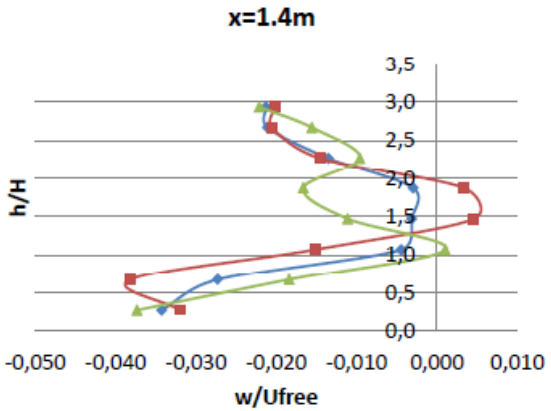
x=1.4m
h/H
3,5
3,0
2,5
2,0
1,5
1,0
0,5
0,0
-0,050 -0,040 -0,030 -0,020 -0,010 0,000 0,010
w/Ufree

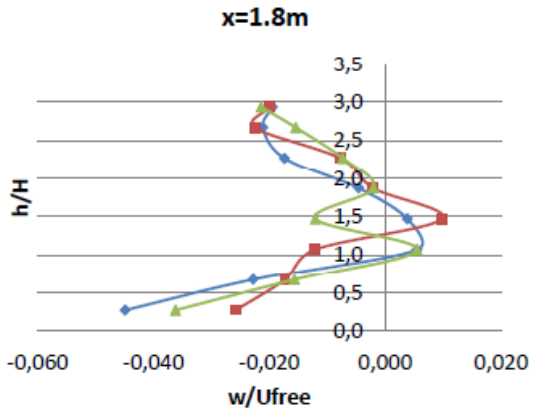
x=1.8m
h/H
3,5
3,0
2,5
2,0
1,5
1,0
0,5
0,0
-0,060 -0,040 -0,020 0,000 0,020
w/Ufree

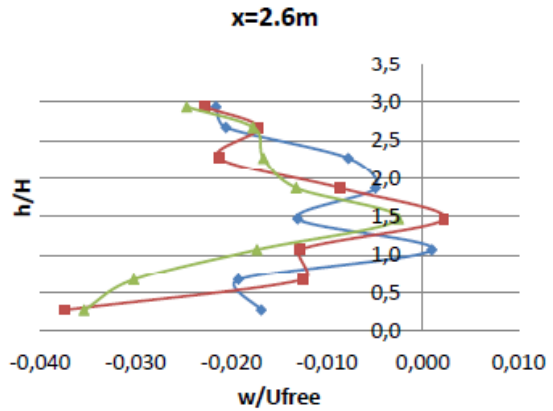
x=2.6m
h/H
3,5
3,0
2,5
2,0
1,5
1,0
0,5
0,0
-0,040 -0,030 -0,020 -0,010 0,000 0,010
w/Ufree

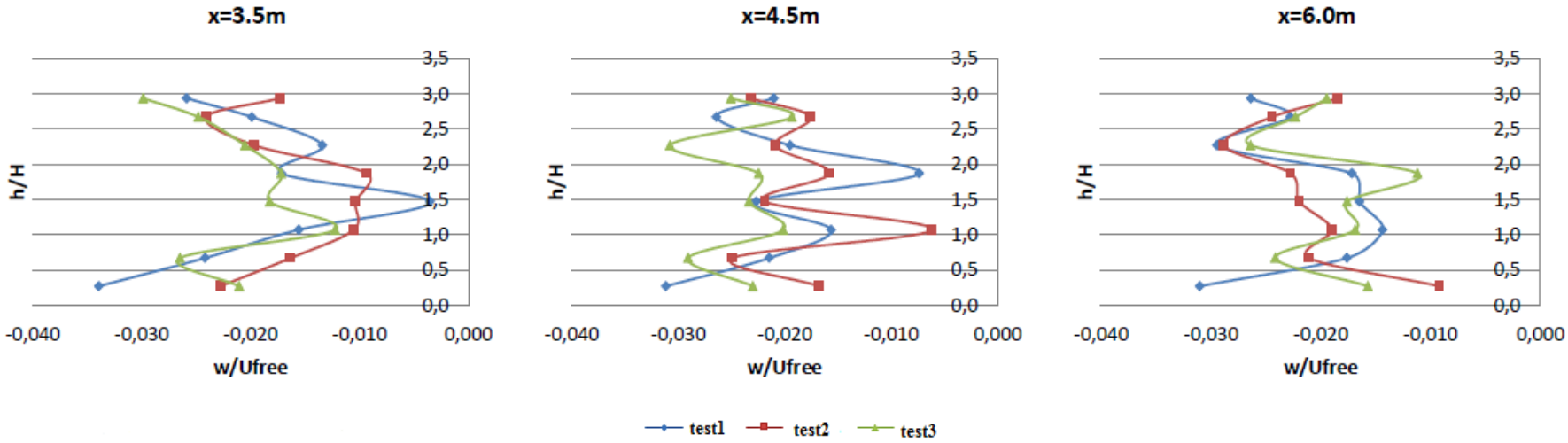

App-Fig. 3: The normalized *w* profiles at different x positions for the case B

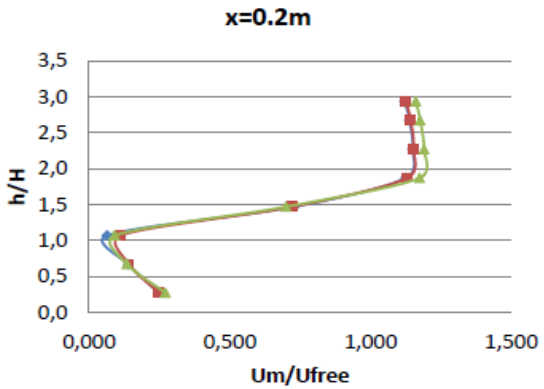
x=0.2m
h/H
3,5
3,0
2,5
2,0
1,5
1,0
0,5
0,0
0,000
0,500
1,000
1,500
Um/Ufree

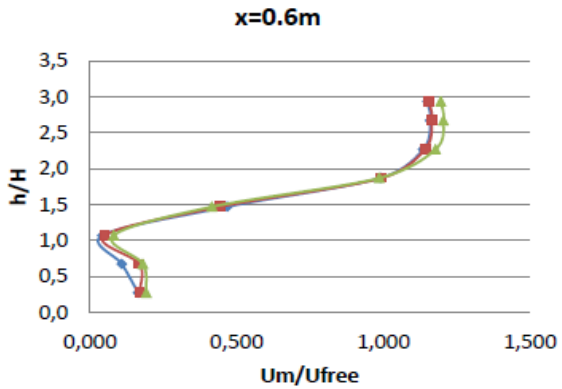
x=0.6m
h/H
3,5
3,0
2,5
2,0
1,5
1,0
0,5
0,0
0,000
0,500
1,000
1,500
Um/Ufree

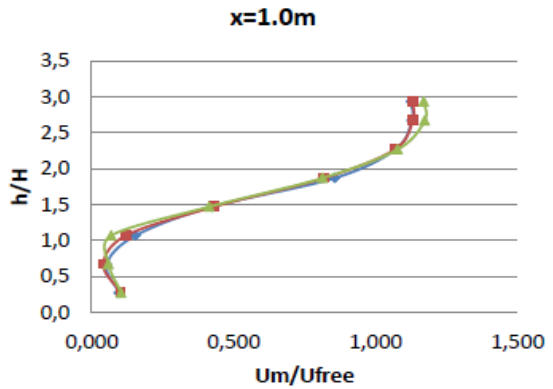
x=1.0m
h/H
3,5
3,0
2,5
2,0
1,5
1,0
0,5
0,0
0,000
0,500
1,000
1,500
Um/Ufree

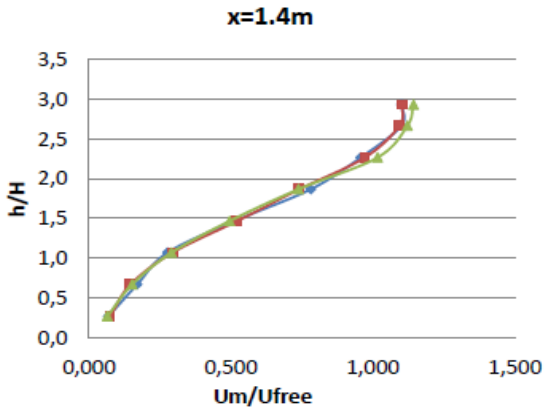
x=1.4m
h/H
3,5
3,0
2,5
2,0
1,5
1,0
0,5
0,0
0,000
0,500
1,000
1,500
Um/Ufree

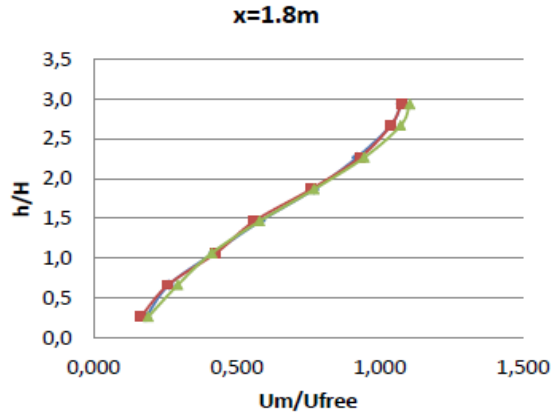
x=1.8m
h/H
3,5
3,0
2,5
2,0
1,5
1,0
0,5
0,0
0,000
0,500
1,000
1,500
Um/Ufree

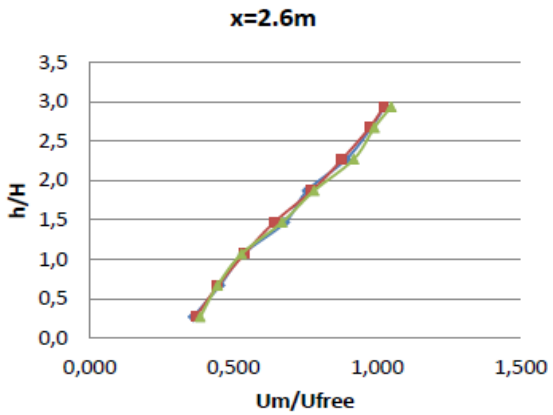
x=2.6m
h/H
3,5
3,0
2,5
2,0
1,5
1,0
0,5
0,0
0,000
0,500
1,000
1,500
Um/Ufree

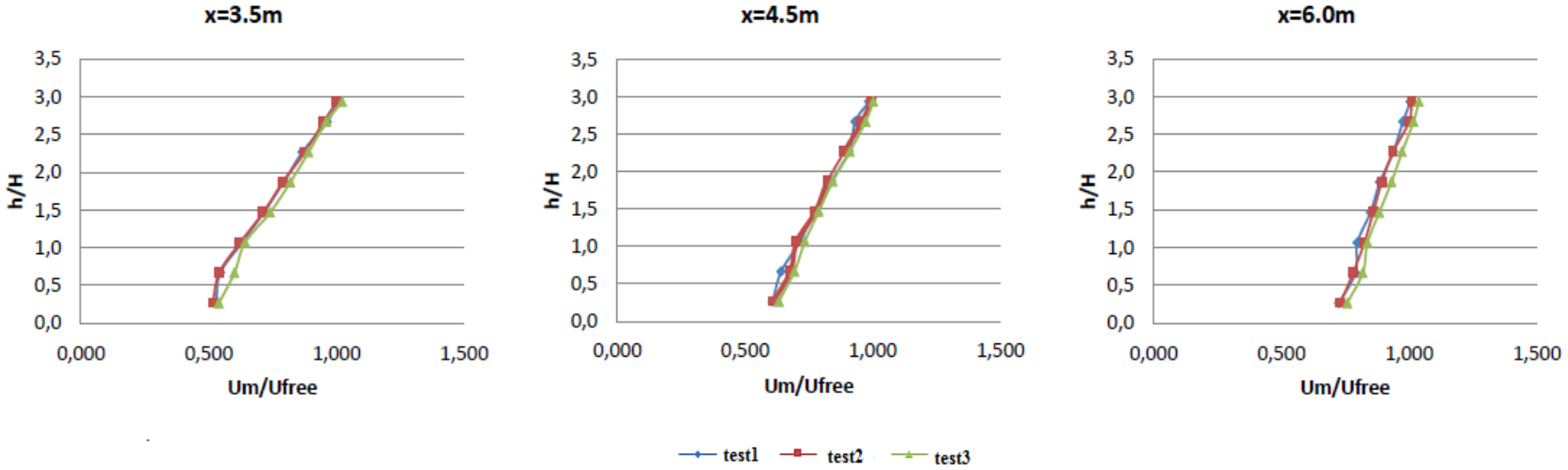

App-Fig. 4: The normalized velocity magnitude profiles at different x positions for the case B

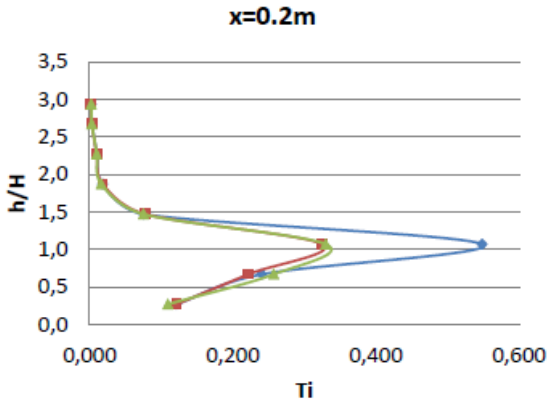
x=0.2m
h/H
3,5
3,0
2,5
2,0
1,5
1,0
0,5
0,0
0,000
0,200
0,400
0,600
Ti

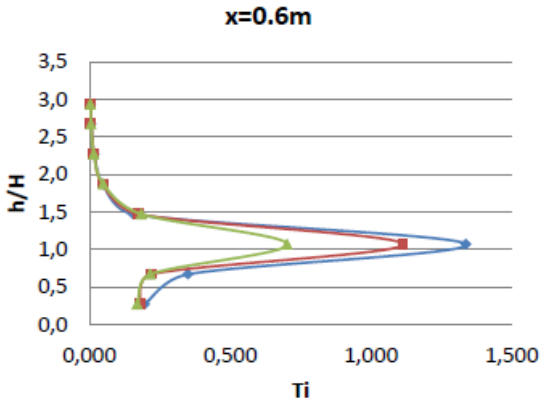
x=0.6m
h/H
3,5
3,0
2,5
2,0
1,5
1,0
0,5
0,0
0,000
0,500
1,000
1,500
Ti

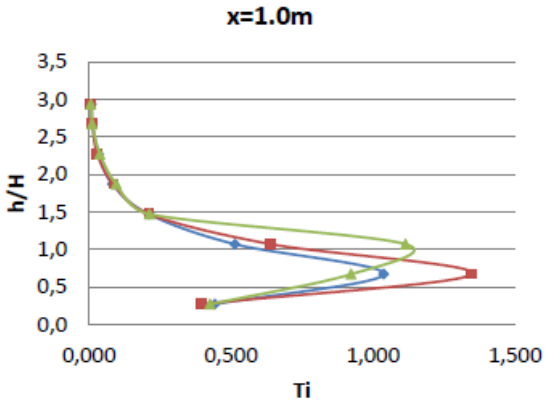
x=1.0m
h/H
3,5
3,0
2,5
2,0
1,5
1,0
0,5
0,0
0,000
0,500
1,000
1,500
Ti

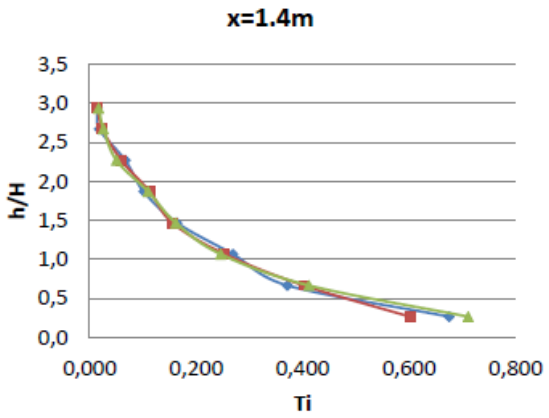
x=1.4m
h/H
3,5
3,0
2,5
2,0
1,5
1,0
0,5
0,0
0,000
0,200
0,400
0,600
0,800
Ti

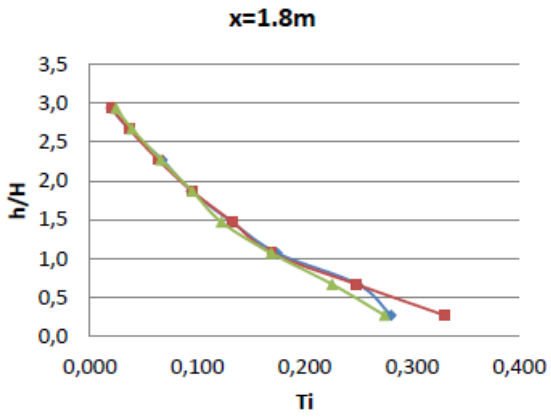
x=1.8m
h/H
3,5
3,0
2,5
2,0
1,5
1,0
0,5
0,0
0,000
0,100
0,200
0,300
0,400
Ti

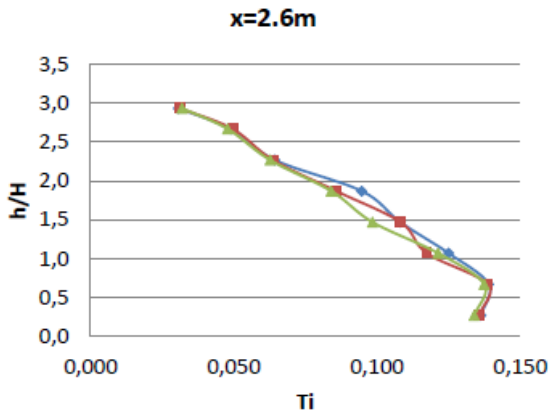
x=2.6m
h/H
3,5
3,0
2,5
2,0
1,5
1,0
0,5
0,0
0,000
0,050
0,100
0,150
Ti

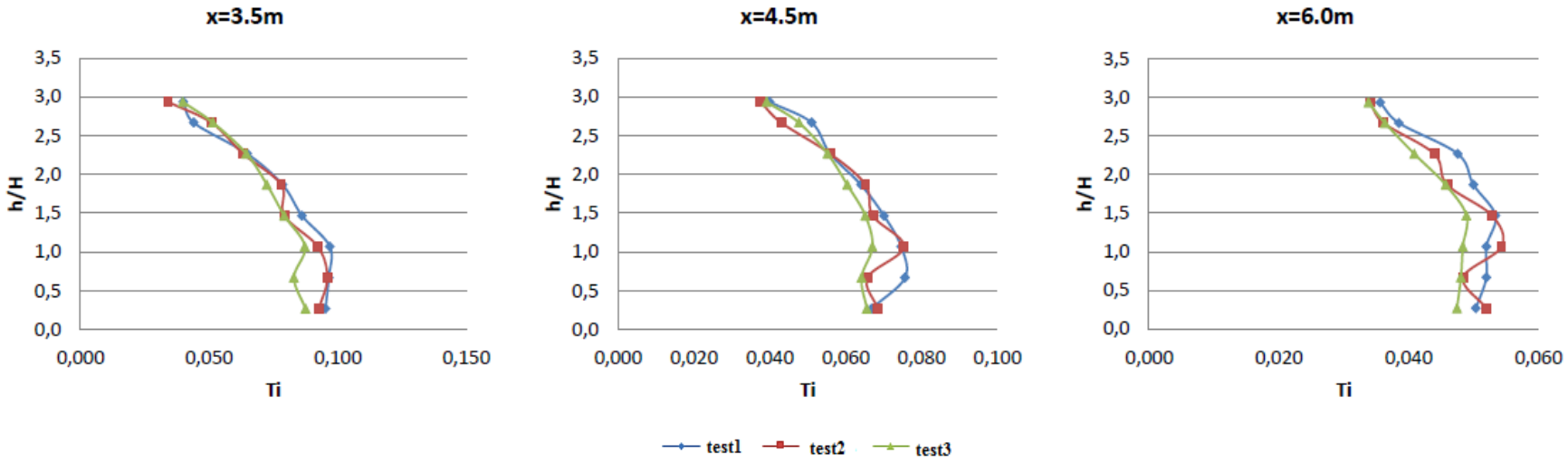

App-Fig. 5: The turbulence intensity profiles at different x positions for the case B

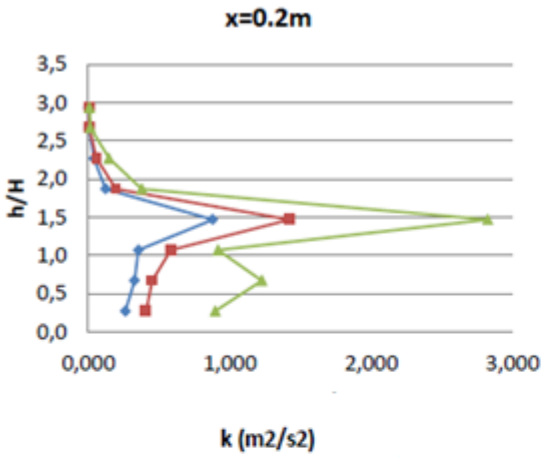
x=0.2m
h/H
3,5
3,0
2,5
2,0
1,5
1,0
0,5
0,0
0,000
1,000
2,000
3,000
k (m2/s2)

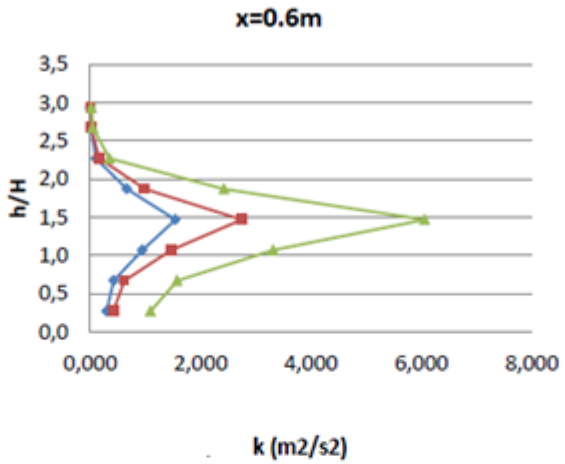
x=0.6m
h/H
3,5
3,0
2,5
2,0
1,5
1,0
0,5
0,0
0,000
2,000
4,000
6,000
8,000
k (m2/s2)

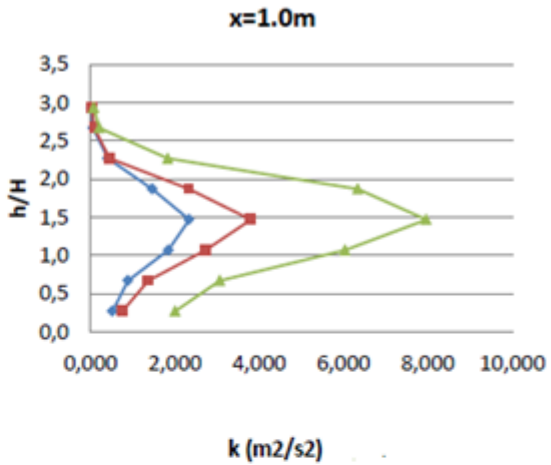
x=1.0m
h/H
3,5
3,0
2,5
2,0
1,5
1,0
0,5
0,0
0,000
2,000
4,000
6,000
8,000
10,000
k (m2/s2)

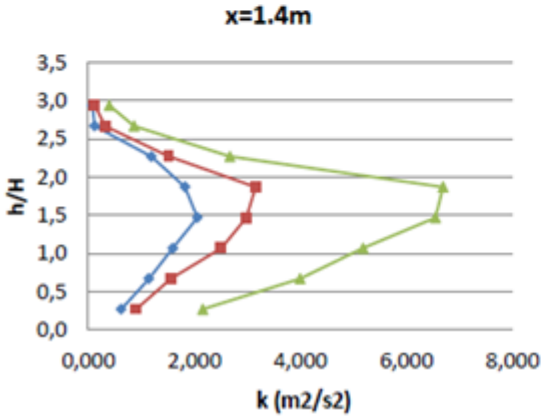
x=1.4m
h/H
3,5
3,0
2,5
2,0
1,5
1,0
0,5
0,0
0,000
2,000
4,000
6,000
8,000
k (m2/s2)

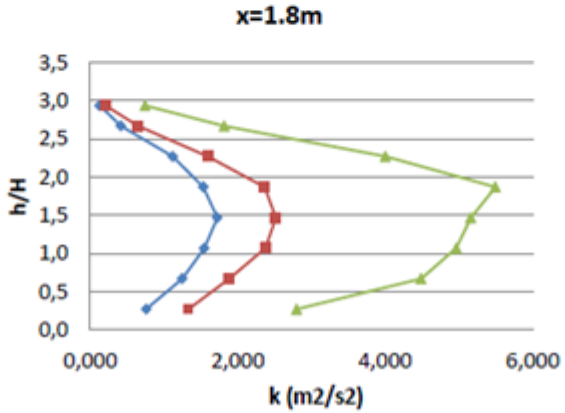
x=1.8m
h/H
3,5
3,0
2,5
2,0
1,5
1,0
0,5
0,0
0,000
2,000
4,000
6,000
k (m2/s2)

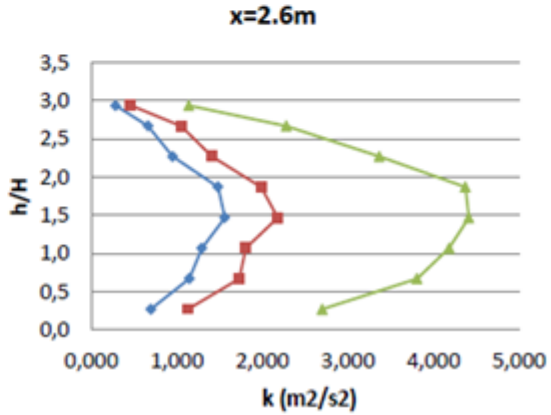
x=2.6m
h/H
3,5
3,0
2,5
2,0
1,5
1,0
0,5
0,0
0,000
1,000
2,000
3,000
4,000
5,000
k (m2/s2)

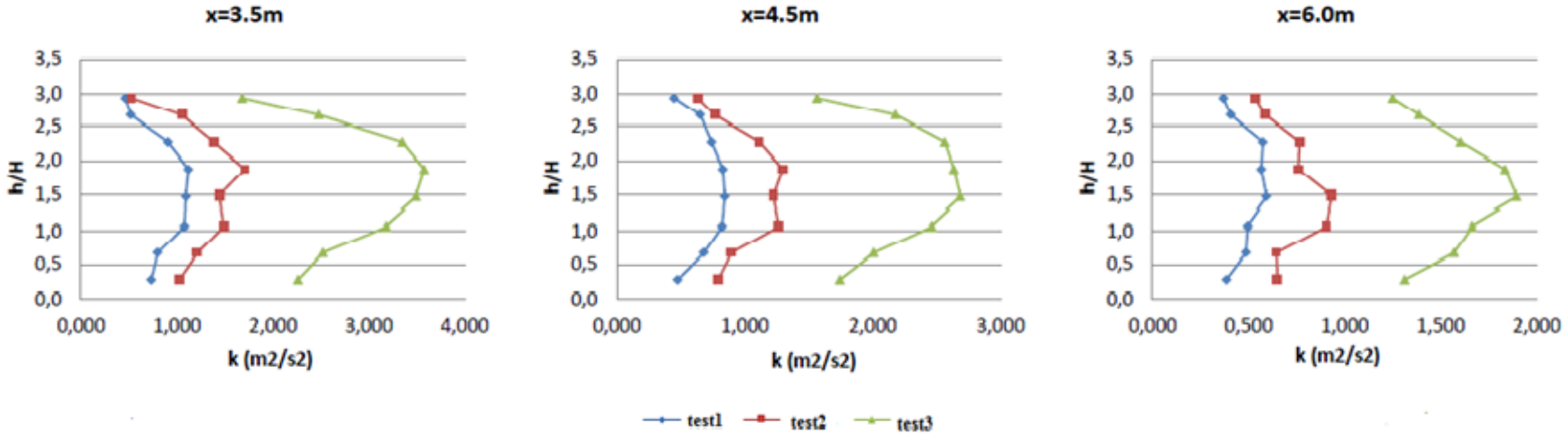

App-Fig. 6: The turbulent kinetic energy profiles at different x positions for the Case B

II. APPENDIX B: THE EXPERIMENTAL CHARTS FOR THE CASE C STUDY

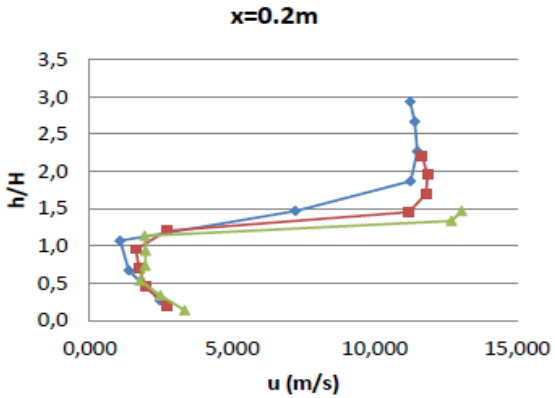

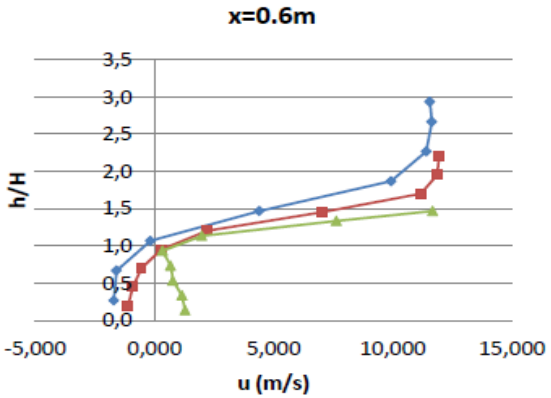

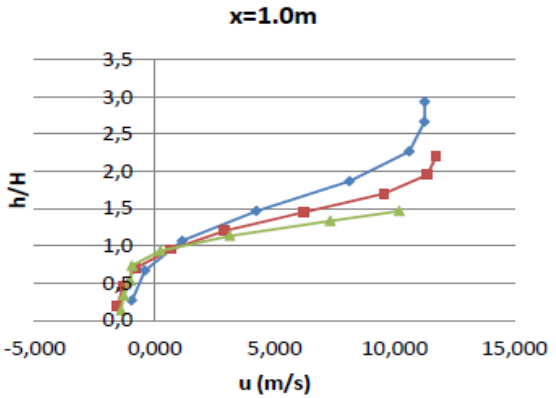

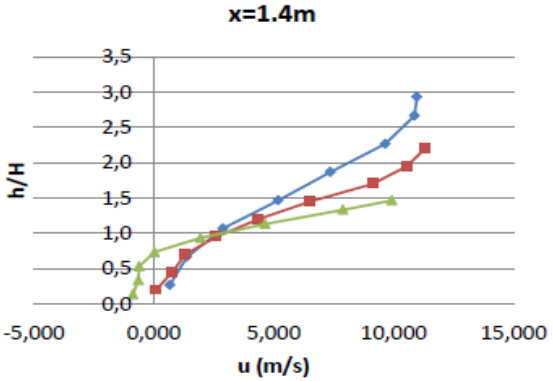

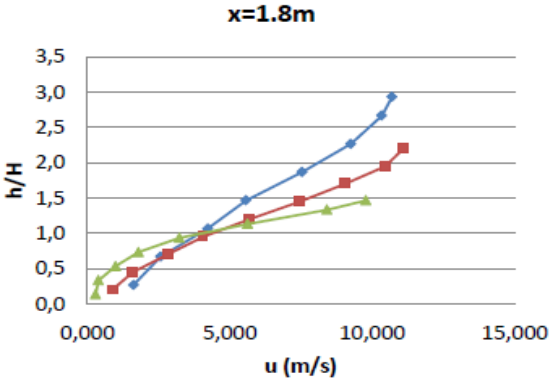

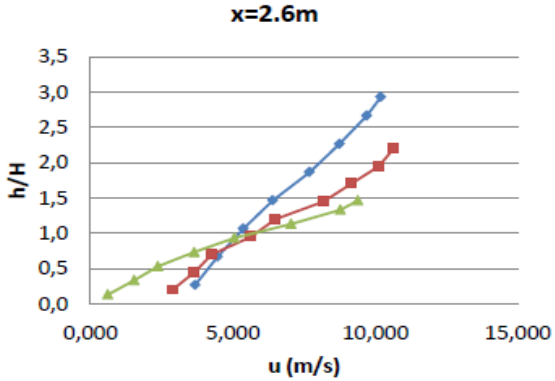

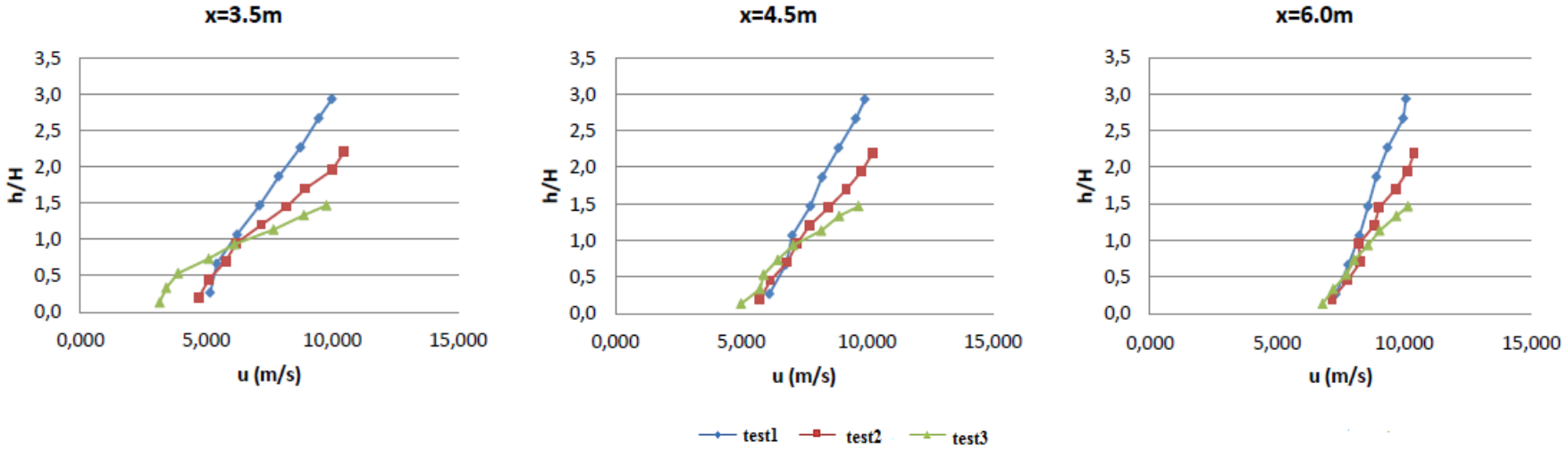

App-Fig. 7: The u profiles at different x positions for the case C

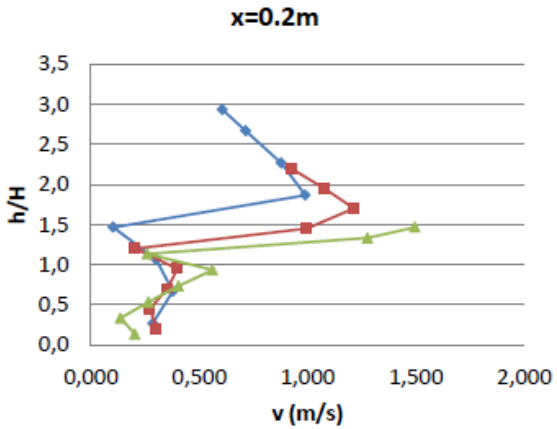
x=0.2m
h/H
3,5
3,0
2,5
2,0
1,5
1,0
0,5
0,0
0,000
0,500
1,000
1,500
2,000
v (m/s)

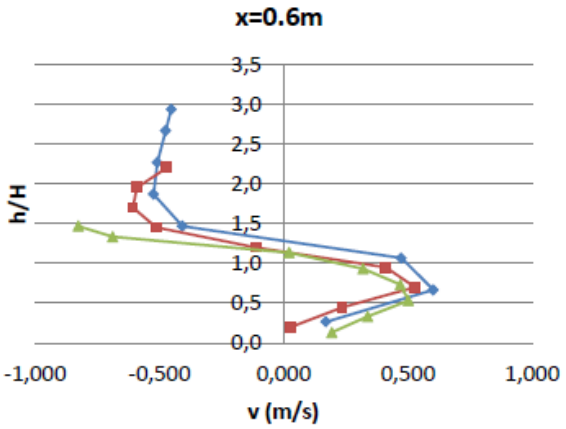
x=0.6m
h/H
3,5
3,0
2,5
2,0
1,5
1,0
0,5
0,0
-1,000
-0,500
0,000
0,500
1,000
v (m/s)

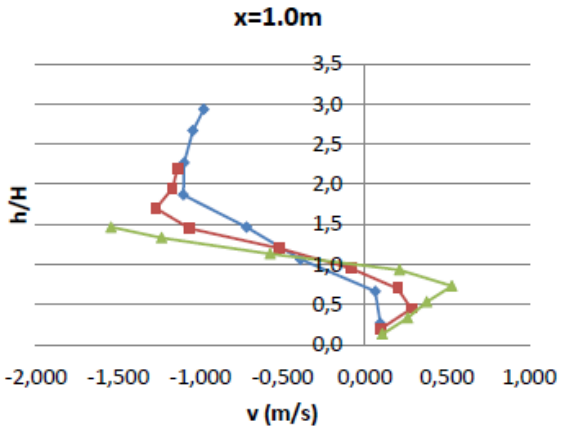
x=1.0m
h/H
3,5
3,0
2,5
2,0
1,5
1,0
0,5
0,0
-2,000
-1,500
-1,000
-0,500
0,000
0,500
1,000
v (m/s)

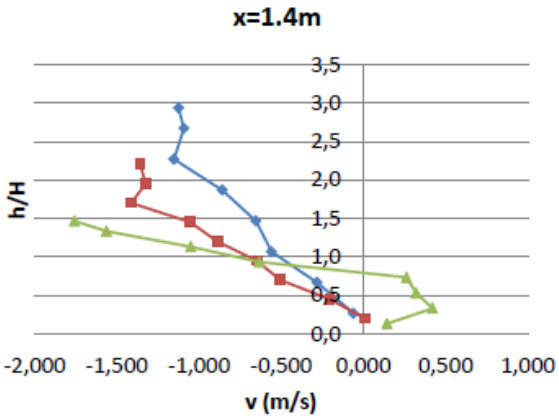
x=1.4m
h/H
3,5
3,0
2,5
2,0
1,5
1,0
0,5
0,0
-2,000
-1,500
-1,000
-0,500
0,000
0,500
1,000
v (m/s)

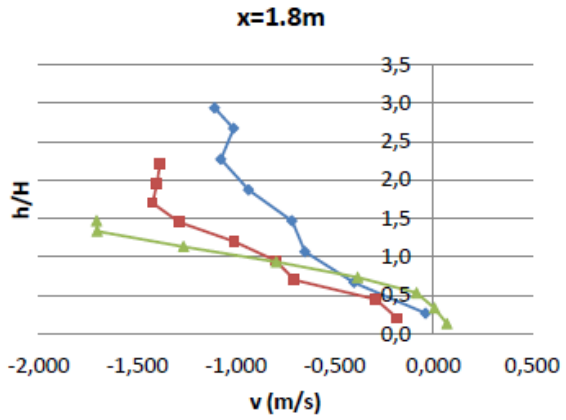
x=1.8m
h/H
3,5
3,0
2,5
2,0
1,5
1,0
0,5
0,0
-2,000
-1,500
-1,000
-0,500
0,000
0,500
v (m/s)

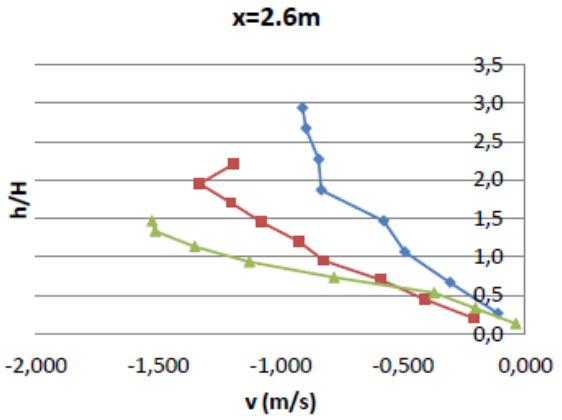
x=2.6m
h/H
3,5
3,0
2,5
2,0
1,5
1,0
0,5
0,0
-2,000
-1,500
-1,000
-0,500
0,000
v (m/s)

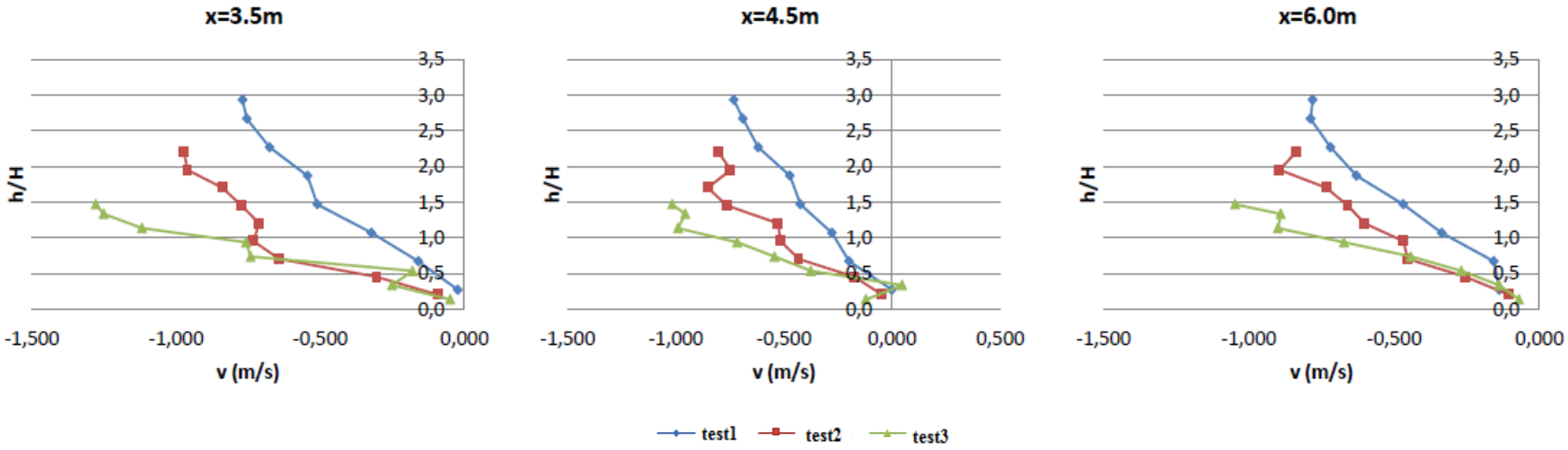

App-Fig. 8: The v profiles at different x positions for the case C

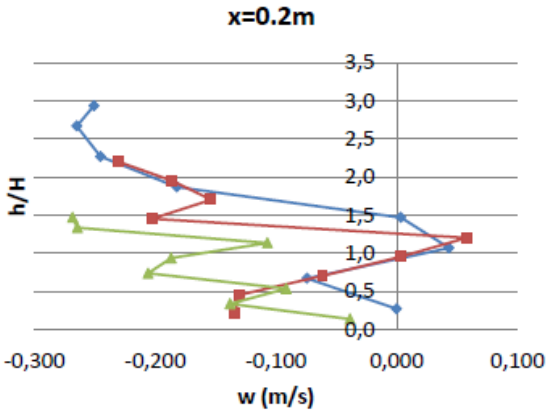
x=0.2m
h/H
3,5
3,0
2,5
2,0
1,5
1,0
0,5
0,0
-0,300
-0,200
-0,100
0,000
0,100
w (m/s)

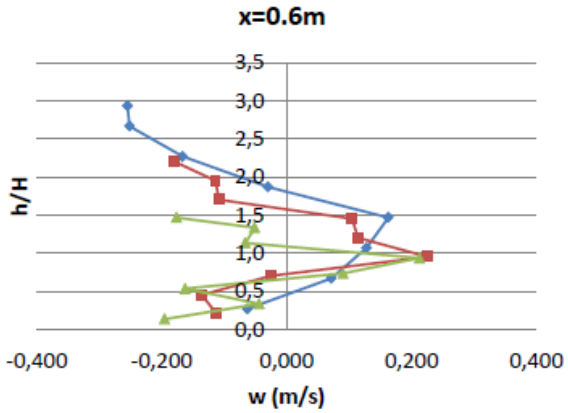
x=0.6m
h/H
3,5
3,0
2,5
2,0
1,5
1,0
0,5
0,0
-0,400
-0,200
0,000
0,200
0,400
w (m/s)

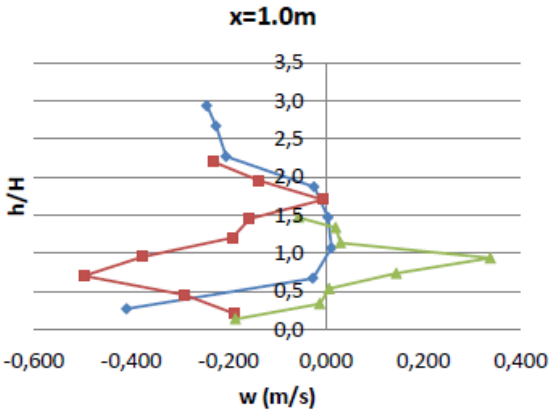
x=1.0m
h/H
3,5
3,0
2,5
2,0
1,5
1,0
0,5
0,0
-0,600
-0,400
-0,200
0,000
0,200
0,400
w (m/s)

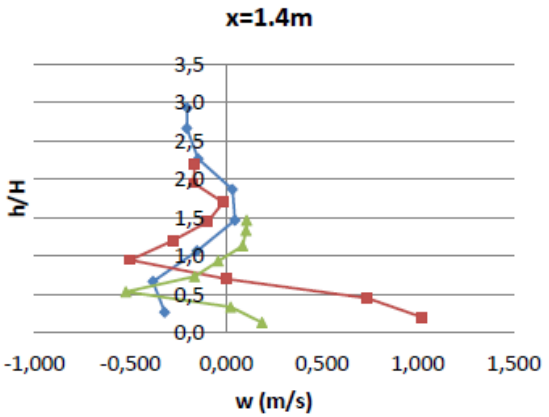
x=1.4m
h/H
3,5
3,0
2,5
2,0
1,5
1,0
0,5
0,0
-1,000
-0,500
0,000
0,500
1,000
1,500
w (m/s)

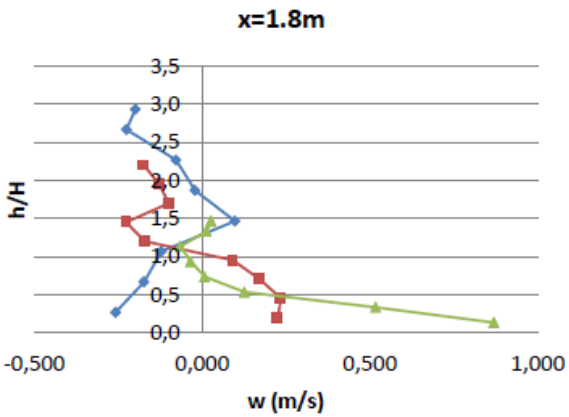
x=1.8m
h/H
3,5
3,0
2,5
2,0
1,5
1,0
0,5
0,0
-0,500
0,000
0,500
1,000
w (m/s)

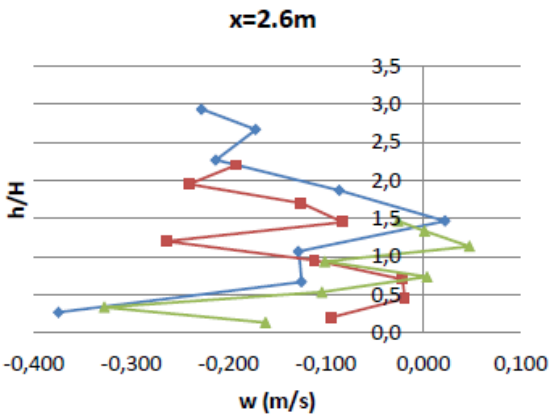
x=2.6m
h/H
3,5
3,0
2,5
2,0
1,5
1,0
0,5
0,0
-0,400
-0,300
-0,200
-0,100
0,000
0,100
w (m/s)

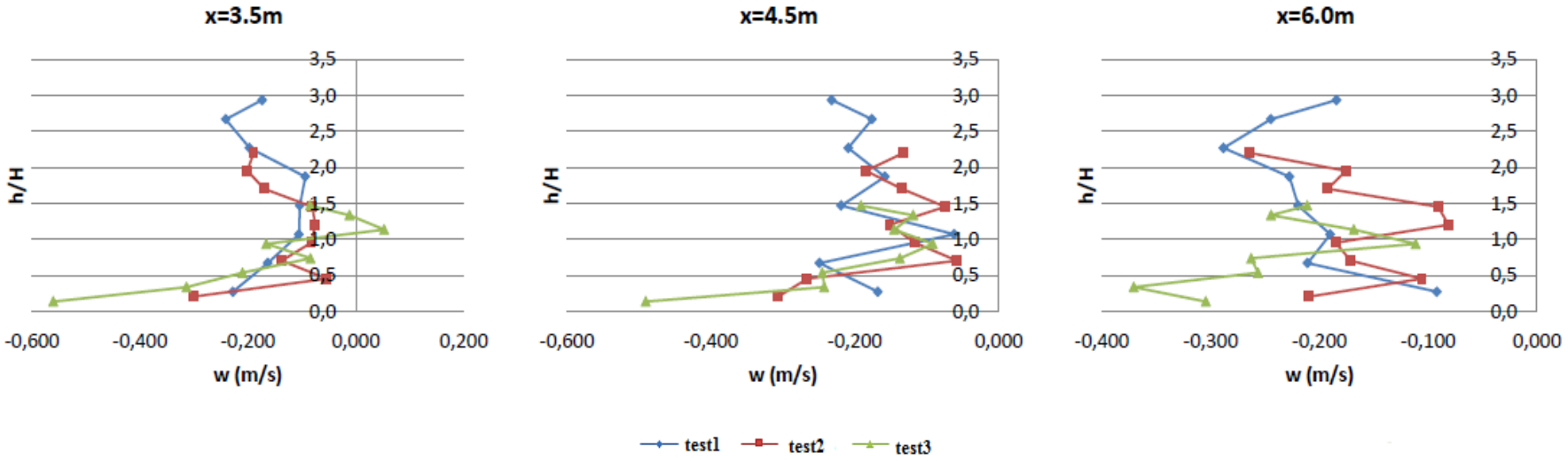

App-Fig. 9: The *w* profiles at different x positions for the case C

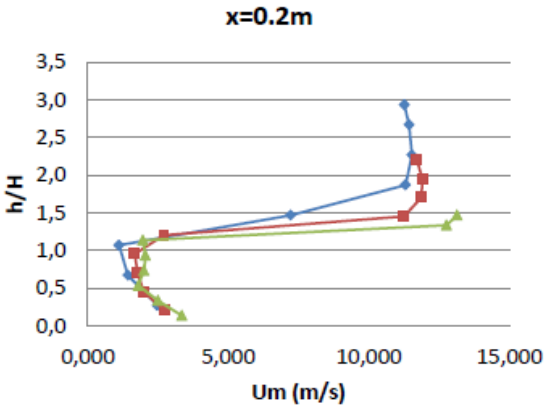
x=0.2m
h/H
3,5
3,0
2,5
2,0
1,5
1,0
0,5
0,0
0,000
5,000
10,000
15,000
Um (m/s)

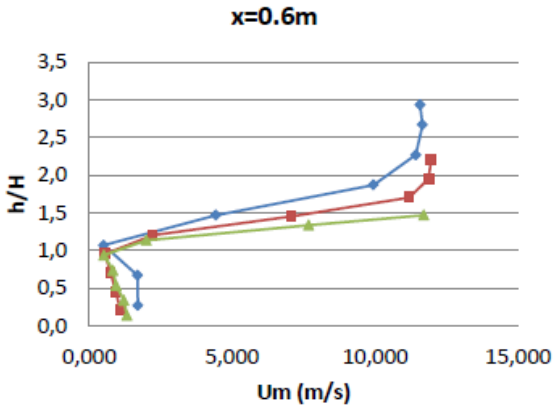
x=0.6m
h/H
3,5
3,0
2,5
2,0
1,5
1,0
0,5
0,0
0,000
5,000
10,000
15,000
Um (m/s)

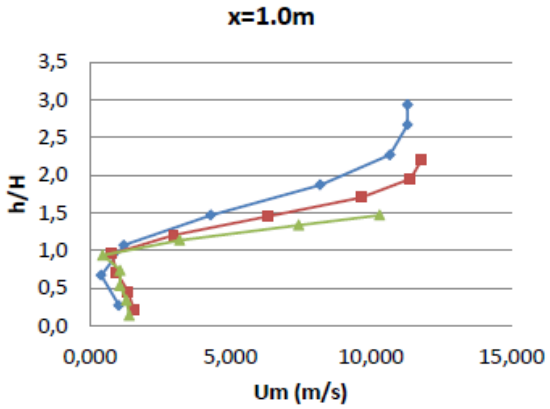
x=1.0m
h/H
3,5
3,0
2,5
2,0
1,5
1,0
0,5
0,0
0,000
5,000
10,000
15,000
Um (m/s)

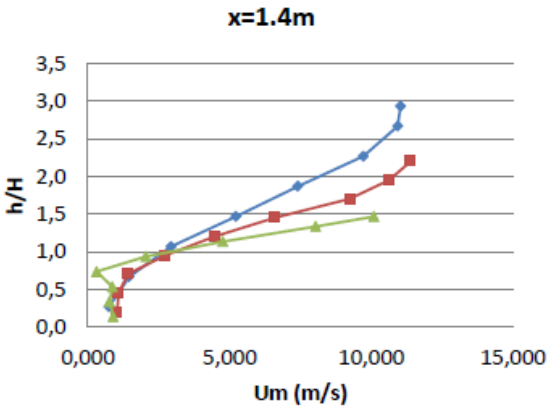
x=1.4m
h/H
3,5
3,0
2,5
2,0
1,5
1,0
0,5
0,0
0,000
5,000
10,000
15,000
Um (m/s)

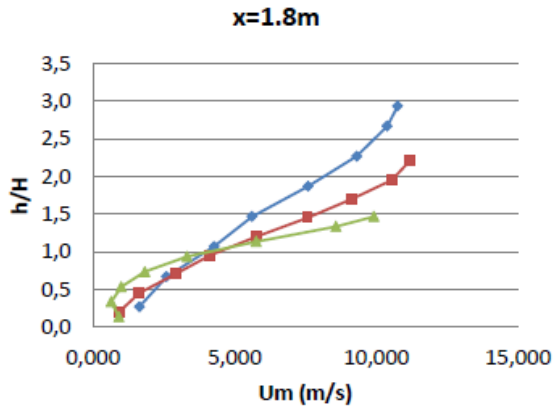
x=1.8m
h/H
3,5
3,0
2,5
2,0
1,5
1,0
0,5
0,0
0,000
5,000
10,000
15,000
Um (m/s)

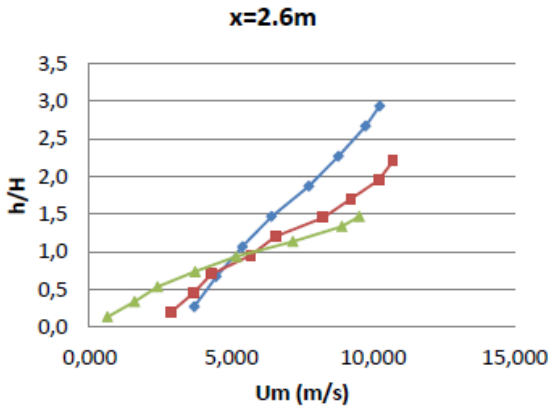
x=2.6m
h/H
3,5
3,0
2,5
2,0
1,5
1,0
0,5
0,0
0,000
5,000
10,000
15,000
Um (m/s)

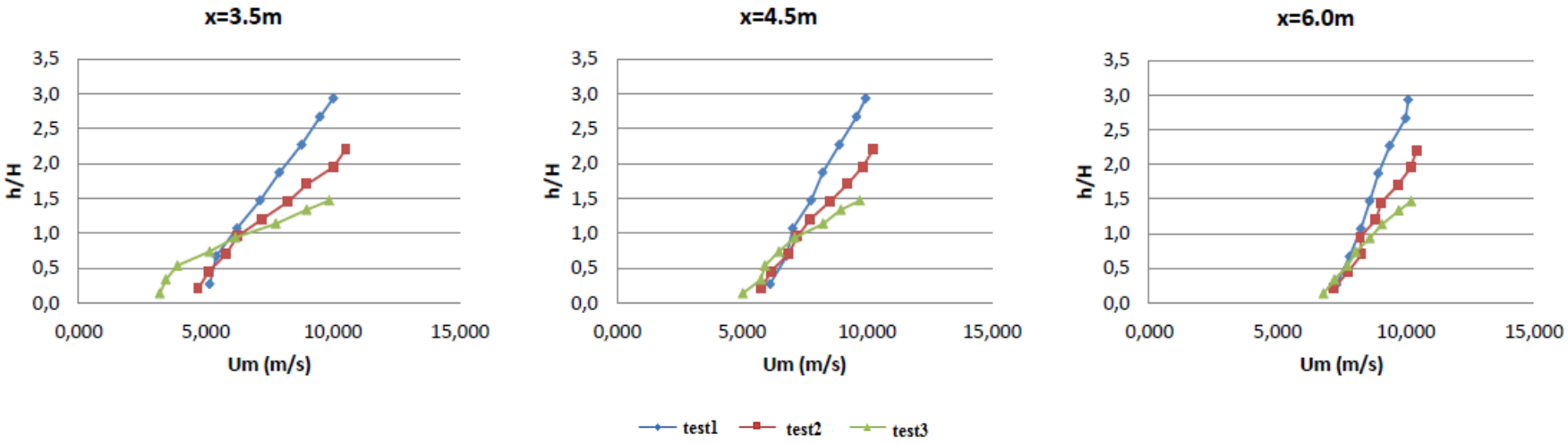

App-Fig. 10: The velocity magnitude profiles at different x positions for the case C

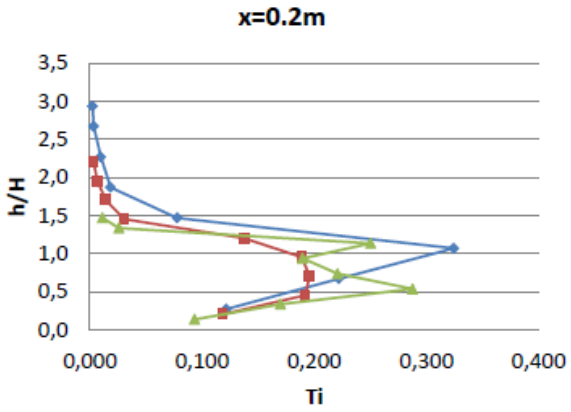
x=0.2m
h/H
3,5
3,0
2,5
2,0
1,5
1,0
0,5
0,0
0,000
0,100
0,200
0,300
0,400
Ti

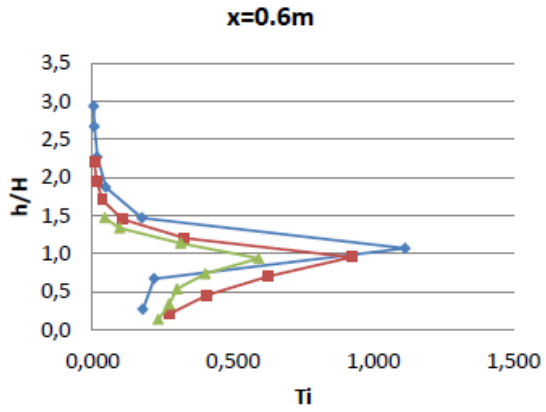
x=0.6m
h/H
3,5
3,0
2,5
2,0
1,5
1,0
0,5
0,0
0,000
0,500
1,000
1,500
Ti

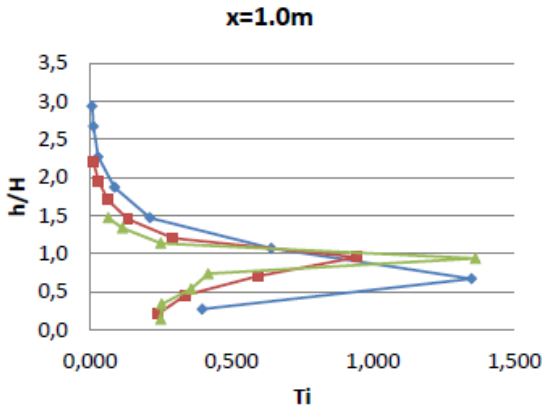
x=1.0m
h/H
3,5
3,0
2,5
2,0
1,5
1,0
0,5
0,0
0,000
0,500
1,000
1,500
Ti

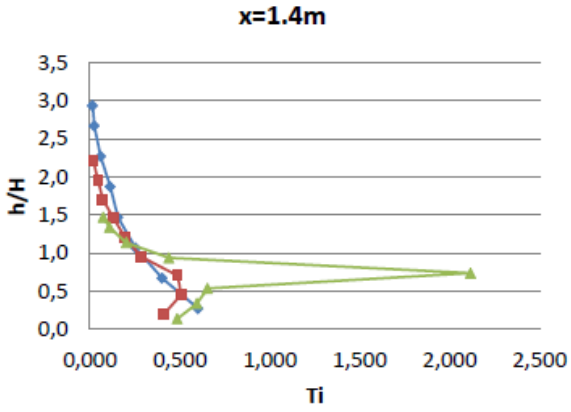
x=1.4m
h/H
3,5
3,0
2,5
2,0
1,5
1,0
0,5
0,0
0,000
0,500
1,000
1,500
2,000
2,500
Ti

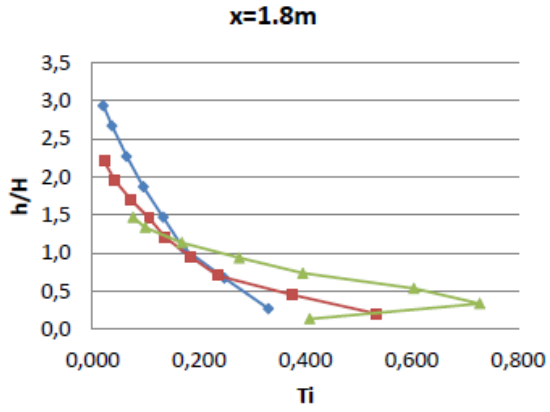
x=1.8m
h/H
3,5
3,0
2,5
2,0
1,5
1,0
0,5
0,0
0,000
0,200
0,400
0,600
0,800
Ti

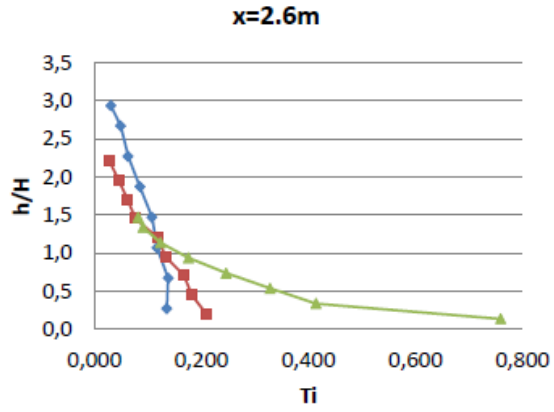
x=2.6m
h/H
3,5
3,0
2,5
2,0
1,5
1,0
0,5
0,0
0,000
0,200
0,400
0,600
0,800
Ti

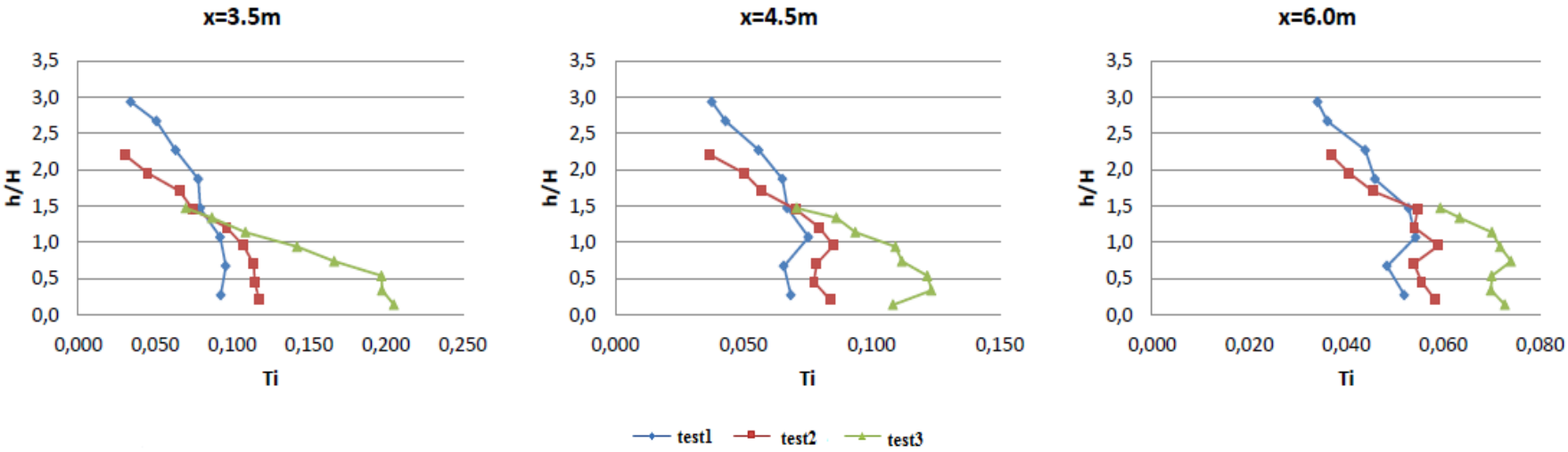

App-Fig. 11: The turbulence intensity profiles at different x positions for the case C

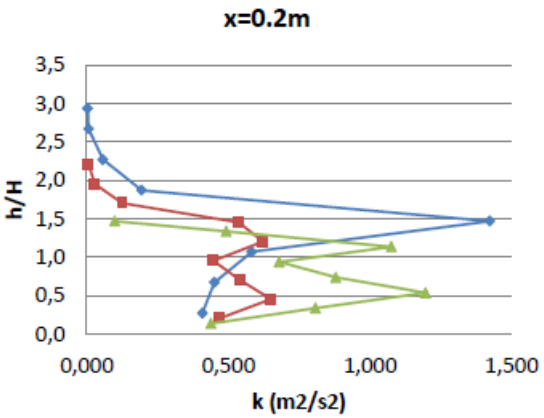
x=0.2m
h/H
3,5
3,0
2,5
2,0
1,5
1,0
0,5
0,0
0,000
0,500
1,000
1,500
k (m2/s2)

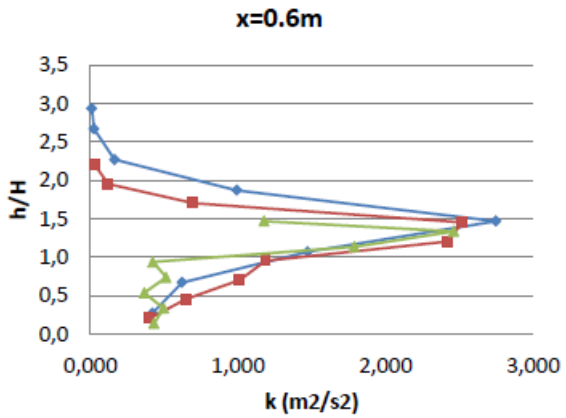
x=0.6m
h/H
3,5
3,0
2,5
2,0
1,5
1,0
0,5
0,0
0,000
1,000
2,000
3,000
k (m2/s2)

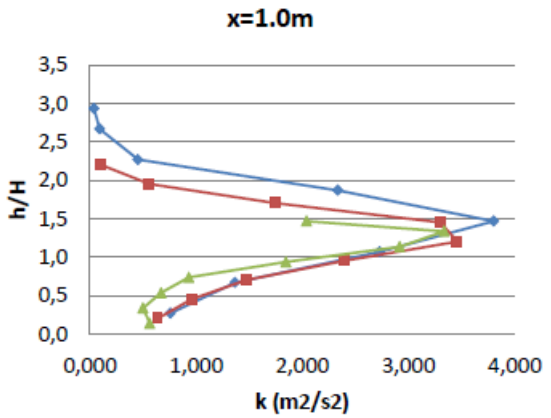
x=1.0m
h/H
3,5
3,0
2,5
2,0
1,5
1,0
0,5
0,0
0,000
1,000
2,000
3,000
4,000
k (m2/s2)

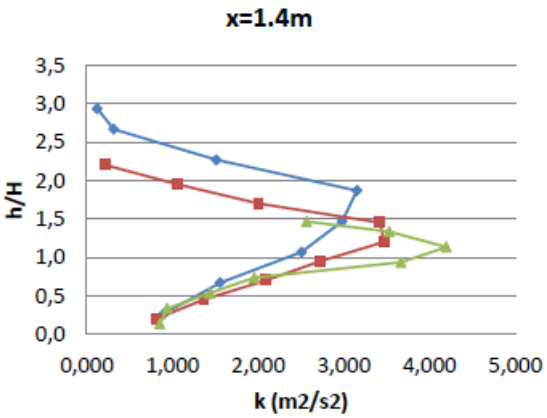
x=1.4m
h/H
3,5
3,0
2,5
2,0
1,5
1,0
0,5
0,0
0,000
1,000
2,000
3,000
4,000
5,000
k (m2/s2)

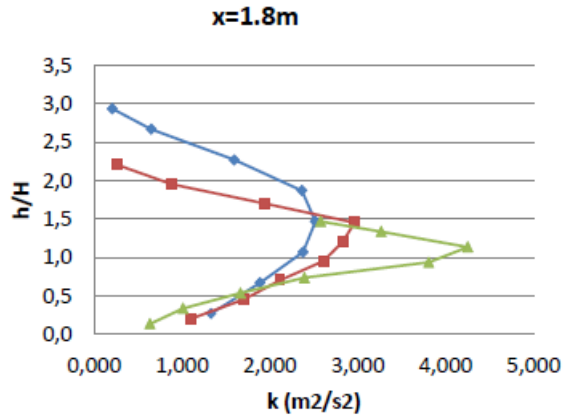
x=1.8m
h/H
3,5
3,0
2,5
2,0
1,5
1,0
0,5
0,0
0,000
1,000
2,000
3,000
4,000
5,000
k (m2/s2)

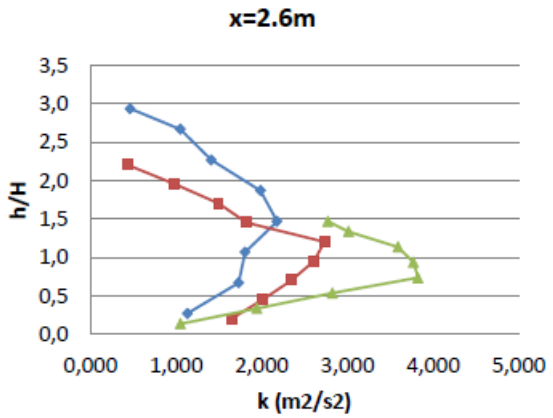
x=2.6m
h/H
3,5
3,0
2,5
2,0
1,5
1,0
0,5
0,0
0,000
1,000
2,000
3,000
4,000
5,000
k (m2/s2)

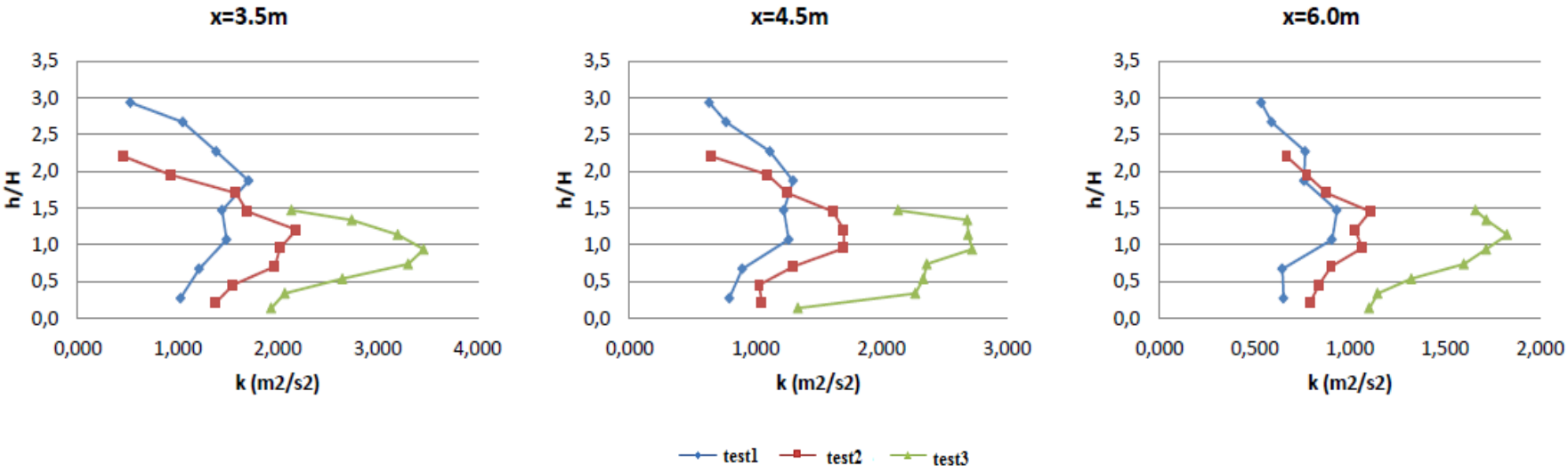

App-Fig. 12: The turbulent kinetic energy profiles at different x positions for the case C

III. APPENDIX C: THE EXPERIMENTAL CHARTS FOR THE CASE D STUDY

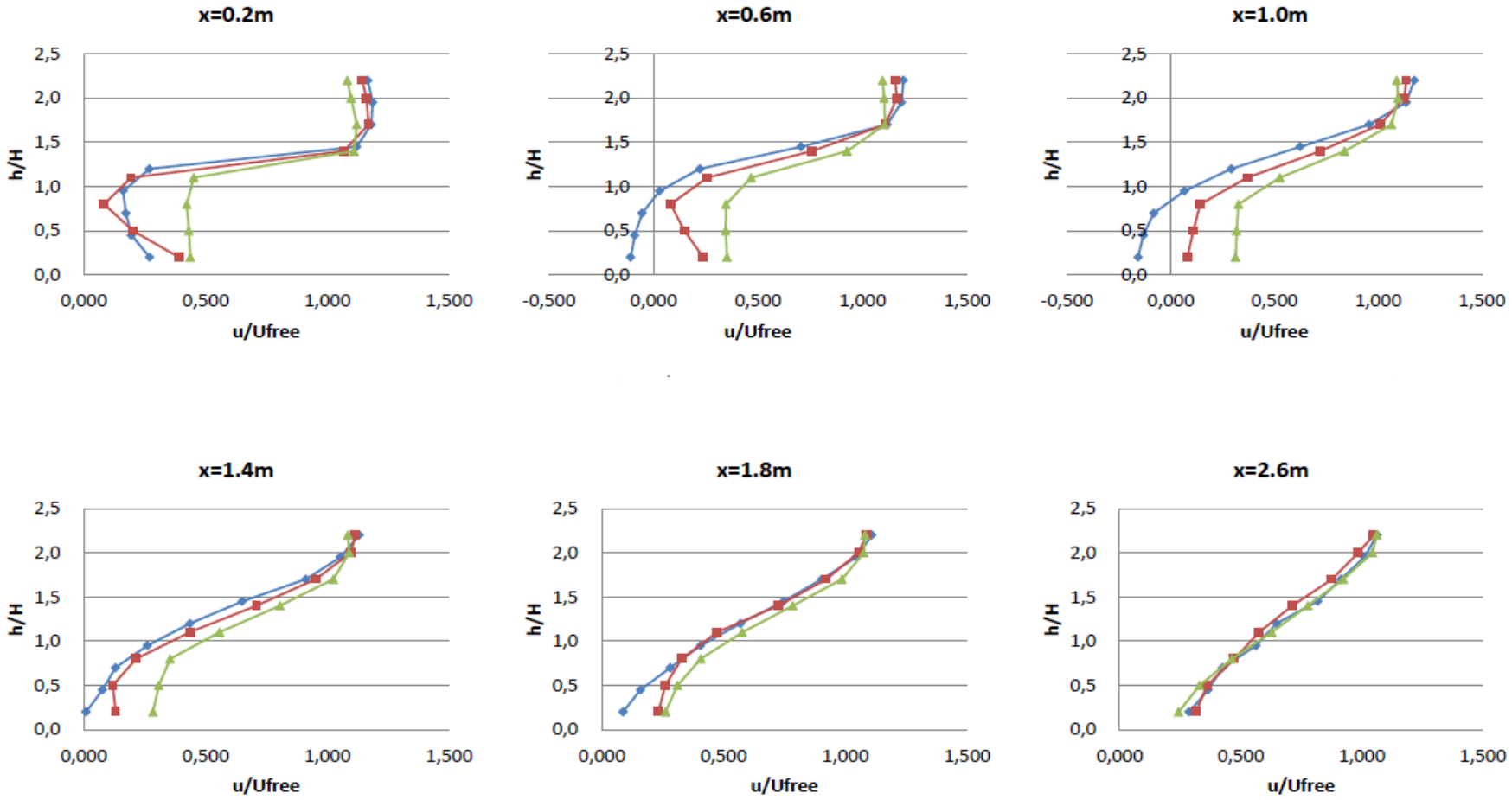

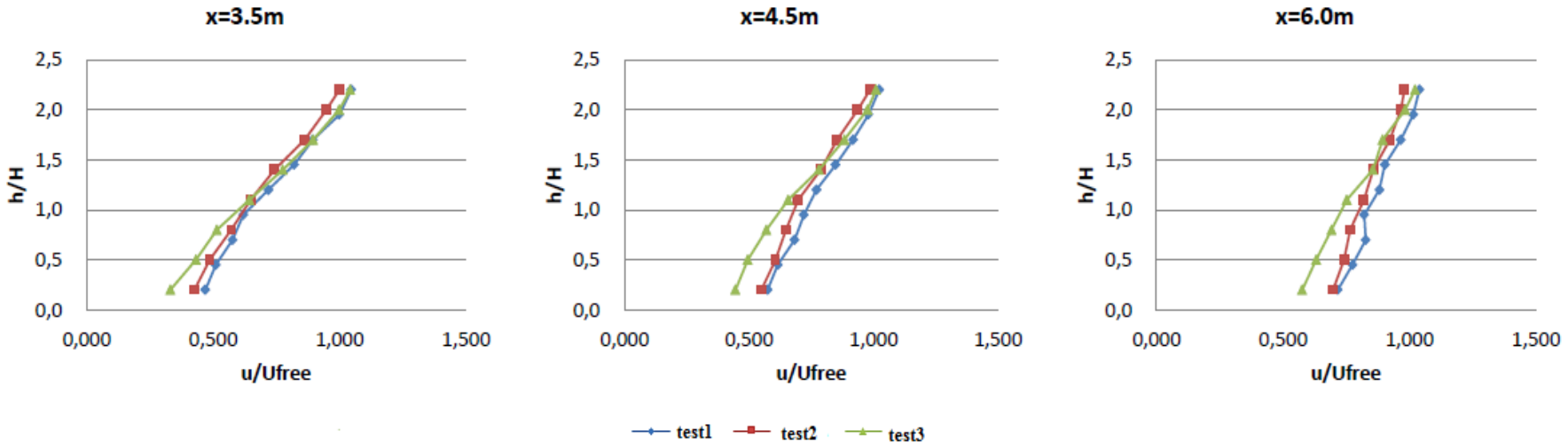

App-Fig. 13: The normalized *u* profiles at different x positions for the case D

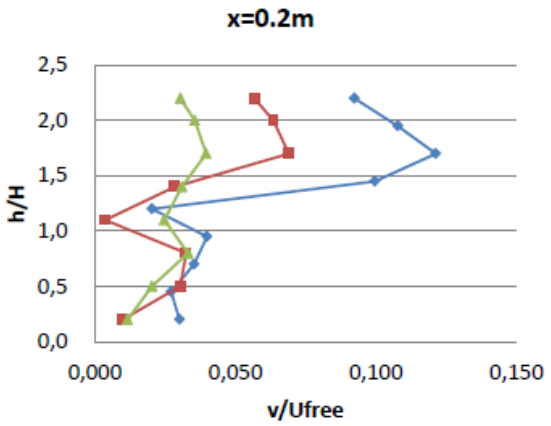
x=0.2m
h/H
2,5
2,0
1,5
1,0
0,5
0,0
0,000
0,050
0,100
0,150
v/Ufree

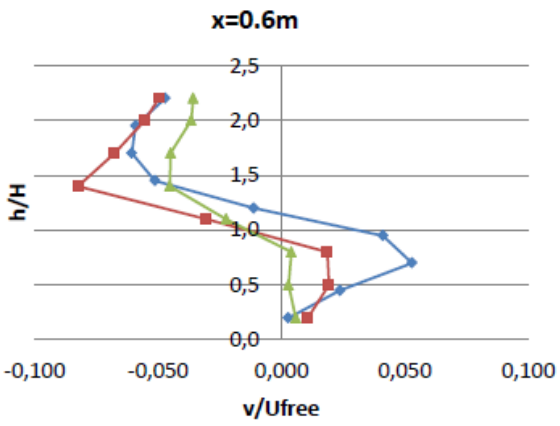
x=0.6m
h/H
2,5
2,0
1,5
1,0
0,5
0,0
-0,100
-0,050
0,000
0,050
0,100
v/Ufree

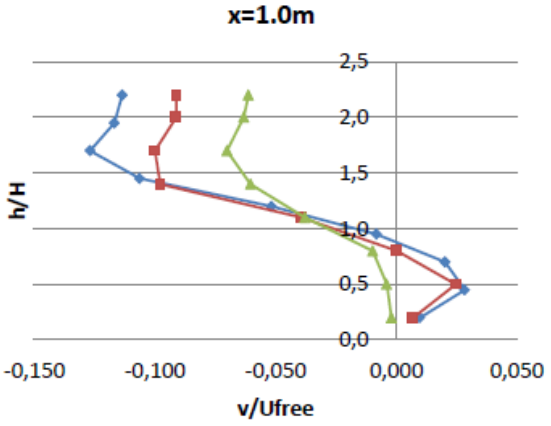
x=1.0m
h/H
2,5
2,0
1,5
1,0
0,5
0,0
-0,150
-0,100
-0,050
0,000
0,050
v/Ufree

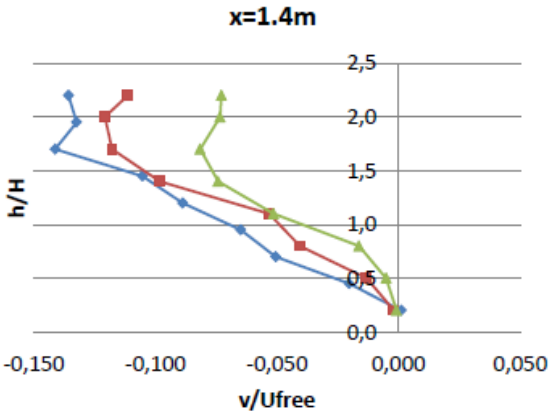
x=1.4m
h/H
2,5
2,0
1,5
1,0
0,5
0,0
-0,150
-0,100
-0,050
0,000
0,050
v/Ufree

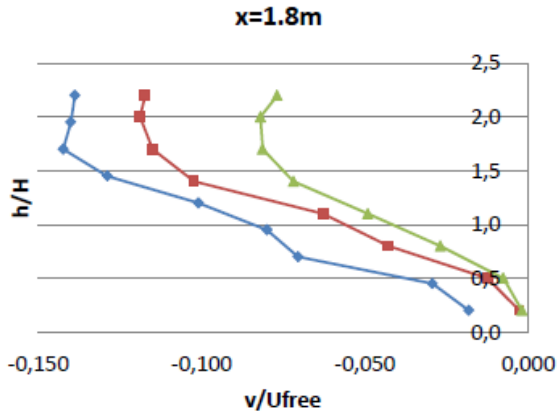
x=1.8m
h/H
2,5
2,0
1,5
1,0
0,5
0,0
-0,150
-0,100
-0,050
0,000
v/Ufree

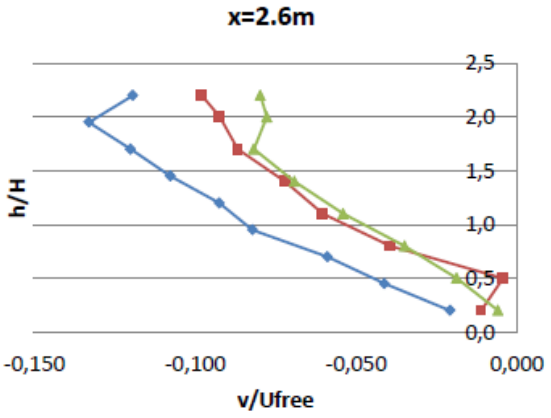
x=2.6m
h/H
2,5
2,0
1,5
1,0
0,5
0,0
-0,150
-0,100
-0,050
0,000
v/Ufree

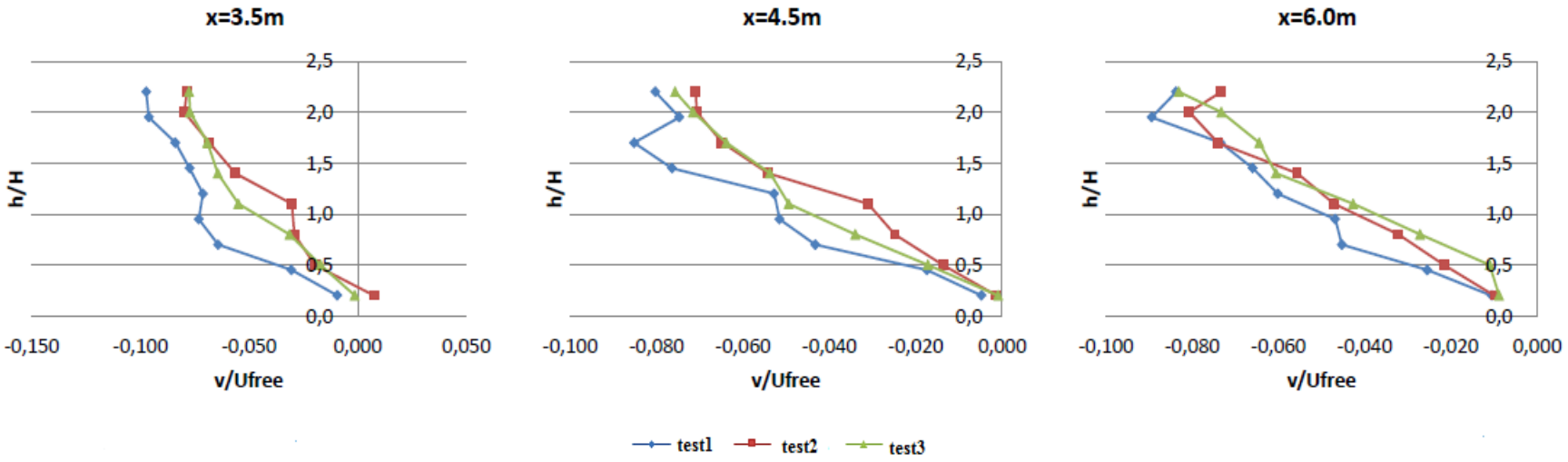

App-Fig. 14: The normalized v profiles at different x positions for the case D

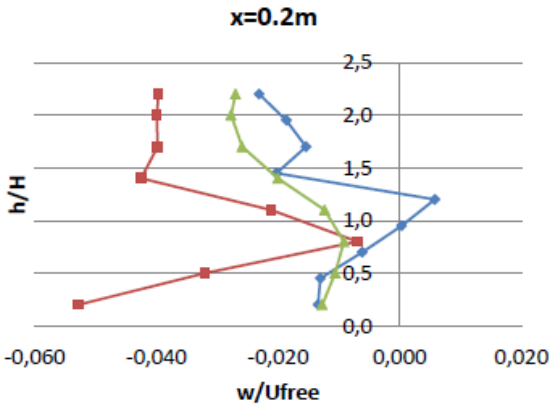
x=0.2m
h/H
2,5
2,0
1,5
1,0
0,5
0,0
-0,060
-0,040
-0,020
0,000
0,020
w/Ufree

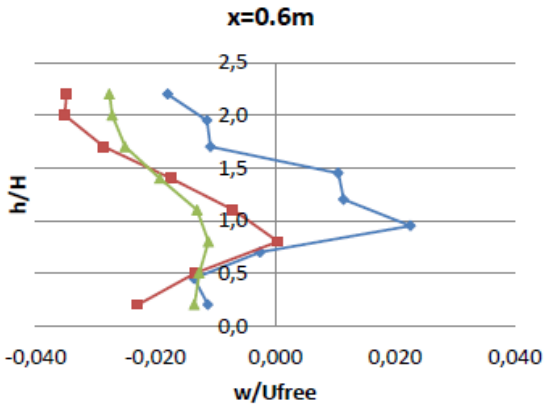
x=0.6m
h/H
2,5
2,0
1,5
1,0
0,5
0,0
-0,040
-0,020
0,000
0,020
0,040
w/Ufree

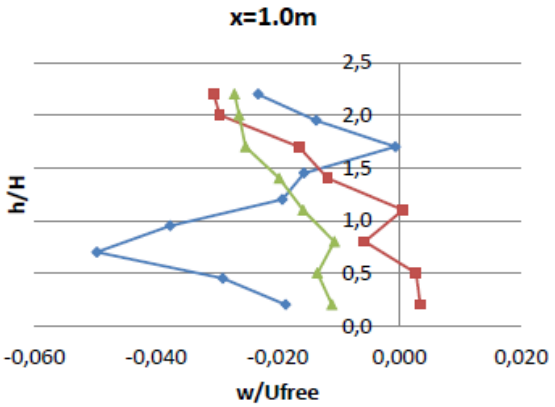
x=1.0m
h/H
2,5
2,0
1,5
1,0
0,5
0,0
-0,060
-0,040
-0,020
0,000
0,020
w/Ufree

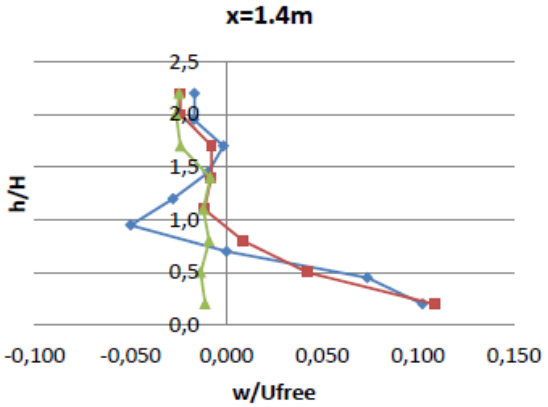
x=1.4m
h/H
2,5
2,0
1,5
1,0
0,5
0,0
-0,100
-0,050
0,000
0,050
0,100
0,150
w/Ufree

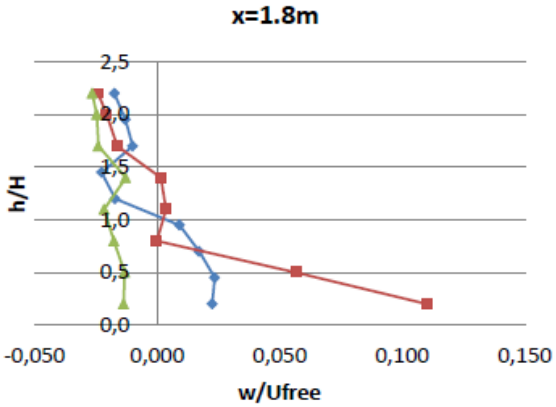
x=1.8m
h/H
2,5
2,0
1,5
1,0
0,5
0,0
-0,050
0,000
0,050
0,100
0,150
w/Ufree

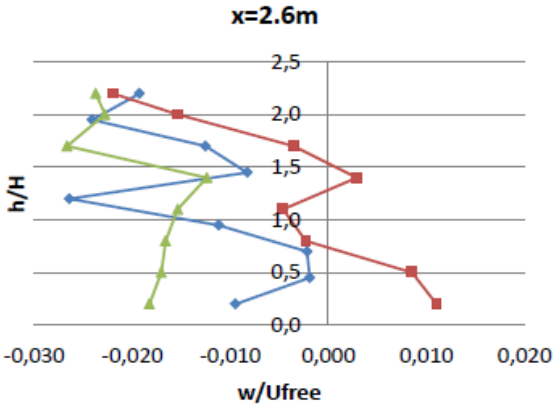
x=2.6m
h/H
2,5
2,0
1,5
1,0
0,5
0,0
-0,030
-0,020
-0,010
0,000
0,010
0,020
w/Ufree

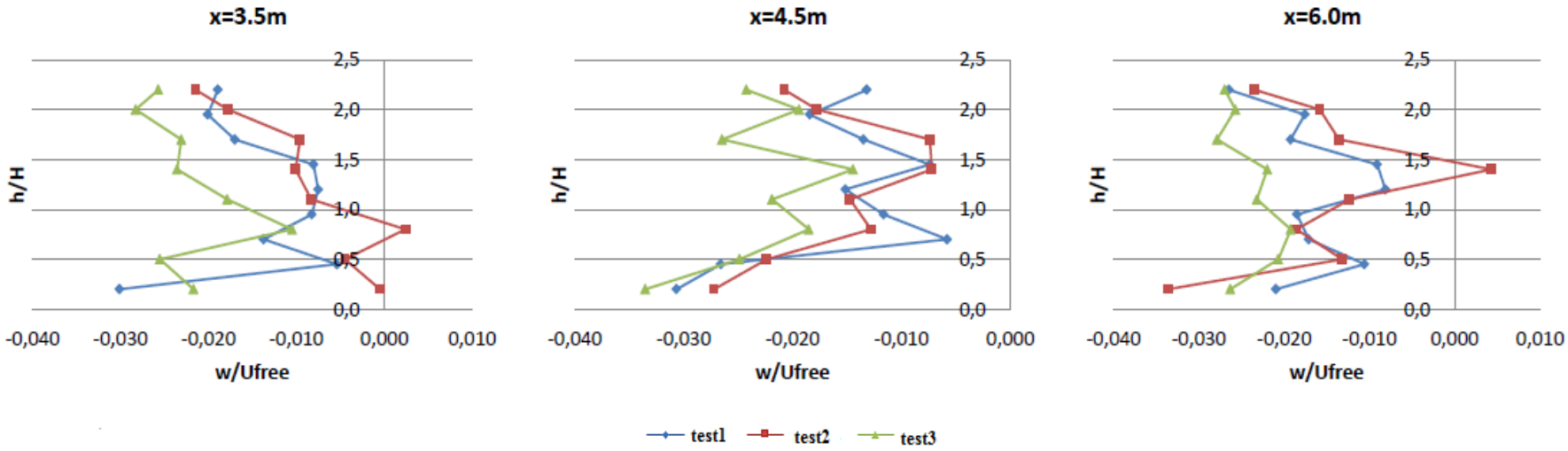

App-Fig. 15: The normalized *w* profiles at different x positions for the case D

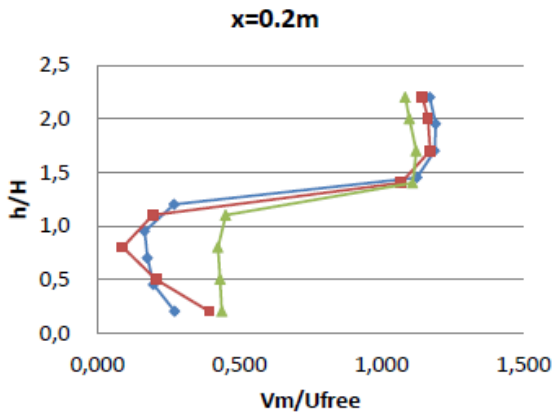
x=0.2m
2,5
2,0
1,5
1,0
0,5
0,0
h/H
0,000
0,500
1,000
1,500
Vm/Ufree

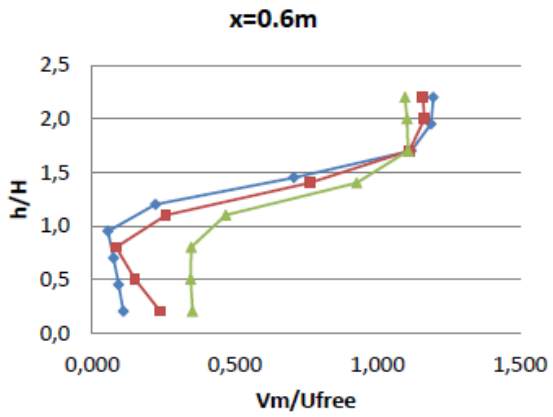
x=0.6m
2,5
2,0
1,5
1,0
0,5
0,0
h/H
0,000
0,500
1,000
1,500
Vm/Ufree

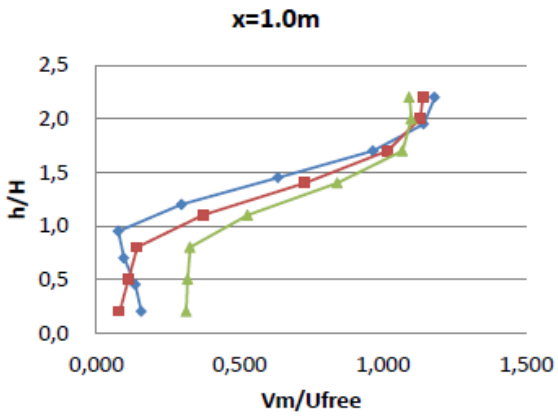
x=1.0m
2,5
2,0
1,5
1,0
0,5
0,0
h/H
0,000
0,500
1,000
1,500
Vm/Ufree

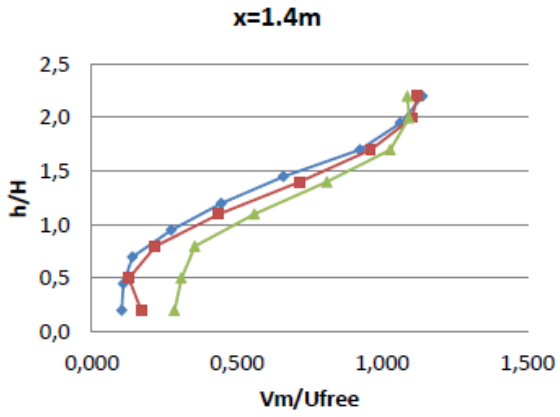
x=1.4m
2,5
2,0
1,5
1,0
0,5
0,0
h/H
0,000
0,500
1,000
1,500
Vm/Ufree

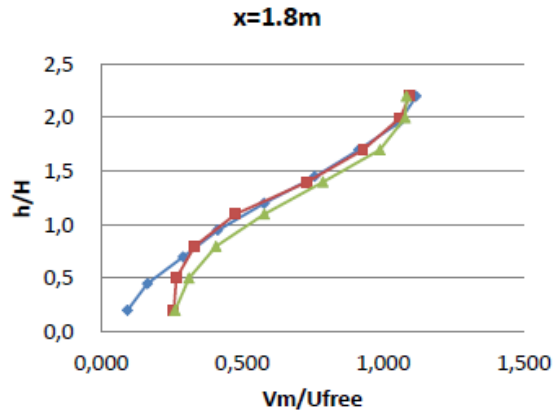
x=1.8m
2,5
2,0
1,5
1,0
0,5
0,0
h/H
0,000
0,500
1,000
1,500
Vm/Ufree

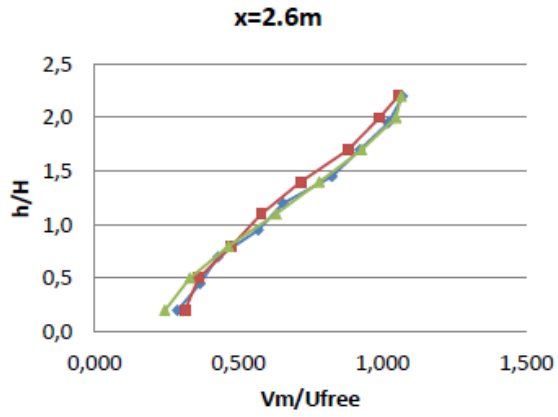
x=2.6m
2,5
2,0
1,5
1,0
0,5
0,0
h/H
0,000
0,500
1,000
1,500
Vm/Ufree

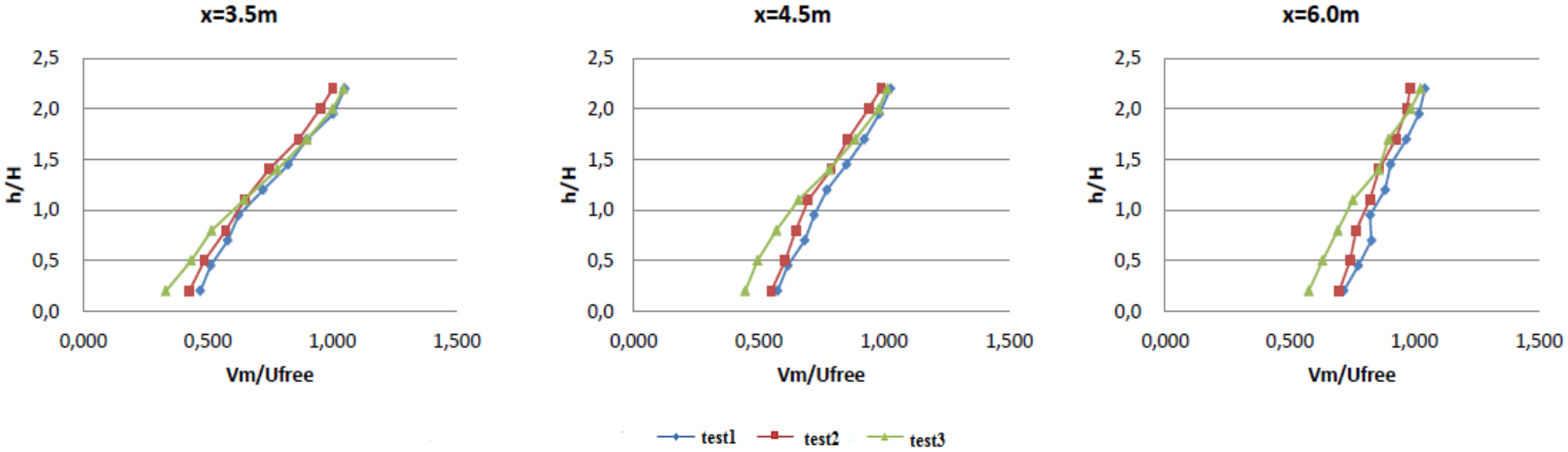

App-Fig. 16: The normalized velocity magnitude profiles at different x positions for the case D

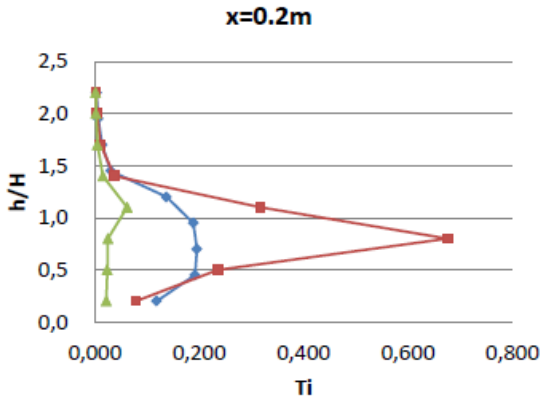
x=0.2m
h/H
2,5
2,0
1,5
1,0
0,5
0,0
0,000
0,200
0,400
0,600
0,800
Ti

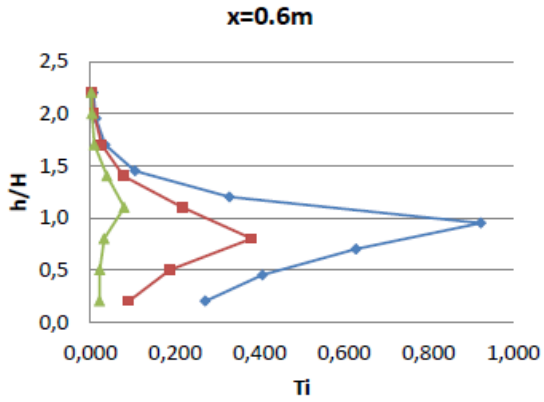
x=0.6m
h/H
2,5
2,0
1,5
1,0
0,5
0,0
0,000
0,200
0,400
0,600
0,800
1,000
Ti

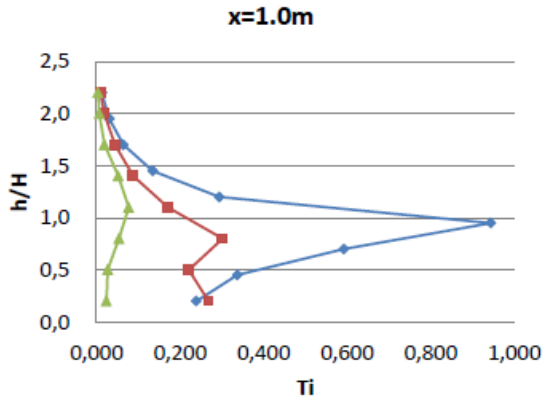
x=1.0m
h/H
2,5
2,0
1,5
1,0
0,5
0,0
0,000
0,200
0,400
0,600
0,800
1,000
Ti

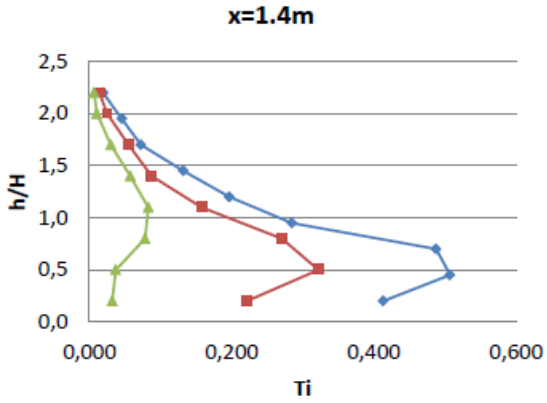
x=1.4m
h/H
2,5
2,0
1,5
1,0
0,5
0,0
0,000
0,200
0,400
0,600
Ti

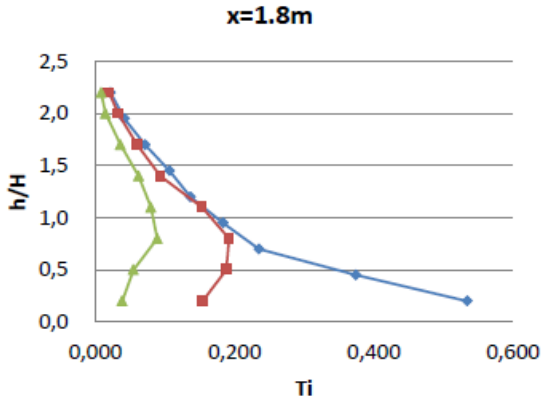
x=1.8m
h/H
2,5
2,0
1,5
1,0
0,5
0,0
0,000
0,200
0,400
0,600
Ti

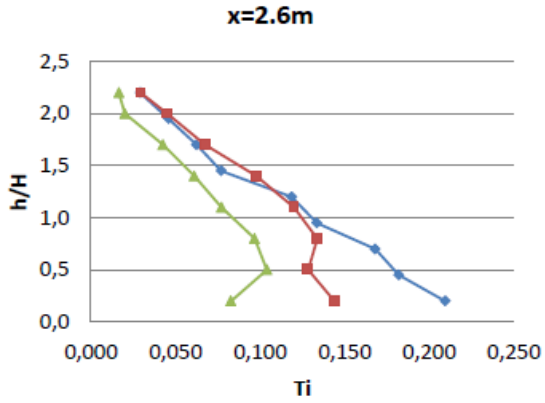
x=2.6m
h/H
2,5
2,0
1,5
1,0
0,5
0,0
0,000
0,050
0,100
0,150
0,200
0,250
Ti

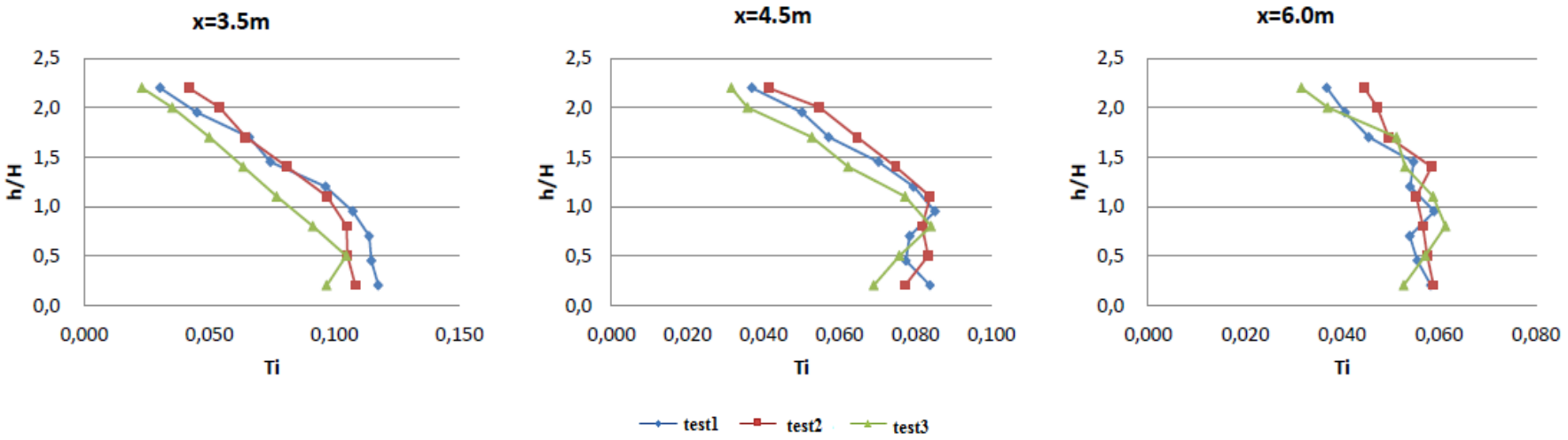

App-Fig. 17: The turbulence intensity profiles at different x positions for the case D

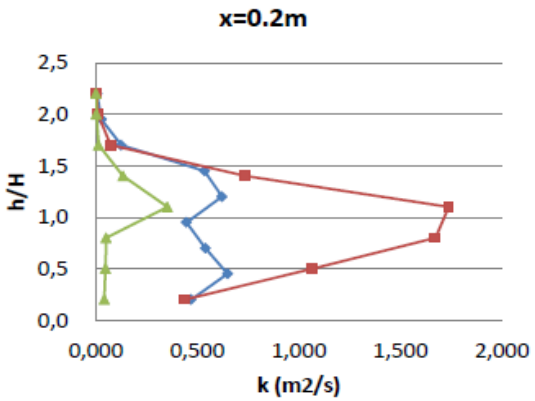
x=0.2m
h/H
2,5
2,0
1,5
1,0
0,5
0,0
0,000
0,500
1,000
1,500
2,000
k (m2/s)

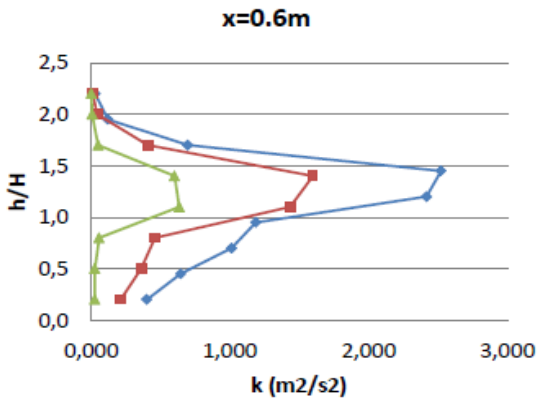
x=0.6m
h/H
2,5
2,0
1,5
1,0
0,5
0,0
0,000
1,000
2,000
3,000
k (m2/s2)

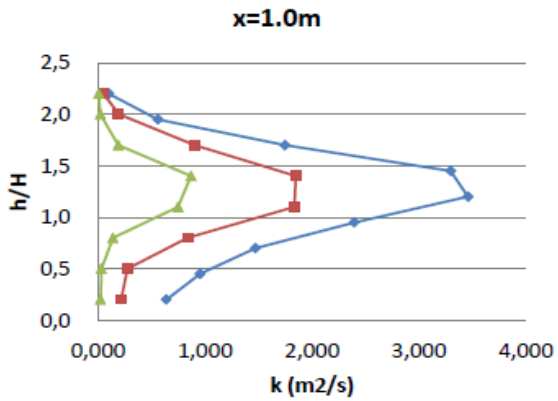
x=1.0m
h/H
2,5
2,0
1,5
1,0
0,5
0,0
0,000
1,000
2,000
3,000
4,000
k (m2/s)

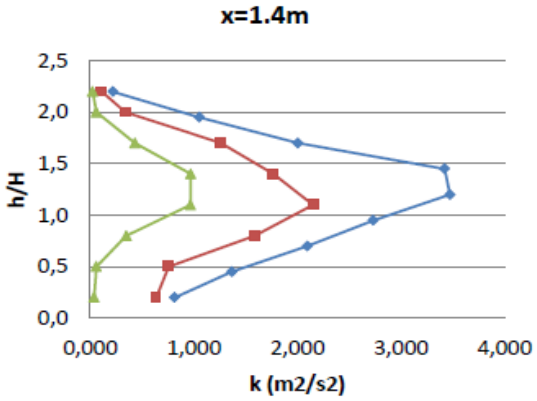
x=1.4m
h/H
2,5
2,0
1,5
1,0
0,5
0,0
0,000
1,000
2,000
3,000
4,000
k (m2/s2)

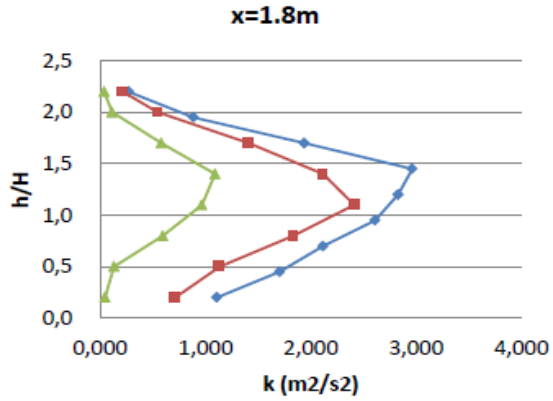
x=1.8m
h/H
2,5
2,0
1,5
1,0
0,5
0,0
0,000
1,000
2,000
3,000
4,000
k (m2/s2)

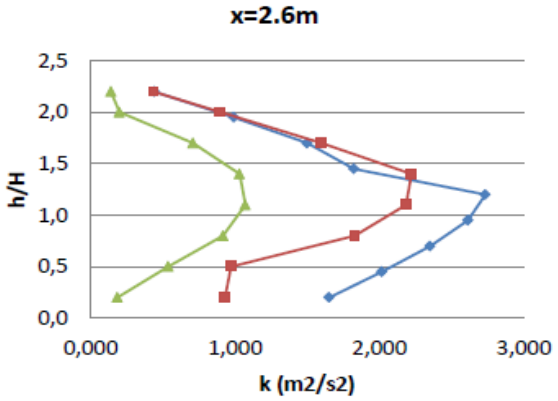
x=2.6m
h/H
2,5
2,0
1,5
1,0
0,5
0,0
0,000
1,000
2,000
3,000
k (m2/s2)

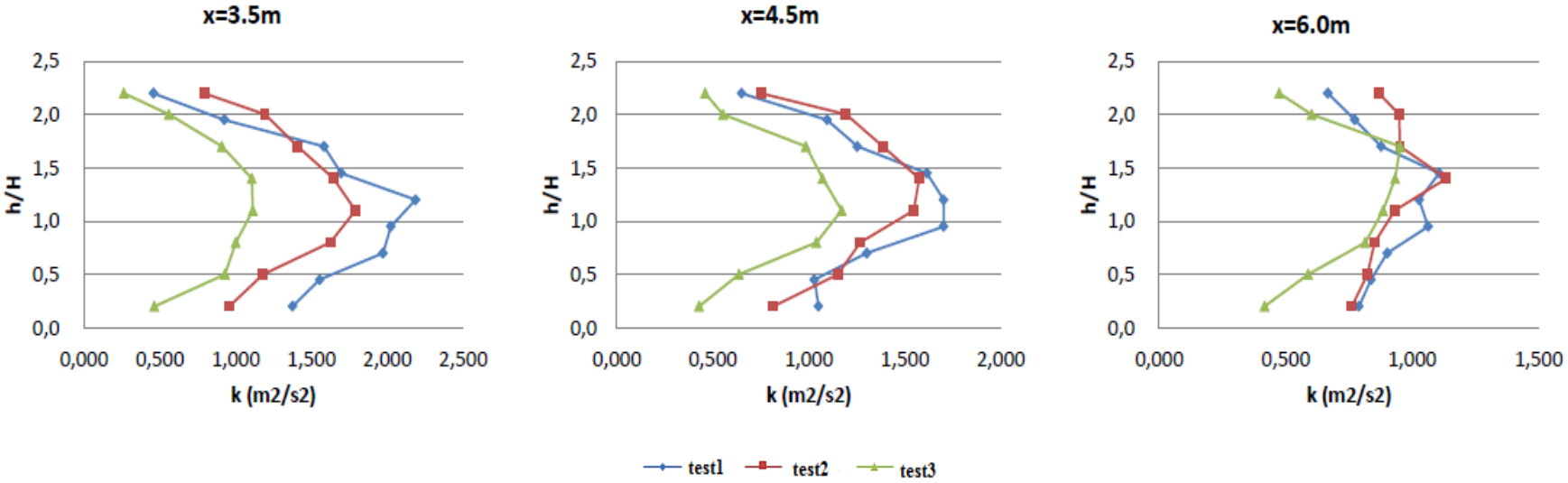

App-Fig. 18: The turbulent kinetic energy profiles at different x positions for the case D

IV. APPENDIX D: THE EXPERIMENTAL CHARTS FOR THE DEVELOPMENT OF SNOW DEPOSITION BEHIND FENCES

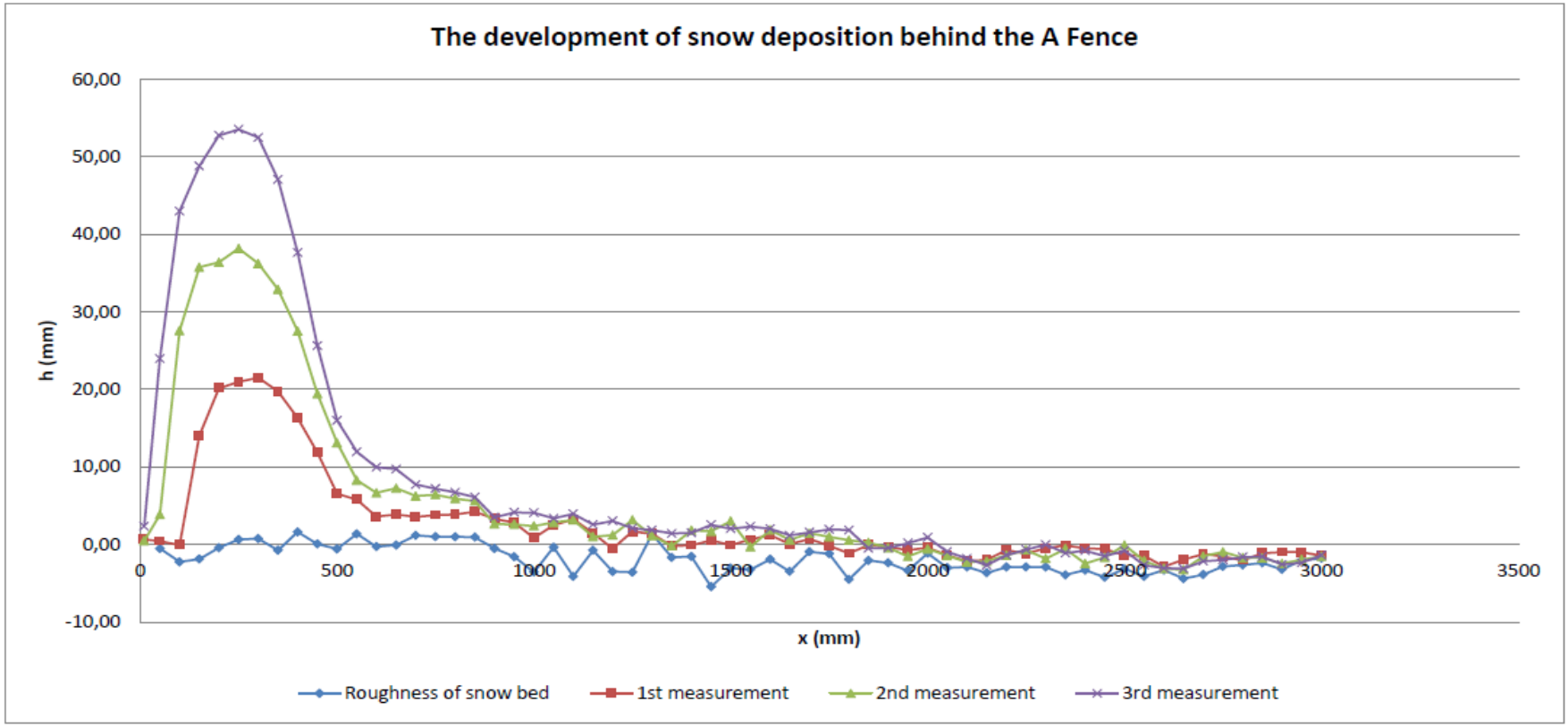

App-Fig. 19: The development of snow deposition behind the A fence. Each measurement taken after running the wind tunnel for 10 minutes

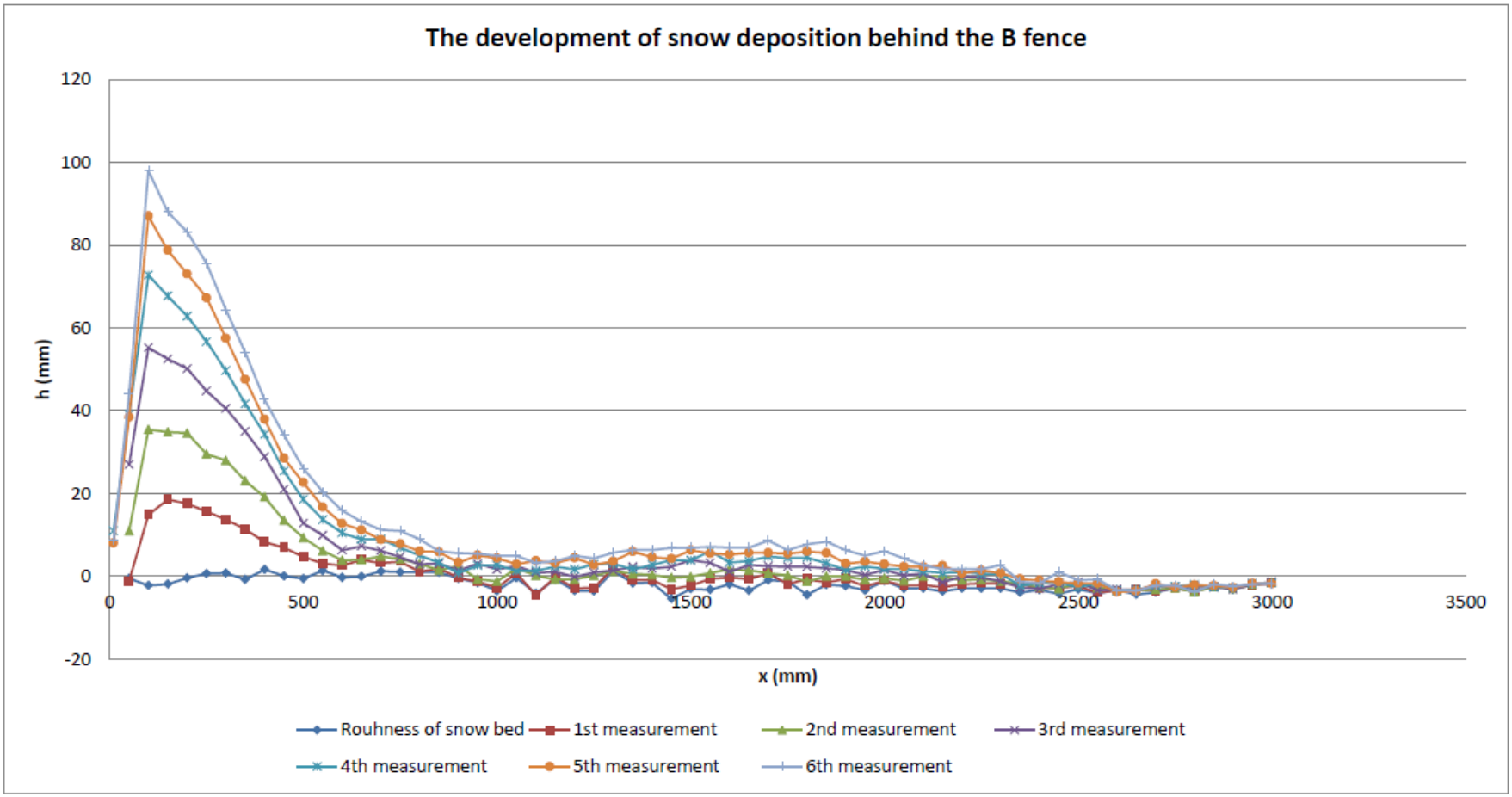

App-Fig. 20: The development of snow deposition behind the B fence. Each measurement taken after running the wind tunnel for 10 minutes

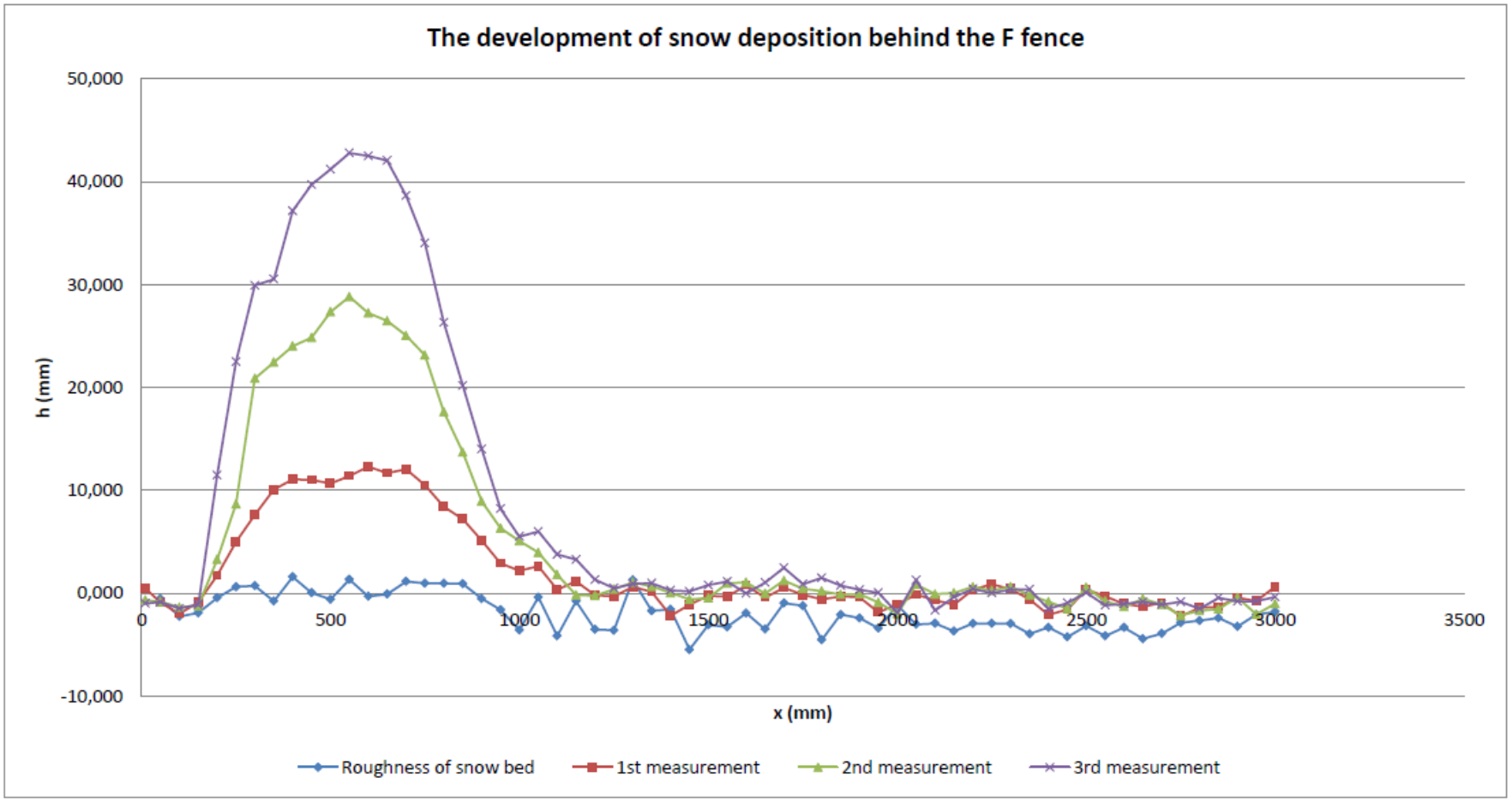

App-Fig. 21: The development of snow deposition behind the F fence. Each measurement taken after running the wind tunnel for 10minutes

V. APPENDIX E: THE SIMULATION AND EXPERIMENTAL RESULTS AT FREESTREAM OF 15M/S

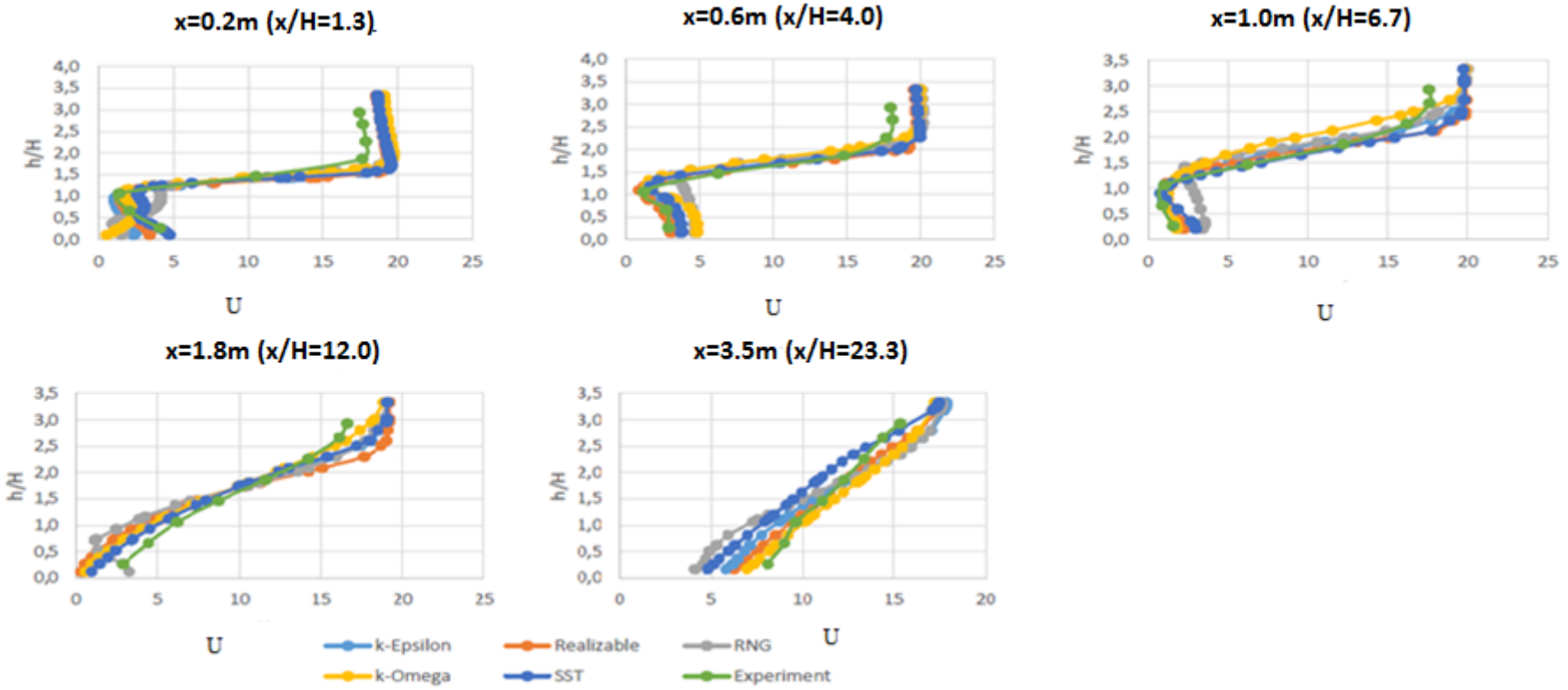

App-Fig. 22: Comparison of velocity magnitudes between simulation and experiment at freestream velocity of 15m/s

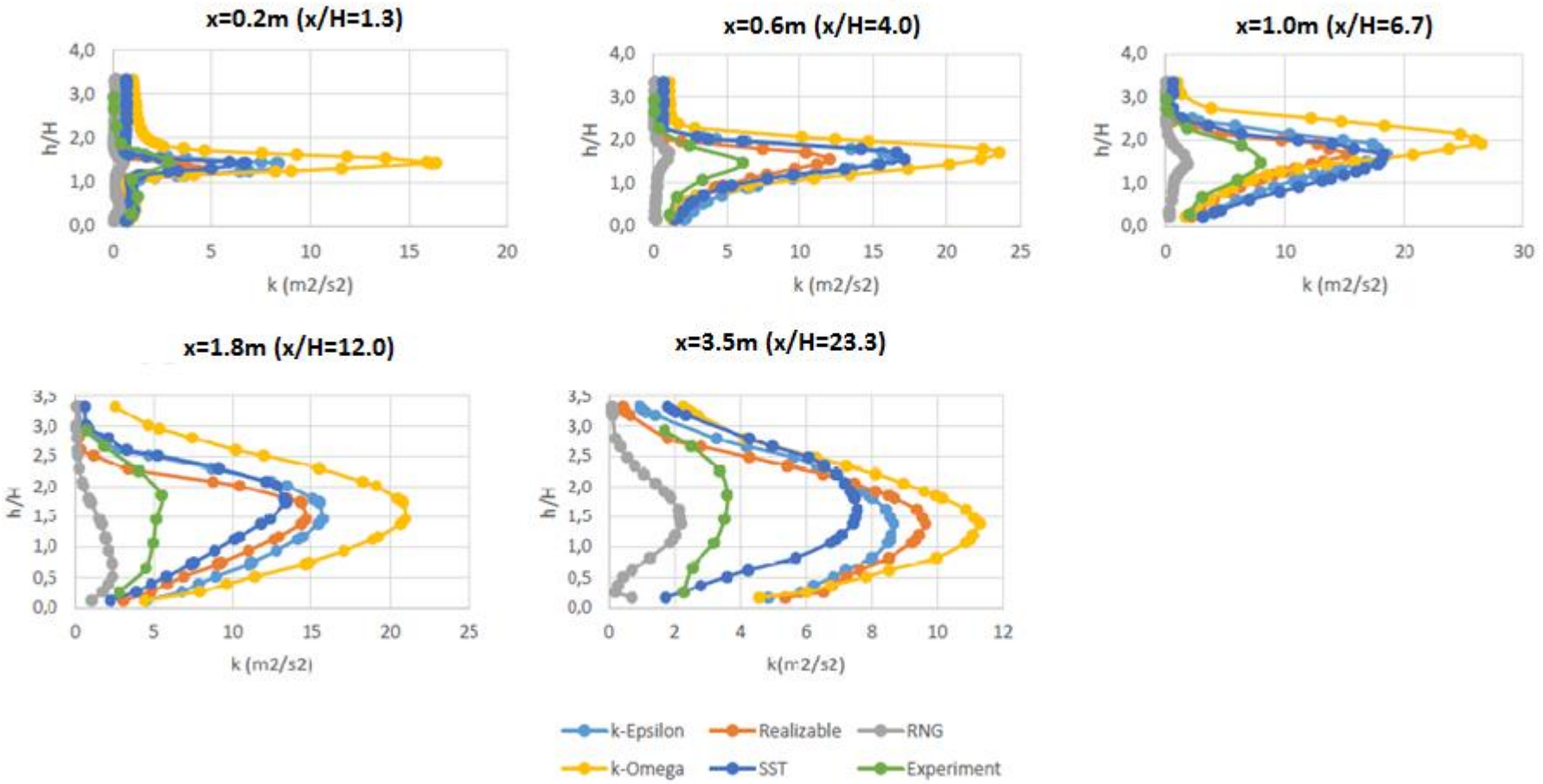

App-Fig. 23: Comparisons of turbulent kinetic energies between simulation and experiment at the freestream velocity of 15m/s

VI. APPENDIX F: THE SIMULATION RESULTS FOR THE FENCES WITH DIFFERENT SIZES OF HOLES

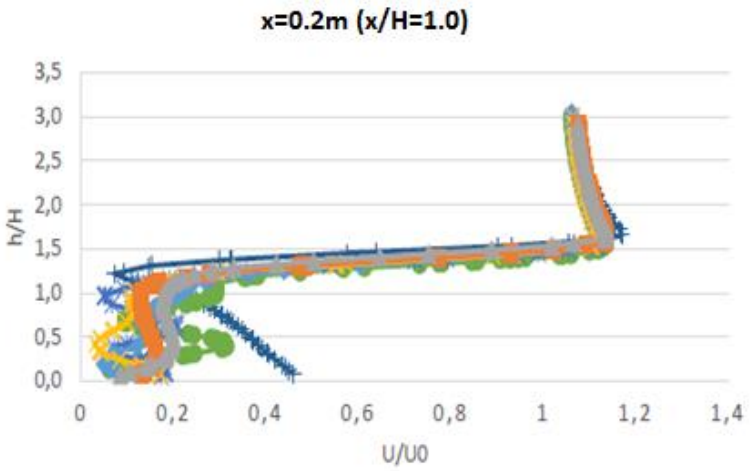

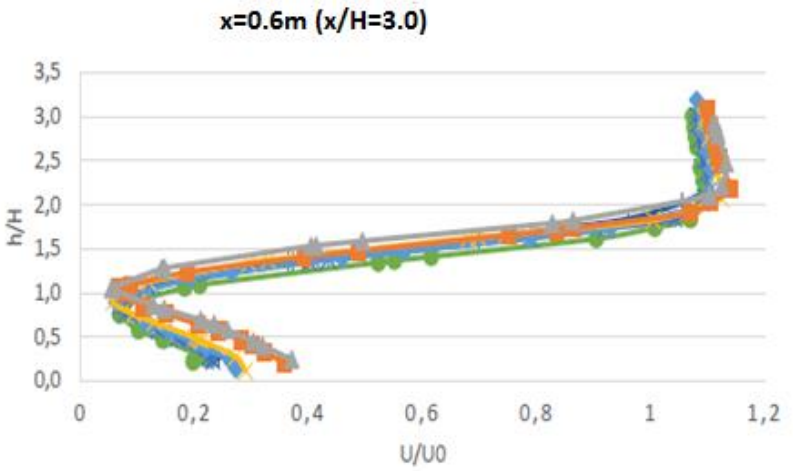

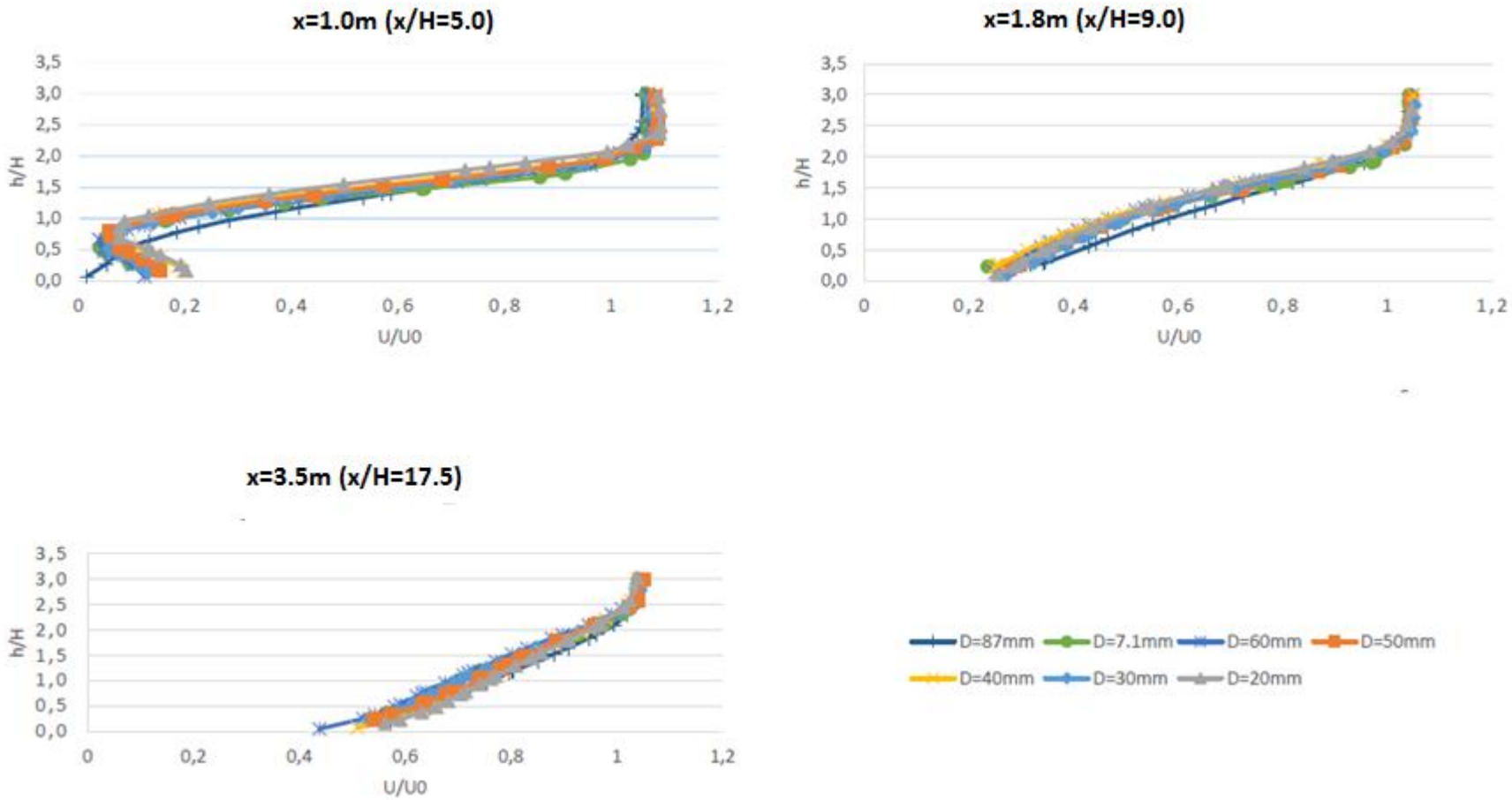

App-Fig. 24: The normalized velocity magnitude profiles for the fences with different sizes of holes

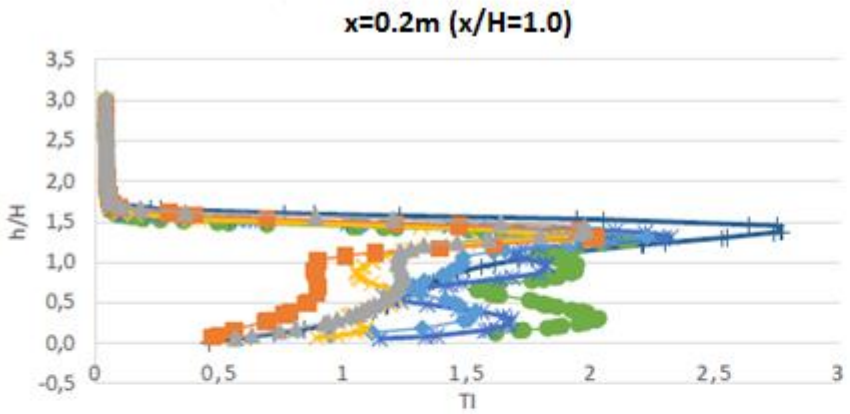
x=0.2m (x/H=1.0)
h/H
TI
3,5
3,0
2,5
2,0
1,5
1,0
0,5
0,0
-0,5
0
0,5
1
1,5
2
2,5
3

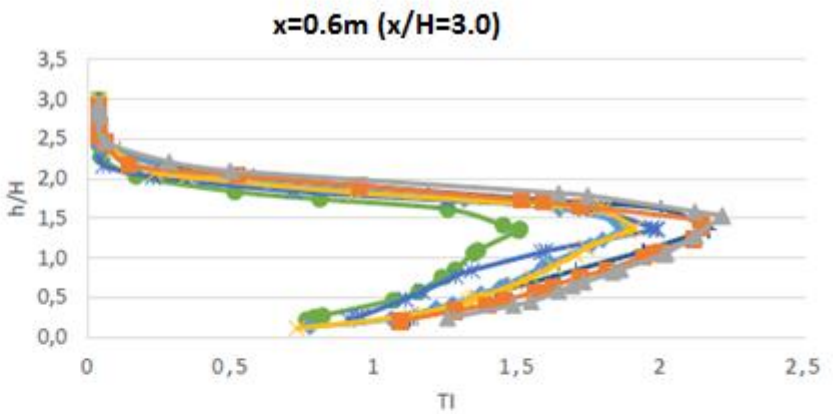
x=0.6m (x/H=3.0)
h/H
TI
3,5
3,0
2,5
2,0
1,5
1,0
0,5
0,0
0
0,5
1
1,5
2
2,5

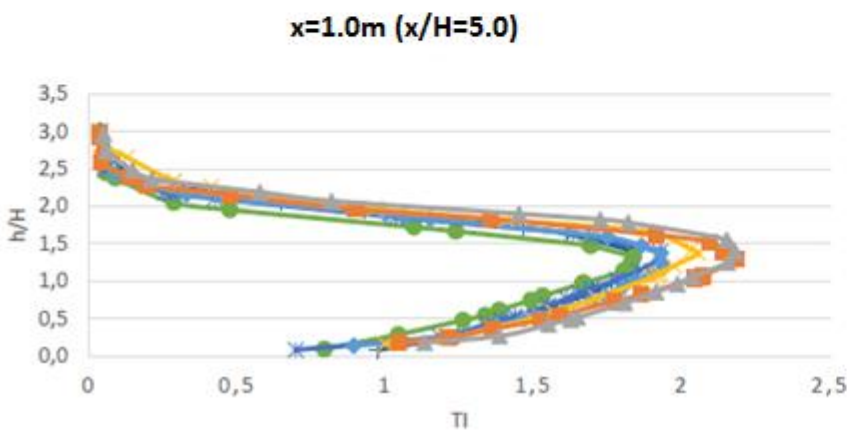
x=1.0m (x/H=5.0)
h/H
TI
3,5
3,0
2,5
2,0
1,5
1,0
0,5
0,0
0
0,5
1
1,5
2
2,5

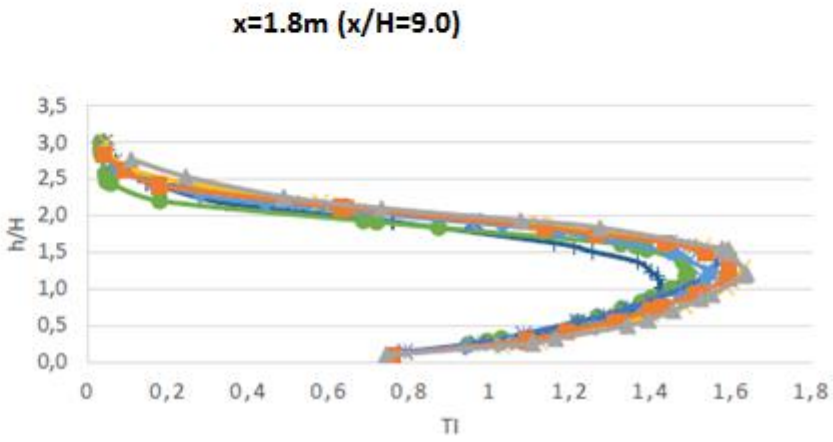
x=1.8m (x/H=9.0)
h/H
TI
3,5
3,0
2,5
2,0
1,5
1,0
0,5
0,0
0
0,2
0,4
0,6
0,8
1
1,2
1,4
1,6
1,8

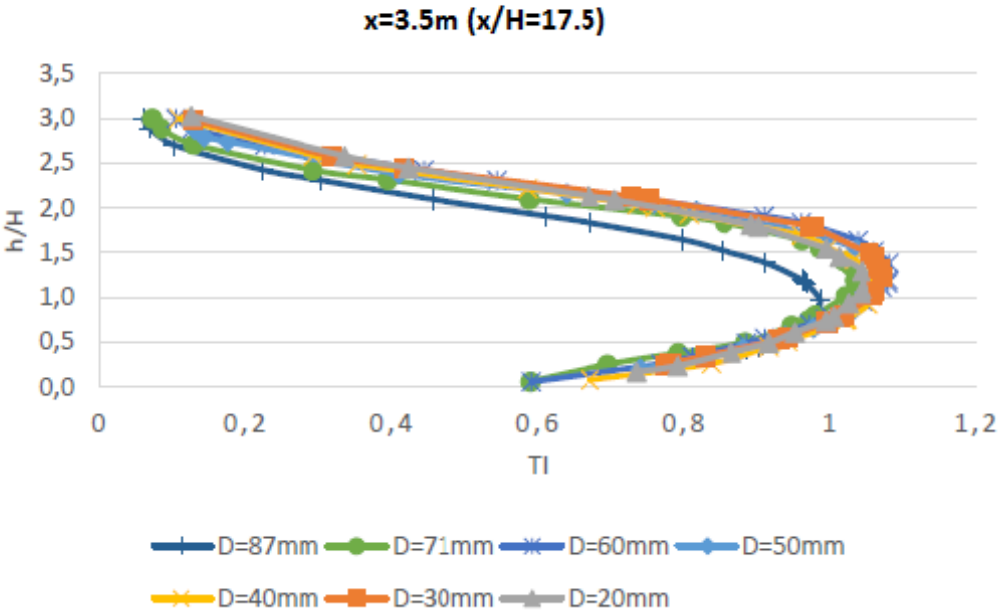

App-Fig. 25: The turbulence intensity profiles for the fences with different sizes of holes